A STUDY OF UNDERBALANCED DRILLING APPLICATION FOR GRANITE BASEMENTS IN VIETNAM

Cuong Nguyen

Submitted for the degree of Doctor of Philosophy

Heriot-Watt University

Institute of Petroleum Engineering

April 2009

ABSTRACT

Underbalanced drilling (UBD) has gained popularity during the recent years as it provides a method to prevent formation damage, minimize lost circulation risks, and increase the rate of penetration. However, drilling with a bottomhole pressure less than the formation pore pressure will often increase the risk of borehole instability due to the shear or compression failure of the rock adjacent to the wellbore. The extent of rock failure is related directly to the pressure in the annulus between the drillpipe, collars and the wellbore which can only be calculated through modelling multiphase flow in the drilling system. The relationship between rock failure and wellbore hydraulics becomes more complex due to the appearance of the influx formation fluid in UBD. Therefore, the aim of this research is to describe methods to solve the complex interaction of wellbore stability, rock yielding, collapse, wellbore hydraulics, and production capacity during UBD operations.

To achieve the aim, analytical and numerical solutions have been codified into two programs WELLST, and UBDRILL. Commercial software packages such as ABAQUS, PERFORM, HYMOD were also used to model the process. Field data from granite basement reservoirs of Basin X, Vietnam were used as the parameters input into the model to calculate. This research includes:

- An analysis of the influences of time dependence, thermal and hydraulic diffusivity, wellbore pressure changes, inclination and azimuth variation, poroelastic and thermo-poroelastic deformation, cooling and heating effects on wellbore stability in UBD.
- An analysis of pressure, temperature, fluid properties distribution in the annulus and inside the drillpipe while UBD.
- An analysis of the suggested liquid gas rate window (LGRW) which gives field engineers flexibility in the selection of liquid and gas injection rates on the drilling site when UBD is applied.
- An estimation of production capacity in UBD operations.

These results were obtained by analyzing the field data of granite basement formations and clastic formations of Basin X, Vietnam which is under compression in a strike-slip environment.

ACKNOWLEDGEMENTS

I would like to express my sincere gratitude to Prof. Brian Smart and Dr. Jim Somerville for their guidance, and encouragement during this research. Without their support, this work would have not been accomplished.

I would like to acknowledge the suggestions, and invaluable helps provided by Dr. Min Jin, Dr. Peter Olden, and Mr. Roger Hutcheon during my studies at the Institute of Petroleum Engineering, Heriot Watt University.

Thanks should also go to Department of Geology and Petroleum – HCM City University of Technology for their support during my studying time at UK.

Financial support from Ministry of Education and Training of Vietnam, and Institute of Petroleum Engineering, Heriot Watt University on Underbalanced Drilling Project are gratefully acknowledged.

Finally, I would like to thank my family for their love and support. My gratitude is endless to my wife My Tran for her understanding and support during the long period time required to complete this research.

ACADEMIC REGISTRY
Research Thesis Submission

Name*:*	CUONG NGUYEN		
School/PGI:	INSTITUTE OF PETROLEUM ENGINEERING		
Version: *(i.e. First, Resubmission, Final)*	Final	Degree Sought (Award **and** Subject area)	PhD

Declaration

In accordance with the appropriate regulations I hereby submit my thesis and I declare that:

1) the thesis embodies the results of my own work and has been composed by myself
2) where appropriate, I have made acknowledgement of the work of others and have made reference to work carried out in collaboration with other persons
3) the thesis is the correct version of the thesis for submission and is the same version as any electronic versions submitted*.
4) my thesis for the award referred to, deposited in the Heriot-Watt University Library, should be made available for loan or photocopying and be available via the Institutional Repository, subject to such conditions as the Librarian may require
5) I understand that as a student of the University I am required to abide by the Regulations of the University and to conform to its discipline.

* *Please note that it is the responsibility of the candidate to ensure that the correct version of the thesis is submitted.*

Signature of Candidate*:*		Date:	

Submission

Submitted By *(name in capitals):*	
Signature of Individual Submitting:	
Date Submitted:	

For Completion in Academic Registry

Received in the Academic Registry by *(name in capitals):*			
Method of Submission *(Handed in to Academic Registry; posted through internal/external mail):*			
*E-thesis Submitted (**mandatory from January 2009)***			
Signature:		Date:	

TABLE OF CONTENTS

ABSTRACT---------- ii

ACKNOWLEDGEMENTS ---------- iii

DECLARATION STATEMENT---------- iv

TABLE OF CONTENTS ---------- v

LIST OF TABLES ---------- ix

LIST OF FIGURES ---------- xi

GLOSSARY ----------xxi

LIST OF PUBLICATIONS ---------- xxvii

CHAPTER 1

INTRODUCTION ---------- 1

1.1. Review of Underbalanced Drilling Technique ---------- 1

1.1.1. Benefits of UBD ---------- 1

1.1.2. Disadvantages of UBD ---------- 4

1.1.3. UBD Techniques ---------- 5

1.2. Prospect of UBD Application in Vietnam ---------- 7

1.3. The Appication of UBD for Basin X, South of Vietnam ---------- 8

1.3.1. Overview of the Basin X ---------- 9

1.3.2. Previous Drilling Problems ---------- 10

1.3.3. Investigating for UBD in the Basin X ---------- 10

1.4. The Content of Study ---------- 11

CHAPTER 2

WELLBORE STABILITY EVALUATION IN UBD ---------- 14

2.1. Introduction ---------- 14

2.2. Literature Reviews ---------- 14

2.3. Studies on Wellbore Stability of the Granite Basement in Basin X, Vietnam - 18

2.3.1. Lithology Summary for the Granite Basement of Basin X ---------- 19

2.3.2. Geomechanical Conditions ---------- 22

2.3.3. Rock Strength Parameters ---------- 26

2.4. Wellbore Stability Modelling ---------- 28

2.4.1. Stress around Boreholes ---------- 28

2.4.2. Failure criteria ---------- 39

CHAPTER 3

MODELLING MULTIPHASE FLOW IN UBD ---------- 44

3.1. Introduction ---------- 44

3.2. Modelling Gasified Liquid Flow in UBD ---------- 44

3.2.1. Literature Reviews ---------- 44

3.2.2. Modifications and the Innovative Method ---------- 47

3.3. Modelling Foam Flow in UBD ---------- 63

3.3.1. Literature Reviews ---------- 63

3.3.2. Modifications and the Innovative Method ---------- 66

3.4. Cuttings Carrying Capacity ---------- 71

3.4.1. Minimum kinetic energy ---------- 71

3.4.2. Minimum velocity criterion ---------- 72

CHAPTER 4

COUPLING PRODUCTIVITY IN UBD ---------- 75

4.1. Introduction ---------- 75

4.2. Inflow Performance Relationship ---------- 75

4.2.1. Darcy's Law ---------- 75

4.2.2. Vogel Method ---------- 79

4.2.3. IPR for Horizontal Wells ---------- 84

4.3. Coupling Productivity in UBD ---------- 85

4.3.1. Introduction to PERFORM 3.0 ---------- 85

4.3.2. Coupling Productivity in UBD ---------- 86

CHAPTER 5

WELLST & UBDRILL ---------- 90

5.1. WELLST ---------- 90

5.1.1. Input Data Protocol ---------- 90

5.1.2. Matlab Program ---------- 91

5.1.3. Output Data Protocol ---------- 94

5.2. UBDRILL ---------- 95

5.2.1. Input Data Protocol ---------- 95

5.2.2. Matlab Program ---------- 97

5.2.3. Output Data Protocol ---------- 112

CHAPTER 6

APPLICATION ---------- 115

6.1. Wellbore Stability Evaluation in UBD ---------- 115

6.1.1. ABAQUS - a commercial finite element software ---------- 115

6.1.2. WELLST ---------- 116

6.1.3. Model Definition ---------- 116

6.1.4. Results and Discussions ---------- 120

6.2. Gasified Liquid Drilling Analysis in UBD ---------- 192

6.2.1. UBDRILL ---------- 192

6.2.2. Input Data ---------- 193

6.2.3. Results of Modelling Gasified Flow ---------- 196

6.2.4. Results of Planning LGRW ---------- 205

6.2.5. Results of Coupling Productivity in UBD ---------- 210

6.2.6. Comparing the Results Produced by UBDRILL and the Analytical Solution of Guo and Ghalambor ---------- 211

6.2.7. Analyzing the Sensitivity of Input Data ---------- 213

6.2.8. Verifying the Influence of Solid Phase ---------- 217

6.2.9. Selecting Compressor ---------- 218

6.2.10. Comparing UBDRILL and HYDMOD ---------- 219

6.2.11. Estimating the Convergence ---------- 221

6.3. Foam Drilling Analysis in UBD ---------- 222

6.3.1. Input data ---------- 223

6.3.2. Results of Modelling Foam Flow ---------- 223

6.3.3. Results of Planning LGRW ---------- 224

6.3.4. Results of Coupling Productivity in UBD ---------- 227

6.3.5. Results of Foam Quality in UBD ---------- 227

CHAPTER 7

CONCLUSIONS AND RECOMMENDATIONS ---------- 230

7.1. Conclusions ---------- 230

7.2. Recommendations ---------- 235

APPENDICES ---------- 230

PUBLISHED PAPERS ---------- 255

REFERENCES ---------- 268

LIST OF TABLES

Table 4.1. *Unit for Darcy's Law*

Table 6.1. *Input data*

Table 6.2. *Comparing thermal and hydraulic diffusions*

Table 6.3. *The difference of elastic, poroelastic and thermo-poroelastic formation effects on wellbore stability in the basement section (a = 0^o, t=10 s, and P_{wf} = 31 MPa)*

Table 6.4. *The difference of elastic, poroelastic and thermo-poroelastic formation effects on wellbore stability in the basement section (a = 30^o, t=10 s, and P_{wf} = 31 MPa)*

Table 6.5. *The difference in elastic, poroelastic and thermo-poroelastic formation effects to wellbore stability in the basement section (a = 60^o, t=10 s, and P_{wf} = 31 MPa)*

Table 6.6. *The difference of elastic, poroelastic and thermo-poroelastic formation effects on wellbore stability in the basement section (a = 90^o, t=10 s, and P_{wf} = 31 MPa)*

Table 6.7. *The difference of elastic, poroelastic and thermo-poroelastic formation effects on wellbore stability in the clastic section (a = 0^o, t=10 s, and P_{wf} = 21.58 MPa)*

Table 6.8. *The difference of elastic, poroelastic and thermo-poroelastic formation effects on wellbore stability in the clastic section (a = 30^o, t=10 s, and P_{wf} = 21.58 MPa)*

Table 6.9. *The difference of elastic, poroelastic and thermo-poroelastic formation effects on wellbore stability in the clastic section (a = 60^o, t=10 s, and P_{wf} = 21.58 MPa)*

Table 6.10. *The difference of elastic, poroelastic and thermo-poroelastic formation effects on wellbore stability in the clastic section (a = 90^o, t=10 s, and P_{wf} = 21.58 MPa)*

Table 6.11. *Drilling data*

Table 6.12. *PVT data*

Table 6.13. *Well structure*

Table 6.14. *Inflow Performance Relationship*

Table 6.15. *Pressure distribution in the annulus*

Table 6.16. *Dynamic BHP*

Table 6.17. *Hydrostatic BHP*

Table 6.18. *Liquid Gas Rate Window (LGRW)*

Table 6.19. *Formation fluid influx flow rate*

Table 6.20. *Comparing results produced by UBDRILL and the analytical solution of Guo and Ghalambor*

Table 6.21. *Sensitivity Analysis of wellhead pressure*

Table 6.22. *Sensitivity Analysis of Rate of Penetration*

Table 6.23. *Sensitivity Analysis of Mud density*

Table 6.24. *Sensitivity Analysis of Gas gravity*

Table 6.25. *Influence of solid phase*

Table 6.26. *Comparing results produced by UBDRILL and HYDMOD*

Table 6.27. *The result of convergence analysis*

Table 6.28. *PVT data*

Table 6.29. *Dynamic BHP*

Table 6.30. *Hydrostatic BHP*

Table 6.31. *Liquid Gas Rate Window (LGRW)*

Table 6.32. *Formation fluid influx flow rate*

LIST OF FIGURES

Fig 1.1. *Compressible fluids Technology*

Fig 2.1. *Location of the Basin X*

Fig 2.2. *Random seismic line along a typical well path in the Basin X*

Fig 2.3. *Stratigraphy column of a typical well in Basin X*

Fig 2.4. *Formation and Fracture pressure curves of Basin X*[6]

Fig 2.5. *Leak off test data in Basin X*

Fig 2.6. *In-situ stresses in a strike-slip fault type case of Basin X*

Fig 2.7. *The stress map of Basin X*

Fig 2.8. *The estimated UCS (unconfined compressive strength) of Basin X versus TVD*

Fig 2.9. *Sonic distribution versus TVD*

Fig 2.10. *UCS distribution versus TVD*

Fig 2.11. *Definition of wellbore orientation parameters*

Fig 2.12. *Shape of the g function for various values of* t/t_i

Fig 2.13. *Shape of the Bessel function of the first kind*

Fig 2.14. *Shape of the Bessel function of the second kind*

Fig 2.15. *Mohr Coulomb failure model*

Fig 2.16. *Mohr Coulomb yield surface in meridional and deviatoric planes*

Fig 3.1. *Gas compressibility factor*

Fig 4.1. *Geometry for linear flow*

Fig 4.2. *Radial flow system*

Fig 4.3. *IPR for an undersaturated reservoir*

Fig 4.4. *Perform 3.0 interface*

Fig 5.1. *Main program*

Fig 5.2. *Sheet 1 – Wellbore stability data*

Fig 5.3. *Sheet 2 – Exposure time data*

Fig 5.4. *Matlab Program*

Fig 5.5. g_1, *and* g_2 *functions*

Fig 5.6. *Matlab program*

Fig 5.7. *Input flowchart*

Fig 5.8. *Solving flowchart*

Fig 5.9. *Pressure and Temperature profiles*

Fig 5.10. *Mohr-Coulomb Failure Index (MFI) and Drucker Prager Failure Index (DPFI)*

Fig 5.11. *Sheet 1 - Drilling data*

Fig 5.12. *Sheet 2 - PVT data*

Fig 5.13. *Sheet 3 - Well Trajectory data*

Fig 5.14. *Sheet 4 - IPR data*

Fig 5.15. *Compressibility factor flowchart*

Fig 5.16. *Solution gas ratio at bubble point pressure flowchart*

Fig 5.17. *Solution gas ratio flowchart*

Fig 5.18. *Oil isothermal compressibility flowchart*

Fig 5.19. *Gas formation volume factor flowchart*

Fig 5.20. *Oil formation volume factor at bubble point pressure flowchart*

Fig 5.21. *Oil formation volume factor flowchart*

Fig 5.22. *Drilling mud volume factor flowchart*

Fig 5.23. *Mud weight flowchart*

Fig 5.24. *Mixture density in the annulus flowchart*

Fig 5.25. *Mixture density in the drillpipe flowchart*

Fig 5.26. *Mixture velocity in the annulus flowchart*

Fig 5.27. *Mixture velocity in the drillpipe flowchart*

Fig 5.28. *Gas viscosity flowchart*

Fig 5.29. *Oil viscosity at bubble point pressure flowchart*

Fig 5.30. *Oil viscosity flowchart*

Fig 5.31. *Mixture viscosity in the annulus flowchart*

Fig 5.32. *Mixture viscosity in the drillpipe flowchart*

Fig 5.33. *Reynolds number in the annulus flowchart*

Fig 5.34. *Reynolds number in the drillpipe flowchart*

Fig 5.35. *Friction factor in the annulus flowchart*

Fig 5.36. *Friction factor in the drillpipe flowchart*

Fig 5.37. *Frictional pressure gradient in the annulus flowchart*

Fig 5.38. *Frictional pressure gradient in the drillpipe flowchart*

Fig 5.39. *Hydrostatic pressure gradient in the annulus flowchart*

Fig 5.40. *Hydrostatic pressure gradient in the drillpipe flowchart*

Fig 5.41. *Total pressure gradient in the annulus flowchart*

Fig 5.42. *Total pressure gradient in the drillpipe flowchart*

Fig 5.43. *Matlab program*

Fig 5.44. *Inputdata_L*

Fig 5.45. *Modelling_L*

Fig 5.46. *Mixture velocity in the annulus*

Fig 5.47. *Mixture density in the annulus*

Fig 5.48. *Formation fluid influx flow rate*

Fig 6.1. *Diagram of a typical well*

Fig 6.2. *3D - directional wellbore model*

Fig 6.3. *Cylindrical coordinate system*

Fig 6.4. *The inside area*

Fig 6.5. *Effect of mesh refinement on the accuracy of radial stress calculations*

Fig 6.6. *Effect of mesh refinement on the accuracy of tangential stress calculation*

Fig 6.7. *The stress path*

Fig 6.8. *Mesh refinement (N = 10, 20, 40, 80, 160, unequal mesh)*

Fig 6.9. *Time dependent pressure profiles*

Fig 6.10. *Pressure propagation*

Fig 6.11. *Time dependent temperature profiles*

Fig 6.12. *Temperature propagation*

Fig 6.13. *Comparing the pressure and temperature propagation*

Fig 6.14. *Transient radial stresses*

Fig 6.15. *Transient tangential stresses*

Fig 6.16. *Transient axial stresses*

Fig 6.17. *Effective radial stress*

Fig 6.18. *Effective tangential stresses*

Fig 6.19. *Effective axial stresses*

Fig 6.20. *Effect of decreasing pore pressure after drilling – the Mohr-Coulomb moves to the right preserving its shape*

Fig 6.21. *Mohr Coulomb failure index*

Fig 6.22. *Drucker Prager failure index*

Fig 6.23. *Comparing thermal and hydraulic diffusions*

Fig 6.24. *Effect of hydraulic diffusivity on pressure propagation*

Fig 6.25. *Effect of hydraulic diffusivity on wellbore stability via Mohr Coulomb failure index*

Fig 6.26. *Effect of hydraulic diffusivity on wellbore stability via Drucker Prager failure index*

Fig 6.27. *Effect of hydraulic diffusivity and material cohesion on wellbore stability via Mohr Coulomb failure index*

Fig 6.28. *Effect of hydraulic diffusivity and material cohesion on wellbore stability via Drucker Prager failure index*

Fig 6.29. *Pore pressure profiles in respond to different wellbore pressures in UBD through the basement formation*

Fig 6.30. *Effective radial stress profiles in respond to different wellbore pressures in UBD*

Fig 6.31. *Effective tangential stress profiles in respond to different wellbore pressures in UBD*

Fig 6.32. *Effective axial stress profiles in respond to different wellbore pressures in UBD*

Fig 6.33. *The interested area*

Fig 6.34. *Effect of wellbore pressure on failure index at $\theta = 0^o$ in UBD operations through the basement formation after 10 s*

Fig 6.35. *Mohr-Coulomb failure index around the wellbore in UBD*

Fig 6.36. *Comparing Mohr-Coulomb failure index around the wellbore in UBD operation solved by WELLST and ABAQUS*

Fig 6.37. *Effect of wellbore pressure to failure index at $\theta = 0^o$ after 10 s*

Fig 6.38. *Effect of wellbore pressure to failure index at $\theta = 30^o$ after 10 s*

Fig 6.39. *Effect of wellbore pressure to failure index at $\theta = 60^o$ after 10 s*

Fig 6.40. *Effect of wellbore pressure to failure index at $\theta = 90^o$ after 10 s*

Fig 6.41. *Effect of wellbore pressure on failure index at the vertical wellbore wall in the basement section after 10 s*

Fig 6.42. *Comparing the results of wellbore stability solved by WELLST and ABAQUS in UBD*

Fig 6.43. *The weakest point on the wellbore wall*

Fig 6.44. *The weakest point on the wellbore wall solved by ABAQUS*

Fig 6.45. *Pore pressure profiles in respond to different wellbore pressures in UBD through the clastic formation*

Fig 6.46. *Effect of wellbore pressure on failure index at $\theta = 0^o$ in UBD operations through the clastic formation after 10 s*

Fig 6.47. *Effect of wellbore pressure on failure index at the vertical wellbore wall in the clastic section after 10 s*

Fig 6.48. *The stability at the wellbore wall when wellbore pressure reduces*

Fig 6.49. *Effect of wellbore pressure and wellbore inclination on failure index at the wellbore wall in the basement section after 10 s*

Fig 6.50. *The best inclination to drill in strike-slip formation*

Fig 6.51. *Effect of wellbore inclination on failure index at the wellbore wall in the basement section ($a=0^o$, t=10 s, and P_{wf}=32.34 MPa)*

Fig 6.52. *Effect of wellbore inclination on failure index at the wellbore wall in the basement section ($a=30^o$, t=10 s, and P_{wf}=32.34 MPa)*

Fig 6.53. *Effect of wellbore inclination on failure index at the wellbore wall in the basement section ($a=60^o$, t=10 s, and P_{wf}=32.34 MPa)*

Fig 6.54. *Effect of wellbore inclination on failure index at the wellbore wall in the basement section ($a=90^o$, t=10 s, and P_{wf}=32.34 MPa)*

Fig 6.55. *Effect of wellbore inclination and azimuth variation on failure index at the weakest point of the wellbore wall when P_{wf}=32.34 MPa, t= 10 s*

Fig 6.56. *Effect of wellbore pressure and wellbore inclination on failure index around the wellbore wall in the clastic section after 10 s*

Fig 6.57. *The best inclination to drill in the clastic formation*

Fig 6.58. *Effect of wellbore inclination on failure index at the wellbore wall in the clastic section ($a=0^o$, t=10 s, and P_{wf}=32.34 MPa)*

Fig 6.59. *Effect of wellbore inclination on failure index at the wellbore wall in the clastic section ($a=30^o$, t=10 s, and P_{wf}=32.34 MPa)*

Fig 6.60. *Effect of wellbore inclination on failure index at the wellbore wall in the clastic section ($a=60^o$, t=10 s, and P_{wf}=32.34 MPa)*

Fig 6.61. *Effect of wellbore inclination on failure index at the wellbore wall in the clastic section ($a=900^o$, t=10 s, and P_{wf}=32.34 MPa)*

Fig 6.62. *Effect of wellbore inclination and azimuth variation on failure index at the weakest point of the wellbore wall when P_{wf}=32.34 MPa, t= 10 s*

Fig 6.63. *The difference in elastic, poroelastic and thermo-poroelastic formation effects to wellbore stability in the basement section ($a = 0^o$, t=10 s, and P_{wf} = 31 MPa)*

Fig 6.64. *The difference in elastic, poroelastic and thermo-poroelastic formation effects to wellbore stability in the basement section ($a = 30^o$, t=10 s, and P_{wf} = 31 MPa)*

Fig 6.65. *The difference in elastic, poroelastic and thermo-poroelastic formation effects to wellbore stability in the basement section (a = 60^o, t=10 s, and P_{wf} = 31 MPa)*

Fig 6.66. *The difference in elastic, poroelastic and thermo-poroelastic formation effects to wellbore stability in the basement section (a = 90^o, t=10 s, and P_{wf} = 31 MPa)*

Fig 6.67. *The difference in elastic, poroelastic and thermo-poroelastic formation effects to wellbore stability in the clastic section (a = 0^o, t=10 s, and P_{wf} = 21.58 MPa)*

Fig 6.68. *The difference in elastic, poroelastic and thermo-poroelastic formation effects to wellbore stability in the clastic section (a = 30^o, t=10 s, and P_{wf} = 21.58 MPa)*

Fig 6.69. *The difference in elastic, poroelastic and thermo-poroelastic formation effects to wellbore stability in the clastic section (a = 60^o, t=10 s, and P_{wf} = 21.58 MPa)*

Fig 6.70. *The difference in elastic, poroelastic and thermo-poroelastic formation effects to wellbore stability in the clastic section (a = 90^o, t=10 s, and P_{wf} = 21.58 MPa)*

Fig 6.71. *Elastic, poroelastic, and thermo-poroelastic effects on wellbore stability when wellbore pressure changes from 10 MPa to 31 MPa (a=0^o, i=30^o, and t = 10 s)*

Fig 6.72. *Elastic, poroelastic, and thermo-poroelastic effects on wellbore stability when wellbore pressure changes from 10 MPa to 31 MPa (a=30^o, i=30^o, and t = 10 s)*

Fig 6.73. *Transient elastic effect on wellbore stability when a=30^o, i = 60^o, θ = 30^o*

Fig 6.74. *Transient poroelastic effect on wellbore stability when a=30^o, i = 60^o, θ = 30^o*

Fig 6.75. *Transient thermo-poroelastic effect on wellbore stability when a = 30^o, i = 60^o, θ = 30^o*

Fig 6.76. *Transient temperature profiles when cooling the wellbore in the basement section*

Fig 6.77. *Transient temperature profiles when heating the wellbore in the basement section*

Fig 6.78. *Transient failure index profiles when cooling the wellbore in the basement thermo-poroelastic formation*

Fig 6.79. *Transient failure index profiles when heating the wellbore in the basement thermo-poroelastic formation*

Fig 6.80. *The effect of wellbore temperature change to wellbore stability in the basement thermo-poroelastic formation*

Fig 6.81. *Transient temperature profiles when cooling the wellbore in the clastic section*

Fig 6.82. *Transient temperature profiles when heating the wellbore in the clastic section*

Fig 6.83. *Transient failure index profiles when cooling the wellbore in the clastic thermo-poroelastic formation*

Fig 6.84. *Transient failure index profiles when heating the wellbore in the clastic thermo-poroelastic formation*

Fig 6.85. *The effect of wellbore temperature change to wellbore stability in the clastic thermo-poroelastic formation*

Fig 6.86. *The effect of wellbore temperature change to wellbore stability at the vertical wellbore wall in the basement section*

Fig 6.87. *The effect of wellbore temperature change to wellbore stability at the deviated wellbore wall in the basement section*

Fig 6.88. *The effect of wellbore temperature change to wellbore stability at the horizontal wellbore wall in the basement section*

Fig 6.89. *The effect of wellbore temperature change to wellbore stability at the vertical wellbore wall in the clastic section*

Fig 6.90. *The effect of wellbore temperature change to wellbore stability at the deviated wellbore wall in the clastic section*

Fig 6.91. *The effect of wellbore temperature change to wellbore stability at the horizontal wellbore wall in the clastic section*

Fig 6.92. *Effect of thermal expansion coefficients on wellbore stability*

Fig 6.93. *Wellbore collapse pressure of a horizontal well interval drilled through the basement formation in elastic case, and* $a=0^o$

Fig 6.94. *Wellbore collapse pressure of a horizontal well interval drilled through the basement formation in elastic case, and* $a=30^o$

Fig 6.95. *Wellbore collapse pressure of a horizontal well interval drilled through the basement formation in elastic case, and* $a=60^o$

Fig 6.96. *Wellbore collapse pressure of a horizontal well interval drilled through the basement formation in elastic case, and* $a=90^o$

Fig 6.97. *Wellbore collapse pressure of a horizontal well interval drilled through the basement formation in poroelastic case, and* $a=0^o$

Fig 6.98. *Wellbore collapse pressure of a horizontal well interval drilled through the basement formation in poroelastic case, and* $a=30^o$

Fig 6.99. *Wellbore collapse pressure of a horizontal well interval drilled through the basement formation in poroelastic case, and* $a=60^o$

Fig 6.100. *Wellbore collapse pressure of a horizontal well interval drilled through the basement formation in poroelastic case, and* $a=90^o$

Fig 6.101. *Wellbore collapse pressure of a horizontal well interval drilled through the basement formation in thermo-poroelastic case, and* $a=0^o$

Fig 6.102. *Wellbore collapse pressure of a horizontal well interval drilled through the basement formation in thermo-poroelastic case, and* $a=30^o$

Fig 6.103. *Wellbore collapse pressure of a horizontal well interval drilled through the basement formation in thermo-poroelastic case, and a=60^o*

Fig 6.104. *Wellbore collapse pressure of a horizontal well interval drilled through the basement formation in thermo-poroelastic case, and a=90^o*

Fig 6.105. *Wellbore collapse pressure of a horizontal well interval drilled through the basement formation in elastic case, c=30 MPa, and a=0^o*

Fig 6.106. *Wellbore collapse pressure of a horizontal well interval drilled through the basement formation in poroelastic case, c=30 MPa, and a=0^o*

Fig 6.107. *Wellbore collapse pressure of a horizontal well interval drilled through the basement formation in thermo-poroelastic case, c=30 MPa, and a=0^o*

Fig 6.108. *Wellbore collapse pressure of a deviated well interval drilled through the clastic formation in elastic case, and a=0^o*

Fig 6.109. *Wellbore collapse pressure of a deviated well interval drilled through the clastic formation in elastic case, and a=30^o*

Fig 6.110. *Wellbore collapse pressure of a deviated well interval drilled through the clastic formation in elastic case, and a=60^o*

Fig 6.111. *Wellbore collapse pressure of a deviated well interval drilled through the clastic formation in elastic case, and a=90^o*

Fig 6.112. *Wellbore collapse pressure of a deviated well interval drilled through the clastic formation in poroelastic case, and a=0^o*

Fig 6.113. *Wellbore collapse pressure of a deviated well interval drilled through the clastic formation in poroelastic case, and a=30^o*

Fig 6.114. *Wellbore collapse pressure of a deviated well interval drilled through the clastic formation in poroelastic case, and a=60^o*

Fig 6.115. *Wellbore collapse pressure of a deviated well interval drilled through the clastic formation in poroelastic case, and a=90^o*

Fig 6.116. *Wellbore collapse pressure of a deviated well interval drilled through the clastic formation in thermo-poroelastic case, and a=0^o*

Fig 6.117. *Wellbore collapse pressure of a deviated well interval drilled through the clastic formation in thermo-poroelastic case, and a=30^o*

Fig 6.118. *Wellbore collapse pressure of a deviated well interval drilled through the clastic formation in thermo-poroelastic case, and a=60^o*

Fig 6.119. *Wellbore collapse pressure of a deviated well interval drilled through the clastic formation in thermo-poroelastic case, and a=90^o*

Fig 6.120. *Wellbore collapse pressure of a deviated well interval drilled through the clastic formation in elastic case, c=20 MPa, and a=0^o*

Fig 6.121. *Wellbore collapse pressure of a deviated well interval drilled through the clastic formation in poroelastic case, c=20 MPa, and a=0^o*

Fig 6.122. *Wellbore collapse pressure of a deviated well interval drilled through the clastic formation in thermo-poroelastic case, c=20 MPa, and a=0^o*

Fig 6.123. *Well trajectory*

Fig 6.124. *The wellbore azimuth of a typical well in Basin X*

Fig 6.125. *IPR solving by PERFORM 3.0*

Fig 6.126. *Gas compressibility factor gradient in the annulus when drilling by gasified liquid*

Fig 6.127. *Gas compressibility factor gradient in the drillpipe when drilling by gasified liquid*

Fig 6.128. *Gas solution ratio when drilling by gasified liquid*

Fig 6.129. *Gas formation volume factor gradient in the annulus when drilling by gasified liquid*

Fig 6.130. *Gas formation volume factor gradient in the drillpipe when drilling by gasified liquid*

Fig 6.131. *Fluid formation volume factor gradient in the annulus when drilling by gasified liquid*

Fig 6.132. *Mixture velocity gradient in the annulus when drilling by gasified liquid*

Fig 6.133. *Mixture velocity gradient in the drillpipe when drilling by gasified liquid*

Fig 6.134. *Mixture density gradient in the annulus when drilling by gasified liquid*

Fig 6.135. *Mixture density gradient in the drillpipe when drilling by gasified liquid*

Fig 6.136. *Reynolds number gradient in the annulus when drilling by gasified liquid*

Fig 6.137. *Reynolds number gradient in the drillpipe when drilling by gasified liquid*

Fig 6.138. *Friction factor gradient in the annulus when drilling by gasified liquid*

Fig 6.139. *Friction factor gradient in the drillpipe when drilling by gasified liquid*

Fig 6.140. *Temperature gradient in the annulus when drilling by gasified liquid*

Fig 6.141. *Pressure gradient in the annulus when drilling by gasified liquid*

Fig 6.142. *Pressure gradient in the drillpipe when drilling by gasified liquid*

Fig 6.143. *A typical Gas-Liquid Flow Rate Window (GLRW)*

Fig 6.144. *Dynamic BHP*

Fig 6.145. *Hydrostatic BHP*

Fig 6.146. *Liquid Gas Rate Window (LGRW)*

Fig 6.147. *Pressure gradient in the drillpipe*

Fig 6.148. *HYDMOD software*

Fig 6.149. *Input data in HYDMOD software*

Fig 6.150. *Results solved by HYDMOD software*

Fig 6.151. *The result of convergence analysis*

Fig 6.152. *Foam density in the annulus*

Fig 6.153. *Foam density in the drillpipe*

Fig 6.154. *Pressure gradient in the annulus when drilling by foam*

Fig 6.155. *Pressure gradient in the drillpipe when drilling by foam*

Fig 6.156. *Dynamic BHP*

Fig 6.157. *Hydrostatic BHP*

Fig 6.158. *Liquid Gas Rate Window (LGRW)*

Fig 6.159. *Liquid Gas Rate Window (LGRW)*

Fig 6.160. *Foam quality in the annulus*

Fig 6.161. *Foam quality in the drillpipe*

GLOSSARY

A = cross sectional of flow path area, in^2

B = Skempton pore pressure coefficient

BHP = bottom hole pressure, MPa or psia

B_f = formation fluid volume factor, bbl/STB

B_g = gas formation volume factor, SCF/ft^3

B_o = oil formation volume factor, bbl/STB

B_{ob} = oil formation volume factor at bubble point pressure, bbl/STB

B_w = water formation volume factor, bbl/STB

B_x = mud (or sea water) formation volume factor, bbl/STB

c = material cohesion, MPa

C_D = drag coefficient

C_f = specific heat of fluid, $J/kg.^oC$

C_f = fluid compressibility, psi^{-1}

C_o = oil compressibility, psi^{-1}

C_o, UCS = unconfined compressive strength, MPa

C_p = particle concentration in the flow path, 0.04, volume fraction

$C_\varepsilon m_o$ = volumetric heat capacity, $J/m^3.^oC$

C_ε = specific heat of rock, $J/kg.^oC$

d_b = bit diameter, in

d_H = hydraulic diameter of flow path, in

D_H = hydraulic diameter of flow path, ft

dL = length incremental, ft

d_{in} = inside diameter, in

d_{out} = outside diameter, in

dP/dx = pressure gradient in the direction of flow (negative)

D_S = equivalent solid diameter, ft

DT = delta time, μs/ft

DPFI = Drucker Prager failure index

e = void ratio

E = Modulus of Elasticity, MPa

E = kinetic energy per unit volume, lb/ft^2

FE = Flow Efficiency

f_m = friction factor

g = acceleration of gravity, ft/s^2

G = geothermal gradient, $^o/ft$

G = shear modulus, MPa

h = reservoir thickness, ft

H = vertical depth, ft

IFDM = combination of iterative method and finite differential method

IPR = inflow performance relationship

I_P = pressure reduction ratio

I_T = temperature reduction ratio

J_1^{eff} = effective mean stress, MPa

$J_2^{1/2}$ = shear stress, MPa

J_o = Bessel function order zero of the first kind

γ_o = Bessel function order zero of the second kind

k = permeability of the porous medium, md

K = bulk modulus of dry material, MPa

K = secant bulk modulus

K_B = material drained bulk modulus, MPa

k_f = effective permeability to fluid, md

K_f = fluid bulk modulus, MPa

K_M = matrix bulk modulus, MPa

$K_ı$ = hydraulics diffusivity, $m^3/s.kg$

k_H = effective permeability in the horizontal direction, md

k_V = effective permeability in the vertical direction, md

K_u = material undrained bulk modulus, MPa

L = measured depth calculated based on the trajectory shape, ft

L = latent heat

LGRW = liquid gas rate window

MFI = Mohr-Coulomb failure index

N_{Re} = Reynolds number

P = pressure of interest, psia

p' = the equivalent pressure stress, MPa

P_b = bubble point pressure, psia

P_{col} = collapse pressure, MPa

P_e = pressure at $r = r_e$

P_f = formation pore pressure, psia

P_{Hup} = upstream hydraulic pressure, lb/ft^2

P_{Hdn} = downstream hydraulic pressure, lb/ft^2

P_{frup} = upstream frictional pressure, lb/ft^2

P_{frdn} = downstream frictional pressure, lb/ft^2

PI = productivity index

P_{pc} = pseudo-critical pressure, psia

P_R = reservoir pressure, MPa or psia

P_s = surface pressure, psia

P_w = wellbore pressure, MPa or psia

P_{wf} = wellbore flowing pressure at $r = r_w$, MPa or psia

P_{wfe} = estimated BHP, psia

P_{wfc} = calculated BHP, psia

q' = the Mises equivalent stress, MPa

Q_f = formation fluid influx flow rate at the surface condition, STB/hr

$Q_{f(\max)}^{FE=1}$ = the maximum inflow flow rate being obtained for the well if FE = 1

Q_g = volumetric flow rate of gas, ft^3/s

Q_{gs} = volumetric of injected gas flow rate under standard conditions, SCF/min

Q_l = volumetric flow rate of liquid, ft^3/s

Q_p = volumetric flow rate of particles generated by the drill bit, ft^3/s

Q_s = volumetric flow rate of solid, ft^3/s

Q_{tr} = transported volumetric flow rate of particles in the flow path, ft^3/s

Q_x = mud (or sea water) flow rate at the surface condition, gal/min

R = wellbore radius, m

r' = the third invariant of deviatoric stress, MPa

r_e = well's drainage radius, m

R_p = rate of penetration, ft/hr

R_s = gas solution ratio, SCF/STB

R_{sb} = gas solution ratio at bubble point pressure, SCF/STB

R_∞ = outer radius ($R_\infty >> R$), m

S = water salinity, $^o/_{oo}$

S = the deviatoric stress, MPa

S_g = specific gravity of gas related to air

S_f = specific gravity of formation fluid related to fresh water

S_s = specific gravity of solid (cutting)

T = temperature of interest, ^oF

T_{av} = the average temperature, ^oR

T_{pc} = pseudo-critical temperature, ^oR

T_s = surface temperature

T_{wf} = wellbore temperature, ^oC

UBD = underbalanced drilling

v = apparent fluid velocity, ft/s

v_m = mixture velocity, ft/s

v_f = formation influx fluid velocity, ft/s

v_j = injection fluid velocity, ft/s

ν_p = compressional velocity, ft/s

ν_s = shear velocity, ft/s

v_{sl} = terminal setting velocity, ft/s

v_{tr} = required particle transport velocity, ft/s

W_g = weight flow rate of gas, lb/s

W_l = weight flow rate of liquid, lb/s

W_x = mud weight, ppg

W_{x0} = mud (or sea water) weight at the surface condition, kg/m^3

W_s = weight flow rate of solid, lb/s

Z = compressibility factor

α = Biot's coefficient

α_B = drained thermal expansion coefficient, $1/^oC$

α_f = fluid thermal expansion coefficient, $1/^oC$

α_P = irrotational pore pressure coefficient, 1/MPa

α_T = irrotational temperature coefficient, $1/^oC$

α_u = undrained thermal expansion coefficient, $1/^oC$

ε = equivalent roughness, in

ϕ = porosity

ϕ = friction angel, degree

ϕ = wellbore inclination, degree

η = Biot's modulus

κ = thermal conductivity coefficient, $W/m.^oC$

λ = Lamé's parameter

μ = fluid viscosity, cp

μ_f = formation fluid viscosity, cp

μ_g = gas viscosity, cp

μ_L = liquid viscosity, cp

μ_m = mixture viscosity, cp

μ_o = oil viscosity, cp

μ_x = mud (or sea water) viscosity, cp

μ_w = water viscosity, cp

ν = Poisson' ratio

ν = kinematic viscosity, ft^2/s

θ = angle of the point of interest from x-axis, degree

ρ_g = gas density, lb/ft^3

ρ_f = fluid density, kg/m^3

ρ_m = mixture density, lb/ft^3

ρ_R = rock density, kg/m^3

ρ_s = solid phase density, kg/m^3

σ = total average stress, MPa

$\sigma_1, \sigma_2, \sigma_3$ = principal stresses, MPa

σ_{max} = the maximum principal stress, MPa

σ_{min} = the minimum principal stress, MPa

σ_a = axial stress along wellbore, MPa

σ_r = radial stress, MPa

σ_θ = tangential stress, MPa

σ_z = axial stress, MPa

σ_x = normal stress in x direction, MPa

σ_y = normal stress in y direction, MPa

σ_z = normal stress in z direction, MPa

σ_H = maximum horizontal in situ stress, MPa

σ_h = minimum horizontal in situ stress, MPa

σ_V = vertical in situ stress, MPa

τ = shear stress, MPa

τ_{xy} = τ_{yx}, shear stress, MPa

τ_{yz} = τ_{zy}, shear stress, MPa

τ_{xz} = τ_{zx}, shear stress, MPa

$\tau_{r\theta}$, τ_{rz}, $\tau_{\theta z}$ = shear stress in cylindrical coordinate system, MPa

ΔP_c = calculated pressure drop, psi

ΔP_s = assumed pressure drop, psi

ΔP_{skin} = pressure change caused by skin effect, psi

Γ = foam quality

Γ_{up} = upstream foam quality

Γ_{dn} = downstream foam quality

ψ = sphericity factor

ψ = dilation angle, degree

LIST OF PUBLICATIONS

1. Nguyen, K.C., Smart, B.G.D., and Somerville, J.M., "Predicting the Production Capacity During Underbalanced Drilling Operations in Vietnam," SPE 122266-PP presented at the IADC/SPE Managed Pressure Drilling and Underbalanced Operations Conference and Exhibition held in San Antonio, Texas, 12–13 February, 2009.

CHAPTER 1 - INTRODUCTION

1.1. Review of Underbalanced Drilling Technique

Underbalanced drilling (UBD) is defined as a technique in which the drilling fluid pressure in the borehole, while drilling the well, is maintained at some pressure less than the pore pressure of the formation rock in the open-hole section. As a result, an influx of formation fluids is allowed into the wellbore during drilling, circulated out, with control at the surface. This condition can be generated naturally by using low density fluids (sea water or light hydrocarbon systems) or by adding gas into the drilling fluid as it being pumped in some situations where high natural pressure exists in the formation. UBD techniques have often been applied for horizontal wells where formation damage is a concern particularly because of longer fluid contact times and a greater prevalence of open-hole completions. This is because even relatively shallow invasive damage can significantly reduce the productivity of an open-hole horizontal well in comparison with a cased and perforated vertical well.

UBD is more and more considered because of the simple reason that it can improve the financial returns on drilling the well. This improvement can come from a variety of different advantages from reducing the cost of drilling the well to increasing its productivity once drilled. However, this drilling technique also causes wellbore instability once the bottomhole pressure is maintained less than the formation pore pressure. Evaluating wellbore stability and predicting how much formation influx fluid (oil, water) can be obtained from the reservoir during UBD have always been difficult questions for drilling engineers. It is because of the complex relationship of the drilling fluid, the invaded formation fluid, and the nature of the rock in the penetrated formations, especially in the region around the wellbore where there are the hydraulics and thermal diffusivities between the reservoir and the wellbore.

The study of coupling the wellbore stability, wellbore hydraulics, and productivity in UBD has not been investigated fully so far. Therefore, this research will focus on the approach which is established to evaluate the relationship between the rock mechanics around the wellbore, drilling hydraulics, and production capacity of a typical well in a granite basement under UBD operations. Once these information are known, the feasibility of UBD application will be qualified. And this is the important factor for operators to decide whether UBD should be applied or not. The proposed method and developed software is validated by applying to examples of UBD in a granite basement reservoir in Vietnam, SE Asia.

1.1.1. Benefits of UBD

Reduction in invasive formation damage

Bennion et al. (1998) [1] presented that types of formation damage during conventional overbalanced drilling operations have been found from a variety of different reasons.

- Physical migration of in-situ fines and clays caused by elevated fluid leakoff velocities at highly overbalanced conditions.
- The invasion of artificial or naturally generated solids present in the mud system into the formation matrix (particularly an issue in open-hole completions where penetration of physically shallow but potentially very severe damage of this type by perforating/fracturing is not normally considered).
- A poor knowledge of the formation pore size distribution or a significant bimodal size distribution that makes the design and formation of a low-permeability sealing filter cake that inhibits deep invasive damage in an overbalanced mode difficult to achieve.
- High permeability zones presenting the potential of severe invasive fluid loss (large macro fractures, highly interconnected large vugs, extremely high permeability sands, or inter crystalline carbonates).
- Susceptibility to aqueous or hydrocarbon phase traps that may result in the retention of water or hydrocarbon based invaded fluid filtrates, which may cause a permanent reduction in the productive capacity of the near wellbore region because of adverse relative permeability effects.
- Potential adverse reaction between invaded filtrate and the formation (swelling clays, formation dissolution, chemical adsorption, wettability alterations).
- Potential adverse reaction between invaded filtrates and in-situ fluids (emulsions, and scales).

When properly designed and executed, UBD minimizes problems associated with the invasion of particulate matter into the formation as well as a number of other problems such as adverse clay reactions, phase trapping, organic and inorganic precipitation, and emulsification. These effects may be caused by the invasion of incompatible mud filtrates in an overbalanced condition.

Increased rate of penetration (ROP)

Many UBD operations exhibit significantly greater ROP's than conventional overbalanced applications. This can reduce drilling time in extended reach horizontal sections, improve bit life, and may reduce drilling costs. Problems with differential sticking, which may be encountered in conventional overbalanced drilling operations, are also obviated. In certain reservoir cases, the prime motivation for UBD has been for these reasons rather than simply formation damage reduction. [2]

Increased bit life

It is often claimed that bit life is increased when lightened fluids are used instead of conventional drilling muds. Drilling underbalanced removes the confinement imposed on the rock by the overbalance pressure. This should decrease the apparent strength of the rock and reduce the work that must be done to drill away a given volume

of rock. It is reasonable that increased drilling efficiency should increase the amount of hole that can be drilled before the bit reaches a critical wear state. [2]

Minimized lost circulation

More frequently, lost circulation involves flow into natural fractures that intersect the wellbore or into fractures induced by excessive drilling fluid pressure. Lost circulation can be very costly during conventional drilling. The lost fluid has to be replaced, and the losses have to be mitigated, usually by adding lost circulation material to the mud before drilling can safely be resumed. Since there is no physical force driving fluid into the formation if the well is drilled underbalanced, UBD effectively prevents lost circulation problems.

This is not to say that lost circulation cannot occur when drilling with lightened fluids. It is possible to lose circulation whenever the wellbore pressure exceeds the formation pore pressure. Using a lightened fluid does not, by itself, guarantee underbalanced conditions. [2]

Minimized differential sticking

In a well drilled conventionally, a filter cake forms on the borehole wall from solids deposited when liquid flows from the drilling mud into permeable zones, due to an overbalance pressure. If the drillstring becomes embedded in the filter cake, the pressure differential between the wellbore and the fluid in the filter cake can act over such a large area that the axial force required moving the string can exceed its tensile capacity. The drillstring is then differentially stuck. There will be no filter cake and no pressure acting to "clamp" the drillstring if the well is underbalanced. Other mechanisms can cause sticking; underbalanced drilling does not eliminate the possibility of a stuck drillstring. [2]

Earlier production

When a well is drilled underbalanced, hydrocarbon production can begin as soon as a productive zone is penetrated. With suitable surface equipment, it is possible to collect formation fluid while drilling. Some underbalanced wells have paid for themselves entirely from production before drilling operations were completed. [2]

Reduced stimulation requirements

Following conventional drilling operations, wells are often stimulated to increase their productivity. Stimulation can include acidizing or surfactant treatments, to remove formation damage; or hydraulic fracturing can be used to guarantee adequate production in low permeability reservoirs or to bypass damage in higher permeability formations. Reduced formation damage means lower stimulation costs. [2]

Providing a rapid indication of productive reservoir zones

Because the hydrostatic pressure of the circulating fluid system in a truly underbalanced operation is less than the formation pressure, a condition of net outflow of formation fluids (oil, water or gas) should occur given sufficient formation pressure and in-situ permeability. Proper flow monitoring of the produced fluids at surface can

provide a good indication of productive zones of the reservoir and act as a valuable aid in the geo steering of the well (if horizontal application). Significant production of liquid hydrocarbons (because gas is usually flared) during the drilling operation may provide some early cash to partially defer some of the additional costs associated with the UBD operation. [1]

Ability to flow/well testing while drilling

Recently, several operators have taken advantage of the flowing condition occurring during UBD to conduct either single or multirate drawdown tests to evaluate the productive capacity of the formation and formation properties during the drilling operation. [2]

1.1.2. Disadvantages of UBD

Although UBD offers several advantages over conventional drilling programs, there are a few limitations such as:

Expense

The increase of initial cost of UBD come from the cost of extra equipment and rig time, pipe connections, and mechanical problems including sticking, bit jetting and flushing, and mud-pulsed logging. There is also a cost associated with the rental of compressors. This rental cost can considerablely increase the daily drilling cost in comparison with the use of other fluids. [3]

Safety concerns

If air is used as the gas phase, the potential exists for drill string corrosion and also for the formation of hydrocarbon/oxygen mixtures with an active explosive range given temperature conditions and frictional sources of ignition downhole. In general, there is an overall increased risk due to the complexibility of the UBD operation. [4]

Wellbore stability concerns

Wellbore compaction issues have been a longstanding concern in UBD operations, particularly in poorly consolidated or highly depleted formations.

Failure to maintain a continuously underbalanced condition

A major factor in the disappointing results from many UBD operations conducted in the past is that the underbalanced condition is not maintained 100% of the time during drilling and completion operations.

There are many potential reasons why an underbalanced condition may be lost during drilling.

If the rotary rig is used, the underbalanced condition is potentially compromised each time gas injection must be terminated to make a pipe connection. Rapid connections and circulating out to pure gas before each pipe connection tends to minimize the effect of these overbalanced pulses, but fluctuations in bottom hole pressure are still common in most operations. The use of real-time downhole pressure

measurement equipment to ensure a continuous downhole underbalance pressure condition is essential for a properly executed UBD operation.

Periodic kill jobs to conduct bit trips result in balanced to full hydrostatic pressure being required to control the well unless the string is snubbed out in a flowing mode. A compression wave occurs in front of the pipe when rerunning the string if rapid running of the pipe occurs, which can aggravate the overbalanced condition.

If a concentric or parasite string configuration is used to obtain a continuous underbalanced condition, full hydrostatic pressure will be present at the jets on the drill bit because a full hydrostatic column of fluid is present in the centre of the drillstring. Orifice effects will drop rapidly as the fluid leaves the bit area. Pressure in the majority of the returning fluid column will be controlled by the parasite/concentric string injector scheme. [1]

Spontaneous imbibition and countercurrent imbibition effects

Because of adverse capillary pressure effects, it is possible to imbibe water-based (and in some cases hydrocarbon-based) fluids into the formation in the near wellbore region where they may cause a reduction in permeability because of rock/fluid or fluid/fluid incompatibility effects, or a reduction in flow capacity because of aqueous or hydrocarbon phase trapping and relative permeability effects. The absence of sealing and very low permeability filter cake, which can act as a barrier to long-term spontaneous imbibition effects (as long as high initial spurt loss is not present) created during a conventional well-designed overbalanced drilling operation, potentially, can result in more severe problems with imbibition being present in a UBD operation than in a normal overbalanced situation. In UBD operation, imbibition effects can cause phase trapping and damage problems in a number of different reservoir scenarios. [1]

1.1.3. UBD Techniques

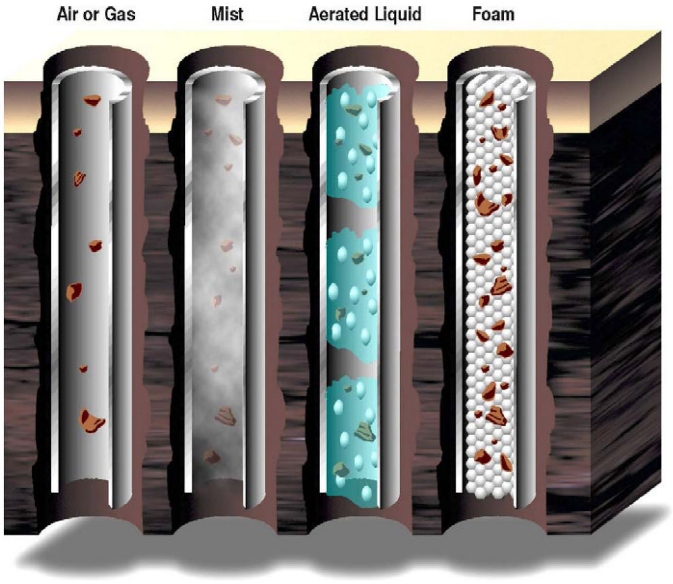

Fig 1.1. *Compressible fluids Technology [5]*

There are UBD drilling techniques applied nowadays such as air, gas, foam, mist, or gasified liquid (aerated liquid). However, only two UBD drilling techniques are involved in this research.

Gasified liquid drilling operations

Gasified or aerated fluid is any fluid in which gas and liquid phases have been intentionally mixed to decrease the density of the fluid. Gasified systems are unstable because nothing ties the gas and liquid together. The gas in this case is introduced into the fluid at the surface before it is pumped through the drillpipe.

The benefits of a gasified UBD drilling are to avoid lost circulation, to reduce formation damage, to avoid differential sticking, and to increase the rate of penetration. However, the biggest problem with a gasified system is the discontinuous nature of the operations. Each time the normal operation is interrupted for some technical reason, the gasified fluid begins to separate, mainly in the annulus. Once the circulation is re-established, the resultant slugs of pure liquid can exert a hydrostatic pressure downhole in the formation that may exceed the reservoir pore pressure. [2, 6]

Gasified design often requires computer programs because the complex nature of fluid mixture in drilling system where water, gas, cuttings and fluid influx from the penetrated formations are present. Computer simulation indicates that an air injection rate exists which yields the lowest flowing annulus pressure for a given mud rate and well geometry. Simulations also indicate an unfavourable range of mud flow rate which provides poor carrying capacity of the gasified mud for some air injection rates investigated. Guo et al. [7, 8] show that by considering both the carrying capacity and flowing annulus pressure, an optimum combination of mud and air rates can be determined for gasified liquid drilling.

Foam drilling operations

Foam systems are created when water and gas mixed with a surfactant or foaming agent, in the liquid phase stabilities the films that form the bubble walls, which allow the foam structure to persist. The structure of foam is made up of bubbles of gas surrounded by a liquid film. Foam normally contains about 97% gas and only about 3% liquid at surface conditions. [6]

Besides the advantages like other fluid UBD, drilling by foam has also some limitations such as:

- Corrosion: corrosion control is not an impossible limitation to foam drilling. Adding an effective corrosion inhibitor and oxygen scavenger to the injected liquid will, in many instances, slow corrosion of downhole equipment to an acceptably low level. Its function should not be affected by any formation fluid inflows that might occur. Corrosion problems with foam increase with increasing depth, principally because of the associated increases in temperature.

- Wellbore instability: wellbore erosion has been lessened by reducing wellbore boundary shear stress in naturally fractured formations, drilled overbalanced. This occurs because foams are efficient at cuttings transport at low annular velocities. High quality foams normally used in drilling have high viscosities at low shear rates. It is reasonable to think that foam should have a lower tendency to erode the borehole wall.

- Mechanical instability: when drilling with foam, borehole pressures tend to be higher than those encountered when drilling with dry gas or mist. The difference may or may not be sufficient to have a beneficial effect on wellbore stability. Using foam could increase the borehole pressure. This would decrease the difference between circumferential stress and borehole pressure, but still may not provide adequate support. This will help reduce mechanically induced wellbore instability in weak rock.

- Chemical instability: foam is often used when significant formation water inflows are encountered. These inflows will alter the composition of the foam liquid phase and may promote interaction with water sensitive shales, exposed farther uphole.

- Downhole fires: fires occurred when the foam separates, forming an air continuous phase, which could support combustion on the top side of the hole.

- Foam disposal: the economic benefit of continuing to drill underbalanced with foam must be balanced against the cost of handling and disposing it. Because of environmental concerns in many areas, it is not acceptable to put large volumes of foam into a reserve pit or to pump it overload.

1.2. Prospect of UBD Application in Vietnam

UBD has gained strong momentum in recent years because of a number of advantages of the technology. There are some oil companies in Vietnam interested in applying UBD for basement reservoirs. However, up to now, they have not carried out this technique because of the lack of research investigating deeply and thoroughly the ability of UBD to be applied to Vietnam reservoirs, especially in natural granite basements.

First of all, the geological conditions need to be assessed to determine if basement reservoirs in Vietnam are good candidates for UBD. According to drilling engineers working in oil companies in Vietnam, one of the most important problems in drilling is lost circulation while drilling due to low pore pressure in faults or fractures with large apertures up to 10 mm. Sometimes, severe lost circulation in drilling has reached to 40,000 bbl/well [9] causing pipe sticking and blow out because the hydrostatic pressure in this case can not maintain the well in safety from the kick of formation influx fluid. To solve this severe lost circulation drilling engineers often proceed in two ways:

(1) Using LCM to prevent the invasion of drilling fluid into the formation. This method is used in limiting lost circulation but often causes formation damage.

(2) Filling up sea water in the annulus to maintain the hydrostatic pressure then using sea water to drill through the low pore pressure section to reduce the cost of drilling mud due to lost circulation and this way is really effective because drilling by sea water is rather cheap. In the case of a kick, engineers close the annular space at the surface then pump sea water with high pressure through drill pipes to push all drilling fluid and cuttings into the formation. It is unknown where sea water and cuttings are going because there is no trace of drilling sea water and cuttings in produced oil after kicking off. It proves the fractures in the penetrated formations are very large and communicate together. This is the solution which oil companies were applying now.

Applying UBD in basement reservoirs of Vietnam may overcome these above difficulties because low wellbore pressure helps to eliminate this lost circulation problem while drilling. Besides, granite formations in the basement are often very hard, consolidated, and stable, so it is possible to apply UBD because a good candidate for UBD requires the stability of the wellbore while drilling. Moreover, if conventional drilling is used in drilling through hard rock formation it will take a lot of time and cost. Therefore, replacing conventional drilling by UBD will not only reduce the cost for drilling because of saving time, cost for personnel and equipment.but also increase considerably penetration rate because drilling underbalanced removes the confinement imposed on the rock by overbalanced pressure, decrease the apparent strength of the rock and reduce the work that must be done to drill away a given volume of rock. Another reason making basement reservoirs in Vietnam become a good candidate for UBD is the fact that there are a lot of wells with the skin factor of 5 or higher. One more problem in drilling through basement reservoirs in Vietnam that is inflow gas sometimes appears while drilling. So if UBD is applied, dry air should not be used because of combustion possibility, and using foam must consider the foam components because invading gas can change foam structure. As a result, depending on all above reasons, it is recognized that the hard rock formation in basement of granite reservoirs, offshore Vietnam, are the prospect candidates of UBD at least from geological issues.

Secondly, economical study must be calculated as well. Oil production and exploration industry of Vietnam are developing quickly. Besides producing oilfields such as White Tiger, Big Bear, Ruby, Pearl, Black Lion, Nam Con Son, there are a lot of oilfields just discovered and in development plan stage such as White Lion, Yellow Lion etc. The prospect of drilling oil wells of new oilfields and extending the exploration around the existing oilfields is considerable. JVPC, Petronas, CuuLong JOC, and Vietsovpetro are carrying out drilling over thousands meters everyday so far. Applying UBD in Vietnam now has really a good market, especially when the oil price has increased recently.

Briefly, the granite basement of fractured reservoirs in Vietnam is really a good candidate for applying UBD. However, to be sure that the UBD projects will be economical, the investigation and preparation should be estimated carefully and fully.

1.3. The Application of UBD for Basin X, South of Vietnam

The granite basement reservoir of the Basin X, South of Vietnam, is the most prospective area which can benefit from UBD technology. Low rate of penetration (ROP) and extremely short bit life while drilling the basement are the frequent results when drilled overbalanced in this basin. Besides, massive losses of drilling fluids have occurred once the faults in the basement are encountered. In order to increase ROP, improve bit life and eliminate lost return issues, a study of UBD application in the Basin X should be carried out.

The study determines the viability of applying UBD technology to granite basements in Basin X by investigating technical feasibilities of the project. The results of the feasibility study are presented for review and consideration. [9]

1.3.1. Overview of the Basin X [9]

Basin X is located in an area of about 60m water depth, along the south eastern continental self, offshore Vietnam. The formations are mainly clastics of Eocene, Oligocene to Quaternary. The basin is highlighted tectonically by the tilted fault basement blocks, creating northeast-southwest striking graben, half graben and horst.

The main oil production reservoir is the Pre-Tertiary granite basement, located at approximately 3,400 - 3,500 m. This reservoir varies in thickness from several hundred meters to as much as 1,000 meters.

The fractured basement reservoir includes matrix rock with almost zero porosity, and various types of fractures. These fractures are connected through extremely complicated heterogeneous fracture system. Although there are fractures anywhere in the basement, flow contributing fractures are only observed near major structural features, such as faults, and associated damaged zones. Micro fractures normally have their apertures less than 0.5mm, typically in the range of 0.1-0.3mm, whereas macro fractures/faults have their apertures in the range of centimetre to meter. The porosity of macro fractures/faults can be up to 15% and the permeability of macro fractures/faults can be thousands of mD. Fractures, both micro and macro, are mineral filled or partly filled with Zeolite, reducing the flow potential.

The degree of reservoir impairment delivered by wells drilled overbalanced in the Basin X is difficult to quantify, however, there are clear indications that conventional (overbalanced) drilling (OBD) has seriously compromised productivity. An example of this is found in a field in the basin, where experience shows that killing a well with seawater prior to workover reduces productivity by 30%. This damage has been shown to be long term, as the production level never recovers. Generally, previous wells in the basin deliver skin factors in the range of 10-30, typically in the range of 15-20.

Historically, almost 400 exploration and development wells were drilled in the basin. Currently, oil and associated gas are being produced from five oil fields. Several other oil fields are being prepared for development. However, no Field Development Plan in the basin has yet been prepared with UBD. This is despite the fact that at least 7

different operators are currently active in the basin and most consider that UBD is probably the ideal solution.

Drilling activities in the Basin X is typically accomplished using a cantilever jack-up rig. The proposed future well for this study is designed as a horizontal well drilled from the platform, with a perpendicular intersection with the faults in the basement.

In this study report, only the drilling of 8 ½" hole section is considered, as this is the section that is proposed to be drilled underbalanced. The formation throughout the 8 ½" section is expected to be granite, with possibly large hard rock zones.

1.3.2. Previous Drilling Problems

The fundamental problem in drilling into the granite basement productive zone is low ROP and bit life due to hard rock, coupled with massive lost circulation due to heavily fractured, productive zone. Almost all the specific drilling problems observed in the past while drilling the granite section in the basin are consequences of this fundamental problem. [9]

ROP and Bit Life

Historically, 4 to 8 bit runs have been needed in drilling the 8 ½" hole section through fractured granite basement with average bit life of 100m, and the average ROP is from 3.2 to 8.2 m/hr depending on the well location in Basin X.

Lost Circulation

The granite basement, along with being hard, is also heavily fractured; leading to massive lost circulation problems while drilling overbalanced. Generally, average total losses of 40,000 bbl/well were typically encountered in most fields in the basin. This problem has been tackled, with mixed results, by using lost circulation material (LCM). Even if the LCM does work in controlling losses, it significantly damages the formation, and it is difficult to realize the true production potential of the producing zone if LCM is used.

Differential Sticking and Pack-off

Differential sticking has been a problem, but careful control of mud weight has reduced this problem in OBD. Moreover, many incidents of stuck pipe as a consequence of cuttings pack-off have been observed in the past while drilling the granite basement. These are thought to be a consequence of lost circulation, coupled with the use of large amounts of LCM, which could create a sudden pressure variation within the wellbore on plugging off the faults.

1.3.3. Investigating for UBD in the Basin X [9]

UBD is being considered for drilling the productive zone in the Basin X to mainly combat low ROP, short bit life and massive losses experienced in previous wells. History indicates that the Basin X presents conditions that are uniquely suitable for taking advantage of UBD.

In previous worldwide UBD applications where granite formations with similar hardness have been drilled, ROP increases of 2-10 times, and bit life improvement of 2-8 times over OBD have been recorded. An example of this is the recent experience of wells drilled through fractured granite bedrock in Arun Field, Indonesia. This field historically had similar problems as the Basin X in drilling the productive interval with average ROP around 1.8m/hr and bit life averaging 85m. When UBD was applied, the average ROP was 7.2m/hr with the last bit lasting 230m. When drilled conventionally, massive losses occurred while drilling in excess of 40,000 bbl/well. Losses were eliminated while drilling underbalanced.

Experience has shown that formations with a sonic travel times below 70 microseconds will show a significant increase in ROP. The Basin X production zone has sonic travel times in the 50 microsecond range. This indicates that a significant increase in ROP can be expected. An improvement in bit life can also be expected as a result of the lower weight on bit (WOB) required to drill underbalanced.

UBD in the Basin X will also eliminate the lost circulation problems historically encountered in the basin. Since the circulating bottom-hole pressure (BHP) is lower than the pore pressure by design, lost circulation is impossible. Instead, it is expected that the formation fluids will flow into the wellbore once faults have been encountered. Since the well is drilled underbalanced, differential sticking concerns are also eliminated. Moreover, the previous pack-off problems are also likely to be alleviated, as circulation to surface is maintained, and use of LCM is reduced or eliminated.

Because the formation being drilled (granite) is stable, it can withstand a significant amount of the underbalance. Formation instability problems are not anticipated in the granite reservoir section.

1.4. The Content of Study

The content of UBD study applied for Basin X, Vietnam will be carried out through following steps:

- Calculating the stability of the borehole in both clastic and granite basement formations and investigating the effect of inclination angle and azimuth variations, UBD operation to wellbore stability.
- Coupling pore pressure and thermal influence into the calculation of wellbore stability in UBD.
- Estimating the time dependent effects, thermal expansion, cooling and heating effects to the wellbore stability in UBD.
- Evaluating the collapse pressure of the directional wellbore in the strike-slip compression stress field of Basin X.
- Developing WELLST program to simulate all above computations.

- Comparing the solution by WELLST with commercial software (ABAQUS).
- Modelling the borehole multiphase flow in UBD by an innovative method IFDM (interactive method and finite differential method).
- Estimating the pressure loss in the total drilling system to select the suitable compressor.
- Developing UBDRILL program to analyse drilling hydraulics in UBD.
- Coupling UBD parameters and production capacity of the reservoir by combining two programs: UBDRILL and Perform 3.0 of IHS Energy Group.
- Suggesting the optimum well control method in UBD by designing Liquid Gas Rate Window (LGRW).
- Evaluating the accuracy of UBDRILL by comparing to HYDMOD. [10]
- Estimating the sensitivity of hydraulics input data in UBD and the convergence of the results.
- Coupling two developed program UBDRILL and WELLST to solve the complex interaction of borehole stability, rock yielding, collapse, and wellbore hydraulics during UBD operations.

All above steps will be kept on through real data of Basin X and the results can be used to refer to the next UBD wells in Basin X. So, the organization of this dissertation will be presented step by step in the following chapters.

Chapter 1 deals with brief comments about the concepts of UBD and the possibility of UBD in granite basement reservoirs, Vietnam. A general view about the contents of research is described.

Chapter 2 presents the feasibility studies of the wellbore stability in UBD. It will generate geomechanical evaluations of the existing wells in Basin X, Vietnam which were introduced in chapter 1 to provide wellbore stability reviews and drilling strategies for planned wells in Basin X. This chapter will also express equations to estimate the wellbore stability condition in UBD and consider the calculation of collapse pressure which will be used to set up the right boundary of Liquid Gas Rate Window (LGRW) in chapter 6.

Chapter 3 displays analytical algorithms, new methods and the way to calculate multiphase flow in UBD. The innovative method called IFDM (the combination of the iterative method and the finite differential method) which was developed from equations of Guo, B and Ghalambor, A will be developed in this chapter. These calculations will cover multiphase flow of commonly used drilling fluids in two categories: 1) gasified liquid; 2) stable foam. The results from this research are the distribution of pressure, temperature, drilling fluid properties in the annulus and the drillpipe of directional wells.

Chapter 4 serves two purposes. First, it summarizes the flow equations from the reservoirs to the well which has been called inflow performance relationship (IPR) and often used to calculate the hydraulic problems in production. Secondly, it points out the method to couple the productivity and drilling parameters in UBD by coupling IPR equations in this chapter and equations set up in chapter 3.

Chapter 5 presents WELLST and UBDRILL programs. These are programs developed in this research through the combination of Microsoft Excel and Matlab in which Microsoft Excel was used to store the input and output data, and Matlab was applied to solve the numerical equations.

These simulators can be used to evaluate the wellbore stability condition of directional wells in anisotropic stress fields, model the multiphase flow in UBD operation, predict production capacity in UBD, calculate total pressure drop in drilling system, and suggest the optimum well control method in UBD by designing liquid gas rate window (LGRW).

Chapter 6 shows the results of the wellbore stability evaluation, hydraulics drilling analysis, and production capacity prediction in UBD of a typical well in Basin X.

Chapter 7 presents the conclusions and recommendations for this research.

CHAPTER 2 - WELLBORE STABILITY EVALUATION IN UBD

This chapter has the aim to present the feasibility studies of wellbore stability in UBD. It will generate geomechanical evaluations of the existing wells in Basin X, Vietnam which was introduced in chapter 1 to provide wellbore stability reviews and drilling strategies for planned wells in Basin X. The author has developed a piece of software (WELLST) to present the results of modelling wellbore stability in UBD operations.

2.1. Introduction

UBD techniques are often considered to avoid or mitigate formation damage, reduce lost circulation risk, and increase drilling rate of penetration. However, drilling with a bottomhole pressure less than the formation pore pressure will usually increase the risk of borehole instability due to yielding or failure of the rock adjacent to the borehole. There are a number of powerful numerical approaches for modelling the borehole stability. These approaches can be solved by finite element codes but until recently, it has been difficult to couple a program which can formulate the fluid flow behaviour such as ECLIPSE and another program which can be used to model mechanical deformation such as ANSYS, VISAGE, etc. So instead of using two different software to calculate the borehole stability, it is better to carry out this problem by programming only one software which can couple transient thermo-poro-elastic effects on 3D wellbore stability. This software is called WELLST and developed by the author from equations of Charlez [11, 12], and Farahani et al [13]. The results solved by WELLST will be compared to the results of ABAQUS (chapter 6), the commercial finite element software which can couple stress – pore pressure – thermal into one model, to verify the accuracy of the solution.

This chapter will express equations to estimate the wellbore stability condition in UBD and consider the calculation of collapse pressure which will be used to set up the right boundary of Liquid Gas Rate Window (LGRW) in chapter 6. So, the following contents will be presented in sequence:

- Literature reviews of wellbore stability.
- Rock mechanics study of granite basements in Vietnam.
- Steps to solve the transient thermo-poro-elastic equations which help to model the behaviours of pore pressure, temperature, and stress distribution around the borehole at the initial time and after different periods. These are equations help to establish WELLST program which can model transient thermo-poro-elastic effects on 3D wellbore stability in UBD.

2.2. Literature Reviews [14]

Simulation of wellbore stability has the purpose of predicting the redistribution of stresses around the wellbore as results of drilling, completion, or production operations. The most important elements needed to simulate geomechanical problems are the rock's constitutive behaviour model and an appropriate failure criterion. Constitutive behaviour models used to forecast wellbore stability range from those using the theory of elasticity to more complex models which take into account the theories of elasticity and plasticity, porosity of the materials, temperature, and time dependent effects. Comparison of the stresses obtained by using some of these constitutive models with an adequate rock failure criterion determines whether the rock around the borehole is likely to fail or not.

Bradley (1979) [15] first of all attempted to analytically formulate the wellbore stability problem. He combines Kirsch's equations with the solution proposed by Fairhurst in 1968 to develop analytical expressions of stress distribution around deviated boreholes using the linear elastic theory. Kirsch's equations formulated to calculate stresses in an infinite plate subjected to an initial state of stress expressed that the presence of a circular hole at the center of the plate produces a disturbance within the solid plate that modifies the initial stress condition. Because Kirsch's equations were derived from the assumption that rock was isotropic and homogeneous, Bradley's equations keep this condition and assuming that there was no interaction between drilling mud and in-situ formation fluid. In addition, plane strain condition is also assumed, indicating that the strain component parallel to the wellbore axis is negligible in comparison to the radial and tangential strain components. Mechanical stresses in the near wellbore rock immediately after the drilling perturbation can be obtained from linear elasticity [15, 16]. For a linear and isotropic case, the solution can be applied to deviated wells rather than to vertical wells only. Since most petroleum rocks are porous, poroelastic effects have to be considered for rock failure [17, 18] because fluid pressure in pores play an important role in distributing rock total stress. Rice and Cleary [19] developed basic stress diffusion equations for fluid-saturated elastic porous media.

Bratli et al (1983) [20] then investigated the sand control problem occurring during production in poorly consolidated sandstones. They analyzed the rock stress behaviour in the region where high effective stress concentration happens and concluded that failure area was located in a zone around the wellbore, known as the plastic zone.

Aadnoy and Chenevert (1987) [21] and Aadnoy (1988) [22] use Bradley's approach to make a detailed analysis about the influence of the inclination to borehole stability. Two different compressive failure criteria, the Von Mises and the Jaeger [23] criteria, were considered in their research to analyze borehole collapse. The first of these takes into account the intermediate principal stress while the second neglects this. Jaeger's criterion, which is an extension of the Mohr-Coulomb criterion, is applied usefully for laminated sedimentary rocks because it considers the existence of a plane of weakness that may affect rock behaviour. McLean and Addis (1990) [24] also use Bradley's solution, but they focus their analysis by selecting an appropriate failure criterion to compute safe-drilling fluid densities. They found that when using a linear

elastic constitutive model, the criteria that do not consider the influence of the intermediate principal stress such as Mohr-Coulomb are likely to underestimate the rock strength.

Aadnoy (1988) [22], and Ong and Roegiers (1993) [25] attempted to provide a better understanding of the effects of rock properties anisotropies on the stability of a wellbore. Rock was assumed as homogeneous, isotropic and behaves as linear elastic formation. Moreover, a condition of plane strain prevails, and there is no interaction between in-situ formation fluids and drilling mud in their work. To fully describe the mechanical behaviour of the rock, Ong and Roegiers suggested five elastic constants that including two moduli of elasticity, two Poisson's ratios and one shear modulus. They concluded that anisotropy strongly influences rock stability, especially when wellbore inclinations are high or horizontal.

Detournay and Cheng (1988) [26] and Cui et al. (1997) [27] presented analytical solutions for a circular wellbore embedded in a homogeneous and isotropic formation, which behaves linearly and according to the poroelastic theory. These solutions are the first attempts to formulate the time-dependent problem originated from the diffusion process through the porous medium related to the hydraulic conductivity of the rock. These solutions are restricted to the condition where the wellbore axis coincides with the direction of the vertical principal stress. Then, Cui et al. give the analytical solution for a circular wellbore, whose axis is inclined with respect to the principal stresses, in a linear, poroelastic, homogeneous medium where the in-situ stress anisotropy is consistent. Explicit and analytical solutions for wellbore stress and pore pressure distribution are also presented by Yew and Liu [28] for a deviated well. Fluid diffusion into or out of rock formations is considered in the above poroelastic analyses.

Fonseca (1998) [29] carried out his research by developing a chemical poroelastic model applicable to shales. He based it on the poroelastic solution proposed by Detournay and Cheng. To investigate the chemical aspect of the instability problem, he took a microscopic approach of the forces acting in a clay-fluid system, which is based on the Double-Layer Verwey and Overbeek (DLVO) theory and a macroscopic approach that evaluates the influence of osmotic potential between shale and fluid. He found that the total flow of fluid into or out of the shale is driven by two mechanisms: hydraulic pressure and chemical potential for the water based mud-shale one-dimensional system. He reported that the chemical potential can be introduced into a wellbore stability model as a pore pressure alteration, and it is controlled by the ratio between the water activity of the shale and the water activity of the drilling fluid. He concluded that by controlling the water activity of the mud it is possible to produce a chemical potential that counterbalances the hydraulic pressure so that the shale behaves as an impermeable formation. A particular case where a mud with a water activity is lower than the water activity of the shale will induce flow of water out of the shale. This condition is beneficial for the stability of the wellbore.

In recent years, since finite element theory was successfully implemented in other disciplines, researchers in geomechanics focused their attention on this theory.

Pan and Hudson (1988) [30] developed a couple of non linear axisymmetric finite element models in 2-D and 3-D to study the behaviour of stresses and displacements in the rock surrounding tunnel excavations. They used an elasto-viscoplastic model proposed by Zienckiewicz and Cormeau (1974) [31] that considers the time-dependent response of the rock associated with its plastic properties. They directed their study to find the differences between the results predicted by assuming plane strain in the 2-D model versus the results obtained by the 3-D model. Development of the 3-D model gave them the opportunity to compare the results of classical analysis in 2-D, a one-step tunnel excavation, versus multi-step analysis in 3-D. Among other conclusions, they found that modelling tunnel excavations in 2-D underestimates deformation compared with the results of the 3-D analysis. They concluded that this discrepancy obeys the plastic response of the rock behind the tunnel face, a response that a 2-D model cannot reproduce.

Ewy (1993) [32] also used commercial finite element software to study the behaviour of sedimentary rocks to analyze wellbore stability in directional and horizontal wells. He assumed rock formation behaves according to the elastoplastic theory and developed a 3D model by assuming that a “thin slice” of elements orthogonal to the well axis may represent the rock behaviour. Similar analysis was done by Zervos et al. (1998) [33], who modeled wellbore stability of weak sedimentary rocks for a wide range of wellbore orientations and deviations. They found that the risk of hole closure increases as wellbore inclination increases. Orientation of the wellbore becomes important only for deviations between 30 and 60 degrees. Also wellbores with inclinations of up to 15 degrees can be treated as vertical wells while for inclinations of more than 75 degrees, wellbores can be analyzed as horizontal wells.

Wang and Papamichos [34] showed that thermally induced pore pressure changes can be significant inside a low permeability formation. An increase of 30% over the isothermal pore pressure can be obtained for certain specified changes of temperature. For shale, thermal effects on wellbore stability are also important because thermal diffusion is much faster than hydraulic diffusion. In shale formations, convective heat transfer can be neglected because of their low permeability. In the case where the shale formation is cooled by the mud, a shale stability effect is achieved because both the pore pressure and the borehole hoop stress are reduced [12].

Chen et al (2000) [35] developed a new three-dimensional wellbore stability model that takes into account thermal stresses and the flux of both water and solutes from drilling fluids into and out of low-permeable porous medium like shale. They reported that indeed wellbore failure may first occur inside the formation, not on the wellbore wall. Such failure points also result in time dependent critical mud weights. They also concluded that the effect of temperature on horizontal wells is smaller as compared to the effect on vertical wells when determining collapse mud weights, because a higher earth stress environment dominates rock compressive failure for horizontal wells. Formations with higher thermal expansion coefficients can cause higher thermal stresses under the same temperature difference and can therefore be fractured with less pressure.

Farahasi et al (2006) [13] presented a 3D thermo-poroelastic model that accounts for the effect of convective heat transfer. Transient coupled pore pressure and temperature equations for non-isothermal conditions are developed based on conservation laws in their research. They concluded that the effects of pressure and temperature changes on wellbore stability are significant. In high permeability formations, convection is the dominant type of heat transfer and should be incorporated into wellbore stability models. They found that both compressive and tensile failure change as a result of temperature variation. Tensile failure is more sensitive than collapse failure with temperature changes. Heating the formation will reduce the chance of fracture, and cooling the formation has reverse effect. Therefore, some instability problems like lost circulation can be treated by controlling the temperature of drilling fluid. Moreover, in their research, temperature and pressure induced failures are considered as time dependent, and the critical mud weight window may decrease due to thermal effects.

2.3. Studies on Wellbore Stability of the Granite Basement in Basin X, Vietnam

Basin X (not the actual Basin's name) is located in an area of about 60m water depth, along the southeastern continental self, offshore Vietnam. The formations are mainly clastics of Eocene, Oligocene to Quaternary. The basin is highlighted tectonically by the tilted fault basement blocks, creating northeast-southwest striking graben, half graben and horst.

The main oil production reservoir is the Pre-Tertiary fractured granite basement, located at approximately 3,400-3,500mtvdss. This reservoir varies in thickness from several hundred meters to as much as 1,000 meters.

The fractured basement reservoir includes matrix rock with almost zero porosity, and various types of fractures. These fractures are connected through extremely complicated heterogeneous fracture system. Although there are fractures in anywhere in the basement, flow contributing fractures are only observed near major structural features, such as faults, and associated damaged zones. Micro fractures normally have their apertures less than 0.5mm, typically in the range of 0.1-0.3mm, whereas macro fractures/faults have their apertures varied in the range of centimeter to meter. The porosity of macro fractures/faults can be up to 15% and the permeability of macro fractures/faults can be thousands of mD. Fractures, both micro and macro, are mineral filled or partly filled with Zeolite, reducing the flow potential [9].

The studies on wellbore stability of granite basements in Vietnam [9, 36] have been carried out in recent years to generate geomechanical evaluations of existing wells in the Basin X, to provide wellbore stability reviews and develop optimum mud weight windows and drilling strategies for planned wells in the basement.

To do that, the descriptions of the rock mechanical properties, including strength, elastic parameters, the state of stress, studies of drilling results, log data from several wells and earlier studies and interpretations were gathered and analyzed.

According to these analyses, the major findings of the studies on rock mechanics of granite basements are as follows.

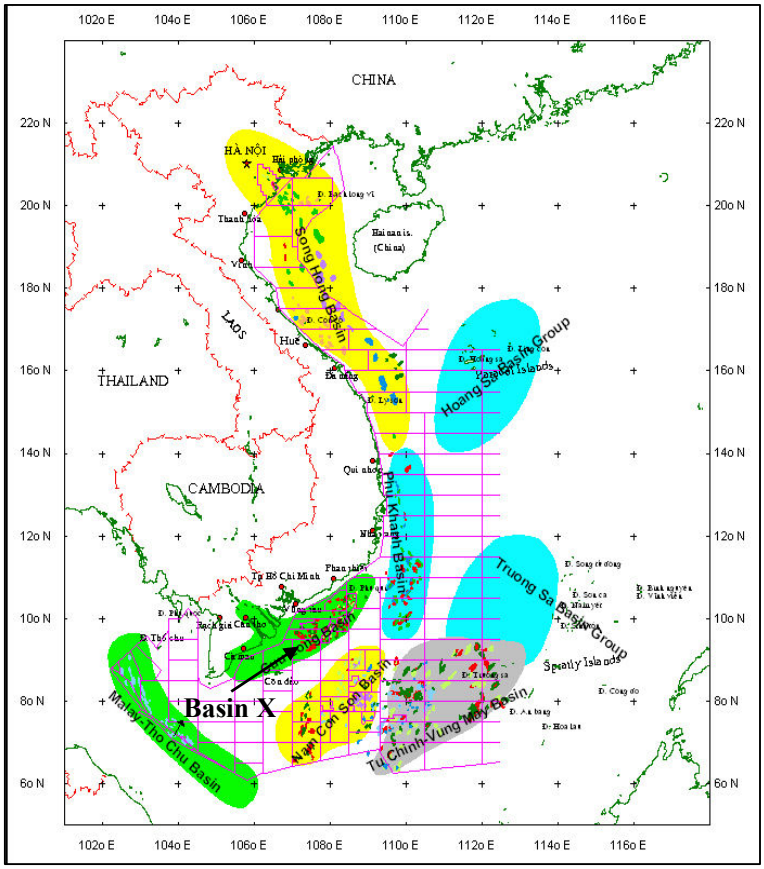

Fig 2.1. *Location of the Basin X*

2.3.1. Lithology summary for the granite basement of Basin X

The top of granite basement was approximately 30 meters shallower than prognosis, at 3250 m, which was based on the formation cuttings and wireline data from a typical well. For details, refer to the Fig 2.2 [9].

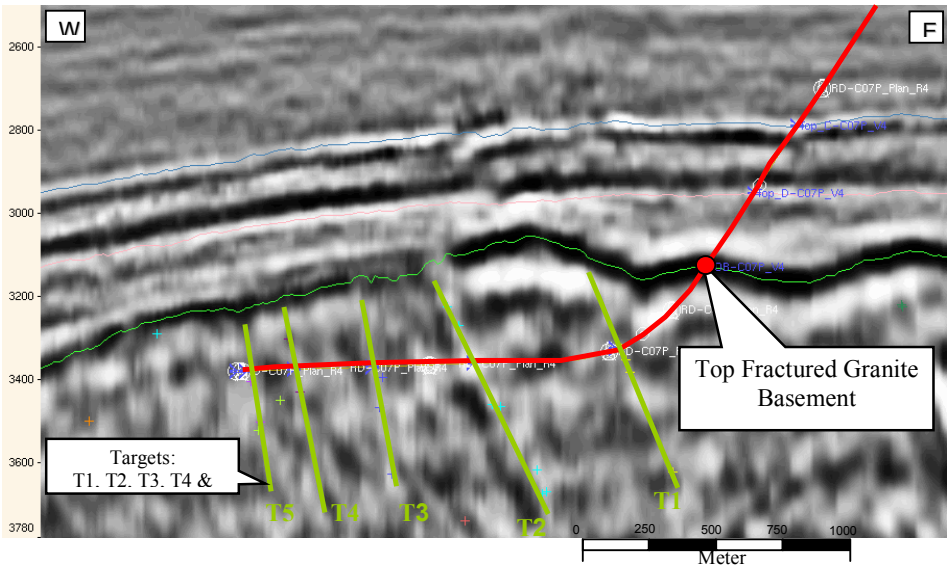

Fig 2.2. *Random seismic line along a typical well path in the Basin X [9]*

The drilled cuttings, sidewall cores suggested the lithology to be predominately granite to a granodiorite. The monzonite, granite to granodiorite is cut by several igneous dykes, commonly basaltic dykes.

The weathered zone can also be distinguished from the altered zone by observing the feldspars and mineral composition for evidence of being reworked, by either chemical and/or mechanical processes. The potassic feldspars are slightly softer then plagioclase and plagioclase is slightly softer then quartz and therefore the potassic feldspar will show the first indications of weathering, followed by the plagioclases. Generally, the weathering process will include feldspar kaolinitization, hydromica and increase in chlorite, hornblende and mica. The sodium/potassium ratio will also generally decrease significantly due to the easier sodium Na dissolution to meteoric water. In general, the sodic plagioclases are characteristic of granitic rocks and calcic plagioclases are more characteristic in the basalts.

Based on offset well data from several typical wells of Basin X and initial observation from the cutting samples the granite was estimated to be composed of approximately 15-25% quartz, 15-30% K-feldspar (predominately orthoclase and occasional microcline), 25-40% plagioclase (predominately albite to oligioclase) and 2-10% mica (biotite and muscovite). Secondary minerals commonly identified are chlorite, calcite, epidote, sphene-titanite, hornblende, zeolite and opaque minerals such as pyrite and occasional iron oxides. The monzonite is composed of 2 to 10% quartz, 30 to 40% K-feldspar, 35 to 45% plagioclase (predominately oligioclase) and 1 to 3% mica (biotite and muscovite), with similar secondary minerals to the dominate basement granite. The increase in quartz content to the 10 to 20% would indicate the rock was changing from the monzonite to a granodiorite. The basalt is composed of 15 to 25% phenocryst (plagioclase and orthoclase), with a groundmass of 75 to 85% microcrystalline plagioclase, nil-30% pyroxenes, with minor olivine.

The cuttings description is based primarily upon observation of the mineral assemblage, texture and degree of alteration. Almost all of the drilled basement section in Basin X appears to be moderately to heavily altered granite to granodiorite, occasionally becoming a monzonite, occasionally intersected by basaltic dykes and dyke swarms. Generally the normally textured granite will consist of 10% olive black-copper brown biotite, within a clear, translucent to opaque quartz and opaque white, grey to rarely pinkish feldspar groundmass, with common calcite, zeolite, chlorite and good traces of epidote, hornblende, sphene (titanite), magnetite and pyrite. Plagioclase could be recognised in fresh to slightly altered granite, from the coarse crystal texture, using a normal binocular microscope and examining the laths by rotating the laths and observing for reflectivity, indicating twinning. Plagioclase is slightly soluble in hydrochloric acid and provides a hazy suspension.

The extent of alteration is estimated from sample cuttings size and the hardness, the amount of kaolinite (varying from 10% in fresh through to 30% in heavily altered granite), and the degree of alteration of the mafic minerals. Fresh granite is typified by the very hard clear to translucent felsite groundmass, with very coarse "books" of

lustrous olive black biotite. The slight alteration produces opaque patches of partially kaolinised feldspar and peripheral chloritisation gives a greenish rim to the mica flakes; progressively the heavier alteration results in a friable kaolinite rich groundmass and the decay of mafics to greenish and dark grey argillaceous streaks. Plagioclases are also notably altered at various degrees and lab results indicated that they have been sericitised, calcitised and epidotised. Most of the plagioclase appeared to have minor evidence of fracturing possibly filled with calcite, zeolite and other nondescript clay minerals. In wells of Basin X, the hornblende in the sample was easily identifiable in the granodiorite and appeared to be occasionally altered, with evidence of being chloritised and epidotised. Alteration is probably the result of hydrothermal activity associated with volcanic intrusion; a zone of heavier alteration is often seen in proximity to the intrusive dykes. The uppermost basement portion of a typical well was moderately to heavily altered granite to granodiorite and intersected by several dykes, predominately basaltic dykes. The cuttings samples indicated a possible dyke swarm from 3260 m to 3460 m, where granite is intersected by numerous (1 to 4m thickness) basaltic dykes and another dyke swarm from 3560 m to 3650 m, where a monzonite is intersected by several (1 to 4 m thickness) basaltic dykes. Zeolite crystals were commonly observed in the cuttings samples and generally associated in close proximity to dykes and fractures. There are numerous different types of zeolites and in general it is an alumino-silicate (tectosilicate) mineral, with H_2O loosely bound within the mineral crystal structure and capable of exchanging ions such as sodium, potassium and calcium. Zeolites commonly occurs as a secondary mineral in the cavities of rocks such as basalt and other extrusive igneous rocks, rich in these minerals such as sodium, potassium and calcium. In general, zeolite has a hardness of approximately 3-5.5 on the Mohs hardness scale and a density of 2.2 to 2.3 g/cc and is softer and lighter when compared with other tectosilicates. The zeolite, identified in spot samples in Basin X was clear translucent, with orthorhombic, needle-like acicular crystals, occasionally radiating as aggregate and generally associated in close proximity of the dykes and/or fracture zones. The development of secondary minerals in the fracture zone is one of the risk factors in the basement reservoir and zeolite development is related to volcanic activity and generally implies the possibility of faults and fractures, which intrude along the zones of weakness. An increase in calcite, occasionally with perfect euhedral crystal development was also observed in several spot samples and identified with hydrocarbon shows, which were in close proximity to the dykes and commonly associated with possible fractures. Most of the basalt has been heavily altered in Basin X and the alterations were identified by the increase in chloritisation, epidotisation and calcitisation of plagioclase present in the groundmass. Numerous basalt samples, especially throughout basaltic dyke swarm had evidence of fractures commonly filled with both zeolite and calcite.

It was observed in the other drilled wells in Basin X that the borehole rugosity might have been caused by the direction of schistosity and foliation of the basement in relation to the direction of the borehole. One possibility is that the borehole path is crisscrossing the schistosity and foliation, which causes the granite basement to

fragment, and rock to break away from the sides of the borehole. This observation was first noted in several wells in both the deviated well and the sidetrack well (Fig 2,8, chapter 2).

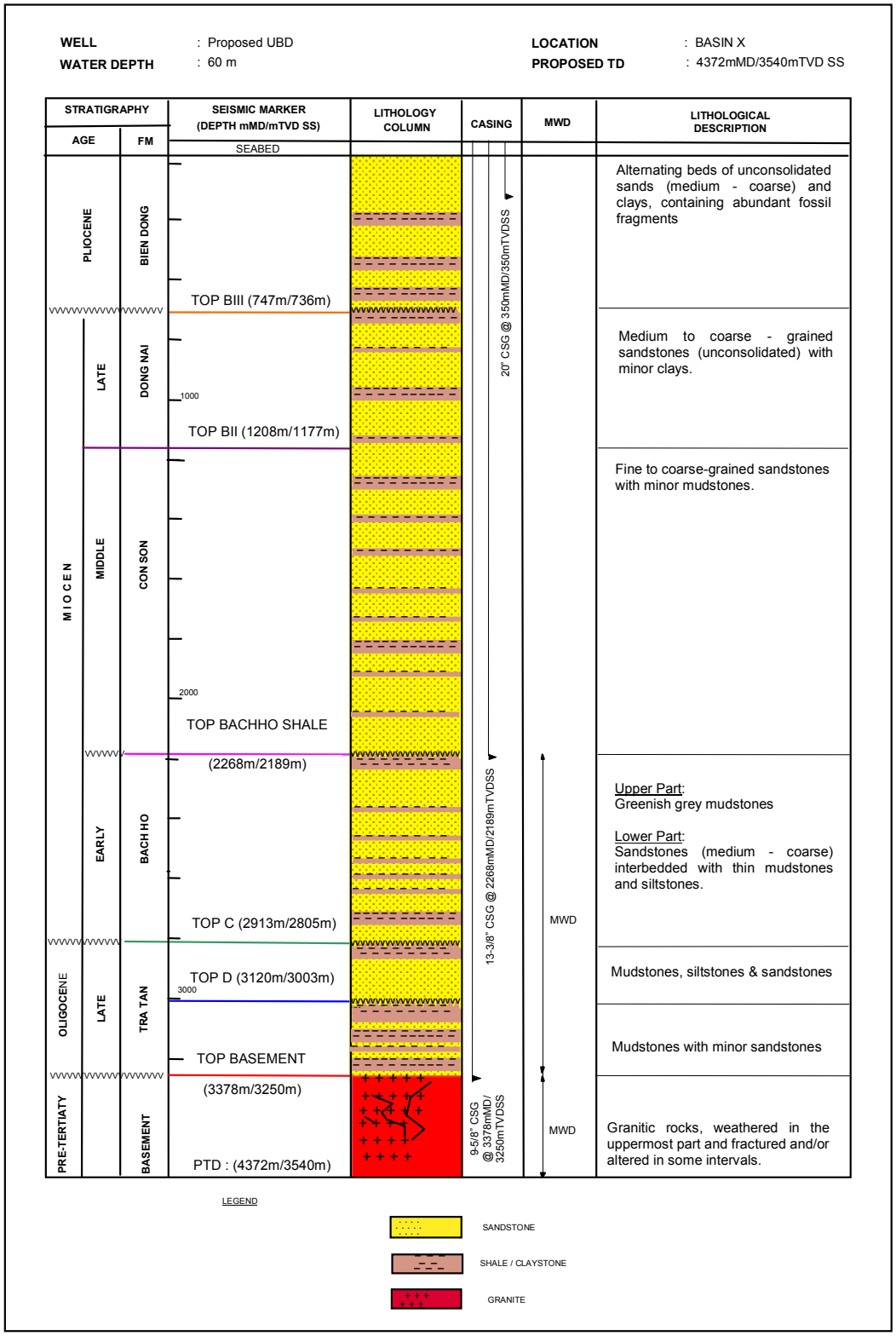

Fig 2.3. *Stratigraphy column of a typical well in Basin X [9]*

It was observed in the other drilled wells in Basin X that the borehole rugosity might have been caused by the direction of schistosity and foliation of the basement in

relation to the direction of the borehole. One possibility is that the borehole path is crisscrossing the schistosity and foliation, which causes the granite basement to fragment, and rock to break away from the sides of the borehole. This observation was first noted in several wells in both the deviated well and the sidetrack well (Fig 2,8, chapter 2).

2.3.2. Geomechanical conditions [9, 36]

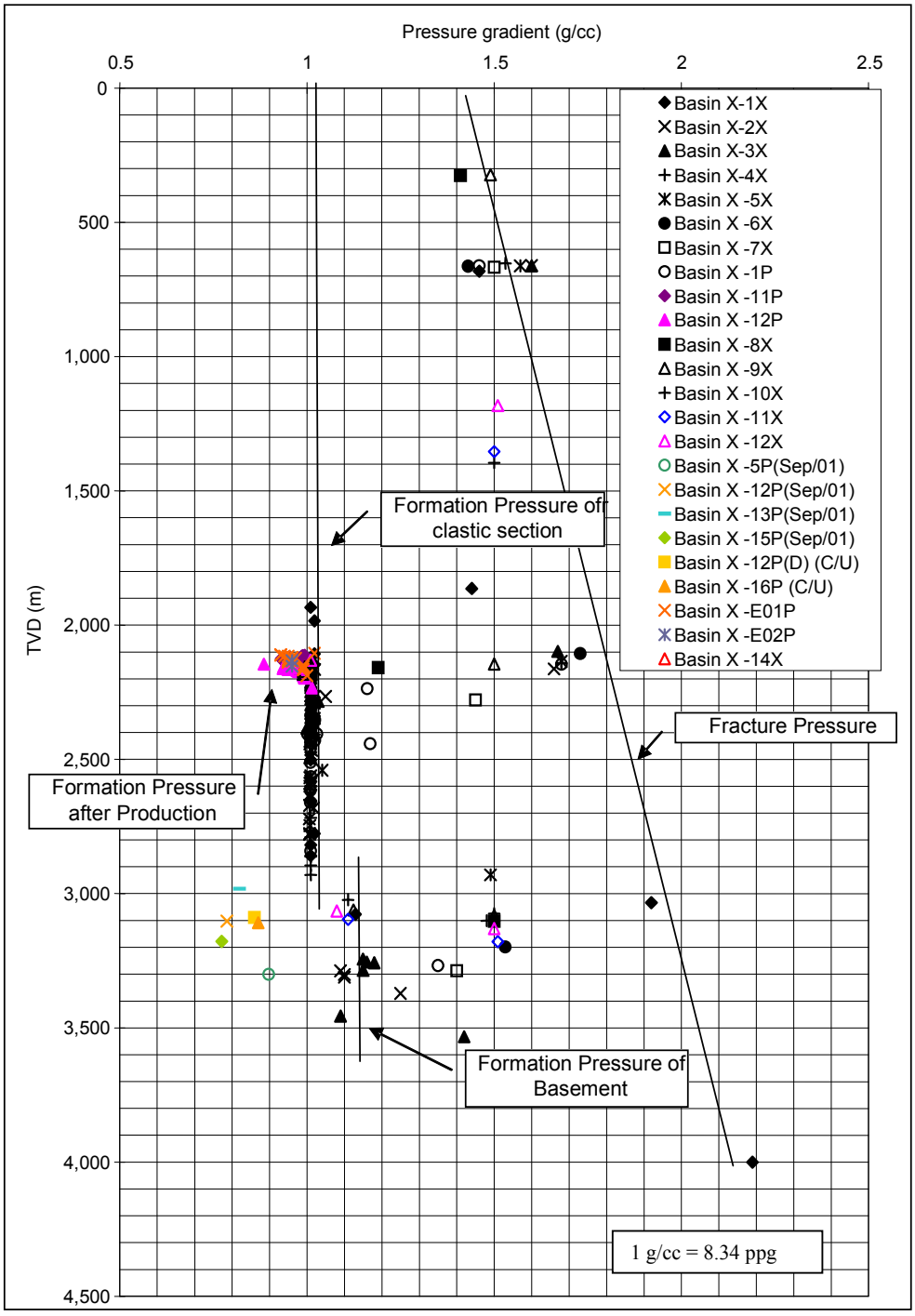

Fig 2.4. *Formation and Fracture pressure curves of Basin X [9]*

The pore pressure gradient in Basin X is 0.442 psi/ft in the overburden and 0.338 psi/ft in the oil zone (basement). It has some overpressure, starting from the thick shale sections just above the basement and reaching a value of about 9.25 ppg (0.48 psi/ft) at the top of the basement. Pore pressure curves have been estimated based on pressure measurements (MDT, well tests, interpretations) in the study wells. The general pore pressure curves for a field in Basin X are presented in Fig 2.4.

Based on the available geology overviews, literature and earlier studies on granite basements in Vietnam, it was assumed that the Basin X is under compression in a strike-slip environment. This would make the overburden stress the intermediate stress. It has to be noted though that this statement is only globally true, and refers to the stresses in the earth's crust as a whole. On a more detailed scale, and especially in the near surface rocks, it has to be recognized that stresses are lithology dependent and that the order of the stresses may change depending on lithology.

Estimates of vertical (overburden) stress magnitudes, from surface to well true depth, were computed using integrated formation density where available. Over zones without density logs, a density estimate was constructed from volumetric analysis and trends based on published studies. For all horizons, the vertical stress σ_z was assumed to be one of the in-situ principal stresses, though not necessarily the largest.

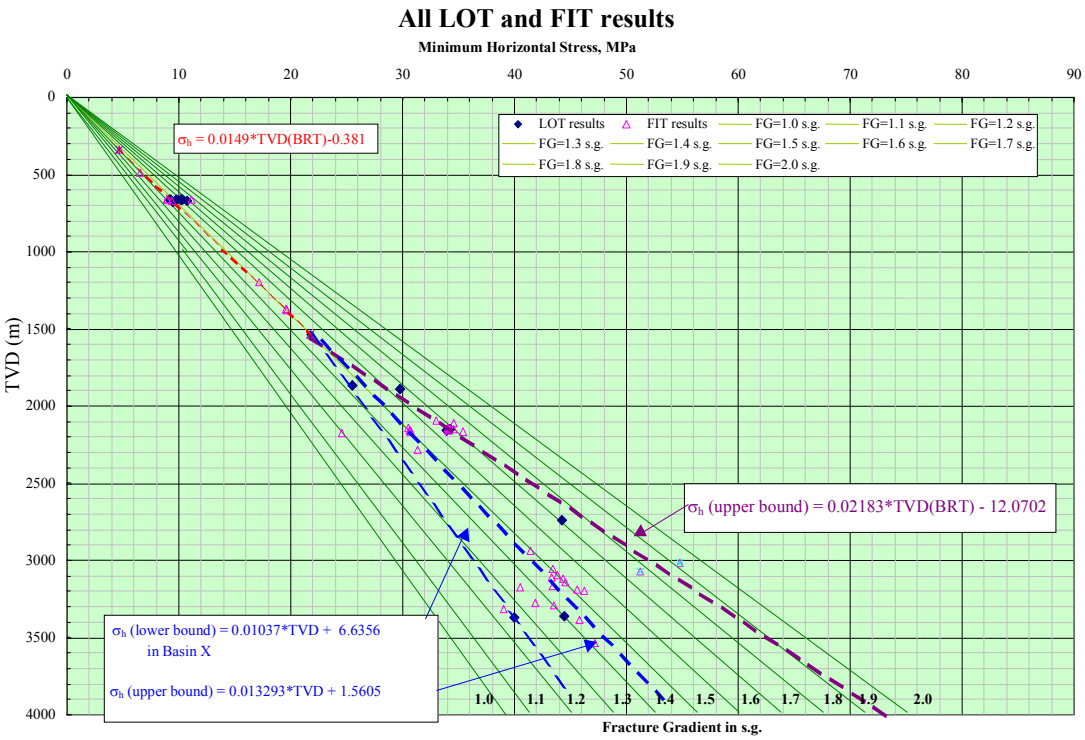

Fig 2.5. *Leak off test data in Basin X [9]*

The minimum horizontal stress σ_h was computed, initially using a Mohr Coulomb failure model which was then calibrated with drilling data. The drilling reports contain information on several Leak-off tests (LOT) in the field. Fig 2.5 above shows the peak pressures reached versus TVD for all the LOTs described in the drilling reports. Although none of the LOTs was carried through to the point of measuring the

formation closure stress, and detailed pressure data versus time or pumped volume was not available, the LOTs nevertheless provided limits to the minimum horizontal stress at several depths in clastic and granite basement formations and were found to be very useful for the study. Please note however that individual LOTs may provide values that are not representative of the stress field, for instance due to failure of the casing shoe or differing LOT procedures, reporting deficiencies, etc.

The maximum horizontal stress cannot be measured directly but was constrained by an upper boundary computed from a Mohr Coulomb model using the calibrated σ_h. The upper bound maximum horizontal stress was then back-calibrated using breakout observations and stress ratios inferred from observations on the input wells.

It was possible to get a good estimate of the stresses by using a comparatively complete set of image log data. Image logs are integral to constraining the orientation and magnitude of the in situ stress tensor. In addition they can provide vital structural and sedimentological information at a resolution greater than seismic data. It was also to recognize various different modes of shear and tensile failure of the wellbore wall on the image logs and these observations made it possible to tightly constrain the minimum and maximum horizontal stresses. A good estimate of stress direction and inversion for stress magnitudes was therefore possible. A plot of in-situ stresses in a strike-slip fault type case was presented in Fig 2.6.

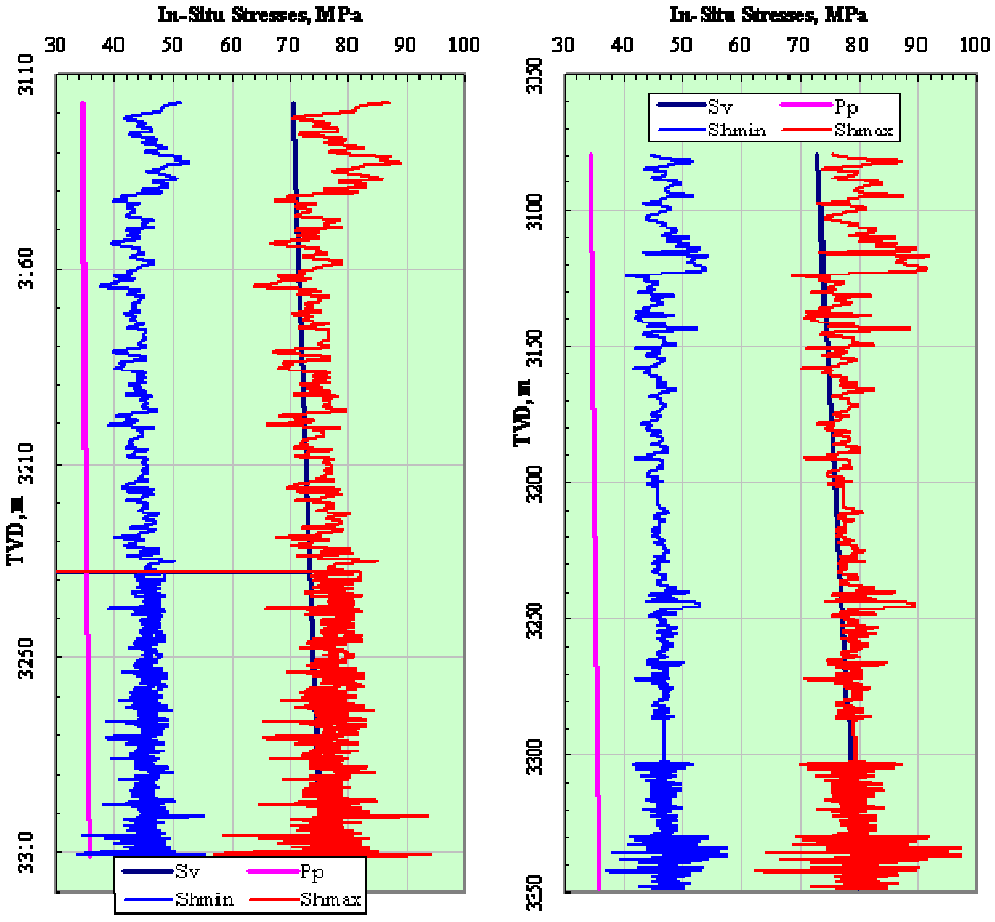

Fig 2.6. *In-situ stresses in a strike-slip fault type case of Basin X [9]*

The stress map is provided in Fig 2.7 plotting the azimuth of the maximum horizontal stress from observations made in the wells at different geological horizons. The maximum horizontal stress direction in the basement section was found to be consistent over the fields/wells in the study, with variations of +/-10^o between the wells in Basin X. The maximum horizontal stress azimuth is SE-NW (around 130^o-310^o) in Basin X. This value was found to be in broad accordance with geological information, regional stress maps and the own research of some petroleum companies in Vietnam.

The principal stress order characterizes the tectonic setting as strike-slip in the basement, i.e. the vertical stress is the intermediate stress over most of the section. In the clastic overburden, the horizontal stresses are somewhat less anisotropic, with the maximum horizontal stress about equal to the vertical stress in the most competent formations (with high modulus of elasticity) but fairly close to the minimum horizontal stress in the softest formations (with low modulus of elasticity).

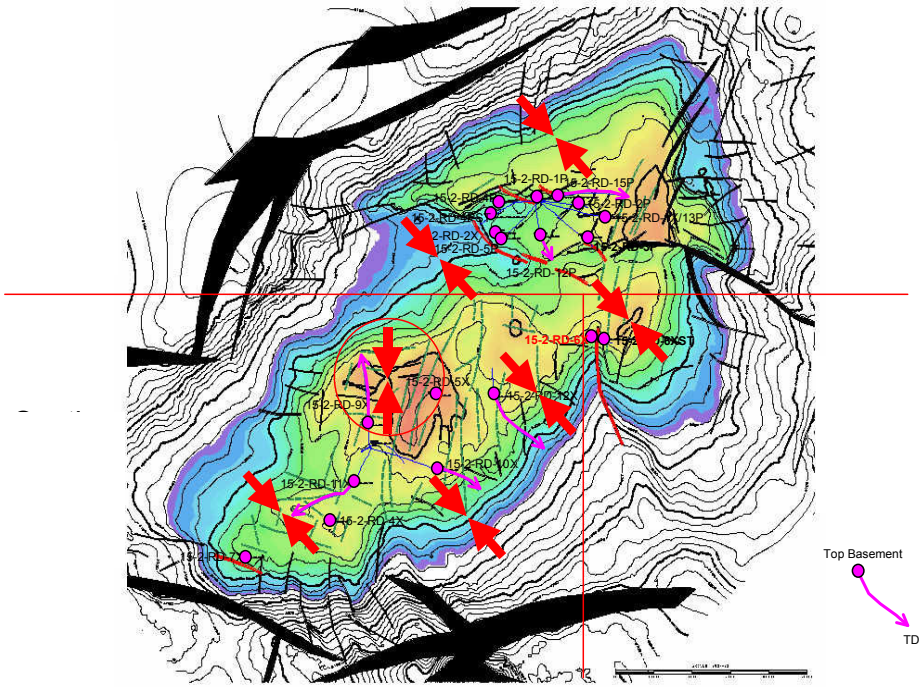

Fig 2.7. *The stress map of Basin X [9]*

2.3.3. Rock strength parameters

Rock strength is evaluated using tri-axial tests that used rock cores from deeper section, and correlation by the sonic velocity log. The typical unconfined strength (UCS) in the basement of Basin X seems to be 10,000 to 40,000 psi (68.9 – 275.6 MPa), and the friction angle is 25-30 deg.

Rock strength parameters such as UCS, friction angle and cohesion of material can be estimated by core tests or from sonic wave velocity measurements. Compressional, but no shear transit times were available over the basement sections of Basin X. The sonic compressional transit times, in combination with density data, were therefore used to estimate shear wave transit times for use in basement rock strength correlations. Historical analysis of available basement data from Basin X showed that a fixed v_p/v_s ratio = 1.47 could be used to synthesize the approximate shear velocities in

basement. From the delta time (50-75 μs/ft), compressional velocity, shear velocity, shear modulus, and Young's modulus have been calculated by:

$$v_p = \frac{1}{DT(\mu s / ft)}$$

$$v_s = \frac{v_p}{1.47}(ft/s) \qquad \text{----------} \quad (2.1)$$

$$G = \rho_R v_s^2 (MPa)$$

$$E = 2G(1+\nu)(MPa)$$

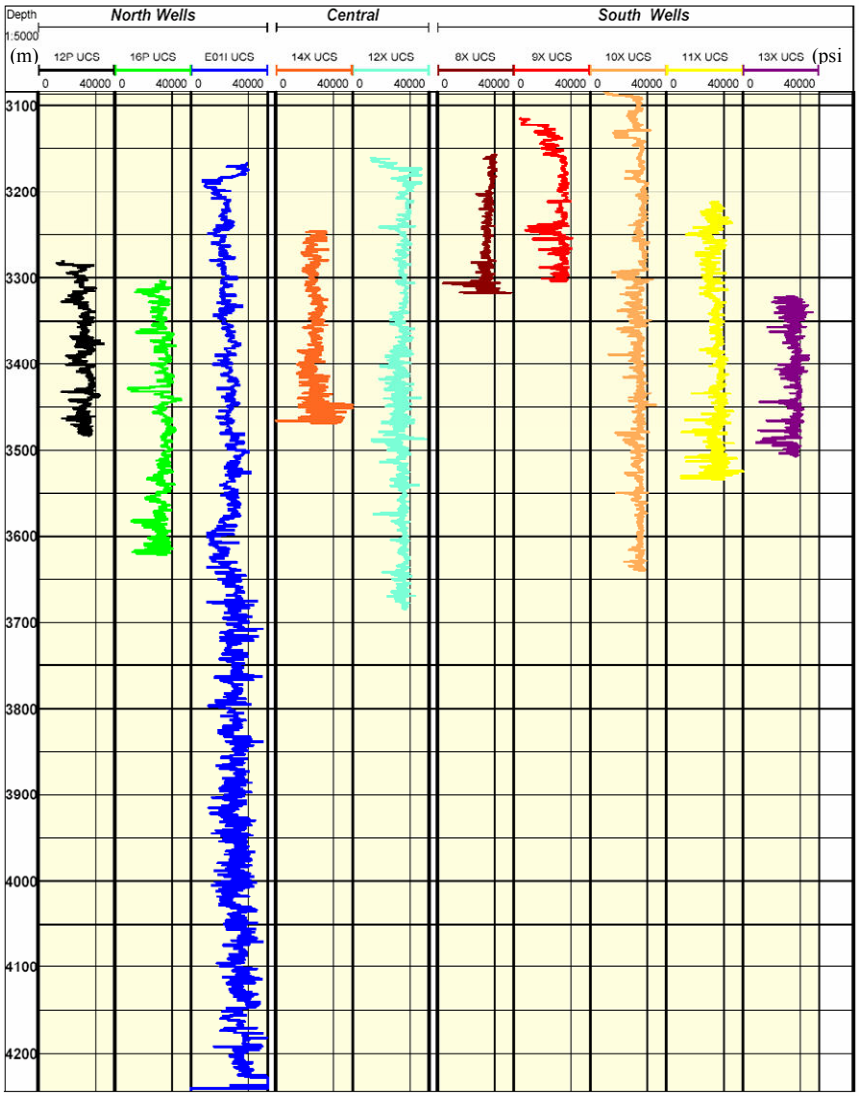

Fig 2.8. *The estimated UCS (unconfined compressive strength) of Basin X versus TVD [9]*

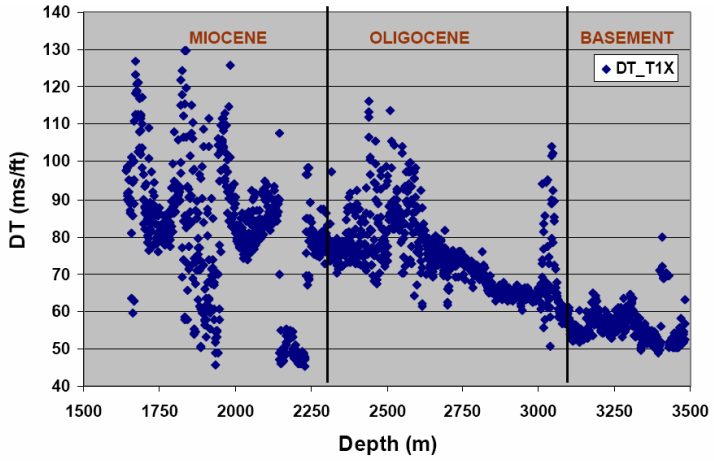

Fig 2.9. *Sonic distribution versus TVD [9]*

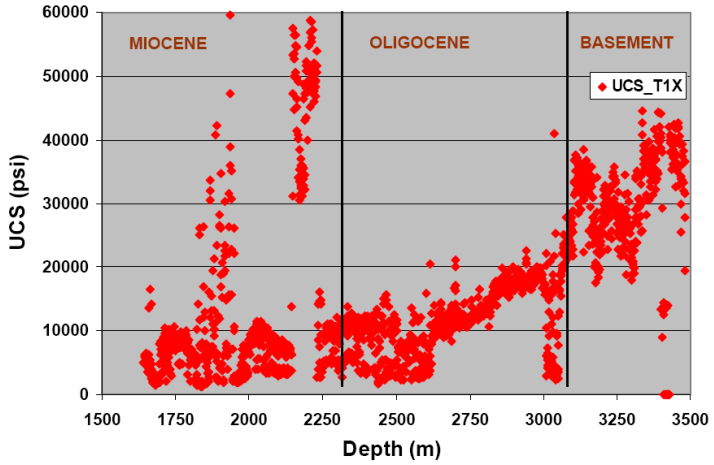

Fig 2.10. *UCS distribution versus TVD [9]*

The recommendations based on the above plot can be expressed as follows:

The sonic distribution (1640 to 2750 m TVD) shows a general average trend of sonic values from approximately 130-70 μs/ft. The corresponding UCS average trend is from approximately 5,000 to 15,000 psi. With reference to drillability, this can be regarded as soft medium to medium.

Extrusive in the Miocene (1825 to 1950 m TVD) shows a general average trend of sonic values from approximately 70-50 μs/ft. The corresponding UCS average trend is from approximately 30,000 to 40,000 psi. With reference to drillability, this can be regarded as extremely hard.

Intrusive in the Miocene (2150 to 2230 m TVD) shows a general average trend of sonic values from approximately 50-45 μs/ft. The corresponding UCS average trend is from approximately 40,000 to 50,000 psi. With reference to drillability, this can be regarded as extremely hard.

Toward the end (2750 to 3100 m TVD), the general average trend of sonic values is approximately at 65 μs/ft. The corresponding UCS average trend is from approximately at 20,000 psi.

The basement (3100 to 3500 m TVD) shows a general average trend of sonic values from approximately 80-50 μs/ft. The corresponding UCS average trend is from approximately 10,000 to 40,000 psi.

2.4. Wellbore Stability Modelling

2.4.1. Stress around boreholes

Underground formations are always under some stress, mostly due to overburden pressure and tectonic stresses. When a well is drilled in a formation, stressed solid material is removed and replaced with a fluid under pressure. Since the well fluid pressure normally does not match exactly the stress state of the formation around the well, it produces a disturbance within this initial stress condition. This stress alteration is important, since large stress deviations may lead to failure in the formation and consequently large operational problems in the well.

Due to the geometry, the stresses in a rock surrounding a borehole will be a function of the position relative to the borehole, and only match some of the external stresses at the boundaries. Calculation of the stresses, which is a necessity for subsequent failure analyses, is therefore not trivial in borehole geometry.

Stresses and strains in cylindrical coordinates [37]

In order to examine the stresses in the rocks surrounding a borehole, it is convenient to express the stresses and strains in cylindrical co-ordinates. The stresses at a point P identified by the cylindrical co-ordinates r, θ, z are then denoted σ_r, σ_θ, σ_z, $\tau_{r\theta}$, τ_{rz}, and $\tau_{\theta z}$. σ_r is called the radial stress, σ_θ the tangential stress, and σ_z the axial stress. These stresses relate to the Cartesian co-ordinate stresses as:

$$\begin{aligned}
\sigma_r &= \sigma_x \cos^2\theta + \sigma_y \sin^2\theta + 2\tau_{xy}\sin\theta\cos\theta \\
\sigma_\theta &= \sigma_x \sin^2\theta + \sigma_y \cos^2\theta - 2\tau_{xy}\sin\theta\cos\theta \\
\sigma_z &= \sigma_z \\
\tau_{r\theta} &= (\sigma_y - \sigma_x)\sin\theta\cos\theta + \tau_{xy}(\cos^2\theta - \sin^2\theta) \\
\tau_{rz} &= \tau_{xz}\cos\theta + \tau_{yz}\sin\theta \\
\tau_{\theta z} &= \tau_{yz}\cos\theta - \tau_{xz}\sin\theta
\end{aligned} \quad \text{----------} \quad (2.1)$$

The strain are in cylindrical coordinates denoted ε_r, ε_θ, ε_z, $\Gamma_{r\theta}$, Γ_{rz} and $\Gamma_{\theta z}$. if the displacement in r-direction is denoted u, in θ-direction v, and in z-direction w, the strains are:

$$\varepsilon_r = \frac{\partial u}{\partial r}$$
$$\varepsilon_\theta = \frac{1}{r}\left(u + \frac{\partial v}{\partial \theta}\right)$$
$$\varepsilon_z = \frac{\partial w}{\partial z}$$
$$\Gamma_{r\theta} = \frac{1}{2r}\left(\frac{\partial u}{\partial \theta} - v\right) + \frac{\partial v}{\partial r} \quad \text{----------(2.2)}$$
$$\Gamma_{rz} = \frac{1}{2}\left(\frac{\partial w}{\partial r} + \frac{\partial u}{\partial z}\right)$$
$$\Gamma_{rz} = \frac{1}{2}\left(\frac{1}{r}\frac{\partial w}{\partial \theta} + \frac{\partial v}{\partial z}\right)$$

These strains relate to the Cartesian coordinate strains as:

$$\varepsilon_r = \varepsilon_x \cos^2\theta + \varepsilon_y \sin^2\theta + 2\Gamma_{xy}\sin\theta\cos\theta$$
$$\varepsilon_\theta = \varepsilon_x \sin^2\theta + \varepsilon_y \cos^2\theta - 2\Gamma_{xy}\sin\theta\cos\theta$$
$$\varepsilon_z = \varepsilon_z$$
$$\Gamma_{r\theta} = \left(\varepsilon_y - \varepsilon_x\right)\sin\theta\cos\theta + \Gamma_{xy}\left(\cos^2\theta - \sin^2\theta\right) \quad \text{----------(2.3)}$$
$$\Gamma_{rz} = \Gamma_{xy}\cos\theta + \Gamma_{yz}\sin\theta$$
$$\Gamma_{\theta z} = \Gamma_{yz}\cos\theta - \Gamma_{xz}\sin\theta$$

For an isotropic material, the stress-strain relations are easily transferred into cylindrical coordinates:

$$\sigma_r = (\lambda + 2G)\varepsilon_r + \lambda\varepsilon_\theta + \lambda\varepsilon_z$$
$$\sigma_\theta = \lambda\varepsilon_r + (\lambda + 2G)\varepsilon_\theta + \lambda\varepsilon_z$$
$$\sigma_z = \lambda\varepsilon_r + \lambda\varepsilon_\theta + (\lambda + 2G)\varepsilon_z \quad \text{----------(2.4)}$$
$$\tau_{r\theta} = 2G\Gamma_{r\theta}$$
$$\tau_{rz} = 2G\Gamma_{rz}$$
$$\tau_{\theta z} = 2G\Gamma_{\theta z}$$

λ: Lamé's parameter

G: shear modulus

Stress around a borehole – general linear elastic solution in the anisotropic stress field [37]

The principal stresses in the virgin formation are assumed σ_v, the vertical stress, σ_H the maximum horizontal stress, and σ_h, the minimum horizontal stress. A coordinate system (x_o, y_o, z_o) is oriented so that x_o is parallel to σ_H, y_o is parallel to σ_h, and z_o is parallel to the borehole.

A transform from (x_o, y_o, z_o) to (x, y, z) can be obtained in two operations (Fig 2.11), a rotation *a* around z_o axis, and then 2) a rotation ϕ around y axis. The angle ϕ

represents the wellbore deviation (inclination), and the angle *a* represents the azimuth angle.

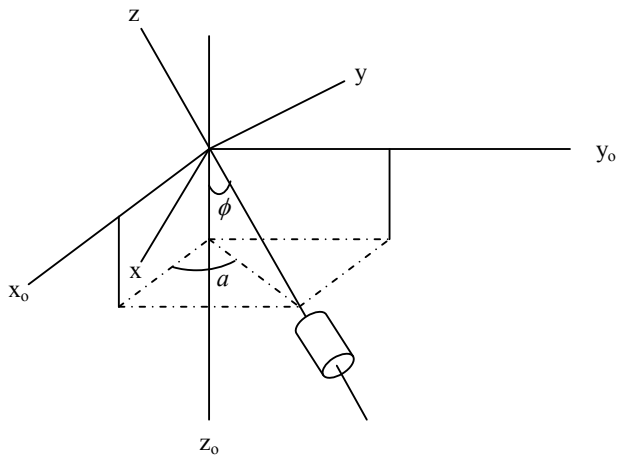

Fig 2.11. *Definition of wellbore orientation parameters*

The transform can be described mathematically by the direction cosines:

l_{xxo}, l_{xyo}, l_{xzo} = the cosines of the angles between the x-axis and the x_o, y_o, z_o axes, respectively.

l_{yxo}, l_{yyo}, l_{yzo} = the cosines of the angles between the y-axis and the x_o, y_o, z_o axes, respectively.

l_{zxo}, l_{zyo}, l_{zzo} = the cosines of the angles between the z-axis and the x_o, y_o, z_o axes, respectively.

The direction cosines relate to the angles *a* and *i* as:

$$\begin{array}{lll} l_{xxo} = \cos a \cos\phi & l_{xyo} = \sin a \cos\phi & l_{xzo} = -\sin\phi \\ l_{yxo} = -\sin a & l_{yyo} = \cos a & l_{yzo} = 0 \\ l_{zxo} = \cos a \sin\phi & l_{zyo} = \sin a \sin\phi & l_{zzo} = \cos\phi \end{array} \quad \text{----------} \quad (2.5)$$

Expressed in the (x,y,z) coordinate system, the formation stresses σ_H, σ_h, and σ_v become:

$$\begin{aligned} \sigma_x &= l_{xxo}^2\sigma_H + l_{xyo}^2\sigma_h + l_{xzo}^2\sigma_v \\ \sigma_y &= l_{yxo}^2\sigma_H + l_{yyo}^2\sigma_h + l_{yzo}^2\sigma_v \\ \sigma_z &= l_{zxo}^2\sigma_H + l_{zyo}^2\sigma_h + l_{zzo}^2\sigma_v \\ \tau_{xy} &= l_{xxo}l_{yxo}\sigma_H + l_{xyo}l_{yyo}\sigma_h + l_{xzo}l_{yzo}\sigma_v \\ \tau_{yz} &= l_{yxo}l_{zxo}\sigma_H + l_{yyo}l_{zyo}\sigma_h + l_{yzo}l_{zzo}\sigma_v \\ \tau_{zx} &= l_{zxo}l_{xxo}\sigma_H + l_{zyo}l_{xyo}\sigma_h + l_{zzo}l_{xzo}\sigma_v \end{aligned} \quad \text{----------} \quad (2.6)$$

According to Bradley (1979) [15], the complete stress solution around the wellbore is:

$$\begin{cases} \sigma_r = \dfrac{(\sigma_x+\sigma_y)(1-\dfrac{R^2}{r^2})}{2} - \dfrac{(\sigma_x-\sigma_y)(1+3\dfrac{R^4}{r^4}-4\dfrac{R^2}{r^2})\cos 2\theta}{2} + \tau_{xy}(1+3\dfrac{R^4}{r^4}-4\dfrac{R^2}{r^2})\sin 2\theta + P_{wf}\dfrac{R^2}{r^2} \\ \sigma_\theta = \dfrac{(\sigma_x+\sigma_y)(1+\dfrac{R^2}{r^2})}{2} - \dfrac{(\sigma_x-\sigma_y)(1+3\dfrac{R^4}{r^4})\cos 2\theta}{2} - \tau_{xy}(1+3\dfrac{R^4}{r^4})\sin 2\theta - P_{wf}R^2/r^2 \\ \sigma_a = \sigma_z - \nu\left[2(\sigma_x-\sigma_y)\dfrac{R^2}{r^2}\cos 2\theta + 4\tau_{xy}\dfrac{R^2}{r^2}\sin 2\theta\right] \\ \tau_{r\theta} = \dfrac{(\sigma_x-\sigma_y)(1+3\dfrac{R^4}{r^4}-4\dfrac{R^2}{r^2})\sin 2\theta}{2} + \tau_{xy}(1-3\dfrac{R^4}{r^4}+2\dfrac{R^2}{r^2})\cos 2\theta \\ \tau_{\theta z} = (-\tau_{xz}\sin\theta + \tau_{yz}\cos\theta)(1+\dfrac{R^2}{r^2}) \\ \tau_{rz} = (\tau_{xz}\cos\theta + \tau_{yz}\sin\theta)(1-\dfrac{R^2}{r^2}) \end{cases} \quad \text{----------} (2.7)$$

The solutions given by Eq (2.7) are more complicated because the shear stresses are here non zero. Thus, σ_r, σ_θ, and σ_a are not principal stresses in the general case when the borehole is deviated, or the horizontal stress is anisotropic.

Notice that the general solutions (2.7) also depend on θ, the angle between the interested point and x-axis, so the stresses vary with the position around the borehole.

Stress around a borehole – general linear poroelastic solution in the isotropic stress field [37]

The isotropic stress distribution around a vertical hole in a stressed formation was discussed above assuming linear elasticity, and treating rock as a solid material. The fact that the rock is permeable and porosity influences the stress solution will now be described. The solution, as given by Bratli et al (1983) [20], is presented as follows:

$$\begin{cases} \sigma_r = \sigma_h + (\sigma_h - P_{wf})\dfrac{R^2}{R_\infty^2 - R^2}\left[1-\left(\dfrac{R_\infty}{r}\right)^2\right] - (P_R - P_{wf})\dfrac{1-2\nu}{2(1-\nu)}\alpha\left\{\dfrac{R^2}{R_\infty^2-R^2}\left[1-\left(\dfrac{R_\infty}{r}\right)^2\right] + \dfrac{\ln(R_\infty/r)}{\ln(R_\infty/R)}\right\} \\ \sigma_\theta = \sigma_h + (\sigma_h - P_{wf})\dfrac{R^2}{R_\infty^2 - R^2}\left[1+\left(\dfrac{R_\infty}{r}\right)^2\right] - (P_R - P_{wf})\dfrac{1-2\nu}{2(1-\nu)}\alpha\left\{\dfrac{R^2}{R_\infty^2-R^2}\left[1+\left(\dfrac{R_\infty}{r}\right)^2\right] + \dfrac{\ln(R_\infty/r)}{\ln(R_\infty/R)} - \dfrac{1}{\ln(R_\infty/R)}\right\} \\ \sigma_z = \sigma_v + 2\nu(\sigma_h - P_{wf})\dfrac{R^2}{R_\infty^2 - R^2} - (P_R - P_{wf})\dfrac{1-2\nu}{2(1-\nu)}\alpha\left\{\nu\dfrac{2R^2}{R_\infty^2-R^2} + \dfrac{2\ln(R_\infty/r)}{\ln(R_\infty/R)} - \dfrac{\nu}{\ln(R_\infty/R)}\right\} \end{cases} \quad \text{----------} (2.8)$$

Notice that the way the solutions have been written, the boundary conditions must be satisfied:

$$\begin{cases} \sigma_z(R_\infty) = \sigma_v \\ \sigma_r(R_\infty) = \sigma_\theta(R_\infty) = \sigma_h \\ P_f(R_\infty) = P_R \\ \sigma_r(R) = P_{wf} \\ P_f(R) = P_{wf} \end{cases} \quad \text{----------} (2.9)$$

Assuming $R_\infty >> R$, the solutions reduce to:

$$\begin{cases} \sigma_r = \sigma_h - (\sigma_h - P_{wf})\left(\frac{R}{r}\right)^2 + (P_R - P_{wf})\frac{1-2\nu}{2(1-\nu)}\alpha\left\{\left(\frac{R}{r}\right)^2 - \frac{\ln(R_\infty / r)}{\ln(R_\infty / R)}\right\} \\ \sigma_\theta = \sigma_h + (\sigma_h - P_{wf})\left(\frac{R}{r}\right)^2 - (P_R - P_{wf})\frac{1-2\nu}{2(1-\nu)}\alpha\left\{\left(\frac{R}{r}\right)^2 + \frac{\ln(R_\infty / r)}{\ln(R_\infty / R)}\right\} \\ \sigma_z = \sigma_v - (P_R - P_{wf})\frac{1-2\nu}{2(1-\nu)}\alpha\frac{2\ln(R_\infty / r) - \nu}{\ln(R_\infty / R)} \end{cases} \text{---------- (2.10)}$$

where

P_{wf}: wellbore pressure, MPa

P_R: reservoir pressure, MPa

R: wellbore radius, m

R_∞: outer radius ($R_\infty >> R$), m

ν: Poisson's ratio

α: Biot constant.

Stress around a borehole - general linear thermo-poroelastic solution with diffusion process in the anisotropic stress field [11, 12, 13]

Deeper, deviated, and horizontal wells can be drilled by UBD technology in recent years. However, these wells demand operating under high pressure and temperature conditions and as a result generate increased wellbore stability problems. This stability of the borehole is influenced by the state of stresses and material properties. Whenever the state of stresses changes, the failure indexes at the point of interest around the wellbore changes, as a results the stability condition of the wellbore change. While material properties are often considered to be constants of the rock character for the purpose of wellbore stability, the state of stresses is affected considerably by pore pressure and temperature. So coupling the temperature and pore pressure factors in modelling stress distribution around the borehole is a necessary demand. The first factor, thermal effect, is generated by the difference of wellbore temperature and drilled formation temperature, and increases as the temperature imbalance increases. Cooling the formation is found to be helpful in lowering collapse pressure, resulting in a more stable borehole. However, it is also found that a formation is more vulnerable to fracture because cooling also lowers the breakdown pressure so the wellbore may be more sensitive toward unstable by the tensile mode. A higher mud weight is required to fracture the formation when hot drilling fluid is used because hotter fluids increase the breakdown pressure. Also higher mud density is needed to prevent a wellbore from collapsing when a hotter fluid is being circulated through it. The second one, pore pressure effect, should be considered in analyzing the behaviour of rock around the wellbore. Pore pressure changes will contribute to the state of stresses by redistribution of the pressure profile and additional stresses on the matrix.

Pore pressure changes in UBD occur as a result of hydraulic diffusion of the formation fluid into the wellbore ($P_{wf} < P_R$) from fractures, and thermal effects.

In this research, the borehole is assumed to be infinitely long parallel to its axis, directional, and located in anisotropic stress field (horizontal stresses are not the same in all directions). The calculation of the perturbation can be performed under plane strain hypothesis ($\varepsilon_{zz} = 0$). Finally, convection effects are ignored. The only mode of heat transfer taken into account is conduction [5]. So the steps to carry out this problem include solving the hydraulic diffusivity and thermal diffusivity equations, then coupling these equations into the complete thermo-poro-elastic model to calculate the stress distribution around the borehole in underbalanced drilling.

The diffusivity equations satisfy the following boundary conditions:

$$\begin{array}{lll} t \le 0 & P(r) = P_R & T(r) = T_R \\ t > 0 & P(r = R, t) = P_{wf} & P(r = \infty, t) = P_R \\ & T(r = R, t) = T_{wf} & T(r = R, t) = T_R \end{array} \quad \text{---------- (2.11)}$$

The hydraulic diffusivity equation is obtained by introducing Darcy's law into the mass balance. For a linear thermo-poroelastic material, the hydraulic diffusivity equation is such that [12]:

$$\frac{1}{\eta}\frac{\partial P}{\partial t} - \alpha\frac{\partial \varepsilon_{kk}}{\partial t} - \frac{L\rho_o}{T_R\eta}\frac{\partial T}{\partial t} = \frac{k}{\mu}\nabla^2 P \quad \text{---------- (2.12)}$$

k and μ being respectively rock permeability (assumed to be isotropic) and fluid viscosity (assumed to be Newtonian). η is a constant called Biot's modulus which can be expressed as a function of other thermo-poroelastic parameters:

$$\eta = \frac{BK_u}{\alpha} \quad \text{---------- (2.13)}$$

$$L = \frac{T_R}{\rho_f}\frac{\alpha_u K_u - \alpha_B K}{\alpha} \quad \text{---------- (2.14)}$$

where α is Biot's coefficient, K_u is undrained bulk modulus of material, α_u and α_B are undrained and drained thermal expansion coefficient, and B is known as the Skempton pore pressure coefficient.

$$\alpha = 1 - \frac{K}{K_M} \quad \text{---------- (2.15)}$$

$$K_u = \frac{K}{1 - \alpha B} \quad \text{---------- (2.16)}$$

$$B = \frac{\frac{1}{K} - \frac{1}{K_M}}{\phi\left[\frac{1}{K_f} - \frac{1}{K_M}\right] + \left[\frac{1}{K} - \frac{1}{K_M}\right]} \quad \text{---------- (2.17)}$$

and K, K_M, K_f are bulk modulus of dry material, matrix, and fluid, $\phi = \frac{e}{1+e}$ is rock porosity with *e,* void ratio.

In particular, such as incompressible solid constituent ($K_M \to \infty$) when the compressibility of the solid phase is negligible compared to that of drained bulk material, simplified expressions for the thermo-poroelastic coefficients become:

$$\alpha = 1 \quad \text{---------- (2.18)}$$

$$B = \frac{K_f}{K_f + \phi K} \quad \text{---------- (2.19)}$$

$$\eta = \frac{K_f}{\phi} \quad \text{---------- (2.20)}$$

$$L = \frac{T_R}{\rho_f}\alpha_f K_f \quad \text{---------- (2.21)}$$

L and α_f are latent heat and thermal expansion coefficients of fluid.

The thermal diffusivity equation is obtained by introducing Fourier's law into the energy balance equation:

$$-\frac{\rho_f L}{\eta}\frac{\partial P}{\partial t} + \left(C_\varepsilon m_o + \frac{\rho_f^2}{\eta}\frac{L^2}{T_R}\right)\frac{\partial T}{\partial t} - \alpha_B K T_R \frac{\partial \varepsilon_{kk}}{\partial t} - \frac{k}{\mu}\rho_f C_f \nabla P \nabla T + \frac{k}{\mu} T_R \alpha_f (\nabla P)^2 = \kappa \nabla^2 T \quad \text{------ (2.22)}$$

where $C_\varepsilon m_o$ (J/m^3.^{o}C) and κ (W/m.^{o}C) are volumetric heat capacity and thermal conductivity coefficient of the fluid-solid association respectively, C_f (J/kg.^{o}C) in this case is the specific heat of fluid at constant pressure.

$$C_\varepsilon m_o = C_\varepsilon \rho_r = C_\varepsilon(\phi\rho_f + (1-\phi)\rho_s \quad \text{---------- (2.23)}$$

with C_ε (J/kg.^{o}C) is specific heat of rock, ρ_f is fluid density (kg/m^3), ρ_s is dry solid phase density (kg/m^3), and ρ_r is rock density (kg/m^3).

Substituting the following Navier's equation:

$$\varepsilon_{kk} = -\alpha_P(P - P_R) - \alpha_T(T - T_R) \quad \text{---------- (2.24)}$$

into diffusion Eqs (2.12), and (2.22), one is led to the following differential system:

$$\frac{\partial}{\partial t}\begin{bmatrix} P \\ T \end{bmatrix} = C\nabla^2 \begin{bmatrix} P \\ T \end{bmatrix} \quad \text{---------- (2.25)}$$

where C is an asymmetrical matrix [2,2] developed by Charlez [12]:

$$C^{-1} = \begin{bmatrix} \frac{D_{PP}\mu}{k} & \frac{D_{PT}\mu}{k} \\ \frac{D_{PT}T_R}{\kappa} & \frac{D_{TT}T_R}{\kappa} \end{bmatrix} \text{ ---------- (2.26)}$$

D_{PP}, D_{PT} and D_{TT} are coupling constants depending on thermo-poroelastic parameters:

$$D_{PP} = \frac{1}{\eta} + \alpha\alpha_P \text{ ---------- (2.27)}$$

$$D_{PT} = \alpha\alpha_T - \frac{\rho_f L}{\eta T_R} \text{ ---------- (2.28)}$$

$$D_{TT} = \frac{C_\varepsilon m_o}{T_R} + \frac{\rho_f^2 L^2}{\eta T_R^2} + \alpha_T \alpha_B K \text{ ---------- (2.29)}$$

$$\alpha_P = \frac{3\alpha}{3K + 4G} \text{ ---------- (2.30)}$$

$$\alpha_T = \frac{3\alpha_B K}{3K + 4G} \text{ ---------- (2.31)}$$

The finite differential method can be used to solve the couple problem (equation 2.25). However, the previous solutions of Chen (2001) indicated that the analytical solution to the partially decoupled problem matches the solution to the coupled problem. Therefore, the partially decoupled problem can reflect the coupling behaviour of rocks and can be used to analyze the effect of temperature and pore pressure changes on wellbore stability. The differential system Eqs (2.25) taking into account the boundary condition (2.11) can be solved using Laplace transforms. The general solution of Coussy (1991) [38] for P and T is such that:

$$P(r,t) = P_R + \frac{P_{wf} - P_R}{\sqrt{\Delta}}\left[\alpha_2 g_2(r,t) - \alpha_1 g_1(r,t)\right] - \frac{\kappa D_{PT}(T_{wf} - T_R)}{T_R\sqrt{\Delta}}\left[g_1(r,t) - g_2(r,t)\right] \text{ ---------- (2.32)}$$

$$T(r,t) = T_R + \frac{T_{wf} - T_R}{\sqrt{\Delta}}\left[\alpha_2 g_1(r,t) - \alpha_1 g_2(r,t)\right] - \frac{\frac{k}{\mu} D_{PT}(P_{wf} - P_R)}{\sqrt{\Delta}}\left[g_1(r,t) - g_2(r,t)\right] \text{ ---------- (2.33)}$$

in which Δ, α_1, and α_2 are constants depending on the various thermo-poroelastic parameters.

$$\alpha_1 = \frac{1}{2}\left(\frac{\kappa}{T_R} D_{PP} - \frac{k}{\mu} D_{TT} - \sqrt{\Delta}\right) \text{ ---------- (2.34)}$$

$$\alpha_2 = \frac{1}{2}\left(\frac{\kappa}{T_R}D_{PP} - \frac{k}{\mu}D_{TT} + \sqrt{\Delta}\right) \text{ ---------- (2.35)}$$

$$\Delta = \left(\frac{k}{\mu}D_{TT} - \frac{\kappa}{T_R}D_{PP}\right)^2 + \frac{4\frac{k}{\mu}\kappa}{T_R}D_{PT}^2 \text{ ---------- (2.36)}$$

and g_1, g_2 are integral functions such that

$$g_i(r,t) = 1 - \frac{2}{\pi}\int_0^{\infty} e^{-\frac{tx^2}{t_i}} \frac{J_o(x)\gamma_o\left(x\frac{r}{R}\right) - J_o\left(x\frac{r}{R}\right)\gamma_o(x)}{J_o^2(x) + \gamma_o^2(x)}\frac{dx}{x} \text{ ---------- (2.37)}$$

For a given radial distance, g_i varies from 0 (initial time) to 1 (infinite time) (Fig 2.12).

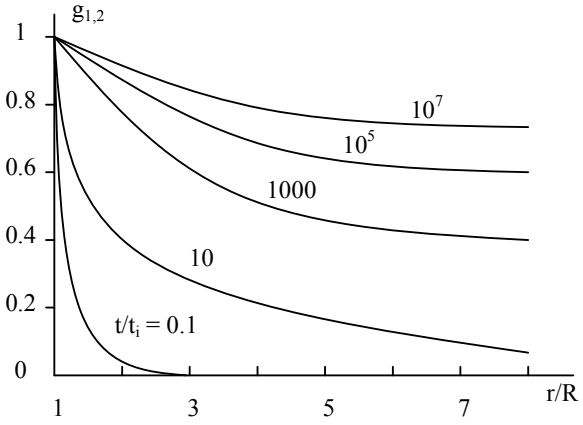

Fig 2.12. *Shape of the g function for various values of t/t_i*

In the Eq (2.37) t_i is the characteristic diffusion time (i = 1 for hydraulic diffusion, i = 2 for thermal diffusion), and J_o and γ_o are the Bessel functions [39] order zero of the first kind and second kind.

$$t_i = \frac{R^2}{C_i} \text{ ---------- (2.38)}$$

C_1, and C_2 are two diffusion constants:

$$C_1 = \frac{\frac{k}{\mu}D_{TT} + \frac{\kappa}{T_R}D_{PP} + \sqrt{\Delta}}{2(D_{PP}D_{TT} - D_{PT}^2)} \text{ ---------- (2.39)}$$

$$C_2 = \frac{\frac{k}{\mu}D_{TT} + \frac{\kappa}{T_R}D_{PP} - \sqrt{\Delta}}{2(D_{PP}D_{TT} - D_{PT}^2)} \text{ ---------- (2.40)}$$

The Bessel function order zero of the first kind can be expressed by the following equation with n = 0 and shown in Fig 2.13.

$$J_n(x) = \sum_{k=0}^{\infty} \frac{(-1)^k}{k!\Gamma(n+k+1)} \left(\frac{x}{2}\right)^{n+2k} \quad \text{---------- (2.41)}$$

where $\Gamma(n+k+1) = \int_0^{\infty} e^{-n} x^{n+k} dx$ ---------- (2.42)

is the Gamma function.

While the Bessel function order zero of the second kind can be expressed by the following equation the shape of this function are shown in Fig 2.14.

$$Y_o(x) = \frac{2}{\pi}\left[\left(\ln\frac{x}{2} + C\right)J_o(x) + \frac{2}{1}J_2(x) - \frac{2}{2}J_4(x) + \frac{2}{3}J_6(x) - \ldots\right] \quad \text{--------- (2.43)}$$

where C = 0.577215665.

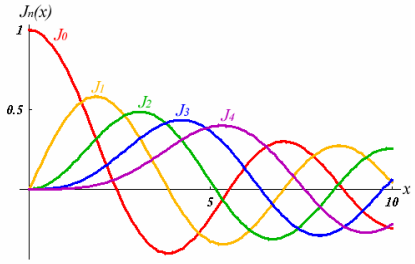

Fig 2.13. *Shape of the Bessel function of the first kind*

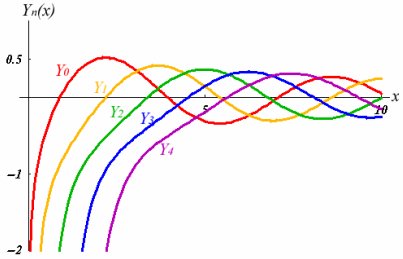

Fig 2.14. *Shape of the Bessel function of the second kind*

After the coupled diffusivity equations for temperature and pore pressure in Eqs (2.30), and (2.31) are set up, stresses around the wellbore [13] induced as the result of pressure and temperature changes can be calculated by the following:

$$\Delta\sigma_r = \frac{\alpha(1-2\nu)}{1-\nu}\frac{1}{r^2}\int_R^r \left(P(r,t) - P_R\right)rdr + \frac{E\alpha_B}{3(1-\nu)}\frac{1}{r^2}\int_R^r \left(T(r,t) - T_R\right)rdr \quad \text{-- (2.44)}$$

$$\Delta\sigma_\theta = -\frac{\alpha(1-2\nu)}{1-\nu}\left[\frac{1}{r^2}\int_R^r \left(P(r,t) - P_R\right)rdr - P(r,t) + P_R\right] \quad \text{---------- (2.45)}$$
$$-\frac{E\alpha_B}{3(1-\nu)}\left[\frac{1}{r^2}\int_R^r \left(T(r,t) - T_R\right)rdr - T(r,t) + T_R\right]$$

$$\Delta\sigma_z = \frac{\alpha(1-2\nu)}{1-\nu}\left(P(r,t) - P_R\right) + \frac{E\alpha_B}{3(1-\nu)}\left(T(r,t) - T_R\right) \quad \text{---------- (2.46)}$$

The complete thermo-poro-elastic model is obtained by superimposing mechanical (in-situ), thermal and hydraulic induced stress effects. After including the thermo-pressure induced stresses into Eqs (2.7), the resultant equations are as follows [13].

$$\begin{cases} \sigma_r = \dfrac{(\sigma_x+\sigma_y)(1-\dfrac{R^2}{r^2})}{2} - \dfrac{(\sigma_x-\sigma_y)(1+3\dfrac{R^4}{r^4}-4\dfrac{R^2}{r^2})\cos 2\theta}{2} \\ +\tau_{xy}(1+3\dfrac{R^4}{r^4}-4\dfrac{R^2}{r^2})\sin 2\theta + P_{wf}\dfrac{R^2}{r^2} + \Delta\sigma_r \\ \sigma_\theta = \dfrac{(\sigma_x+\sigma_y)(1+\dfrac{R^2}{r^2})}{2} - \dfrac{(\sigma_x-\sigma_y)(1+3\dfrac{R^4}{r^4})\cos 2\theta}{2} \\ -\tau_{xy}(1+3\dfrac{R^4}{r^4})\sin 2\theta - P_{wf}\dfrac{R^2}{r^2} + \Delta\sigma_\theta \\ \sigma_a = \sigma_z - \nu\left[2(\sigma_x-\sigma_y)\dfrac{R^2}{r^2}\cos 2\theta + 4\tau_{xy}\dfrac{R^2}{r^2}\sin 2\theta\right] + \Delta\sigma_z \\ \tau_{r\theta} = \dfrac{(\sigma_x-\sigma_y)(1-3\dfrac{R^4}{r^4}+2\dfrac{R^2}{r^2})\sin 2\theta}{2} + \tau_{xy}(1-3\dfrac{R^4}{r^4}+2\dfrac{R^2}{r^2})\cos 2\theta \\ \tau_{\theta z} = (-\tau_{xz}\sin\theta + \tau_{yz}\cos\theta)(1+\dfrac{R^2}{r^2}) \\ \tau_{rz} = (\tau_{xz}\cos\theta + \tau_{yz}\sin\theta)(1-\dfrac{R^2}{r^2}) \end{cases} \text{---------- (2.47)}$$

2.4.2. Failure criteria [13]

Failure criteria determine the amount of stress that can be tolerated by a formation before failure. In other words, it defines the limit of deformation before the rock fails. If the induced stresses are greater than the formation compression or tensile strength then the rock under stress fails. When stresses at any point around the wellbore are calculated, it is possible to compare the computed stresses against the formation strength. At points where the failure index, Mohr-Coulomb Failure Index (MFI) or Drucker Prager Failure Index (DPFI), shown in Eqs (2.61), and (2.62), is less than zero failure is considered to have initiated. The failure index defines whether the stress state has exceeded formation strength or not. Most failure criteria are expressed in terms of principal stresses. The principal stresses can be calculated using the following equations after stress tensor around the wellbore is obtained from previous equations.

$$\sigma_1 = \sigma_r \text{ ---------- (2.48)}$$

$$\sigma_2 = \frac{\sigma_\theta+\sigma_z}{2} + \sqrt{\left(\frac{\sigma_\theta-\sigma_z}{2}\right)^2 + \tau_{\theta z}^2} \text{ ---------- (2.49)}$$

$$\sigma_3 = \frac{\sigma_\theta+\sigma_z}{2} - \sqrt{\left(\frac{\sigma_\theta-\sigma_z}{2}\right)^2 + \tau_{\theta z}^2} \text{ ---------- (2.50)}$$

$$\sigma_{\max} = \max(\sigma_1, \sigma_2, \sigma_3) \text{ ---------- (2.51)}$$

$$\sigma_{\min} = \min(\sigma_1, \sigma_2, \sigma_3) \quad \text{---------- (2.52)}$$

Boreholes may fail in tensile (fracture) or compression (breakdown) modes depending on the pressure inside the wellbore. However, this research focuses on the stability of wellbore in UBD when wellbore pressure is lower than pore pressure so only compressive failure criteria are interested in. There are numerous compressive failure criteria used to define the failure of rock in compression. Mclean and Addis [24] categorized and compared some of these criteria and analyzed the effects of some parameters such as intermediate principal stress. Here only the two most commonly used criteria, with respect to wellbore stability analysis, are reviewed, are Mohr-Coulomb and Drucker Prager (also known as the extended Von Mises) [40]. These criteria are implemented in WELLST simulator so that the user can have the option of which criteria to choose according to the situation.

Mohr-Coulomb criterion

The Mohr-Coulomb criterion assumes that failure occurs when the shear stress on any point in a material reaches a value that depends linearly on the normal stress in the same plane. The Mohr-Coulomb model is based on plotting Mohr's circle for states of stress at failure in the plane of the maximum and minimum principal stresses. The failure line is the best straight line that touches these Mohr's circles (Fig 2.15).

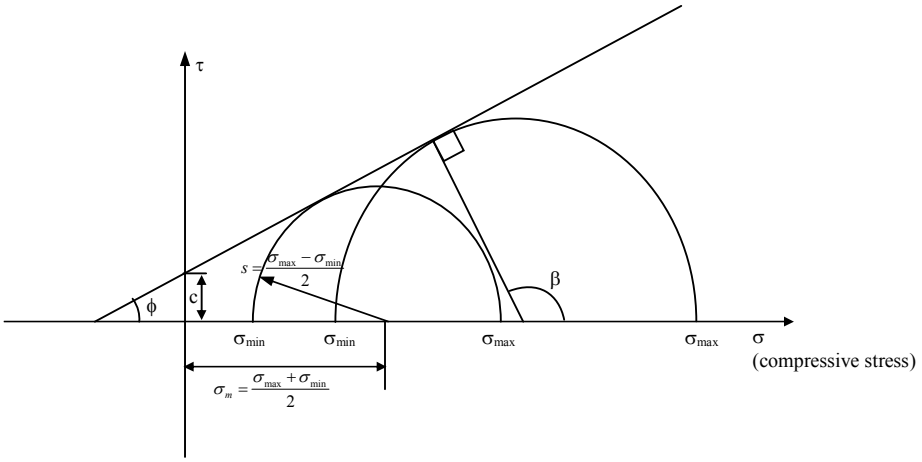

Fig 2.15. *Mohr Coulomb failure model*

Therefore, the Mohr-Coulomb model is defined by:

$$\tau = c + \sigma \tan\phi \quad \text{---------- (2.53)}$$

From Mohr Coulomb circle,

$$\begin{aligned} \tau &= s\cos\phi \\ \sigma &= \sigma_m - s\sin\phi \end{aligned} \quad \text{---------- (2.54)}$$

Substituting for τ and σ, multiplying both sides by cosϕ, and reducing, the Mohr Coulomb model can be written as:

$$s - \sigma_m \sin\phi - c\cos\phi = 0 \quad \text{---------- (2.55)}$$

where

$$s = \frac{1}{2}\left(\sigma_{\max} - \sigma_{\min}\right) \text{ ---------- (2.56)}$$

is half of the difference between the maximum principal stress, σ_{max}, and the minimum principal stress, σ_{min} (and is, therefore, the maximum shear stress),

$$\sigma_m = \frac{1}{2}\left(\sigma_{\max} + \sigma_{\min}\right) \text{ ---------- (2.57)}$$

is the average of the maximum and minimum principal stress, c is material cohesion, and ϕ is the friction angle.

Continuing to substitute Eqs (2.56), and (2.57) into (2.55):

$$\frac{1}{2}\left(\sigma_{\max} - \sigma_{\min}\right) - \frac{1}{2}\left(\sigma_{\max} + \sigma_{\min}\right)\sin\phi - c\cos\phi = 0 \text{ ---------- (2.58)}$$

$$\sigma_{\max} = 2c\frac{\cos\phi}{1-\sin\phi} + \sigma_{\min}\frac{1+\sin\phi}{1-\sin\phi} \text{ ---------- (2.59)}$$

If $\sigma_{min} = 0$, the unconfined compressive strength C_o can be obtained:

$$C_o = 2c\frac{\cos\phi}{1-\sin\phi} \text{ ---------- (2.60)}$$

Mohr-Coulomb failure index (MFI) is used to define the stability of the wellbore in WELLST program. The positive MFI will stands for a stable wellbore without collapse (compressive) failure.

$$MFI = 2c\frac{\cos\phi}{1-\sin\phi} + \frac{1+\sin\phi}{1-\sin\phi}\left(\sigma_{\min} - P(r,t)\right) - \left(\sigma_{\max} - P(r,t)\right) \text{ ---------- (2.61)}$$

Drucker Prager criterion

The Drucker Prager criterion is expressed in terms of principal stresses as:

$$DPFI = -\sqrt{J_2} + mJ_1^{eff} + \tau_o \text{ ---------- (2.62)}$$

$$J_1^{eff} = \frac{\sigma_1 + \sigma_2 + \sigma_3}{3} - P(r,t) \text{ ---------- (2.63)}$$

$$\sqrt{J_2} = \frac{1}{3}\sqrt{\left(\sigma_1 - \sigma_2\right)^2 + \left(\sigma_2 - \sigma_3\right)^2 + \left(\sigma_3 - \sigma_1\right)^2} \text{ ---------- (2.64)}$$

$$m = \frac{2\sqrt{2}\sin\phi}{3-\sin\phi} \text{ ---------- (2.65)}$$

$$\tau_o = \frac{2\sqrt{2}c\cos\phi}{3-\sin\phi} \text{ ---------- (2.66)}$$

where J_1^{eff} is the effective mean stress, and $\sqrt{J_2}$ is the shear stress. The positive DPFI will also symbol for a stable wellbore without collapse (compressive) failure.

In ABAQUS software, for general states of stress the model is more conveniently written in terms of three stress invariants as:

$$F = R_{mc}q' - p'\tan\phi - c = 0 \text{ ---------- (2.67)}$$

$$R_{mc}(\Theta,\phi) = \frac{1}{\sqrt{3}\cos\phi}\sin\left(\Theta + \frac{\pi}{3}\right) + \frac{1}{3}\cos\left(\Theta + \frac{\pi}{3}\right)\tan\phi \text{ ---------- (2.68)}$$

where Θ is the deviatoric polar angle defined as:

$$\cos(3\Theta) = \left(\frac{r'}{q'}\right)^3 \text{ ---------- (2.69)}$$

and

$p' = -\frac{1}{3}trace(\sigma)$ is the equivalent pressure stress,

$q' = \sqrt{\frac{3}{2}(S:S)}$ is the Mises equivalent stress,

$r' = \left(\frac{9}{2}S \cdot S : S\right)^{\frac{1}{3}}$ is the third invariant of deviatoric stress,

$S = \sigma + p'I$ is the deviatoric stress.

The friction angle controls the shape of the yield surface in the deviatoric plane as shown in Fig 2.16. The friction angle can range from 0^o to 90^o. In the case of $\phi = 0^o$ the Mohr Coulomb model reduces to the pressure independent Tresca model with a perfectly hexagonal deviatoric section. In the case of $\phi = 90^o$ the Mohr-Coulomb model reduces to the "tension cut-off" Rankine model with a triangular deviatoric section and $R_{mc} = \infty$ (this limiting case is not permitted within the Mohr Coulomb model described here).

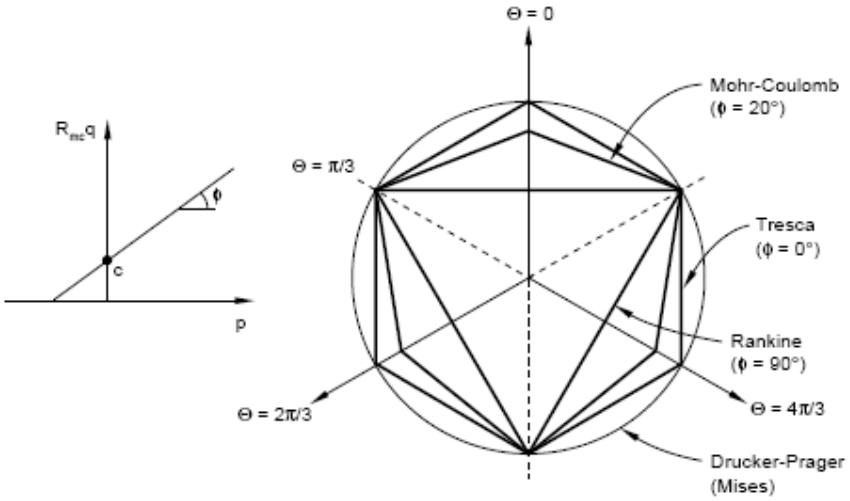

Fig 2.16. *Mohr Coulomb yield surface in meridional and deviatoric planes*

In summary, equations in this section will help to set up the pore pressure (2.32) and temperature profiles (2.33) around the wellbore which are also known as hydraulic diffusivity and thermal diffusivity equations. Then the changes of pore pressure and temperature will be coupled into the stress distribution Eq (2.7) to complete the general Eq (2.47) of state of stresses around the wellbore in the thermo-poro-elastic formation and the initial anisotropic stress field. As a result, this general Eq (2.47) and compressive failure criteria will be used to model the wellbore stability in UBD. The WELLST program which will be presented in chapter 5 is developed from these equations.

CHAPTER 3 - MODELLING MULTIPHASE FLOW IN UBD

3.1. Introduction

One of the important tasks in UBD design is to model multiphase flow in the well under given drilling conditions. Due to the complex nature of multiphase flow including water, oil, gas, and solids in the UBD systems, numerous runs of sophisticated computer programs are required to calculate the distribution of drilling fluid properties along the wellbore and in the drillpipe. According to engineers who are in charge of UBD designs and operations, it is highly desirable to have a program that can accurately perform such predictions.

This chapter will present analytical algorithms, new methods of solution, and the way to model multiphase flow in UBD. These calculations will cover multiphase flow of commonly used drilling fluids in two categories: 1) gasified liquid; 2) stable foam. The results from this research are the distribution of pressure, temperature, drilling fluid properties in the annulus and the drillpipe of the directional well and these will be used to solve some applications presented in subsequent sections. The results are shown not only in graphs but also as exported Excel data to be able to use them in other applications.

3.2. Modelling Gasified Liquid Flow in UBD

3.2.1. Literature Reviews

Gasified drilling fluids have been used to drill boreholes since the 1930's [41]. Gasified liquid drilling is also referred to as gasified mud. The density of a gasified liquid is between 4 ppg and 7 ppg under in-situ borehole conditions.

As drilling technologies advanced in recent years, UBD has been applied to horizontal wells, shallow wells, and offshore development. This technology is also expanding to other technologies such as multilateral drilling, and extended reach drilling.

Selection of a UBD technique requires considering a number of technical and economic factors including the main objectives, geological conditions, equipment availability, safety issues, and cost. The primary concern is the contrast between formation pressure and bottomhole pressure (BHP) during drilling [42, 43].

The section in which the finite differential equations are developed to model wellbore multiphase flow in UBD will be presented and after that the application of these to model will be considered.

Guo and Ghalambor [44] set up the multiphase flow equations in UBD with the major assumption in the derivation of the analytical solution is that the effect of cutting volume (not weight) on the annulus pressure is negligible. This is usually valid because

the volumetric flow rate of solid is normally less than 5% of the total volumetric flow rate in gasified liquid. However, this assumption will be checked again in the chapter 6.

The following equation can be used for solving the hydraulic (frictionless) pressure at upstream. The way to set up this equation can be referred from "Gas Volume Requirements for Underbalanced Drilling" of Guo and Ghalambor [44]:

$$b''(P_{Hup} - P_{Hdn}) + \ln\left(\frac{P_{Hup}}{P_{Hdn}}\right) = a'' L\cos(\phi) \text{ ---------- (3.1)}$$

where

P_{Hup}: upstream hydraulic pressure, lb/ft^2

P_{Hdn}: downstream hydraulic pressure, lb/ft^2

L: measured depth, ft

ϕ: inclination angle, degree

The constant a'', b'' are given by

$$a'' = \frac{9.45\times10^{-5} d_b^2 S_s R_p + 1.667\times10^{-2} W_x Q_x + 9.7327\times10^{-2} S_f Q_f + 1.275\times10^{-3} S_g Q_{gs}}{6.7846\times10^{-2} T_{av} Q_{gs}}$$

$$b'' = \frac{2.2283\times10^{-3} Q_x + 1.5597\times10^{-3} Q_f}{6.7846\times10^{-2} T_{av} Q_{gs}}$$

where

T_{av}: the average temperature, ^oR

W_x: mud weight, ppg

Q_x: mud flow rate, gal/min

S_g: specific gravity of gas related to air

S_s: specific gravity of solid (cutting)

S_f: specific gravity of formation fluid related to fresh water

Q_{gs}: volumetric of injected gas flow rate under standard conditions, SCF/min

Q_f: formation fluid influx flow rate, bbl/hr

R_p: rate of penetration, ft/hr

d_b: bit diameter, in

The following equations can be used for solving the frictional pressure at upstream in a section: [45]

$$P_{frup} = P_{fr1up} + P_{fr2up} + P_{fr3up} \text{ ---------- (3.2)}$$

where

$$b''(P_{fr1up} - P_{fr1dn}) + \ln\left(\frac{P_{fr1up}}{P_{fr1dn}}\right) = a''d''^2\, e''L$$

$$\frac{b''}{2}(P_{fr2up}^2 - P_{fr2dn}^2) + (P_{fr2up} - P_{fr2dn}) = 2a''c''d''e''L$$

$$\frac{b''}{3}(P_{fr3up}^2 - P_{fr3dn}^2) + \frac{1}{2}(P_{fr3up}^3 - P_{fr3dn}^3) = a''c''^2\, e''L$$

where the constants are defined by:

$$c'' = \frac{9.77TQ_g}{A}$$

$$d'' = \frac{0.33Q_x + 0.22Q_f}{A}$$

and

$$e'' = \frac{f_m}{2gD_H}$$

A: cross sectional of flow path area, in^2

L: calculated based on the trajectory shape.

g: acceleration of gravity, 32.2 ft/s^2

The friction factor can be calculated using the following equation:

$$f_m = \left[\frac{1}{1.74 - 2\log\left(\frac{2\varepsilon}{d_H}\right)}\right]^2 \quad \text{----------} \quad (3.3)$$

where

d_H : hydraulic diameter of flow path, in

Applying equations of Guo and Ghalambor can help to formulate the pressure drop in each section along the wellbore. This is only valid in the case that the drilling fluid properties are assumed to be constant in the section of interest. So the Eqs (3.1) and (3.2) are only applied when the section length is small enough to satisfy the fact that the drilling fluid properties are constant. Besides, the temperature and pressure change correspondingly at each small section in the wellbore, and the fluid properties depend on pressure and temperature so they will change respectively. For example, f, Q_f, and Q_x in above equations are considered as constant. However, in reality, three values are decided by formation volume factor and velocity so they will change according to pressure and temperature. Moreover, the pressure in this case is the unknown parameter so the best way to solve this problem is using the combination of the iterative method and the finite differential method called IFDM which will be developed in this research.

The development and modification of Guo and Ghalambor method will be carried step by step in next sections.

3.2.2. Modifications and the innovative method

The author suggests the following modification to solve the problem by modifying the influence of pressure and temperature to the change of fluid properties along the wellbore and the influence of the inflow to the bottomhole pressure. The flowing borehole pressure can be formulated on the basis of the first law of thermodynamics. [44]

Modifications and development

- *The pressure gradient equation in the annulus*

$$\frac{dP}{dL} = \rho_m \cos\phi + \frac{6\rho_m f_m v_m^2}{g d_H} \quad \text{----------} \quad (3.4)$$

where

ρ_m : mixture density, lb/ft^3

ϕ: inclination angle, degree

f_m : friction factor

v_m : mixture velocity, ft/s

d_H = d_{out} – d_{in}, hydraulic diameter of flow path, in

dL : length incremental, ft

dP: pressure drop in the section of interest, psi

g: acceleration of gravity, 32.2 ft/s^2

The mixture density is expressed as:

$$\rho_m = \frac{W_s + W_l + W_g}{Q_s + Q_l + Q_g}$$

The volumetric flow rate of a solid is usually negligible (less than 5% of the total volumetric flow rate) in gasified fluid (this concept will be verified in 6.2.8 of chapter 6), so the previous equation can be simplified to be:

$$\rho_m = \frac{W_s + W_l + W_g}{Q_l + Q_g} \quad \text{----------} \quad (3.5)$$

The weight of a solid depends on bit diameter d_b (in), rate of penetration R_p (ft/hr), and specific gravity of solids S_s:

$$W_s = 62.4\frac{\pi}{4}\left(\frac{d_b}{12}\right)^2 S_s\left(\frac{R_p}{3600}\right) = 9.45\times10^{-5} d_b^2 S_s R_p \quad \text{----------} \quad (3.6)$$

The weight rate of gas depends on volumetric gas flow rate Q_{gs} and the specific gravity of gas S_g:

$$W_g = 0.0765 S_g Q_{gs} \quad \text{----------} (3.7)$$

where

Q_{gs}: volumetric of injected gas flow rate under standard conditions, SCF/s

S_g: gravity of gas

The weight rate of liquid depends on the mud flow rate and formation fluid influx rate:

$$W_l = 8.344 \times 10^{-3} W_{x0} \left(\frac{Q_x}{60} \right) + 62.4 S_f \left(\frac{5.615 Q_f}{3600 \times 24} \right) = 1.391 \times 10^{-4} W_{x0} Q_x + 4.056 \times 10^{-3} S_f Q_f \quad (3.8)$$

where

W_{x0}: mud (or sea water) weight at the surface condition, kg/m^3

Q_x: mud (or sea water) flow rate delivered by pump at the surface condition, gal/min

S_f: specific gravity of formation fluid related to fresh water

Q_f: volumetric flow rate of formation fluid influx at the surface condition, STB/Day

Because sea water was often used as drilling fluid in Vietnam reservoirs, so the Eq (3.8) will be modified with following equations to calculate sea water weight.

The density of sea water (kg/m^3) at standard atmosphere is to be computed from the practical salinity (S) and the temperature (^oF) by the following equations [46]:

$$\begin{aligned} W_{x0} = W_{xmow} + b_0 + b_1 \frac{T-32}{1.8} + b_2 \left(\frac{T-32}{1.8} \right)^2 + b_3 \left(\frac{T-32}{1.8} \right)^3 + \ldots \\ b_4 \left(\frac{T-32}{1.8} \right)^4 + \left[c_0 + c_1 \frac{T-32}{1.8} + c_2 \left(\frac{T-32}{1.8} \right)^2 \right] S\sqrt{S} + d_0 S^2 \end{aligned} \quad \text{----------} (3.9)$$

where

b_0 = 8.24493e-1;

b_1 = -4.0899e-3;

b_2 = 7.6438e-5;

b_3 = -8.2467e-7;

b_4 = 5.3875e-9;

c_0 = -5.72466e-3;

c_1 = +1.0227e-4;

c_2 = -1.6546e-6;

d_0 = 4.8314e-4;

S: water salinity, $^{o}/_{oo}$

The density of the Standard Mean Ocean Water (SMOW) (kg/m^3) taken as pure water reference is given by:

$$W_{xmow} = a_0 + a_1\frac{T-32}{1.8} + a_2\left(\frac{T-32}{1.8}\right)^2 + a_3\left(\frac{T-32}{1.8}\right)^3 + \ldots a_4\left(\frac{T-32}{1.8}\right)^4 + a_5\left(\frac{T-32}{1.8}\right)^5 \quad \text{---------- (3.10)}$$

where

a_0 = 999.842594;

a_1 = 6.793952e-2;

a_2 = -9.095290e-3;

a_3 = 1.001685e-4;

a_4 = -1.120083e-6;

a_5 = 6.536332e-9;

T: temperature, ^{o}F

The density of seawater (kg/m^3) at high pressure is to be computed from the practical salinity (S), the temperature (^{o}F), and the applied pressure (psia) with the following equation: [46]

$$W_x = \frac{W_{xo}}{1-\left(\frac{P}{14.7}\right)\left(\frac{1}{K}\right)}$$

If the unit of density is pound per gallon (ppg)

$$W_x = 8.3444\times10^{-3}\frac{W_{xo}}{1-\left(\frac{P}{14.7}\right)\left(\frac{1}{K}\right)} \quad \text{---------- (3.11)}$$

K is secant bulk modulus given by:

$$K = K_0 + A_s\left(\frac{P}{14.7}\right) + B_s\left(\frac{P}{14.7}\right)^2 \quad \text{---------- (3.12)}$$

$$K_0 = K_{sw} + \left[f_0 + f_1\left(\frac{T-32}{1.8}\right) + f_2\left(\frac{T-32}{1.8}\right)^2 + f_3\left(\frac{T-32}{1.8}\right)^3\right]S + \ldots \left[g_0 + g_1\left(\frac{T-32}{1.8}\right) + g_2\left(\frac{T-32}{1.8}\right)^2\right]S\sqrt{S} \quad \text{------ (3.13)}$$

$$A_s = A_{sw} + \left[i_0 + i_1 \frac{T-32}{1.8} + i_2 \left(\frac{T-32}{1.8} \right)^2 \right] S + j_0 S\sqrt{S} \quad \text{---------- (3.14)}$$

$$B_s = B_{sw} + \left[m_0 + m_1 \frac{T-32}{1.8} + m_2 \left(\frac{T-32}{1.8} \right)^2 \right] S \quad \text{---------- (3.15)}$$

where

f_3 = -6.1670E-5;

f_2 = 1.09987E-2;

f_1 = -0.603459;

f_0 = 54.6746;

g_2 = -5.3009E-4;

g_1 = 1.6483E-2;

g_0 = 7.944E-2;

j_0 = 1.91075E-4;

i_2 = -1.6078E-6;

i_1 = -1.0981E-5;

i_0 = 2.2838E-3;

m_2 = 9.1697E-10;

m_1 = 2.0816E-8;

m_0 = -9.9348E-7;

The pure water terms K_{sw}, A_{sw}, and B_{sw} of the secant bulk modulus are given by:

$$K_{sw} = e_0 + e_1 \frac{T-32}{1.8} + e_2 \left(\frac{T-32}{1.8} \right)^2 + e_3 \left(\frac{T-32}{1.8} \right)^3 + e_4 \left(\frac{T-32}{1.8} \right)^4 \quad \text{------ (3.16)}$$

$$A_{sw} = h_0 + h_1 \frac{T-32}{1.8} + h_2 \left(\frac{T-32}{1.8} \right)^2 + h_3 \left(\frac{T-32}{1.8} \right)^3 \quad \text{---------- (3.17)}$$

$$B_{sw} = k_0 + k_1 \frac{T-32}{1.8} + k_2 \left(\frac{T-32}{1.8} \right)^2 \quad \text{---------- (3.18)}$$

where

e_4 = -5.155288E-5;

e_3 = 1.360477E-2;

e_2 = -2.327105;

e_1 = 148.4206;

e_0 = 19652.21;

h_3 = -5.77905E-7;

h_2 = +1.16092E-4;

h_1 = +1.43713E-3;

h_0 = +3.239908;

k_2 = 5.2787E-8;

k_1 = -6.12293E-6;

k_0 = 8.50935E-5;

The volumetric flow rate of gas Q_g (ft^3/s) can be expressed in terms of gas flow rate at in-situ conditions through the real gas law: [47]

$$Q_g = B_g Q_{gs} = \frac{0.0283Z(T+460)}{P} Q_{gs} \quad \text{---------- (3.19)}$$

where

B_g: gas formation volume factor, SCF/ft^3

T: temperature, ^oF

P: pressure, psia

Z: compressibility factor

The gas compressibility factor or Z-factor is a function of the pseudo-reduced pressure and temperature of the gas. The correlation shown in Fig 3.1, from Standing and Katz [48] gives good values for hydrocarbon gases. The pseudo-reduced values are defined as:

$$P_{pr} = \frac{P}{P_{pc}}$$
$$T_{pr} = \frac{(T+460)}{T_{pc}} \quad \text{---------- (3.20)}$$

where

P: pressure of interest, psia

T: temperature of interest, ^oF

P_{pc}: pseudo-critical pressure, psia

T_{pc}: pseudo-critical temperature, ^oR

If the gas composition is unknown, the pseudo-criticals may be estimated from

$$T_{pc} = 170.5 + 307.3S_g$$
$$P_{pc} = 709.6 - 58.7S_g \quad \text{---------- (3.21)}$$

Several equations or algorithms are available for reproducing Fig 3.1, and the most accurate ones are trial and error or iterative. One of the simplest equations, which

give values sufficiently accurate for two-phase flow calculations, was published by Brill and Beggs [49] and modified by Standing [50]. The equation is:

$$Z = A + (1 - A)Exp(-B) + C(P_{pr})D \text{ ---------- (3.22)}$$

where

$$A = 1.39\sqrt{T_{pr} - 0.92} - 0.36T_{pr} - 0.101$$

$$B = P_{pr}(0.62 - 0.23T_{pr}) + P_{pr}^2\left(\frac{0.066}{T_{pr} - 0.86} - 0.037\right) + \frac{0.32P_{pr}^6}{Exp\left[20.723(T_{pr} - 1)\right]}$$

$$C = 0.132 - 0.32\log_{10}(T_{pr})$$

$$D = Exp(0.715 - 1.128T_{pr} + 0.42T_{pr}^2$$

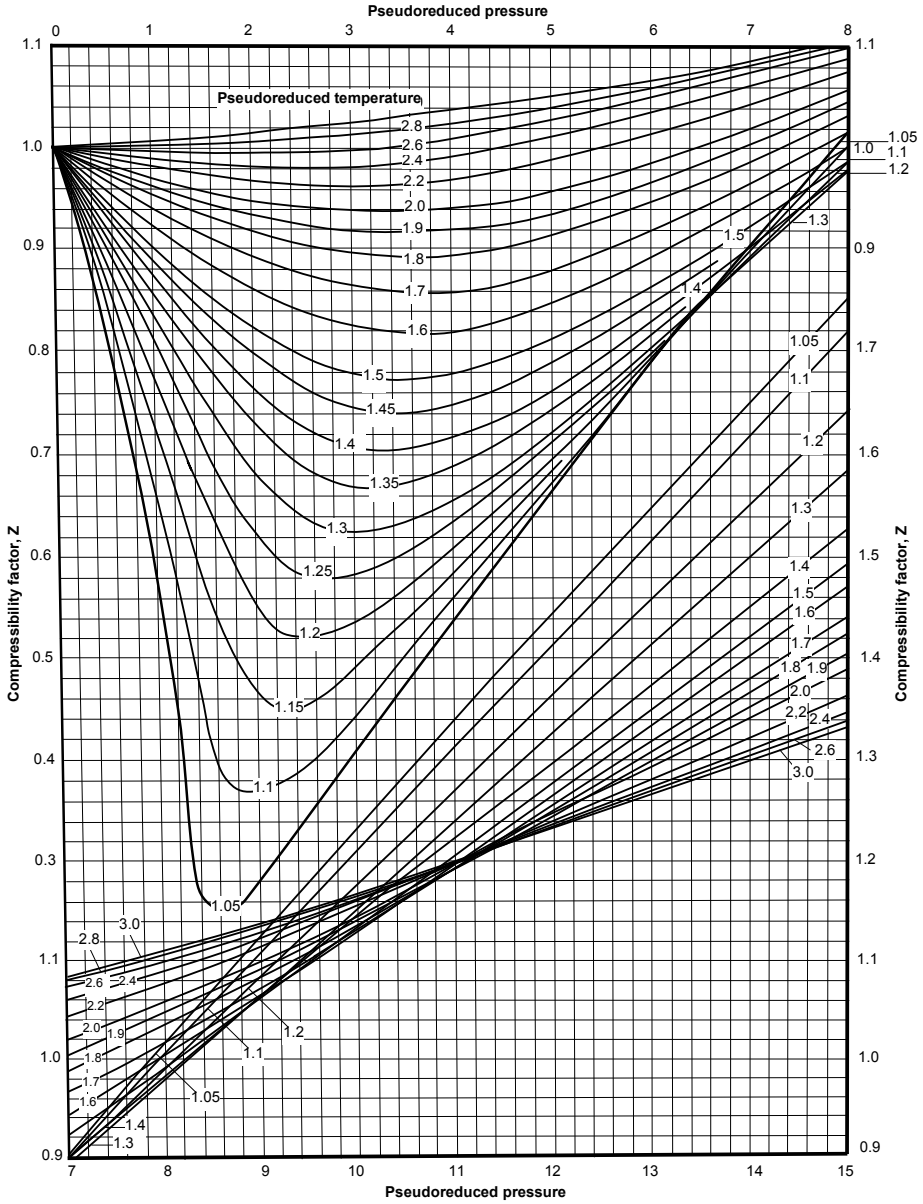

Fig 3.1. *Gas compressibility factor [47]*

The volumetric flow rate Q_s (ft^3/s) at which the particles are generated by the bit is expressed as:

$$Q_s = \frac{\pi}{4}\left(\frac{d_b}{12}\right)^2\left(\frac{R_p}{3600}\right) = 1.515\times10^{-6} d_b^2 R_p \quad \text{---------- (3.23)}$$

The volumetric flow rate of liquid Q_l (ft^3/s) can be expressed as:

$$Q_l = 2.2283\times10^{-3} Q_x B_x + 6.499\times10^{-5} Q_f B_f \quad \text{---------- (3.24)}$$

Seawater formation volume factor B_x can be given by:

$$B_x = \frac{W_{x0}}{W_x} = 1 - \left(\frac{P}{14.7}\right)\left(\frac{1}{K}\right) \quad \text{---------- (3.25)}$$

If drilling liquid is mud, the alteration of mud volume can be neglected so B_x = 1.

Fluid formation volume factor B_f (bbl/STB) [47, 51] can be defined in this research as follows.

If formation fluid is water: $B_f = B_w$, else if formation fluid is oil $B_f = B_o$ (3.26)

B_w is formation volume factor for water, bbl/STB:

$$B_w = c_1 + c_2 P + c_3 P^2$$

where

$$c_1 = 0.9911 + 6.35\times10^{-5} T + 8.5\times10^{-5} T^2$$

$$c_2 = 1.093\times10^{-6} - 3.497\times10^{-9} T + 4.57\times10^{-12} T^2$$

$$c_3 = -5\times10^{-11} + 6.429\times10^{-13} T - 1.43\times10^{-15} T^2$$

T: temperature, ^oF

P: pressure, psia

Standing [52] expressed his proposed graphical correlation in the following more convenient mathematical form to estimate B_o (bbl/STB) as a function of specific gravity of gas S_g, API, gas solution ratio R_s and T. The equation is:

If $P \le P_b$

$$B_o = 0.972 + 0.000147\left(1.15T + R_S\sqrt{\frac{S_g}{S_o}}\right)^{1.175} \quad \text{---------- (3.27)}$$

$$R_S = S_g\left(\frac{P}{18\times10^{0.00091T - 0.0125\,API}}\right)^{1.204}$$

If $P > P_b$

$$B_o = B_{ob}\exp\left(C_o\left(P_b - P\right)\right) \quad \text{---------- (3.28)}$$

$$B_{ob} = 0.972 + 0.000147\left(1.15T + R_{Sb}\sqrt{\frac{S_g}{S_o}}\right)^{1.175}$$

$$R_{Sb} = S_g\left(\frac{P_b}{18\times 10^{0.00091T-0.0125API}}\right)^{1.204}$$

$$C_o = \left(\frac{5R_{sb} + 17.2T - 1180S_g + 12.61API - 1433}{10^5 P}\right)$$

where:

P_b: bubble point pressure, psia

R_s: gas solution ratio, SCF/STB

R_{sb}: gas solution ratio at bubble point pressure, SCF/STB

B_{ob}: oil formation volume factor at bubble point pressure, bbl/STB

API: oil API gravity

C_o: oil compressibility, psi^{-1}

The results of mixture density (lbm/ft^3) can be shown:

$$\rho_m = \frac{9.45\times 10^{-5} d_b^2 S_s R_p + 1.391\times 10^{-4} W_{x0} Q_x + 4.056\times 10^{-3} S_f Q_f + 0.0765 S_g Q_{gs}}{2.2283\times 10^{-3} Q_x B_x + 6.499\times 10^{-5} Q_f B_f + Q_{gs} B_g}$$

---------- (3.29)

Mixture velocity (ft/s)

$$v_m = \frac{Q_l + Q_g}{A} = \frac{2.2283\times 10^{-3} Q_x B_x + 6.499\times 10^{-3} Q_f B_f + Q_{gs} B_g}{A}$$ ---------- (3.30)

$A = \frac{1}{144}\frac{\pi}{4}(d_{out}^2 - d_{in}^2)$: cross sectional area of the flow path, ft^2

d_{out}: outside diameter, in

d_{in}: inside diameter, in

The friction factor may be calculated explicitly from the Eq (3.3) of Nikuradse [53] or from the equation of Colebrook and White [54]:

$$f_m = \left[\frac{1}{1.74 - 2\log\left(\frac{2\varepsilon}{d_H} + \frac{18.7}{N_{\mathrm{Re}}\sqrt{f_m}}\right)}\right]^2$$ ---------- (3.31)

The estimated value of f_m can be calculated from the equation:

$$f_m = 0.0056 + 0.5 N_{\mathrm{Re}}^{-0.32}$$ ---------- (3.32)

In the annulus, the outside roughness can be the borehole roughness if the well is open hole completed or casing roughness if completed with casing. In that case, the borehole roughness often falls into the range from 0.06-0.12 in, and the roughness of commercial steel casing is 0.0018 in. The inside roughness is the roughness of the outside drillpipe which approximates 0.0018 in.

$$\varepsilon = \left(\frac{\varepsilon_{out} d_{out} + \varepsilon_{in} d_{in}}{d_{out} + d_{in}} \right) \quad \text{---------- (3.33)}$$

The Reynolds number [47] can be estimated by the following equation:

$$N_{RE} = \frac{124.0136 \rho_m v_m dH}{\mu_m} \quad \text{---------- (3.34)}$$

where

ρ_m : mixture density, lbm/ft^3

v_m : mixture velocity, ft/s

μ_m : mixture viscosity, cp

$d_H = d_{out} - d_{in}$, in

124.0136: change from SI unit to Field unit

Mixture viscosity in gasified liquid can be calculated from the equation:

$$\mu_m = \mu_L f_L + \mu_g f_g \quad \text{---------- (3.35)}$$

$$\mu_g = 10^{-4} A \exp(B \times \rho_g^C) \quad \text{---------- (3.36)}$$

$$\mu_L = \mu_x f_x + \mu_f f_f \quad \text{---------- (3.37)}$$

where

$$A = \frac{9.4 + 0.02 \times 29 S_g (T + 460)^{1.5}}{209 + 19 \times 29 S_g + (T + 460)}$$

$$B = \frac{3.5 + 0.01 \times 29 S_g + 986}{T + 460}$$

$$C = 2.4 - 0.2B$$

$$\rho_g = \frac{0.0433 S_g P}{Z(T + 460)}$$

T: temperature, ^{o}F

P: pressure, psia

Oil viscosity can be estimated from the equation:

If $P \leq P_b$

$$\mu_o = A\mu_{od}^{\ B} \quad \text{---------- (3.38)}$$

where

$$A = 10.715(R_s + 150)^{-0.515}$$

$$B = 5.44(R_s + 150)^{-0.338}$$

$$z = 3.0324 - 0.0203API$$

$$y = 10^z$$

$$x = yT^{-1.163}$$

$$\mu_{od} = 10^x - 1$$

If $P > P_b$

$$\mu_o = \mu_{ob}\left(\frac{P}{P_b}\right)^m \quad \text{---------- (3.39)}$$

where

$$C_1 = 2.6$$

$$C_2 = 1.187$$

$$C_3 = -11.513$$

$$C_4 = -8.98 \times 10^{-5}$$

$$m = C_1 P^{C_2} \exp(C_3 + C_4 P)$$

$$A = 10.715(R_{sb} + 150)^{-0.515}$$

$$B = 5.44(R_{sb} + 150)^{-0.338}$$

$$z = 3.0324 - 0.0203API$$

$$y = 10^z$$

$$x = yT^{-1.163}$$

$$\mu_{od} = 10^x - 1$$

$$\mu_{ob} = A\mu_{od}^{\ B}$$

Water viscosity

$$\mu_w = \exp(1.003 - 1.479 \times 10^{-2} T + 1.982 \times 10^{-5} T^2) \quad \text{---------- (3.40)}$$

If influx fluid from formation is oil, $\mu_f = \mu_o$, else if influx fluid from formation is water, $\mu_f = \mu_w$ ---------- (3.41)

Formation fluid influx velocity in the annulus:

$$v_f = \frac{6.499 \times 10^{-5} Q_f B_f}{A} \quad \text{---------- (3.42)}$$

Injection fluid velocity in the annulus:

$$v_j = \frac{2.2283 \times 10^{-3} Q_x B_x}{A} \quad \text{---------- (3.43)}$$

A: cross sectional area of the flow path, ft^2

$$f_x = \frac{v_j}{v_j + v_f} \quad \text{---------- (3.44)}$$

$$f_f = \frac{v_f}{v_j + v_f} \quad \text{---------- (3.45)}$$

$$f_L = \frac{v_j + v_f}{v_j + v_f + B_g Q_{gs}} \quad \text{---------- (3.46)}$$

$$f_g = 1 - f_L \quad \text{---------- (3.47)}$$

If drilling liquid is mud, $\mu_x = \mu_{mud}$, else if drilling liquid is sea water, sea water viscosity can be calculated by Hardy formula: [55]

$$\mu_x = \frac{1.052 \times 1.787}{1 + 0.03338\left(\frac{T-32}{1.8}\right) + 1.8325 \times 10^{-4}\left(\frac{T-32}{1.8}\right)^2} \quad \text{---------- (3.48)}$$

As a results, the pressure gradient equation in the annulus can be withdrawn by substituting Eqs (3.29), (3.30), and (3.31) into Eq (3.4). The method applied to solve this equation will be shown in the next section, IFDM.

- *The pressure gradient equation in the drillpipe*

$$\frac{dP}{dL} = -\rho_m \cos(\phi) + \frac{6\rho_m f_m v_m^2}{g d_H} \quad \text{---------- (3.49)}$$

where

ρ_m : mixture density, lb/ft^3

ϕ: inclination angle, radian

f_m : friction factor

v_m : mixture velocity, ft/s

d_H = d_{in} inside diameter of drillpipes, in

dL : length incremental, ft

Because the pressure gradient in the drillpipe is calculated from the bottom hole to the surface so the hydrostatic pressure gradient in Eq (3.49) has the negative sign. Moreover, the value of mixture density and mixture velocity in the drillpipe will be different from theirs in annulus so they must be set up again.

Because the flow in drillpipes only includes air flow and misting liquid flow (mud or sea water), so the mixture density can be simplified to be:

$$\rho_m = \frac{W_l + W_g}{Q_g + Q_l} \quad \text{---------- (3.50)}$$

The weight rate of liquid depends on the misting liquid flow rate:

$$W_l = 8.344 \times 10^{-3} W_{x0} \left(\frac{Q_x}{60} \right) = 1.391 \times 10^{-4} W_{x0} Q_x \quad \text{---------- (3.51)}$$

The weight rate of gas (W_g) and the volumetric flow rate of gas (Q_g) can be calculated by Eqs (3.7) and (3.19).

The volumetric flow rate of liquid Q_l can be expressed as:

$$Q_l = 2.2283 \times 10^{-3} Q_x B_x \quad \text{---------- (3.52)}$$

Therefore, the mixture density and mixture velocity are:

$$\rho_m = \frac{1.391 \times 10^{-4} W_{x0} Q_x + 0.0765 S_g Q_{gs}}{2.2283 \times 10^{-3} Q_x B_x + Q_{gs} B_g} \quad \text{---------- (3.53)}$$

$$v_m = \frac{2.2283 \times 10^{-3} Q_x B_x + Q_{gs} B_g}{A} \quad \text{---------- (3.54)}$$

where

$A = \left(\frac{1}{144} \right) \frac{\pi}{4} d_{in}^2$: cross sectional area of the flow path, ft^2

Friction factor in the drillpipe can be calculated the same as Eqs (3.31) and (3.32) in which the roughness in the drillpipe is around 0.0018 in.

The Reynolds number can be estimated by the Eq (3.34) with $d_H = d_{in}$.

Mixture viscosity in the drillpipe can be calculated from this equation:

$$\mu_m = \mu_x f_L + \mu_g f_g \quad \text{---------- (3.55)}$$

$$f_L = \frac{v_j}{v_j + B_g Q_{gs}}$$

$$f_g = 1 - f_L$$

Substituting Eqs (3.31), (3.53), and (3.54) into the Eq (3.49), the pressure gradient equation is solved.

Iterative method and Finite Differential Method (IFDM)

IFDM method is suggested to solve differential Eqs (3.4) and (3.43) by combining the **I**terative method and **F**inite **D**ifferential **M**ethod in which variables of these equations such as mixture flow rate, mixture velocity, friction factor were modified by adding parameters such as formation volume factor to consider the alteration of fluid volume along the wellbore, Z factor to calculate the compressibility of gas, and sea water properties to apply for sea water drilling. The fundamental of IFDM approach and the method of Guo and Ghalambor is the same. However, Guo and Ghalambor solved basic differential equations by integrating them and calculated directly these integral Eqs (3.1) and (3.2). So the calculation of Guo and Ghalambor will give a certain error if the calculated well section is quite long because the drilling fluid properties in this case must be assumed constant in the whole long section and this is unreal because the drilling fluid properties change at each point in the well. However, if the calculated well section is short, and parameters such as fluid formation volume factor, compressibility factor were added, the method of Guo and Ghalambor will be the same as IFDM method. To sum up, IFDM method is the general method and it can be modified with new variables as required.

To solve two differential Eqs (3.4) and (3.49), the IFDM method is suggested as following steps:

1. With the given ΔL, for example 50 ft, it was assumed the respective $\Delta P_s = 100$ psi. So the average pressure in this 50ft section is $P_{av} = P_s+\Delta P_s/2$, and the average temperature is $T_{av} = T_s + G\cos(\phi)\Delta L/2$ with G is geothermal gradient (noticing that the smaller ΔL, the better result, however, the longer run time). The subscript "s" refers to "surface".

2. At this average pressure and temperature, all parameters on the right hand are calculated to give ΔP_c on the left hand.

3. If this value of ΔP_c is equal to ΔP_s assumed at the first step, it means that this value is correct, and the calculation for the pressure drop in the next section (50 ft) continues. When ΔP_c is different to ΔP_s, ΔP_c is taken as the new ΔP_s value and return to the first step. These iterative steps will continue until the correct pressure drop value can be reached.

4. Continue to the next section until the total $\sum\Delta L = L$

All steps above are applied to solve the pressure gradient equation in the annulus. According to the pressure gradient equation in the drillpipe, the calculation will be carried out from the bottom hole to the surface. So, P_{av} and T_{av} in step 1 will be $P_{av} = P_{bot} + \Delta P_s/2$ and $T_{av} = T_{bot} - G\cos(\phi)\Delta L/2$. The details of calculation can be referred fully in the chapter 5 through flow charts of UBD program.

The above algorithms will help to model the pressure, temperature, drilling fluid properties both in the annulus and inside the drillpipe. The calculation is carried out in the direction from the top to the bottom of the annulus, then from the bottom to the top

of the drillpipe. Briefly, modelling the multiphase flow in UBD by the innovative approach (IFDM) as suggested, the better results can be got and this will be verified in the application section (chapter 6) in that the numerical solution of the IFDM method and the analytical solution of Guo and Ghalambor will be compared.

Comparing the modification and development of IFDM with the solution of Guo and Ghalambor

THE PRESSURE GRADIENT

Guo and Ghalambor

Basic equation: $$\frac{dP}{dL} = \rho_m \cos\phi + \frac{\rho_m f_m v_m^2}{2gD_H}$$

Integral Eqs: (3.1) and (3.2)

D_H: diameter, ft

IFDM

Basic equation: $$\frac{dP}{dL} = \rho_m \cos\phi + \frac{6\rho_m f_m v_m^2}{gd_H} \text{ (in the annulus)}$$

$$\frac{dP}{dL} = -\rho_m \cos\phi + \frac{6\rho_m f_m v_m^2}{gd_H} \text{ (in the drillpipe)}$$

Integral equations: not used because can't assume f_m, Q_f, Q_x constant

d_H: diameter, in

The IFDM approach and the method of Guo and Ghalambor are set up from the same equation. However, the wellbore diameter is often expressed by inches, so it leads to a little bit difference between two equations above once the unit is changed from feet to inch.

THE WEIGHT RATE OF A SOLID

The same in two methods and calculated from Eq (3.6)

THE WEIGHT RATE OF LIQUID

Guo and Ghalambor

$$W_l = 1.667\times10^{-2} W_x Q_x + 9.7327\times10^{-2} S_f Q_f$$

W_x: mud weight (constant)

Q_f: bbl/hr (constant)

IFDM

$$W_l = 1.391\times10^{-4} W_{x0} Q_x + 4.056\times10^{-3} S_f Q_f \text{ (in the annulus)}$$

$$W_l = 1.391\times10^{-4} W_{x0} Q_x \text{ (in the drillpipe)}$$

W_{x0}: mud weight or seawater weight (new development) calculated by Eqs (3.9), and (3.10)

Q_f: STB/Day (depending on bottomhole pressure via inflow performance relationship which was calculated by PERFORM 3.0 in chapter 4 when drilling parameters were coupled to productivity in UBD. Bottomhole pressure (P_{wf}) here is the unknown value, so applying the iterative method to solve the differential equation is better than solving directly from the integral equation.

THE WEIGHT RATE OF GAS

Guo and Ghalambor

$$W_g = 1.275 \times 10^{-3} S_g Q_{gs}$$

Q_{gs}: SCF/min

IFDM

$$W_g = 0.0765 S_g Q_{gs}$$

Q_{gs}: SCF/s

THE VOLUMETRIC FLOW RATE OF A SOLID

Negligible in two methods (this will be verified in chapter 6)

THE VOLUMETRIC FLOW RATE OF LIQUID

Guo and Ghalambor

$$Q_l = 2.2283 \times 10^{-3} Q_x + 1.5597 \times 10^{-3} Q_f$$

Q_f: bbl/hr (constant)

IFDM

$$Q_l = 2.2283 \times 10^{-3} Q_x B_x + 6.499 \times 10^{-5} Q_f B_f \text{ (in the annulus)}$$

$$Q_l = 2.2283 \times 10^{-3} Q_x B_x \text{ (in the drillpipe)}$$

Q_f: STB/Day (change with bottom hole pressure)

B_x and B_f are formation volume factors symbolizing for the volume change corresponding with pressure and temperature. These variables can be calculated by Eqs (3.25) and (3.26).

THE VOLUMETRIC FLOW RATE OF GAS

Guo and Ghalambor

$$Q_g = \frac{6.7846 \times 10^{-2} T Q_{gs}}{P}$$

Q_{gs}: SCF/min

T: temperature, ^{o}R

P: pressure, lb/ft^2

The volumetric flow rate of gas is expressed through the ideal gas law.

IFDM

$$Q_g = B_g Q_{gs} = \frac{0.0283Z(T+460)}{P} Q_{gs}$$

Q_{gs}: SCF/s

T: temperature, ^{o}F

P: pressure, psi

The volumetric flow rate of gas is expressed through the real gas law. So the compressibility factor must be added and calculated from the Eq (3.22).

THE MIXTURE DENSITY

Guo and Ghalambor

$$\rho_m = \frac{9.45\times10^{-5} d_b^2 S_s R_p + 1.667\times10^{-2} W_x Q_x + 9.7327\times10^{-3} S_f Q_f + 1.275\times10^{-3} S_g Q_{gs}}{2.2283\times10^{-3} Q_x + 1.5597\times10^{-3} Q_f + \frac{6.7846\times10^{-2} T Q_{gs}}{P}}$$

IFDM

In the annulus:

$$\rho_m = \frac{9.45\times10^{-5} d_b^2 S_s R_p + 1.391\times10^{-4} W_{x0} Q_x + 4.056\times10^{-3} S_f Q_f + 0.0765 S_g Q_{gs}}{2.2283\times10^{-3} Q_x B_x + 6.499\times10^{-5} Q_f B_f + \frac{0.0283Z(T+460)Q_{gs}}{P}}$$

In the drillpipe:

$$\rho_m = \frac{1.391\times10^{-4} W_{x0} Q_x + 0.0765 S_g Q_{gs}}{2.2283\times10^{-3} Q_x B_x + \frac{0.0283Z(T+460)Q_{gs}}{P}}$$

THE MIXTURE VELOCITY

Guo and Ghalambor

$$v_m = \frac{144}{A}\left[2.2283\times10^{-3} Q_x + 1.5597\times10^{-3} Q_f + \frac{6.7846\times10^{-2} T}{P} Q_{gs}\right]$$

A: in^2

IFDM

$$v_m = \frac{2.2283\times10^{-3} Q_x B_x + 6.499\times10^{-3} Q_f B_f + \frac{0.0283Z(T+460)}{P} Q_{gs}}{A} \quad \text{(in the annulus)}$$

$$v_m = \frac{2.2283\times10^{-3} Q_x B_x + \frac{0.0283 Z(T+460)}{P} Q_{gs}}{A}$$ (in the drillpipe)

A: ft^2

FRICTION FACTOR

Guo and Ghalambor

$$f_m = \left[\frac{1}{1.74 - 2\log\left(\frac{2\varepsilon}{d_H}\right)}\right]^2$$

IFDM

$$f_m = \left[\frac{1}{1.74 - 2\log\left(\frac{2\varepsilon}{d_H} + \frac{18.7}{N_{\mathrm{Re}}\sqrt{f_m}}\right)}\right]^2$$

in which N_{Re} and other values are estimated by Eqs (3.32), (3.33), (3.34), and (3.35).

INJECTED LIQUID VISCOSITY

Guo and Ghalambor

Assuming Reynolds number not affected to friction factor so injected liquid viscosity is negligible.

IFDM

Reynolds number is affected by friction factor so injected liquid viscosity can be calculated by the Eq (3.48) (sea water) or input directly from the input data (mud).

3.3. Modelling Foam Flow in UBD

3.3.1. Literature Reviews [44]

Stable foams have been used as circulating fluids in workover and drilling operations since 1960's. Some successful applications have been reported by Hutchison [56, 57], Bleakley [58], Essary et al. [59], Bentsen [60], Lincicome [61], Aderson [62], and Russell [63]. Using stable foams as circulating fluids in drilling has been recognized as having several advantages over gas drilling including (1) no hole washout in unconsolidated formations while drilling because of low velocity of foam in the annulus, (2) excellent carrying capacity for cuttings about 7-8 times that of water [44], and (3) low compression requirements. Therefore, stable foam has become an attractive circulating fluid in many drilling areas in the past 10 years.

Stable foam consists of water, foaming agents (surfactant), and gas or air. Water and surfactants form a continuous cellular structure in foam. The volume fraction of gas phase of foam is termed foam quality. Foam quality is usually expressed as a percentage. With currently used foaming agents, foams are stable when foam quality is between 55% and 97.5%. Density of stable foam varies between 0.3 and 7 ppg depending upon foam quality that is a function of in-situ pressure. When the gas phase fraction is less than 60%, the foam structure tends to break down and gas forms isolated bubbles that are independent of liquid phase to extent that the two phases can move with different velocities.

Stable foam is usually generated when liquids are injected into the gas flow at rates that give foam quality values around 75% at bottomhole pressure and temperature. Under a given combination of gas and liquid injection rates, foam quality varies along a wellbore as a function of pressure. Backpressure is often required to ensure that the foam remains stable when it approaches the surface.

Foams have high viscosities due to the large surface areas. Foam viscosities have a range of values from 35 cp to 115 cp at foam qualities from 75% to 97.5%, respectively. Adding viscosifiers to the injected liquid can increase foam viscosity. These foams are referred as "stiff" foams. [64]

The following equation can be used for solving the hydraulic (frictionless) pressure at upstream:

$$b'(P_{Hup} - P_{Hdn}) + \ln\left(\frac{P_{Hup}}{P_{Hdn}}\right) = a'H \quad \text{---------- (3.56)}$$

where

P_{Hup}: upstream hydraulic pressure, lb/ft^2

P_{Hdn}: down stream hydraulic pressure, lb/ft^2

H: vertical depth, ft

$$a' = \frac{3326b'S_lT_{av} + S_g}{53.3T_{av}} \quad \text{---------- (3.57)}$$

$$b' = \frac{1 - \Gamma_{dn}}{P_1\Gamma_{dn}} \quad \text{---------- (3.58)}$$

where

S_l: specific gravity of liquid

S_g: specific gravity of gas related to air

T_{av}: the average temperature

Γ_{dn}: downstream foam quality

The following equations can be used for solving the frictional pressure. The upstream density of gas can be estimated based on gas law for ideal gas:

$$\rho_{gh} = \frac{S_g P_{Hup}}{53.3 T_{up}} \quad \text{---------- (3.59)}$$

where

T_{up}: temperature, ^{o}R

The upstream volumetric gas flow rate can be estimated accordingly:

$$Q_{gh} = \frac{0.0765}{\rho_{gh}} Q_{gs} \quad \text{---------- (3.60)}$$

where Q_{gs} is gas flow rate under standard conditions. The upstream foam quality can be estimated using:

$$\Gamma_{up} = \frac{Q_{gh}}{Q_l + Q_{gh}} \quad \text{---------- (3.61)}$$

where Q_l is liquid injection rate (ft^3/min).

Foam velocity can be given by the equation:

$$v_m = \frac{144}{60} \frac{Q_{gh} + Q_l}{A} = \frac{144}{60} \frac{\frac{0.0765}{\rho_{gh}} Q_{gs} + Q_l}{A} \quad \text{---------- (3.62)}$$

where

A: in^2

Mass flow rate of foam can be calculated using:

$$\overset{*}{w}_f = 0.0765 S_g Q_{gs} + 8.33 S_l Q_l \quad \text{---------- (3.63)}$$

The average inertial momentum term in the section can be calculated using:

$$D\rho v = 0.02173 \frac{\overset{*}{w}_f}{D_H} \quad \text{---------- (3.64)}$$

The Moody friction factor [65] can be estimated by:

$$f_m = 4 \times 10^{1.444} - 2.5 \log(D\rho v) \quad \text{---------- (3.65)}$$

Upstream frictional pressure can be computed using the following equations:

$$P_{frup} = P_{fr1up} + P_{fr2up} + P_{fr3up} \quad \text{---------- (3.66)}$$

where

$$b'(P_{fr1up} - P_{fr1dn}) + \ln\left(\frac{P_{fr1up}}{P_{fr1dn}}\right) = a' d'^2 e' L$$

$$\frac{b'}{2}(P_{fr2up}^2 - P_{fr2dn}^2) + (P_{fr2up} - P_{fr2dn}) = 2a'c'd'e'L$$

$$\frac{b'}{3}(P_{fr3up}^3 - P_{fr3dn}^3) + \frac{1}{2}(P_{fr3up}^2 - P_{fr3dn}^2) = a'c'^2\, e'L$$

where the constants are defined by:

$$c' = 144\frac{Q_l}{A}\frac{P_{dn}T_{up}}{T_{dn}}\frac{\Gamma_{dn}}{(1-\Gamma_{dn})}$$

$$d' = 144\frac{Q_l}{A}$$

$$e' = \frac{f}{2gD_H}$$

These equations are valid for all types of section trajectory as long as the vertical depth H and section length L are calculated based on the trajectory shape.

3.3.2. Modifications and the innovative method

Modifications and development

- *The pressure gradient equation in the annulus*

$$\frac{dP}{dL} = \rho_m \cos\phi + \frac{6\rho_m f_m v_m^2}{gd_H} \text{ ---------- (3.67)}$$

where

ρ_m : foam density, lb/ft^3

ϕ: inclination angle, radian

f_m : friction factor

v_m : foam velocity, ft/s

d_H = d_{out} – d_{in}, hydraulic diameter of flow path, in

dL : length incremental, ft

This equation is the same as Eq (3.4). However, all parameters such as ρ_m , v_m are calculated by other equations.

The foam density (lb/ft^3) is expressed as:

$$\rho_m = (1-\Gamma)\rho_l + \Gamma\rho_g \text{ ---------- (3.68)}$$

$$\rho_g = \frac{2.7S_gP}{Z(T+460)} \text{ ---------- (3.69)}$$

$$\rho_l = \frac{62.4S_fQ_f + 2139.42S_xQ_x}{Q_fB_f + 34.286B_wQ_x} \text{ ---------- (3.70)}$$

$$\Gamma = \frac{B_g Q_{gs}}{B_g Q_{gs} + 2.2283\times10^{-3} B_w Q_x + 6.499\times10^{-5} B_f Q_f} \text{ ---------- (3.71)}$$

P, T, and Γ are pressure, temperature and foam quality at the centre of computed section.

Mixture velocity (ft/s)

$$v_m = \frac{Q_l + Q_g}{A} = \frac{2.2283\times10^{-3} B_w Q_x + 6.499\times10^{-5} Q_f B_f + B_g Q_{gs}}{A} \text{ ------- (3.72)}$$

where

$A = \frac{1}{144}\frac{\pi}{4}(d_{out}^2 - d_{in}^2)$: cross sectional area of the flow path, ft^2

d_{out}: outside diameter, in

d_{in}: inside diameter, in

Friction factor

$$f_m = \left[\frac{1}{1.74 - 2\log\left(\frac{2\varepsilon}{d_H} + \frac{18.7}{N_{\mathrm{Re}}\sqrt{f_m}}\right)}\right]^2 \text{ ---------- (3.73)}$$

The estimated value of f_m can be calculated from the equation:

$$f_m = 0.0056 + 0.5 N_{\mathrm{Re}}^{-0.32} \text{ ---------- (3.74)}$$

The borehole and drillpipe roughness is calculated as same as the calculation in previous section.

$$\varepsilon = \left(\frac{\varepsilon_{out} d_{out} + \varepsilon_{in} d_{in}}{d_{out} + d_{in}}\right) \text{ ---------- (3.75)}$$

The Reynolds number can be estimated by the following equation:

$$N_{\mathrm{Re}} = \frac{124.0136 \rho_m v_m dH}{\mu_m} \text{ ---------- (3.76)}$$

where

$dH = d_{out} - d_{in}$, in

Mixture viscosity in foam can be calculated from the equation:

$$\mu_m = \mu_L f_L + \mu_g f_g \text{ ---------- (3.77)}$$

$$\mu_L = \mu_x f_x + \mu_f f_f \text{ ---------- (3.78)}$$

in which μ_g, μ_o, and μ_w are calculated the same as previous Eqs (3.36), (3.38), (3.39), and (3.40). μ_x is water viscosity calculated by Eq (3.48).

Formation fluid influx velocity in the annulus:

$$v_f = \frac{6.499\times10^{-5} Q_f B_f}{A} \quad \text{(3.79)}$$

Injection fluid velocity in the annulus:

$$v_j = \frac{2.2283\times10^{-3} Q_x B_w}{A} \quad \text{(3.80)}$$

A: cross sectional area of the flow path, ft^2

$$f_x = \frac{v_j}{v_j + v_f} \quad \text{(3.81)}$$

$$f_f = \frac{v_f}{v_j + v_f} \quad \text{(3.82)}$$

$$f_L = \frac{v_j + v_f}{v_j + v_f + B_g Q_{gs}} \quad \text{(3.83)}$$

$$f_g = 1 - f_L \quad \text{(3.84)}$$

As a result, the pressure gradient equation in the annulus can be withdrawn by substituting Eqs (3.68), (3.72), and (3.73) into Eq (3.67) and using IFDM as the previous section to solve this equation.

- *The pressure gradient equation in the drillpipe*

The pressure gradient in the drillpipe is given by:

$$\frac{dP}{dL} = -\rho_m \cos\phi + \frac{6\rho_m f_m v_m^2}{g d_H} \quad \text{(3.85)}$$

The foam density (lb/ft^3) is expressed as:

$$\rho_m = (1-\Gamma)\rho_l + \Gamma\rho_g \quad \text{(3.86)}$$

$$\rho_g = \frac{2.7 S_g P}{Z(T+460)} \quad \text{(3.87)}$$

$$\rho_l = \frac{62.4 S_x}{B_w} \quad \text{(3.88)}$$

$$\Gamma = \frac{B_g Q_{gs}}{B_g Q_{gs} + 2.2283\times10^{-3} B_w Q_x} \quad \text{(3.89)}$$

P, T, and Γ are pressure, temperature and foam quality at the center of computed section.

Mixture velocity (ft/s)

$$v_m = \frac{Q_l + Q_g}{A} = \frac{2.2283 \times 10^{-3} B_w Q_x + B_g Q_{gs}}{A} \quad \text{---------- (3.90)}$$

where

$A = \frac{1}{144}\frac{\pi}{4} d_{in}^2$: cross sectional area of the flow path, ft^2

d_{in}: inside drillpipe diameter, in

Friction factor f_m, Reynolds number N_{Re} can be given by Eqs (3.31) and (3.34).

Foam viscosity in the drillpipe is different to the foam viscosity in the annulus because there is no the appearance of formation influx fluid in the drillpipe:

$$\mu_m = \mu_x f_L + \mu_g f_g \quad \text{---------- (3.91)}$$

in which μ_g, and μ_x are calculated by Eqs (3.36) and (3.40).

Injection fluid velocity in the annulus:

$$v_j = \frac{2.2283 \times 10^{-3} Q_x B_w}{A} \quad \text{---------- (3.92)}$$

A: cross sectional area of the flow path, ft^2

$$f_L = \frac{v_j}{v_j + B_g Q_{gs}} \quad \text{---------- (3.93)}$$

$$f_g = 1 - f_L \quad \text{---------- (3.94)}$$

As a result, the gradient pressure equation in the drillpipe can be withdrawn by substituting Eqs (3.86), (3.90), and (3.31) into Eq (3.85) and applying IFDM as the previous section to solve this equation.

Comparing the modification and development of IFDM with the solution of Guo and Ghalambor

THE PRESSURE GRADIENT
Guo and Ghalambor Basic equation: $\frac{dP}{dL} = \rho_m \cos(I_S) + \frac{\rho_m f_m v_m^2}{2 g D_H}$ Integral equations: (3.56) and (3.66) D_H: diameter, ft **IFDM**

Basic equation:

$$\frac{dP}{dL} = \rho_m \cos(I_S) + \frac{6\rho_m f_m v_m^2}{g d_H} \quad \text{(in the annulus)}$$

$$\frac{dP}{dL} = -\rho_m \cos(I_S) + \frac{6\rho_m f_m v_m^2}{g d_H} \quad \text{(in the drillpipe)}$$

Integral equations: not used because can't assume f_m, Q_f, Q_x constant

d_H: diameter, in

GAS DENSITY

Guo and Ghalambor

$$\rho_{gh} = \frac{S_g P}{53.3T}$$

P: pressure, lb/ft^2

T: temperature, ^{o}R

IFDM

$$\rho_g = \frac{2.7 S_g P}{Z(T + 460)}$$

P: pressure, psi

T: temperature, ^{o}F

Z: compressibility factor

Modifying compressibility factor to calculate gas density in IFDM method.

FOAM QUALITY

Guo and Ghalambor

$$\Gamma = \frac{Q_{gh}}{Q_l + Q_{gh}} = \frac{\frac{0.0765}{\rho_{gh}} Q_{gs}}{Q_l + \frac{0.0765}{\rho_{gh}} Q_{gs}}$$

Q_{gs}: SCF/min

Q_l: ft^3/min

In this equation Q_l is an in-situ value. However, the in-situ value can't be estimated directly, it must be calculated through the value at surface condition. So, this equation should be changed to an easier form to apply.

IFDM

$$\Gamma = \frac{B_g Q_{gs}}{B_g Q_{gs} + 2.2283\times10^{-3} B_w Q_x + 6.499\times10^{-5} B_f Q_f} \text{ (in the annulus)}$$

$$\Gamma = \frac{B_g Q_{gs}}{B_g Q_{gs} + 2.2283\times10^{-3} B_w Q_x} \text{ (in the drillpipe)}$$

Q_{gs}: SCF/s

Q_x, Q_f in these equations are defined at the surface condition so they can be obtained directly. This makes them easier to apply than previous equations. Moreover, while formation influx flow rate has not considered in the solution of Guo and Ghalambor, this value was modified in IFDM.

FOAM VELOCITY

Guo and Ghalambor

$$v_m = \frac{144}{60}\frac{Q_{gh} + Q_l}{A} = \frac{144}{60}\frac{\frac{0.0765}{\rho_{gh}}Q_{gs} + Q_l}{A}$$

A: in^2

IFDM

$$v_m = \frac{2.2283\times10^{-3} B_w Q_x + 6.499\times10^{-5} Q_f B_f + B_g Q_{gs}}{A} \text{ (in the annulus)}$$

$$v_m = \frac{Q_l + Q_g}{A} = \frac{2.2283\times10^{-3} B_w Q_x + B_g Q_{gs}}{A} \text{ (in the drillpipe)}$$

A: ft^2

FRICTION FACTOR

Guo and Ghalambor

$$f_m = 4\times10^{1.444} - 2.5\log(D\rho v)$$

IFDM

Eq (3.31)

3.4. Cuttings Carrying Capacity

Several criteria and methods for determining the cuttings carrying capacity have been used in the petroleum drilling industry. They fall into two categories: (1) minimum kinetic energy and (2) minimum velocity.

3.4.1. Minimum kinetic energy [44]

The mixture of gas and solid is treated as one homogeneous phase with mixture density and velocity. The interactions between particles and fluids are not considered.

The minimum velocity criterion [44] is based on the experience gained from quarry drilling with air. The minimum annular velocity to effectively remove solid particles from the borehole is usually assumed to be 3000 ft/min, or 50 ft/s, under atmospheric conditions (close to standard condition of 14.7 psia at 60 ^{o}F). This velocity is believed to be high enough to remove dustlike particles in the air drilling. Although big cuttings not removed from the vicinity of the bit by the circulating air are reground by the bit teeth, it would be uneconomical to lift large cuttings without first trying to control their initial size at the bit.

The carrying power of air with velocity of 50 ft/s can be evaluated based on its kinetic energy per unit volume of air:

$$E_{go} = \frac{1}{2}\frac{\rho_{go}}{g}v_{go}^2 \text{ ---------- (3.95)}$$

where

ρ_{go}: 0.0765 pound per cubit foot (lb/ft^3), density of standard air

g: 32.2 ft/s^2

v_{go}: 50 ft/s, minimum required velocity of air under standard conditions

The kinetic energy of 1 ft^3 of standard air moving at a velocity of 50 ft/s is:

$$E_{go} = \frac{1}{2}\left(\frac{0.0765}{32.2}\right)(50)^2 \approx 3\,ft - lb/ft^3 \text{ ---------- (3.96)}$$

which is the minimum kinetic energy of fluid required to effectively lift solid particles. If the carrying capacity of the fluid phase at the point of interest in the hole is equivalent to the carrying power of the velocity of standard air, the following relationship must hold:

$$\frac{1}{2}\frac{\rho_m}{g}v_m^2 = \frac{1}{2}\frac{\rho_{go}}{g}v_{go}^2 \text{ ---------- (3.97)}$$

where

ρ_m: mixture density of drilling fluid at the point interest in the hole, lb/ft^3

v_m: mixture velocity of drilling fluid at the point of interest in the hole, ft/s

So to maintain the cuttings carrying capacity, the minimum energy of drilling fluid must be higher than 3 ft-lb/ft^3.

3.4.2. Minimum velocity criterion [44]

Interactions between particles and fluids are considered in this case. When a solid particle is released in a lower density fluid, it first accelerates under the action of gravity and then decelerates due to the increasing drag force on the particle from the fluid. It is possible to prove mathematically that it will take infinite time for the particle

to reach a constant velocity. However, in reality, after a certain time the variation in particle velocity is not practically detectable and the velocity of the particle reaches a constant velocity, also known as terminal velocity, free-settling velocity, and slip velocity.

Terminal velocity of a particle is influenced by many factors, including size, shape, and density of the particle; density and viscosity of the fluid; flow regime; particle – particle interaction; and particle – wall interaction.

Many mathematical models have been proposed to account for the effects of those factors. Assuming spherical particles, Gray [66] presents the following equation to determine terminal setting velocity:

$$v_{sl} = \frac{\psi}{1 + D_S / D_H} \sqrt{\frac{4 g D_S (\rho_S - \rho_g)}{3 \rho_g C_D}} \quad \text{---------- (3.98)}$$

where

v_{sl}: terminal setting velocity, ft/s

D_S: equivalent solid diameter, ft

ρ_s: density of solid particle, lb/ft^3

C_D: drag coefficient accounting for the effect of particle shape; 1.4 for flat particles (shale and limestone) and 0.85 for angular to sub-rounded particles (sandstone).

ψ: sphericity factor, dimensionless

D_H: hydraulic diameter of flow path, ft

The mixture velocity required to transport the solid particles can be formulated as follows:

$$v_m = v_{sl} + v_{tr} \quad \text{---------- (3.99)}$$

where

v_m: mixture velocity of drilling fluid, ft/s

v_{tr}: required particle transport velocity, ft/s

The required particle transport velocity depends on how fast the particles are generated by the drill bit and the number of moving particles allowed in the borehole during drilling. The volumetric flow rate at which the particles are generated by the bit is expressed as:

$$Q_p = \frac{\pi}{4}\left(\frac{d_b}{12}\right)^2 \left(\frac{R_p}{3600}\right) \quad \text{----------(3.100)}$$

where

Q_p: volumetric flow rate of particles generated by the drill bit, ft^3/s

d_b: bit diameter, in

R_p: rate of penetration, ft/hr

The volumetric flow rate at which the particles are transported in the flow path is expressed as:

$$Q_{tr} = v_{tr} C_p \left(\frac{A}{144} \right) \text{ ---------- (3.101)}$$

where

Q_{tr}: volumetric flow rate of transported particles in the flow path, ft^3/s

C_p: particle concentration in the flow path, 0.04, volume fraction

Based on the material balance for solid particles, the volumetric flow rate of particle transport must equal the volumetric flow rate of particles generated by drill bit, $Q_{tr} = Q_p$

As a result,

$$v_{tr} = \frac{\pi d_b^2}{4 C_p A} \left(\frac{R_p}{3600} \right) \text{ ---------- (3.102)}$$

To sum up, the velocity of drilling fluid at each position in the wellbore must be larger than v_m in Eq (3.99) to be able to carry most cuttings from the bottom hole to the surface.

CHAPTER 4 - COUPLING PRODUCTIVITY IN UBD

4.1. Introduction

When a well is drilled underbalanced, hydrocarbon production can begin as soon as a productive zone is penetrated. With suitable surface equipment, it is possible to collect oil while drilling. However, evaluating how much formation fluid can be produced is not straight forward due to the fact that the relationship between drilling and production parameters is quite complex. In the literature, there are just a few papers dealing with coupling the productivity and drilling parameters in UBD. In this work, the method to evaluate the relationship of production capacity and multiphase flow characteristics is presented. And these constraint equations was used to codify a program named UBDRILL.

4.2. Inflow Performance Relationship [47]

The flow from the reservoir into the well has been called "Inflow Performance" by Gilbert [67] and a plot of producing rate versus bottom hole flowing pressure is called an "Inflow Performance Relationship" or IPR. The establishment of IPR will help to couple the productivity in UBD and this is the main purpose of this chapter.

Although the form of the IPR equation can be quite different for various types of fluids, the basic equation on which all of the various forms are based is Darcy's Law. [68]

4.2.1. Darcy's Law

In 1856, while performing experiments for the design of sand filter beds for water purification, Henry Darcy proposed an equation relating apparent fluid velocity to pressure drop across the filter bed. Although the experiments were performed with flow only in the downward vertical direction, the expression is also valid for horizontal flow, which is of most interest in the petroleum industry.

It should also be noted that Darcy's experiments involved only one fluid, water, and that the sand filter was completely saturated with the water. Therefore, no effects of fluid properties or saturation were involved.

Darcy's sand filters were of constant cross sectional area, so the equation did not account for changes in velocity with location. Written in differential form, Darcy's law is:

$$v = -\frac{k.dP}{\mu.dx} \quad \text{----------} \quad (4.1)$$

or in terms of volumetric flow rate

$$Q_f = vA = -\frac{k.A.dP}{\mu.dx} \quad \text{----------} \quad (4.2)$$

where

k: permeability of the porous medium

v: apparent fluid velocity

Q_f: volumetric flow rate

A: area open to flow

μ: fluid viscosity, and

dP/dx: pressure gradient in the direction of flow (negative).

Linear Flow

For linear flow, which is for constant area flow, the equation may be integrated to give the pressure drop occurring over some length L

$$\int_{p_2}^{p_1} \frac{k.dP}{\mu} = -\frac{Q_f}{A}\int_0^L dx$$

If it is assumed that k, μ, and Q_f are independent of pressure, or that they can be evaluated at the average pressure in the system, the equation becomes:

$$\int_{p_2}^{p_1} dP = -\frac{Q_f.\mu}{k.A}\int_0^L dx$$

Integration gives:

$$P_2 - P_1 = -\frac{Q_f \mu}{kA} L \quad \text{----------} \quad (4.3)$$

$$Q_f = \frac{CkA(P_1 - P_2)}{\mu L} \quad \text{----------} \quad (4.4)$$

where C is a unit conversion factor. The correct value for C is 1.0 for SI and 1.127×10^{-3} for Field units (See Table 4.1).

Table 4.1. *Unit for Darcy's Law*

Variable	Symbol	Unit	
		SI	**Field**
Flow rate	Q_f	cm^3/s	bbl/day
Permeability	k	Darcys	md
Area	A	cm^2	ft^2
Pressure	P	atm	psi
Viscosity	μ	Pas	cp
Length	L	cm	ft

It can be observed from Eq (4.3) that a plot on Cartesian coordinates of P versus L will produce a straight line of constant slope, $-\mu Q_f/kA$. That is, the variation of pressure with distance is linear.

The geometry of the linear system is illustrated in Fig 4.1.

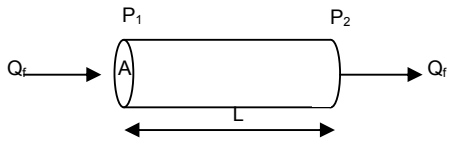

Fig 4.1. *Geometry for linear flow*

Turbulence Flow

For high velocity flow in which turbulence or non-Darcy flow can exist, Darcy's law must be modified to account for the extra pressure drop caused by the turbulence. Applying the turbulence correction to Eq (4.3) gives:

$$P_1 - P_2 = \frac{\mu_f B_f L}{1.127\times10^{-3} k_f A} Q_f + \frac{9.08\times10^{-13} B_f^2 \beta \rho_f L}{A^2} Q_f^2 \text{ ----------} (4.5)$$

where

P_1: upstream pressure, psia

P_2: downstream pressure, psia

μ_f: formation fluid viscosity, cp

B_f: formation fluid volume factor, bbl/STB

L: length of flow path, ft

k_f: permeability to formation fluid, md

A: area open to flow, ft^2

ρ_f: formation fluid density, lbm/ft^3

β: velocity coefficient, ft^{-1}, and

Q_f: formation fluid flow rate, STB/Day.

This flow regime is considered in modelling pressure losses because of the high gas flow rates in UBD.

Radial Flow

Darcy's law can be used to calculate the flow into a well where the fluid is converging radially into a relatively small hole. In this case, the area open to flow is not constant and must therefore be included in the integration of Eq (4.2). Referring to the flow geometry illustrated in Fig 4.2, the cross sectional area open to the flow at any radius is $A = 2\pi rh$.

Also, defining the change in pressure with location to be negative with respect to the direction of flow, dP/dx becomes -dP/dr. Making these substitutions in Eq (4.2) gives:

$$Q_f = \frac{kAdP}{\mu dr} = \frac{2\pi rhkdP}{\mu dr} \text{ ---------- (4.6)}$$

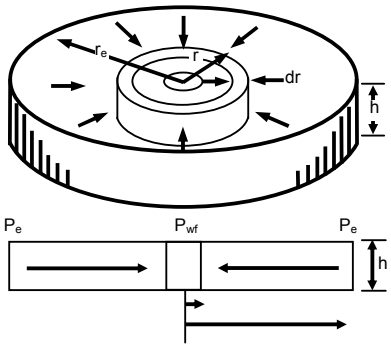

Fig 4.2. *Radial flow system*

When applying the Darcy equation to flow of oil or water in a reservoir, it is assumed that the fluid is only slightly compressible. The small change in Q_f with pressure is handled with the formation fluid volume factor B_f, so that the flow rate can be expressed in surface or stock tank volumes. So the Eq (4.6) becomes:

$$Q_f B_f = \frac{2\pi rhk_f}{\mu_f}\left(\frac{dP}{dr}\right) \text{ ---------- (4.7)}$$

or

$$2\pi h \int_{P_{wf}}^{P_e} \frac{k_f}{\mu_f B_f} dP = Q_f \int_R^{r_e} \frac{dr}{r} \text{ ---------- (4.8)}$$

When integrating this equation, it is usually assumed that the pressure function, $f(P) = k_f/\mu_f B_f$, is independent of pressure or that it can be evaluated at average pressure in the well's drainage volume. This is necessary because no simple analytical equation for this term as a function of pressure can be formulated. Utilizing this assumption and integrating Eq (4.8) over the drainage radius of the well gives:

$$Q_f = \frac{2\pi k_f h(P_e - P_{wf})}{\mu_f B_f \ln(r_e / R)} \text{ ---------- (4.9)}$$

For Field units, Eq (4.9) becomes:

$$Q_f = \frac{0.00708 k_f h(P_e - P_{wf})}{\mu_f B_f \ln(r_e / R)} \text{ ---------- (4.10)}$$

where

Q_f = inflow rate, STB/D,

k_f = effective oil permeability, md,

h = reservoir thickness, ft,

P_e = pressure at $r = r_e$, psia,

P_{wf} = wellbore flowing pressure at $r = r_w$, psia,

r_e = well's drainage radius, ft,

R = wellbore radius, ft,

μ_f = fluid formation viscosity, cp, and

B_f = formation fluid volume factor, bbl/STB.

Eq (4.10) applies for steady state (P_e = const), laminar flow of a well in the centre of a circular drainage area. It is more useful if expressed in terms of average reservoir pressure P_R, and for pseudo-steady state or stabilized flow (P_R - P_{wf} = const) as:

$$Q_f = \frac{0.00708 k_f h (P_R - P_{wf})}{\mu_f B_f \ln(0.472 r_e / R)} \quad \text{---------- (4.11)}$$

where P_R = average pressure in the drainage volume of the well.

The other terms are the same as those defined for Eq (4.10).

Productivity Index Concept

The relationship between well inflow rate and pressure drawdown has often been expressed in the form of a Productivity Index (PI) [69, 70, 71]

$$PI = \frac{0.00708 k_f h}{\mu_f B_f \ln(0.472 r_e / R)} \quad \text{---------- (4.12)}$$

The inflow equation for oil or water flow can then be written as:

$$Q_f = PI(P_R - P_{wf}) \quad \text{---------- (4.13)}$$

$$PI = \frac{Q_f}{P_R - P_{wf}} \quad \text{---------- (4.14)}$$

Solving for P_{wf} in terms of Q_f reveals that a plot of P_{wf} versus Q_f on Cartesian coordinates results in a straight line having a slope of -1/PI and an intercept of P_R at Q_f = 0.

$$P_{wf} = P_R - \frac{Q_f}{PI} \quad \text{---------- (4.15)}$$

If conditions are such that PI is constant with drawdown, once a value of PI is obtained from one production test or calculated using Eq (4.12), it may be used to predict inflow performance for other conditions.

4.2.2. Vogel Method [51]

If all of the variables in the inflow equations could be calculated, the equations resulting from integration of Darcy's law could be used to quantify the IPR. Unfortunately, sufficient information rarely exists to accomplish this and, therefore, empirical methods must be used to predict the inflow rate for a well.

The most widely used empirical method for predicting an IPR for a well is Vogel method [47, 72, 73]. It requires at least one stabilized test on a well, and some require several tests in which P_{wf} and Q_f were measured, P_R is assumed constant.

The Vogel method was developed by using the reservoir model proposed by for a wide range of conditions. Then the IPR is replotted as reduced or dimensionless pressure versus dimensionless flow rate. The dimensionless pressure is defined as the flowing wellbore pressure divided by average reservoir pressure, P_{wf}/P_R. The dimensionless flow rate is defined as the flow rate that would result for the value of P_{wf} being considered, divided by the flow rate that would result from a zero wellbore pressure, that is $Q_f/Q_{f(max)}$. It was found that the general shape of the dimensionless IPR was similar for all of the conditions studied.

After plotting dimensionless IPR curves for all the cases considered, it was arrived at the following relationship between dimensionless flow rate and dimensionless pressure:

$$\frac{Q_f}{Q_{f(\max)}} = 1 - 0.2\frac{P_{wf}}{P_R} - 0.8\left(\frac{P_{wf}}{P_R}\right)^2 \quad \text{---------- (4.16)}$$

The dimensionless IPR for a well with a constant productivity index can be calculated from:

$$\frac{Q_f}{Q_{f(\max)}} = 1 - \frac{P_{wf}}{P_R} \quad \text{---------- (4.17)}$$

Application of Vogel Method - Zero Skin Factor

1. Saturated Reservoirs ($P_R < P_b$)

A complete IPR could be constructed by assuming other values of P_{wf} and calculating the corresponding Q_f from the Eq (4.16).

2. Undersaturated Reservoirs ($P_R > P_b$)

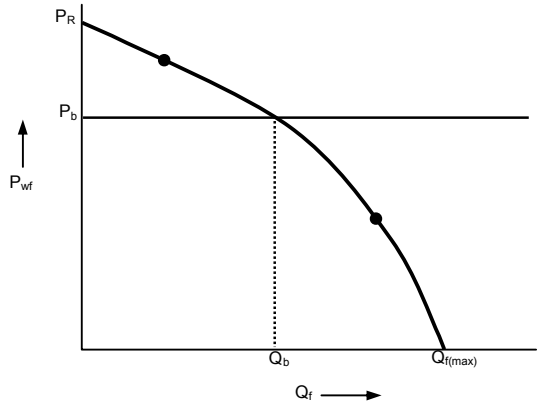

Fig 4.3. *IPR for an undersaturated reservoir*

Two test cases must be considered for applying Vogel's method to undersaturated reservoirs. The flowing wellbore pressure for the test can be either above or below bubble point pressure. The equations can be derived by considering the

productivity index to be constant for $P_{wf} \geq P_b$, and assuming that Vogel's equation applies for $P_{wf} < P_b$. Also, it is assumed that the complete IPR is continuous, that is, the slopes of the two segments are equal at $P_{wf} = P_b$. Fig 4.3 is used to illustrate the IPR for an undersaturated reservoir.

Case 1: test is carried out when $P_{wf} \geq P_b$

Applying Vogel's equation for any flow rate greater than the rate Q_b, corresponding to $P_{wf} = P_b$

$$\frac{Q_f - Q_b}{Q_{f(\max)} - Q_b} = 1 - 0.2\frac{P_{wf}}{P_b} - 0.8\left(\frac{P_{wf}}{P_b}\right)^2$$

$$Q_f = Q_b + \left(Q_{f(\max)} - Q_b\right)\left[1 - 0.2\left(\frac{P_{wf}}{P_b}\right) - 0.8\left(\frac{P_{wf}}{P_b}\right)^2\right] \text{ ---------- (4.18)}$$

The reciprocal slope is defined as the change in flow rate with respect to the change in P_{wf}, or:

$$\frac{dQ_f}{dP_{wf}} = \left(Q_{f(\max)} - Q_b\right)\left(-\frac{0.2}{P_b} - \frac{1.6P_{wf}}{P_b^2}\right)$$

Evaluating the reciprocal slope at $P_{wf} = P_b$, gives:

$$-\frac{dQ_f}{dP_{wf}} = \left(Q_{f(\max)} - Q_b\right)\left(\frac{1.8}{P_b}\right) \text{ ---------- (4.19)}$$

The productivity index is defined as the negative of the reciprocal slope, and if PI is evaluated at any value of $P_{wf} \geq P_b$, Eq (4.19) becomes:

$$PI = \frac{1.8\left(Q_{f(\max)} - Q_b\right)}{P_b}$$

$$Q_{f(\max)} - Q_b = \frac{PI \times P_b}{1.8} \text{ ---------- (4.20)}$$

Substituting Eq (4.20) into Eq (4.18) gives:

$$Q_f = Q_b + \frac{PI \times P_b}{1.8}\left[1 - 0.2\left(\frac{P_{wf}}{P_b}\right) - 0.8\left(\frac{P_{wf}}{P_b}\right)^2\right] \text{ ---------- (4.21)}$$

Once a value of PI at $P_{wf} \geq P_b$ is determined, Eq (4.21) can be used to generate an IPR. If the well test is taken with $P_{wf} \geq P_b$, PI and Q_b, can be calculated directly, since:

$$PI = \frac{Q_f}{P_R - P_{wf}}$$

$$Q_b = PI\left(P_R - P_b\right) \text{ ---------- (4.22)}$$

IPR is generated in this case by the following procedure

1. Calculate PI using test data in Eq (4.14).

2. Calculate Q_b using Eq (4.22).

3. Generate the IPR for values of $P_{wf} < P_b$ using Eq (4.21). The IPR for $P_{wf} \geq P_b$ is linear and can be calculated by using equation $Q_f = PI(P_R - P_{wf})$.

Case 2: test is carried out when $P_{wf} < P_b$

If the test is such that $P_{wf} < P_b$, the calculation of PI is more complex since Q_b will not be known. This is illustrated as Case 2 in Fig 4.3. An expression for PI to use in Eq (4.21) can be obtained by combining Eqs (4.21) and (4.22):

$$PI = \frac{Q_f}{P_R - P_b + \frac{P_b}{1.8}\left[1 - 0.2\frac{P_{wf}}{P_b} - 0.8\left(\frac{P_{wf}}{P_b}\right)^2\right]} \quad \text{---------- (4.23)}$$

1. Calculate PI using test data and Eq (4.23).

2. Calculate Q_b using Eq (4.22).

3. Generate the IPR using Eq (4.21) for $P_{wf} < P_b$. The IPR for $P_{wf} \geq P_b$ is linear and can be calculated by using equation $Q_f = PI(P_R - P_{wf})$.

Application of Vogel Method - Non Zero Skin Factor (Standing Modification)

1. Saturated Reservoirs ($P_R < P_b$)

The method for generating an IPR presented by Vogel did not consider an absolute permeability change in the reservoir. Standing [47, 50, 72] proposed a procedure to modify Vogel's method to account for either damage or stimulation around the wellbore. The degree of permeability alteration can be expressed in terms of Flow Efficiency FE, where:

$$FE = \frac{ideal\ \ drawdown}{actual\ \ drawdown} = \frac{P_R - P_{wf}^{'}}{P_R - P_{wf}} = \frac{q/PI'}{q/PI} = \frac{PI}{PI'} \quad \text{---------- (4.24)}$$

where

$$P_{wf}^{'} = P_{wf} \pm \Delta P_{skin}$$

ΔP_{skin}: pressure change caused by skin effect when formation is stimulated or damaged.

Using the previous definition for flow efficiency, Vogel's equation becomes:

$$\frac{Q_f}{Q_{f(\max)}^{FE=1}} = 1 - 0.2\frac{P_{wf}^{'}}{P_R} - 0.8\left(\frac{P_{wf}^{'}}{P_R}\right)^2 \quad \text{---------- (4.25)}$$

$Q_{f(\max)}^{FE=1}$: the maximum inflow being obtained for the well if FE = 1

A relationship among P_{wf}, P'_{wf} and FE can be obtained by solving Eq (4.24)

$$P'_{wf} = P_R - FE(P_R - P_{wf}) \quad \text{---------- (4.26)}$$

or

$$\frac{P'_{wf}}{P_R} = 1 - FE + FE\left(\frac{P_{wf}}{P_R}\right) \quad \text{---------- (4.27)}$$

The following procedure was used by Standing to construct dimensionless IPR curves for flow efficiencies not equal to one:

1. Select a value for FE.

2. Assume a range of values for P_{wf} / P_R.

3. For each value assumed in step 2, calculate the corresponding value of P'_{wf} / P_R using Eq (4.27).

4. Calculate $Q_f / Q_{f(\max)}^{FE=1}$ for each value of P_{wf} / P_R assumed in step 2 using Eq (4.25). Plot P_{wf} / P_R versus $Q_f / Q_{f(\max)}^{FE=1}$

5. Select a new FE and go to step 2.

Standing's dimensionless IPR curves can be put in equation form by combining Eqs (4.25) and (4.27). This gives:

$$\frac{Q_f}{Q_{f(\max)}^{FE=1}} = 1 - 0.2\left[1 - FE + FE\left(\frac{P_{wf}}{P_R}\right)\right] - 0.8\left[1 - FE + FE\left(\frac{P_{wf}}{P_R}\right)^2\right]$$

$$\frac{Q_f}{Q_{f(\max)}^{FE=1}} = 1.8(FE)\left(1 - \frac{P_{wf}}{P_R}\right) - 0.8(FE)^2\left(1 - \frac{P_{wf}}{P_R}\right)^2 \quad \text{---------- (4.28)}$$

Because of the restriction that $P'_{wf} \geq 0$, Eq (4.28) is valid only if

$$Q_f \leq Q_{f(\max)}^{FE=1} \text{ or } P_{wf} \geq P_R\left(1 - \frac{1}{FE}\right)$$

This restriction will always be satisfied if FE ≤ 1. For values of FE > 1, an approximate relationship between the actual $Q_{(\max)}$ and is:

$$Q_{(\max)} = Q_{f(\max)}^{FE=1}(0.624 + 0.376FE) \quad \text{---------- (4.29)}$$

For the case of FE = 1 ($P_{wf} = P'_{wf}$), Eq (4.28) is identical to the Vogel Eq (4.25).

2. Undersaturated Reservoirs with FE ≠ 1 ($P_R \geq P_b$)

Standing's modification of Vogel's method to be used when the flow efficiency is not equal to one may also be applied to undersaturated reservoirs.

Eq (4.21) may be modified for FE not equal to one to obtain:

$$Q_f = PI(P_R - P_b) + \frac{PI \times P_b}{1.8}\left[1.8\left(1 - \frac{P_{wf}}{P_b}\right) - 0.8(FE)\left(1 - \frac{P_{wf}}{P_b}\right)^2\right] \text{ -------- (4.30)}$$

The following procedures may be used to generate an IPR for any value of FE, including the case for FE = 1.

Case 1: test is carried out when $P_{wf} \geq P_b$

IPR is generated in this case by the following procedure:

1. Calculate PI using test data in Eq (4.14).

2. Generate the IPR for values of $P_{wf} < P_b$ using the known value of FE in Eq (4.30). The IPR for $P_{wf} \geq P_b$ is linear and can be calculated using $Q_f = PI(P_R - P_{wf})$.

Case 2: test is carried out when $P_{wf} < P_b$

1. Calculate PI using test data in Eq (4.30).

2. Generate the IPR for values of $P_{wf} < P_b$ using Eq (4.30). The IPR for $P_{wf} \geq P_b$ is linear and can be calculated using $Q_f = PI(P_R - P_{wf})$.

Besides the methods determining IPR above, there are still others such as Fetkovich method [74], Jones, Blount and Glaze method [75].

4.2.3. IPR for Horizontal Wells [47, 76, 77]

The wells drilled in Basin X have horizontal sections drilled into the producing formation. And according to horizontal holes, the actual production mechanism or reservoir flow regimes are more complicated than those for a vertical well, especially if the horizontal section is of considerable length. Some combination of both linear and radial flow actually exists.

Generation of data to construct an IPR is best accomplished with a numerical reservoir model, and this has been discussed by Sherrard, et al [78]. They also reported that the shape of measured IPR's for horizontal wells completed in the Prudhoe Bay field was similar to those predicted by the Vogel or Fetkovich methods. That is, the productivity index PI decreased with increased drawdown. The productivity index for a horizontal well in which permeability difference in the vertical and horizontal directions is small was described by:

$$PI = \frac{0.00708 k_H}{\mu_f B_f X} \text{ ---------- (4.31)}$$

where

$$X = \frac{1}{h}\ln\left[1 + \frac{\sqrt{1 + (L/2r_e)^2}}{L/2r_e}\right] + \frac{B^2}{L}(h/2R)$$

$$B = \sqrt{k_H / k_V}$$

k_H: effective permeability to oil in the horizontal direction, md

k_V: effective permeability in the vertical direction, md

L: length of the horizontal section, ft, and

h: vertical thickness of the formation, ft.

The complex flow regime existing around a horizontal wellbore probably precludes using a method as simple as that of Vogel to construct an IPR. Bendakhlia and Aziz [79] used a complex reservoir model to generate IPR's for a number of wells and found that the Vogel equation [51] would fit the generated data if expressed as:

$$\frac{Q_f}{Q_{f(\max)}^{FE=1}} = \left[1 - V\frac{P_{wf}}{P_R} - (1-V)\left(\frac{P_{wf}}{P_R}\right)^2\right]^n \quad \text{---------- (4.32)}$$

In order to apply this equation to well test data at least three stabilized tested are required to evaluate the three unknowns, $Q_{f(\max)}$, V and n.

The establishment of IPR in this research has been carried out by using the production software of IHS Energy Group that is PERFORME 3.0, [80] and the results from this software will be used to couple productivity and parameters of UBD.

4.3. Coupling Productivity in UBD

4.3.1. Introduction to PERFORM 3.0

Well PERFORMance Analysis ™ (PERFORM) is a graphical tool used to analyze the performance of a well. PERFORM can help:

- Improve completion design
- Increase well performance
- Optimize production

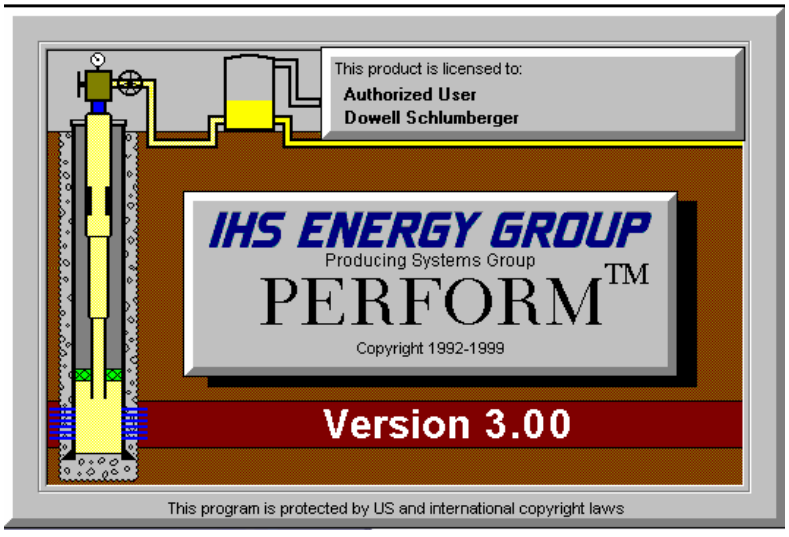

Fig 4.4. *Perform 3.0 interface*

4.3.2. Coupling Productivity in UBD

Coupling Productivity in UBD can be carried out by the following steps:

Step 1: *setting up IPR by using PERFORM 3.0*

All methods applied to calculate IPR of a well such as Darcy, Vogel, constant PI, Jones, Blount and Glaze, even fractured well and horizontal well are available in PERFORM 3.0. After the necessary data corresponding with each suitable method are input in PERFORM 3.0, the result of IPR is the set of data of Q_f versus P_{wf}.

Q_f (STB/Day)	X_1	X_2	X_3	X_4	X_5	…	X_n
P_{wf} (psia)	Y_1	Y_2	Y_3	Y_4	Y_5	…	Y_n

Step 2: *setting up the equation relating between Q_f and P_{wf}*

From the set of data of Q_f and P_{wf} withdrawn from step 1, it is necessary to build up the equation relating Q_f and P_{wf}. Because the relationship between Q_f and P_{wf} is a second degree equation. So, to be able to obtain this relationship, the Least Square Method [81] is often applied. This method can be explained as follow:

$$X = \alpha + \beta Y + \chi Y^2 \text{----------} \quad (4.33)$$

to approximate the given set of data, (Y_1, X_1), (Y_2, X_2), …, (Y_n, X_n), where $n \geq 3$. The best fitting curve f(Y) must have the least square error, i.e.,

$$\prod = \sum_{i=1}^{n} \left[X_i - f(Y_i)\right]^2 = \sum_{i=1}^{n} \left[X_i - (\beta + \beta Y_i + \chi Y_i^2)\right]^2 \text{----------} \quad (4.34)$$

Please note that α, β, and χ are unknown coefficients while all Y_i and X_i are given. To obtain the least square error, the unknown coefficients α, β, and χ must yield zero first derivatives:

$$\begin{cases} \dfrac{\partial \prod}{\partial A} = 2\sum_{i=1}^{n} \left[X_i - (\alpha + \beta Y_i + \chi Y_i^2)\right] = 0 \\ \dfrac{\partial \prod}{\partial B} = 2\sum_{i=1}^{n} Y_i \left[X_i - (\alpha + \beta Y_i + \chi Y_i^2)\right] = 0 \\ \dfrac{\partial \prod}{\partial B} = 2\sum_{i=1}^{n} Y_i^2 \left[X_i - (\alpha + \beta Y_i + \chi Y_i^2)\right] = 0 \end{cases} \text{----------} \quad (4.35)$$

Expanding the equation above:

$$\begin{cases} \sum_{i=1}^{n} X_i = \alpha \sum_{i=1}^{n} n + \beta \sum_{i=1}^{n} Y_i + \chi \sum_{i=1}^{n} Y_i^2 \\ \sum_{i=1}^{n} Y_i X_i = \alpha \sum_{i=1}^{n} Y_i + \beta \sum_{i=1}^{n} Y_i^2 + \chi \sum_{i=1}^{n} Y_i^3 \\ \sum_{i=1}^{n} Y_i^2 X_i = \alpha \sum_{i=1}^{n} Y_i^2 + \beta \sum_{i=1}^{n} Y_i^3 + \chi \sum_{i=1}^{n} Y_i^4 \end{cases} \text{----------} \quad (4.36)$$

The coefficients α, β, and χ can hence be obtained by solving the above linear equations.

As a result,

$$Q_f = \alpha + \beta P_{wf} + \chi P_{wf}^2 \quad \text{----------} \quad (4.37)$$

with α, β, and χ can be calculated by Eq (4.36)

Step 3: *coupling productivity in UBD*

The bottomhole pressure can be calculated by the equation:

$$P_{wf} = \sum_{i=1}^{n} \Delta P \quad \text{----------} \quad (4.38)$$

The gradient pressure Eq (3.4) in chapter 3:

$$\frac{dP}{dL} = \rho_m \cos\phi + \frac{6\rho_m f_m v_m^2}{g d_H} \quad \text{----------} \quad (3.4)$$

can be written in the numerical expression as:

$$\frac{\Delta P}{\Delta L} = \rho_m \cos\phi + \frac{6\rho_m f_m v_m^2}{g d_H} \quad \text{----------} \quad (4.39)$$

or

$$\Delta P = \left(\rho_m \cos\phi + \frac{6\rho_m f_m v_m^2}{g d_H} \right) \Delta L = \left(\rho_m \cos\phi + \frac{6\rho_m f_m v_m^2}{g d_H} \right) \left(\frac{L}{n} \right) \quad \text{----------} \quad (4.40)$$

with n is the number of divided sections along the well trajectory.

So the bottomhole pressure can be expressed as:

$$P_{wf} = \sum_{i=1}^{n} \left(\rho_m \cos\phi + \frac{6\rho_m f_m v_m^2}{g d_H} \right) \left(\frac{L}{n} \right) \quad \text{----------} \quad (4.41)$$

ρ_m, v_m, and f_m in the Eq (4.41) are average values in each section of interest and can be calculated by Eqs (3.29), (3.30), and (3.31) of the previous chapter:

$$\rho_m = \frac{9.45\times10^{-5} d_b^2 S_s R_p + 1.391\times10^{-4} W_{x0} Q_x + 4.056\times10^{-3} S_f Q_f + 0.0765 S_g Q_{gs}}{2.2283\times10^{-3} Q_x B_x + 6.499\times10^{-5} Q_f B_f + Q_{gs} B_g}$$

---------- (3.29)

$$v_m = \frac{Q_l + Q_g}{A} = \frac{2.2283\times10^{-3} Q_x B_x + 6.499\times10^{-3} Q_f B_f + Q_{gs} B_g}{A} \quad \text{-------} \quad (3.30)$$

$$f_m = \left[\frac{1}{1.74 - 2\log\left(\frac{2\varepsilon}{d_H} + \frac{18.7}{N_{\mathrm{Re}}\sqrt{f_m}} \right)} \right]^2 \quad \text{----------} \quad (3.31)$$

Substituting the Eq (4.37) into Eqs (3.29), and (3.30) gives:

$$\rho_m = \frac{9.45\times10^{-5} d_b^2 S_s R_p + 1.391\times10^{-4} W_{x0} Q_x}{2.2283\times10^{-3} Q_x B_x + 6.499\times10^{-5}(\alpha+\beta P_{wf}+\chi P_{wf}^2)B_f + Q_{gs}B_g} + \ldots$$
$$\frac{4.056\times10^{-3} S_f(\alpha+\beta P_{wf}+\chi P_{wf}^2) + 0.0765 S_g Q_{gs}}{2.2283\times10^{-3} Q_x B_x + 6.499\times10^{-5}(\alpha+\beta P_{wf}+\chi P_{wf}^2)B_f + Q_{gs}B_g} \quad (4.42)$$

$$v_m = \frac{2.2283\times10^{-3} Q_x B_x + 6.499\times10^{-3}(\alpha+\beta P_{wf}+\chi P_{wf}^2)B_f + Q_{gs}B_g}{A} \quad \text{-- (4.43)}$$

Step 4: *establishing the relationship between the productivity and UBD parameters*

Solving Eqs (4.40), (4.41), (4.42), and (4.43) by numerical methods will give the results of bottom hole pressure (P_{wf}), gradient pressure along the wellbore, formation influx flow rates.

a. Assuming that the bottomhole pressure is P_{wfe}.

b. With the given $\Delta L = L/n$, for example 50 ft, the respective $\Delta P_s = 10$ psi will be assumed. So the average pressure in this 50 ft section is $P_{av} = P_s + \Delta P_s/2$, and the average temperature is $T_{av} = T_s + G\cos(\phi)\Delta L/2$ (notice that the smaller ΔL, the better result, however, the longer the run time of the computer).

c. At this average pressure and temperature, all parameters on the right hand side of Eq (4.40) will be calculated so ΔP_c on the left hand side will be solved. Notes that the value of P_{wf} substituted into Eqs (3.31), (4.42), and (4.43) to solve Eq (4.40) is the assumed value of the step a.

d. If this value ΔP_c is equal ΔP_s assumed at the step b, it means that this value is correct, and the pressure drop in the next section (50 ft) continues to be calculated. In the case ΔP_c is different with ΔP_s, using ΔP_c as the new ΔP_s value and return to the first step. These iterative steps will be continued until the correct pressure drop value can be reached.

e. Continue to the next section until the total $\sum\Delta L = L$, so the bottom hole pressure P_{wfc} will be calculated.

f. The calculated bottomhole pressure, P_{wfc} will be compared with the estimated bottomhole pressure in step a, P_{wfe}. If P_{wfc} and P_{wfe} have approximate values, it means the bottomhole pressure is accurate, else if the new estimated value of bottomhole pressure will be used.

In summary, applying four above steps will help not only to model the distribution of pressure, temperature, and drilling fluid properties along the well but also to estimate the formation influx flow rate while UBD. Therefore, the success of coupling the productivity and UBD parameters will supply two important results. First of all, the measurements of production rate made while UBD will support enough information that drillstem testing is not required. From that, it will reduce the cost of

evaluating the well because rig time is reduced by not having to make a round trip, rig up and rig down the test tool. Secondly, it will introduce an approximate figure of the financial return prospect to the investment when the production rate while UBD can be estimated. This is innovative development in this research work. All applications and results of this chapter will be presented in chapter 6.

CHAPTER 5 - WELLST & UBDRILL

UBDRILL and WELLST are programs developed in this research through the combination of Microsoft Excel and Matlab. While WELLST is developed to calculate the stress concentration, pore pressure, temperature profiles around the wellbore, and evaluate the wellbore stability in UBD, UBDRILL is used to model the hydraulics calculation in UBD such as modelling the multiphase flow in UBD operation, coupling productivity in UBD, calculating total pressure drop in drilling system, and suggesting the optimum well control method by designing liquid gas rate window (LGRW).

Both programs have the user-friendly interfaces which have been programmed by using Microsoft Excel to store the input and output data, and applying Matlab [82] to solve the numerical equations. The main program [83] can be seen in the following figure.

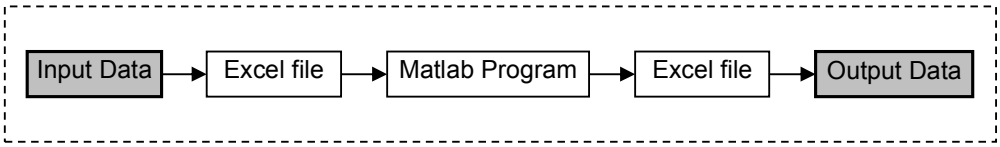

Fig 5.1. *Main program*

5.1. WELLST

WELLST has been developed by using equations shown in chapter 2 which estimate the hydraulics effect and thermal effect to the stress distribution around the directional borehole. The stability of the wellbore is then determined by Drucker-Prager or Mohr-Coulomb failure criteria. This program is a powerful tool for both field use and research. One can easily conduct a sensitivity study on any of the input parameters by plotting the output parameters as a function of a selected input parameter. Therefore, the structure of this program also includes three parts: input data protocol, Matlab program, and output data protocol.

5.1.1. Input data protocol

The input data file is an Excel file including two worksheets, the first one Wellbore Stability Data including rock parameters, initial stress condition, fluid properties, and wellbore trajectory. The second one is the exposure time of wellbore after drilling. Each calculation required 28 parameters to run a single simulation.

Microsoft Excel - Input

File Edit View Insert Format Tools Data Window Help

J30

INPUT DATA

	Parameters	Input Data	Units	Notes
3	Young Module (E)	68670	Mpa	
4	Poison ratio (Poi)	0.28		
5	Granite density (rog)	2800	kg/m3	
6	Cohesion of material (c)	40	Mpa	
7	Frictional angle (phi)	28	degree	
8	Maximum horizontal stress (sigmamax)	88	MPa	
9	Minimum horizontal stress (sigmamin)	54	MPa	
10	Vertical stress (sigmaV)	85	MPa	
11	Fluid compressibility (Cf)	7.90E-04	1/MPa	
12	Void ratio	0.45		
13	Oil density	828.4	kg/m3	
14	Fluid thermal expansion coefficient (alphaf)	9.00E-04	1/oC	
15	Drained thermal expansion coefficient (alphaB)	8.50E-06		
16	Specific heat of granite (Ce)	840	J/kg.oC	
17	Permeability (k)	0.0001	Darcy	
18	Oil Viscosity (muyo)	0.5	Cp	
19	Thermal conductivity (w)	4.5	W/m.oC	
20	Reservoir Temperature (Tr)	131	oC	
21	Wellbore Temperature (Twf)	98	oC	
22	Reservoir Pressure (Pr)	34.45	MPa	
23	Wellbore Pressure (Pwf)	10.34	MPa	
24	Wellbore Radius (Rw)	0.1	m	
25	Boundary Radius (Re)	1.5	m	
26	Number of increments	70		from wellbore to boundary
27	Azimuth (azi)	30	degree	
28	Inclination (incli)	60	degree	
29	The angle around the wellbore (teta)	30	degree	

Fig 5.2. *Sheet 1 – Wellbore stability data*

Microsoft Excel - Input

File Edit View Insert Format Tools Data Window Help

D30

EXPOSURE TIME

Time (s)
0
10
60
600

Fig 5.3. *Sheet 2 – Exposure time data*

5.1.2. Matlab program

File Edit View Favorites Tools Help

Back Search Folders

File and Folder Tasks

Other Places

work
My Documents
Shared Documents
My Computer
My Network Places

Details

WELLSTAB
File Folder
Date Modified: 04 March 2008, 13:21

couplingP.m MATLAB M-file 1 KB
couplingT.m MATLAB M-file 1 KB
graphic.m MATLAB M-file 15 KB
Input.asv ASV File 2 KB
Input.m MATLAB M-file 2 KB
Input.xls Microsoft Excel Worksheet 20 KB
Output.xls Microsoft Excel Worksheet 2,820 KB
P_T.asv ASV File 4 KB
Results.m MATLAB M-file 8 KB
Results.xls Microsoft Excel Worksheet 267 KB
Solving.m MATLAB M-file 7 KB
WELLSTAB.m MATLAB M-file 2 KB

Fig 5.4. *Matlab Program*

The structure of this program now includes 4 procedures:

1. Input

2. Solving

3. Results

4. Graphic

and two functions which calculate the coupling equations of functions g_1, g_2 in chapter 2 were supplied to run these procedures. Before going to explain the role of each procedure, following functions are considered.

Functions

Functions g_1 and g_2 are set up basing on Eq (2.37).

$$g_1 = couplingP(E,\nu,\rho_s,\rho_f,e,C_f,\alpha_f,\alpha_B,k,\mu_f,\kappa,C_\varepsilon,r,t,R_w)$$

$$g_2 = couplingT(E,\nu,\rho_s,\rho_f,e,C_f,\alpha_f,\alpha_B,k,\mu_f,\kappa,C_\varepsilon,r,t,R_w)$$

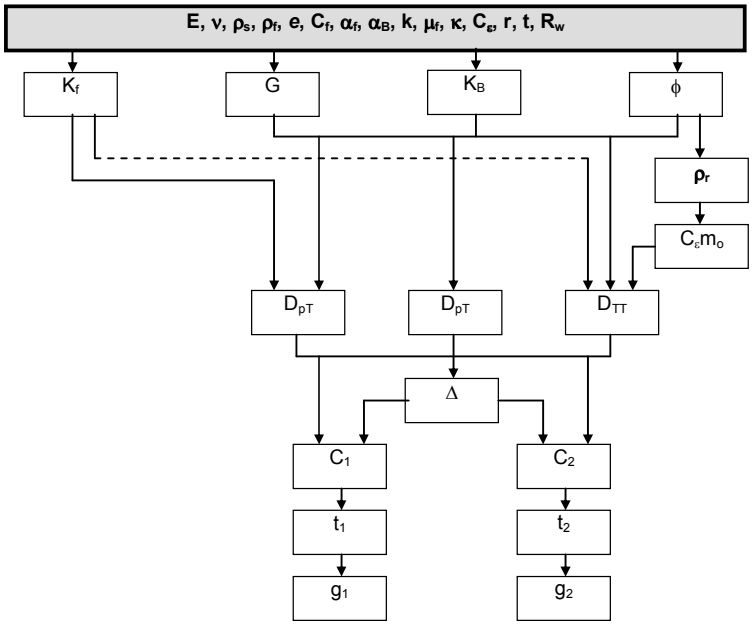

Fig 5.5. *g_1, and g_2 functions*

Procedures

The main program includes 4 procedures in which each procedure will use above functions. The main program is expressed in the following structure:

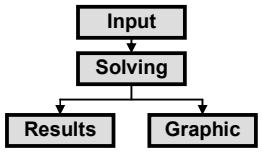

Fig 5.6. *Matlab program*

- *Input*

This procedure reads and saves all input data such as rock parameters, initial

stress condition, fluid properties, wellbore trajectory, and exposure time after drilling from the Excel file.

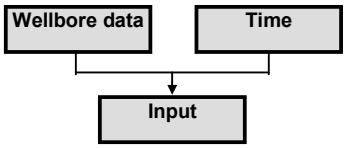

Fig 5.7. *Input flowchart*

- *Solving*

First of all, the pressure and temperature profiles (equations 2.32 and 2.33) around the wellbore will be calculated. Then the coordinate transformation (2.6) will be proceeded to know the stress components in the general situation of directional wells. After that, temperature and pore pressure profiles will be coupled into the stress condition Eq (2.7) in the new coordinate system to get the general solution (2.47). Finally, the borehole stability of rock will be verified by Mohr-Coulomb (2.61) or Drucker Prager (2.62) failure criteria.

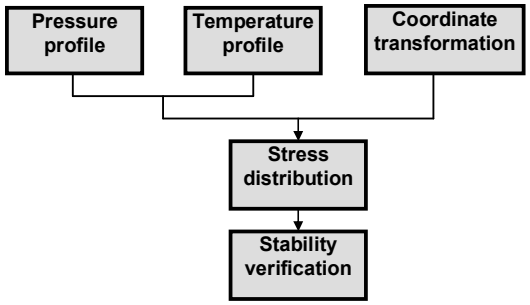

Fig 5.8. *Solving flowchart*

- *Results*

This procedure saves results solved by Matlab and exported to Excel files for using in other applications. These results include:

- Transient pressure profiles around the wellbore.
- Transient temperature profiles around the wellbore.
- Stress components (radial, tangential, axial, shear, and principal stresses) around the wellbore in elastic case.
- Mohr-Coulomb failure index in elastic case.
- Drucker Prager failure index in elastic case.
- Stress components (radial, tangential, axial, shear, and principal stresses) around the wellbore in poroelastic case.
- Effect of hydraulics diffusivity to stress field around the wellbore in poroelastic case.
- Mohr-Coulomb time dependent failure index in poroelastic case.
- Drucker Prager time dependent failure index in poroelastic case.

- Stress components (radial, tangential, axial, shear, and principal stresses) around the wellbore in thermoporoelastic case.
- Effect of hydraulics diffusivity and thermal diffusivity to stress field around the wellbore in thermoporoelastic case.
- Mohr-Coulomb time dependent failure index in thermoporoelastic case.
- Drucker Prager time dependent failure index in thermoporoelastic case.

• *Graphic*

Plot all calculated output data.

5.1.3. Output data protocol

The output data file is an Excel file including result worksheets. This file is created by the procedure "*Results*" of Matlab program. Some result worksheets are shown in the following pictures:

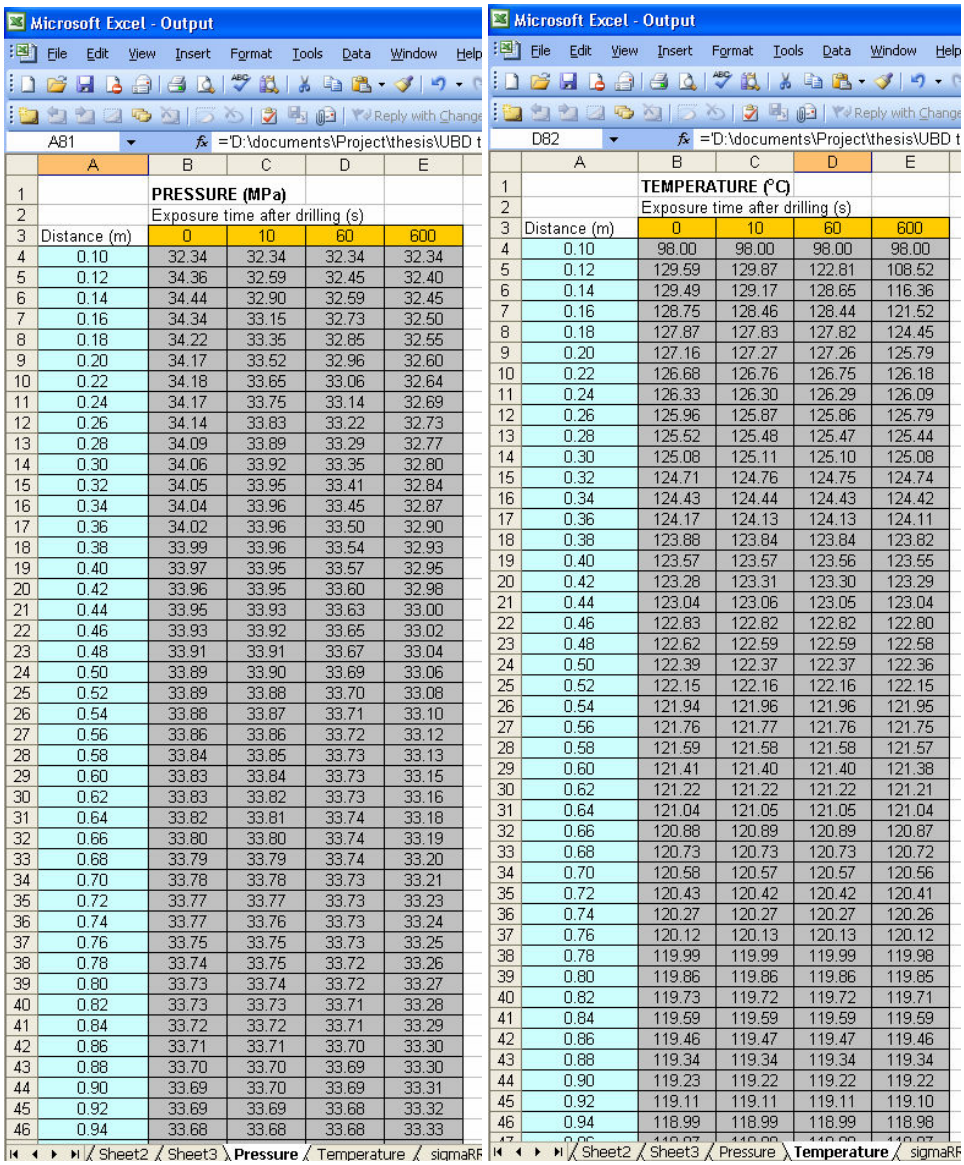

Microsoft Excel - Output

	A	B	C	D	E
1		PRESSURE (MPa)			
2		Exposure time after drilling (s)			
3	Distance (m)	0	10	60	600
4	0.10	32.34	32.34	32.34	32.34
5	0.12	34.36	32.59	32.45	32.40
6	0.14	34.44	32.90	32.59	32.45
7	0.16	34.34	33.15	32.73	32.50
8	0.18	34.22	33.35	32.85	32.55
9	0.20	34.17	33.52	32.96	32.60
10	0.22	34.18	33.65	33.06	32.64
11	0.24	34.17	33.75	33.14	32.69
12	0.26	34.14	33.83	33.22	32.73
13	0.28	34.09	33.89	33.29	32.77
14	0.30	34.06	33.92	33.35	32.80
15	0.32	34.05	33.95	33.41	32.84
16	0.34	34.04	33.96	33.45	32.87
17	0.36	34.02	33.96	33.50	32.90
18	0.38	33.99	33.96	33.54	32.93
19	0.40	33.97	33.95	33.57	32.95
20	0.42	33.96	33.95	33.60	32.98
21	0.44	33.95	33.93	33.63	33.00
22	0.46	33.93	33.92	33.65	33.02
23	0.48	33.91	33.91	33.67	33.04
24	0.50	33.89	33.90	33.69	33.06
25	0.52	33.89	33.88	33.70	33.08
26	0.54	33.88	33.87	33.71	33.10
27	0.56	33.86	33.86	33.72	33.12
28	0.58	33.84	33.85	33.73	33.13
29	0.60	33.83	33.84	33.73	33.15
30	0.62	33.83	33.82	33.73	33.16
31	0.64	33.82	33.81	33.74	33.18
32	0.66	33.80	33.80	33.74	33.19
33	0.68	33.79	33.79	33.74	33.20
34	0.70	33.78	33.78	33.73	33.21
35	0.72	33.77	33.77	33.73	33.23
36	0.74	33.77	33.76	33.73	33.24
37	0.76	33.75	33.75	33.73	33.25
38	0.78	33.74	33.75	33.72	33.26
39	0.80	33.73	33.74	33.72	33.27
40	0.82	33.73	33.73	33.71	33.28
41	0.84	33.72	33.72	33.71	33.29
42	0.86	33.71	33.71	33.70	33.30
43	0.88	33.70	33.70	33.69	33.30
44	0.90	33.69	33.70	33.69	33.31
45	0.92	33.69	33.69	33.68	33.32
46	0.94	33.68	33.68	33.68	33.33

Sheet2 / Sheet3 / Pressure / Temperature / sigmaRF

Microsoft Excel - Output

	A	B	C	D	E
1		TEMPERATURE (°C)			
2		Exposure time after drilling (s)			
3	Distance (m)	0	10	60	600
4	0.10	98.00	98.00	98.00	98.00
5	0.12	129.59	129.87	122.81	108.52
6	0.14	129.49	129.17	128.65	116.36
7	0.16	128.75	128.46	128.44	121.52
8	0.18	127.87	127.83	127.82	124.45
9	0.20	127.16	127.27	127.26	125.79
10	0.22	126.68	126.76	126.75	126.18
11	0.24	126.33	126.30	126.29	126.09
12	0.26	125.96	125.87	125.86	125.79
13	0.28	125.52	125.48	125.47	125.44
14	0.30	125.08	125.11	125.10	125.08
15	0.32	124.71	124.76	124.75	124.74
16	0.34	124.43	124.44	124.43	124.42
17	0.36	124.17	124.13	124.13	124.11
18	0.38	123.88	123.84	123.84	123.82
19	0.40	123.57	123.57	123.56	123.55
20	0.42	123.28	123.31	123.30	123.29
21	0.44	123.04	123.06	123.05	123.04
22	0.46	122.83	122.82	122.82	122.80
23	0.48	122.62	122.59	122.59	122.58
24	0.50	122.39	122.37	122.37	122.36
25	0.52	122.15	122.16	122.16	122.15
26	0.54	121.94	121.96	121.96	121.95
27	0.56	121.76	121.77	121.76	121.75
28	0.58	121.59	121.58	121.58	121.57
29	0.60	121.41	121.40	121.40	121.38
30	0.62	121.22	121.22	121.22	121.21
31	0.64	121.04	121.05	121.05	121.04
32	0.66	120.88	120.89	120.89	120.87
33	0.68	120.73	120.73	120.73	120.72
34	0.70	120.58	120.57	120.57	120.56
35	0.72	120.43	120.42	120.42	120.41
36	0.74	120.27	120.27	120.27	120.26
37	0.76	120.12	120.13	120.13	120.12
38	0.78	119.99	119.99	119.99	119.98
39	0.80	119.86	119.86	119.86	119.85
40	0.82	119.73	119.72	119.72	119.71
41	0.84	119.59	119.59	119.59	119.59
42	0.86	119.46	119.47	119.47	119.46
43	0.88	119.34	119.34	119.34	119.34
44	0.90	119.23	119.22	119.22	119.22
45	0.92	119.11	119.11	119.11	119.10
46	0.94	118.99	118.99	118.99	118.98

Sheet2 / Sheet3 / Pressure / Temperature / sigmaRF

Fig 5.9. *Pressure and Temperature profiles*

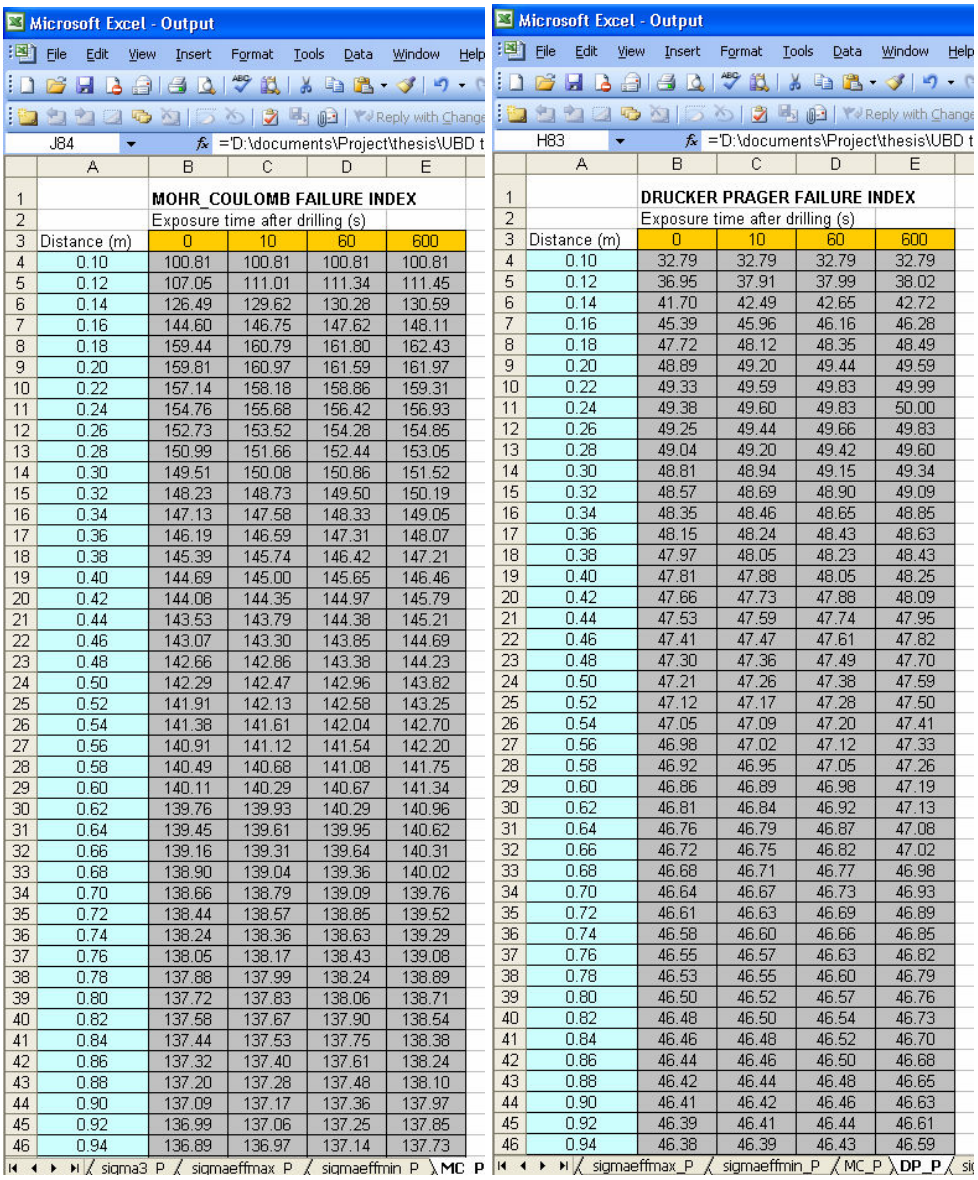

Microsoft Excel - Output

File Edit View Insert Format Tools Data Window Help

J84 ='D:\documents\Project\thesis\UBD t

	A	B	C	D	E
1		MOHR_COULOMB FAILURE INDEX			
2		Exposure time after drilling (s)			
3	Distance (m)	0	10	60	600
4	0.10	100.81	100.81	100.81	100.81
5	0.12	107.05	111.01	111.34	111.45
6	0.14	126.49	129.62	130.28	130.59
7	0.16	144.60	146.75	147.62	148.11
8	0.18	159.44	160.79	161.80	162.43
9	0.20	159.81	160.97	161.59	161.97
10	0.22	157.14	158.18	158.86	159.31
11	0.24	154.76	155.68	156.42	156.93
12	0.26	152.73	153.52	154.28	154.85
13	0.28	150.99	151.66	152.44	153.05
14	0.30	149.51	150.08	150.86	151.52
15	0.32	148.23	148.73	149.50	150.19
16	0.34	147.13	147.58	148.33	149.05
17	0.36	146.19	146.59	147.31	148.07
18	0.38	145.39	145.74	146.42	147.21
19	0.40	144.69	145.00	145.65	146.46
20	0.42	144.08	144.35	144.97	145.79
21	0.44	143.53	143.79	144.38	145.21
22	0.46	143.07	143.30	143.85	144.69
23	0.48	142.66	142.86	143.38	144.23
24	0.50	142.29	142.47	142.96	143.82
25	0.52	141.91	142.13	142.58	143.25
26	0.54	141.38	141.61	142.04	142.70
27	0.56	140.91	141.12	141.54	142.20
28	0.58	140.49	140.68	141.08	141.75
29	0.60	140.11	140.29	140.67	141.34
30	0.62	139.76	139.93	140.29	140.96
31	0.64	139.45	139.61	139.95	140.62
32	0.66	139.16	139.31	139.64	140.31
33	0.68	138.90	139.04	139.36	140.02
34	0.70	138.66	138.79	139.09	139.76
35	0.72	138.44	138.57	138.85	139.52
36	0.74	138.24	138.36	138.63	139.29
37	0.76	138.05	138.17	138.43	139.08
38	0.78	137.88	137.99	138.24	138.89
39	0.80	137.72	137.83	138.06	138.71
40	0.82	137.58	137.67	137.90	138.54
41	0.84	137.44	137.53	137.75	138.38
42	0.86	137.32	137.40	137.61	138.24
43	0.88	137.20	137.28	137.48	138.10
44	0.90	137.09	137.17	137.36	137.97
45	0.92	136.99	137.06	137.25	137.85
46	0.94	136.89	136.97	137.14	137.73

sigma3_P | sigmaeffmax_P | sigmaeffmin_P | MC_P

Microsoft Excel - Output

File Edit View Insert Format Tools Data Window Help

H83 ='D:\documents\Project\thesis\UBD t

	A	B	C	D	E
1		DRUCKER PRAGER FAILURE INDEX			
2		Exposure time after drilling (s)			
3	Distance (m)	0	10	60	600
4	0.10	32.79	32.79	32.79	32.79
5	0.12	36.95	37.91	37.99	38.02
6	0.14	41.70	42.49	42.65	42.72
7	0.16	45.39	45.96	46.16	46.28
8	0.18	47.72	48.12	48.35	48.49
9	0.20	48.89	49.20	49.44	49.59
10	0.22	49.33	49.59	49.83	49.99
11	0.24	49.38	49.60	49.83	50.00
12	0.26	49.25	49.44	49.66	49.83
13	0.28	49.04	49.20	49.42	49.60
14	0.30	48.81	48.94	49.15	49.34
15	0.32	48.57	48.69	48.90	49.09
16	0.34	48.35	48.46	48.65	48.85
17	0.36	48.15	48.24	48.43	48.63
18	0.38	47.97	48.05	48.23	48.43
19	0.40	47.81	47.88	48.05	48.25
20	0.42	47.66	47.73	47.88	48.09
21	0.44	47.53	47.59	47.74	47.95
22	0.46	47.41	47.47	47.61	47.82
23	0.48	47.30	47.36	47.49	47.70
24	0.50	47.21	47.26	47.38	47.59
25	0.52	47.12	47.17	47.28	47.50
26	0.54	47.05	47.09	47.20	47.41
27	0.56	46.98	47.02	47.12	47.33
28	0.58	46.92	46.95	47.05	47.26
29	0.60	46.86	46.89	46.98	47.19
30	0.62	46.81	46.84	46.92	47.13
31	0.64	46.76	46.79	46.87	47.08
32	0.66	46.72	46.75	46.82	47.02
33	0.68	46.68	46.71	46.77	46.98
34	0.70	46.64	46.67	46.73	46.93
35	0.72	46.61	46.63	46.69	46.89
36	0.74	46.58	46.60	46.66	46.85
37	0.76	46.55	46.57	46.63	46.82
38	0.78	46.53	46.55	46.60	46.79
39	0.80	46.50	46.52	46.57	46.76
40	0.82	46.48	46.50	46.54	46.73
41	0.84	46.46	46.48	46.52	46.70
42	0.86	46.44	46.46	46.50	46.68
43	0.88	46.42	46.44	46.48	46.65
44	0.90	46.41	46.42	46.46	46.63
45	0.92	46.39	46.41	46.44	46.61
46	0.94	46.38	46.39	46.43	46.59

sigmaeffmax_P | sigmaeffmin_P | MC_P | DP_P

Fig 5.10. *Mohr-Coulomb Failure Index (MFI) and Drucker Prager Failure Index (DPFI)*

5.2. UBDRILL

UBDRILL has been codified basing on IFDM method and equations presented in chapter 3 and 4. The structure of this program also includes three parts: input data protocol, Matlab program, and output data protocol.

5.2.1. Input data protocol

The input data file is an Excel file grouped into four different categories, the first one is Drilling Data, the second one is PVT Data, the third one is Well Trajectory Data, and the last one is IPR data. The typical screen for all groups is shown as follows:

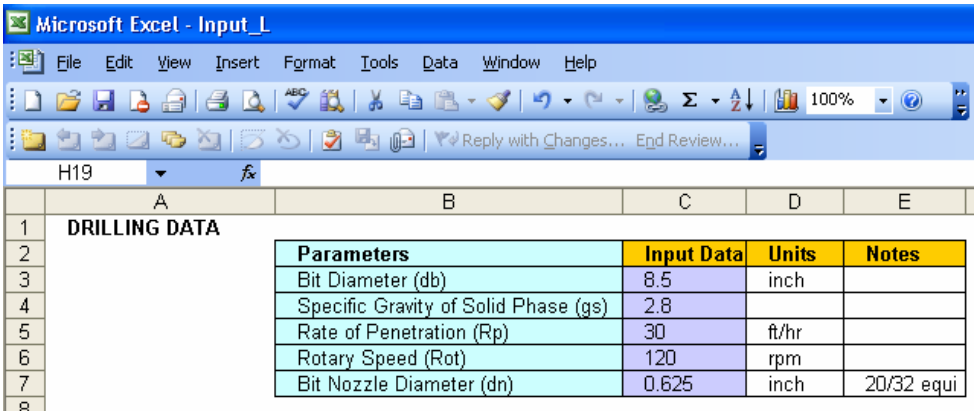

	A	B	C	D	E
1	DRILLING DATA				
2		**Parameters**	**Input Data**	**Units**	**Notes**
3		Bit Diameter (db)	8.5	inch	
4		Specific Gravity of Solid Phase (gs)	2.8		
5		Rate of Penetration (Rp)	30	ft/hr	
6		Rotary Speed (Rot)	120	rpm	
7		Bit Nozzle Diameter (dn)	0.625	inch	20/32 equi

Fig 5.11. *Sheet 1 - Drilling data*

B	C	D	E
	Input Data	**Units**	**Notes**
Formation Pressure (Pfor)	5000	psia	
Bubble Point Pressure (Pb)	4778	psia	
Collapse Pressure (Pcol)	1450	psia	
Wellhead Pressure (Psur)	80	psia	
Surface Temperature (Tsur)	139	°F	
Gas Gravity (gg)	0.65		
API Gravity (API)	39.3		
Specific Gravity of Liquid Injection (gx)	1.02		
Maximum Compressor Flow Rate (Qpumb)	42	SCF/s	
Formation Influx Fluid (a)	1		Oil a = 1; Water a = 2;
Drilling Fluid (b)	2		b=1: drilling with aerated mud, so the mud
Mud Weight (Wx)	8.2	ppg	weight and mud viscosity must be input
Mud Viscosity (muyx)	6	cp	b=2: drilling with aerated sea water, so
Sea Water Salinity	35	‰	only the sea water salinity is input

Fig 5.12. *Sheet 2 - PVT data*

C	D	E	F	G	H	I	J	K	L
MD (ft)	**Section Length (ft)**	**Angle (degrees)**	**TVD (ft)**	**Azimuth (Degrees)**	**Well Diameter (inch)**	**OD (inch)**	**ID (inch)**	**Annulus's roungness (inch)**	**Drillpipe's roungness (inch)**
592	592	0	592.00	0.00	12.615	4.5	3.826	0.0018	0.0018
1148	556	2.4	1147.51	225.00	12.615	4.5	3.826	0.0018	0.0018
1329	181	2.4	1328.35	225.00	12.615	4.5	3.826	0.0018	0.0018
1629	300	10.61	1623.22	180.00	12.615	4.5	3.826	0.0018	0.0018
1729	100	13.6	1720.42	177.00	12.615	4.5	3.826	0.0018	0.0018
1945	216	17.09	1926.88	175.32	12.615	4.5	3.826	0.0018	0.0018
7439	5494	17.26	7173.48	175.40	12.615	4.5	3.826	0.0018	0.0018
11080	3641	17.26	10650.52	175.40	8.681	4.5	3.826	0.0018	0.0018
11142	62	21.81	10708.08	175.42	8.5	4.5	3.826	0.197	0.0018
11342	200	26.36	10887.28	175.42	8.5	4.5	3.826	0.197	0.0018
11442	100	30.91	10973.08	175.43	8.5	4.5	3.826	0.197	0.0018
11542	100	35.46	11054.53	175.43	8.5	4.5	3.826	0.197	0.0018
11642	100	40.02	11131.12	175.44	8.5	4.5	3.826	0.197	0.0018
11742	100	44.57	11202.35	175.44	8.5	4.5	3.826	0.197	0.0018
11842	100	49.12	11267.80	175.44	8.5	4.5	3.826	0.197	0.0018
11942	100	53.67	11327.05	175.44	8.5	4.5	3.826	0.197	0.0018
12042	100	58.22	11379.71	175.45	8.5	4.5	3.826	0.197	0.0018
12142	100	62.78	11425.45	175.45	8.5	4.5	3.826	0.197	0.0018
12242	100	67.33	11463.99	175.45	8.5	4.5	3.826	0.197	0.0018
12342	100	71.88	11495.10	175.45	8.5	4.5	3.826	0.197	0.0018
12442	100	76.43	11518.56	175.45	8.5	4.5	3.826	0.197	0.0018
12542	100	80.98	11534.24	175.45	8.5	4.5	3.826	0.197	0.0018
12642	100	85.54	11542.01	175.45	8.5	4.5	3.826	0.197	0.0018
13377	735	90	11542.01	175.46	8.5	4.5	3.826	0.197	0.0018
14144	767	90	11542.01	175.46	8.5	4.75	2.25	0.193	0.0018
14340	196	90	11542.01	175.46	8.5	5	2.25	0.19	0.0018

Fig 5.13. *Sheet 3 - Well Trajectory data*

	A	C	D
1	INFLOW PERFORMANCE RELATIONSHIP		
2		Flow Rate (STB/Day)	Pressure (psig)
3		0	4985
4		988	4735
5		1961	4485
6		2889	4235
7		3770	3985
8		4604	3735
9		5391	3485
10		6131	3235
11		6824	2985
12		7471	2735
13		8070	2485
14		8623	2235
15		9128	1985
16		9587	1735
17		9999	1485
18		10364	1235
19		10682	985
20		10953	735
21		11177	485
22		11354	235
23		11478	0

Fig 5.14. *Sheet 4 - IPR data*

The IPR data can be obtained from results solved by PERFORM 3.0.

5.2.2. Matlab program

The structure of this program now includes 7 procedures:

1. Inputdata_L
2. Modelling_L
3. Lower_L
4. QxQgsPwf_L
5. Right_Left_L
6. Results_L
7. Graphic_L

and a set of functions supplied to run these procedures. Before describing the role of each procedure, all following functions should be expressed.

Functions

All following functions are set up based on equations developed in chapter 3.

- *Gas compressibility factor (Z)*

$Z = CF(P, T, S_g)$

Compressibility factor is a function of pressure, temperature and gas gravity. It can be calculated by Eqs (3.20), (3.21), and (3.22).

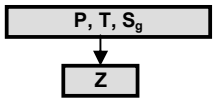

Fig 5.15. *Compressibility factor flowchart*

- *Solution gas ratio at bubble point pressure (R_{sb})*

$$R_{sb} = so\lg asb(P_b, T, S_g, API)$$

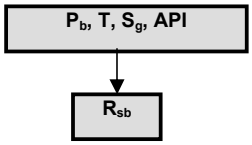

Fig 5.16. *Solution gas ratio at bubble point pressure flowchart*

- *Solution gas ratio (R_s)*

$$R_s = so\lg as(P, T, S_g, API, P_b)$$

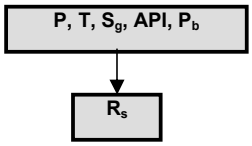

Fig 5.17. *Solution gas ratio flowchart*

- *Oil isothermal compressibility (C_o)*

$$C_o = oilcom(P, T, S_g, API, P_b)$$

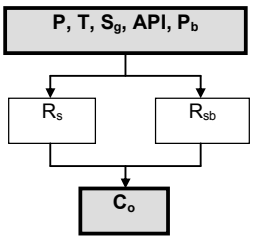

Fig 5.18. *Oil isothermal compressibility flowchart*

- *Gas formation volume factor (B_g)*

$$B_g = GFVF(P, T, S_g)$$

Gas formation volume factor can be given by Eq (3.19).

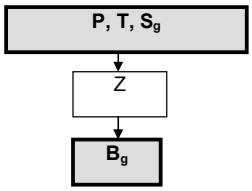

Fig 5.19. *Gas formation volume factor flowchart*

- *Oil formation volume factor at bubble point pressure (B_{ob})*

$$B_{ob} = OFVFb(P_b, T, S_g, API)$$

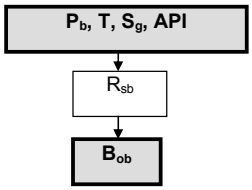

Fig 5.20. *Oil formation volume factor at bubble point pressure flowchart*

- *Oil formation volume factor (B_o)*

$$B_{ob} = OFVF(P, T, S_g, API, P_b)$$

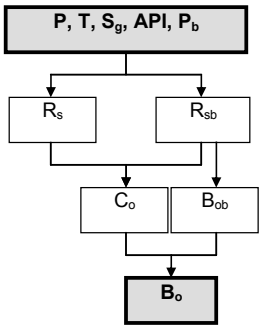

Fig 5.21. *Oil formation volume factor flowchart*

Oil formation volume factor is a function of specific gravity of gas S_g, API, gas solution ratio R_S, bubble point pressure P_b, and T.

- *Water formation volume factor (B_o)*

$$B_w = WFVF(P, T)$$

- *Drilling mud volume factor (B_x)*

$$B_x = MFVF(P, T, S, b, W, \mu)$$

Drilling mud volume factor calculated by Eq (3.25) is a function of pressure, temperature, water salinity (if drilling by sea water) or mud weight and mud viscosity (if drilling by mud), and optional variable (drilling by mud if b = 1 and drilling by sea water if b = 2).

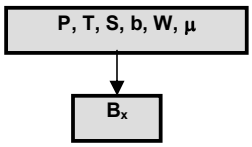

Fig 5.22. *Drilling mud volume factor flowchart*

- *Fluid formation volume factor (B_f)*

$$B_f = FFVF(P, T, S_g, API, P_b, a)$$

Formation fluid comes into the wellbore while UBD can be oil (a = 1) or water (a = 2).

- *Mud weight at the surface condition (W_{x0})*

$$W_{x0} = mudden0(P,T,S,b,W,\mu)$$

This function is given by Eq (3.9).

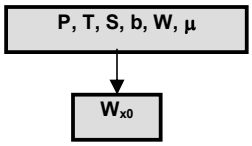

Fig 5.23. *Mud weight flowchart*

- *Mixture density in the annulus (ρ_m)*

$$\rho_m = mixden\_L\_O(P,T,S_g,API,P_b,d_b,S_s,R_b,Q_{gs},S_x,Q_x,P_{for},P_{wfe},\alpha,\beta,\chi,a,S,b,W,\mu)$$

Mixture density in the annulus is a complex function of pressure, temperature, other variables and given by Eq (3.29). The bottomhole pressure P_{wfe} in this function is a assumed variable and solved by iterative approach. The formation influx fluid Q_f which has the relationship to P_{wfe} through IPR is calculated from PERFORM 3.0.

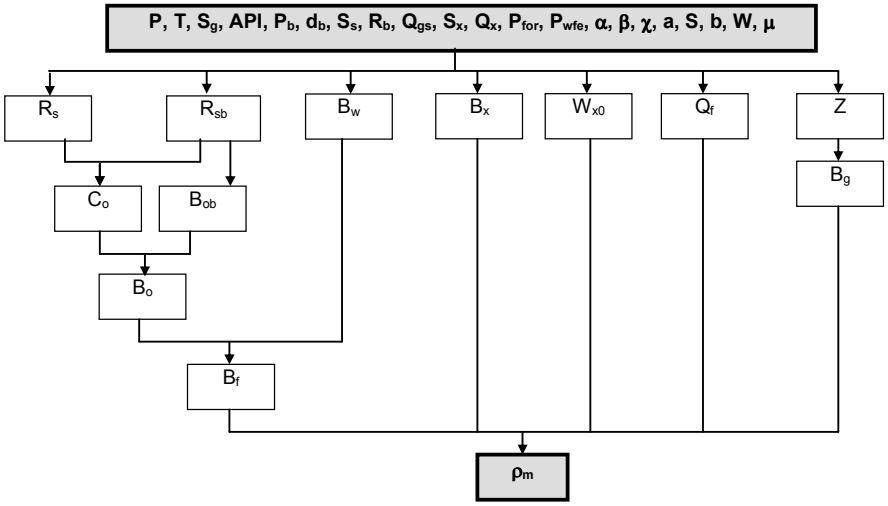

Fig 5.24. *Mixture density in the annulus flowchart*

- *Mixture density in the drillpipe (ρ_m)*

$$\rho_m = mixden\_L\_I(P,T,S_g,API,Q_{gs},S_x,Q_x,S,b,W,\mu)$$

Mixture density in the drillpipe does not depend on the influx fluid from the formation. So this function can be expressed by Eq (3.53).

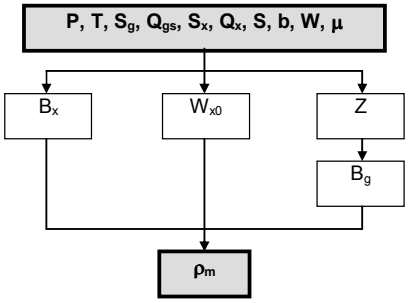

Fig 5.25. *Mixture density in the drillpipe flowchart*

- *Mixture velocity in the annulus (v_m)*

$$v_m = mixvel\_L\_O(P, T, S_g, API, P_b, Q_{gs}, Q_x, P_{for}, P_{wfe}, \alpha, \beta, \chi, d_{out}, d_{in}, a, S, b, W, \mu)$$

Mixture velocity in the annulus can be formulated by the Eq (3.30).

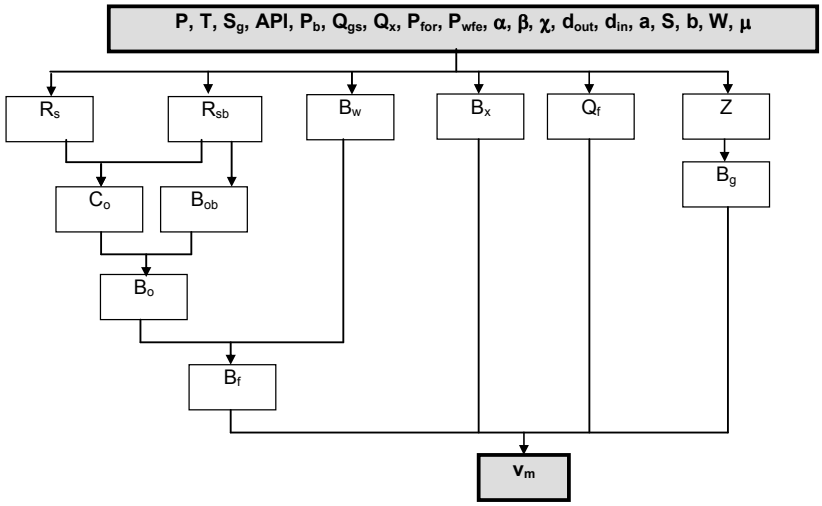

Fig 5.26. *Mixture velocity in the annulus flowchart*

- *Mixture velocity in the drillpipe (v_m)*

$$v_m = mixvel\_L\_I(P, T, S_g, Q_x, d_{in}, S, b, W, \mu)$$

Mixture velocity in the drillpipe can be calculated by the Eq (3.54).

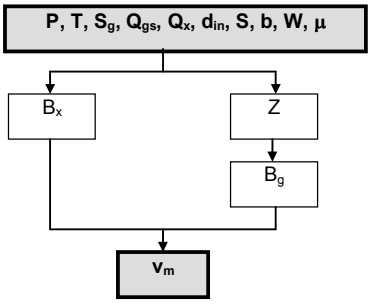

Fig 5.27. *Mixture velocity in the drillpipe flowchart*

- *Gas viscosity (ρ_g)*

$$\mu_g = gasvis(P, T, S_g)$$

Gas viscosity can be expressed by Eq (3.36) in chapter 3.

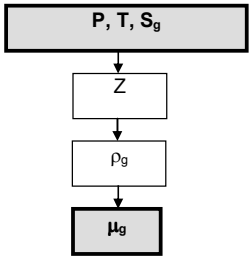

Fig 5.28. *Gas viscosity flowchart*

- *Oil viscosity at bubble point pressure (μ_{ob})*

$$\mu_{ob} = oilvisb(P_b, T, S_g, API)$$

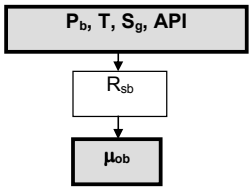

Fig 5.29. *Oil viscosity at bubble point pressure flowchart*

- *Oil viscosity (μ_o)*

$$\mu_o = oilvis(P, T, S_g, API, P_b)$$

The calculation of oil viscosity can be referred from Eqs (3.38) and (3.39).

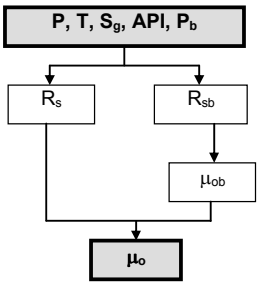

Fig 5.30. *Oil viscosity flowchart*

- *Water viscosity (μ_w)*

$$\mu_w = watvis(T)$$

- *Formation fluid viscosity (μ_f)*

$$\begin{cases} if\ a = 1 \ \ \mu_f = \mu_o \\ if\ a = 2 \ \ \mu_f = \mu_w \end{cases}$$

- *Mud viscosity (μ_x)*

$$\mu_x = mudvis(T, b, \mu)$$

This function can be determined by Eq (3.48).

- *Mixture viscosity in the annulus (μ_m)*

$$\mu_m = mixvis\_L\_O(P,T,S_g,API,P_b,Q_{gs},Q_x,P_{for},P_{wfe},\alpha,\beta,\chi,d_{out},d_{in},a,S,b,W,\mu)$$

The proceeding to calculate the function of mixture viscosity in the annulus can be carried out by the following flow chart which is referred from Eq (3.35).

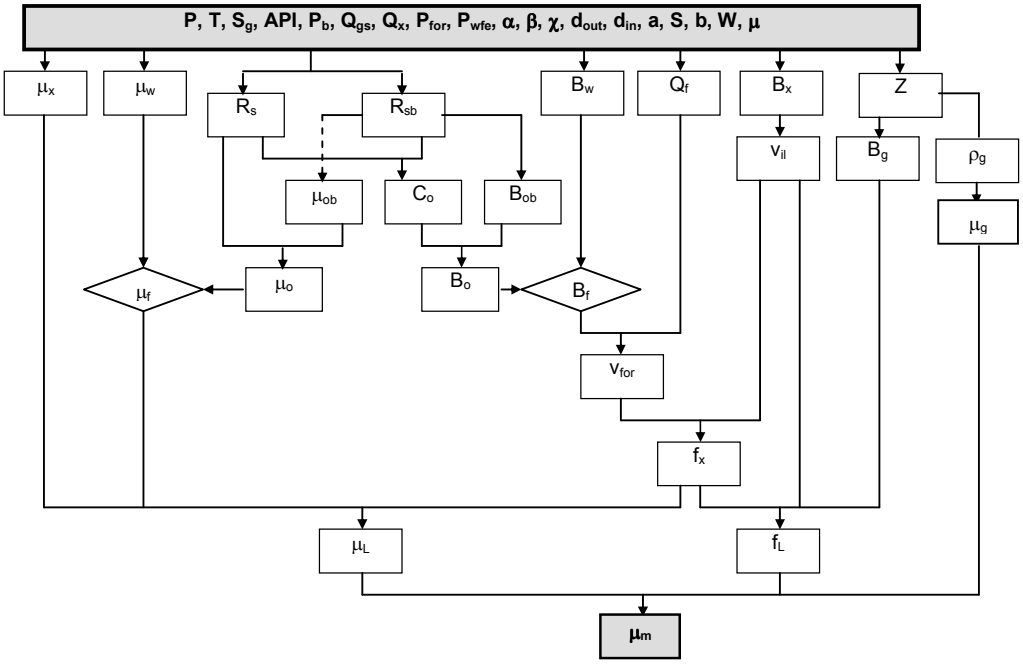

Fig 5.31. *Mixture viscosity in the annulus flowchart*

- *Mixture viscosity in the drillpipe (μ_m)*

$$\mu_m = mixvis\_L\_I(P,T,S_g,Q_{gs},Q_x,d_{in},S,b,W,\mu)$$

The calculation of mixture viscosity in the drillpipe can be referred from Eq (3.55).

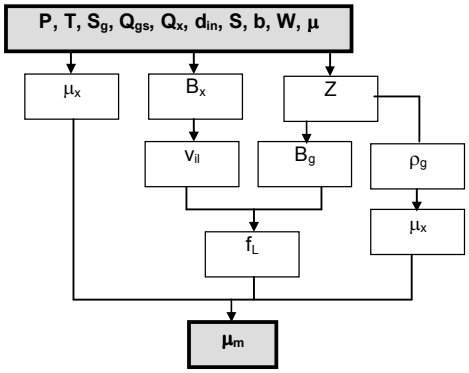

Fig 5.32. *Mixture viscosity in the drillpipe flowchart*

- *Reynolds number in the annulus (N_{Re})*

$$N_{\mathrm{Re}} = Reynolds\_L\_O(P,T,S_g,API,P_b,d_b,S_s,R_b,Q_{gs},Q_x,P_{for},P_{wfe},\alpha,\beta,\chi,d_{out},d_{in},a,S,b,W,\mu)$$

The Reynolds number of drilling fluid can be calculated by the Eq (3.34).

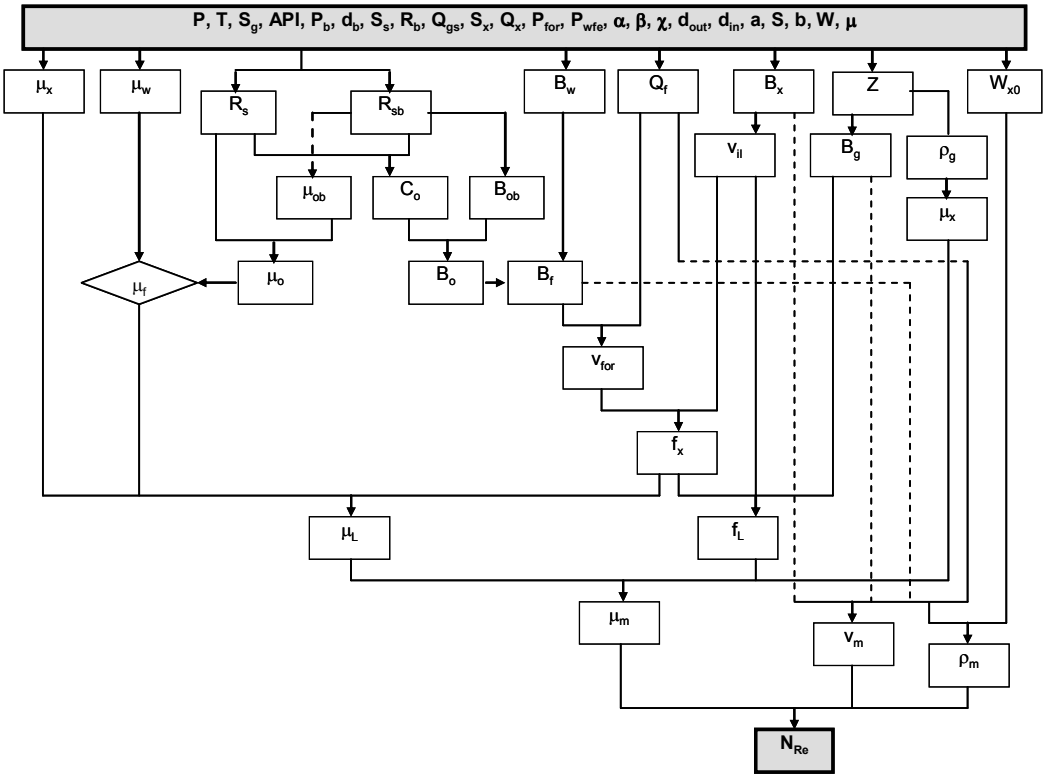

Fig 5.33. *Reynolds number in the annulus flowchart*

- *Reynolds number in the drillpipe (N_{Re})*

$$N_{\mathrm{Re}} = Reynolds\_L\_I(P,T,S_g,Q_{gs},S_x,Q_x,d_{in},S,b,W,\mu)$$

The calculation of the Reynolds number in the drillpipe can be referred from Eq (3.34) with $d_H = d_{in}$.

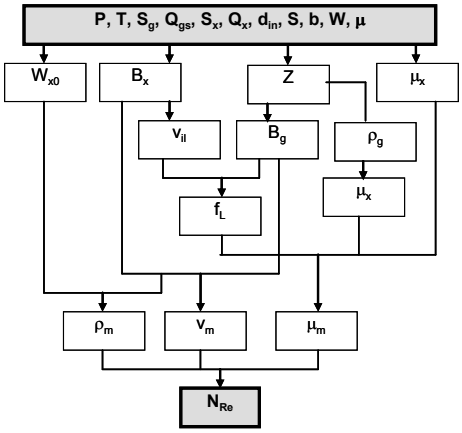

Fig 5.34. *Reynolds number in the drillpipe flowchart*

- *Friction factor in the annulus (N_{Re})*

$$f_m = fricfac\_L\_O(P,T,S_g,API,P_b,Q_{gs},S_x,Q_x,P_{for},P_{wfe},\alpha,\beta,\chi,d_{out},d_{in},a,rough,S,b,W,\mu)$$

Friction factor in the annulus is given by Eq (3.31) and (3.32).

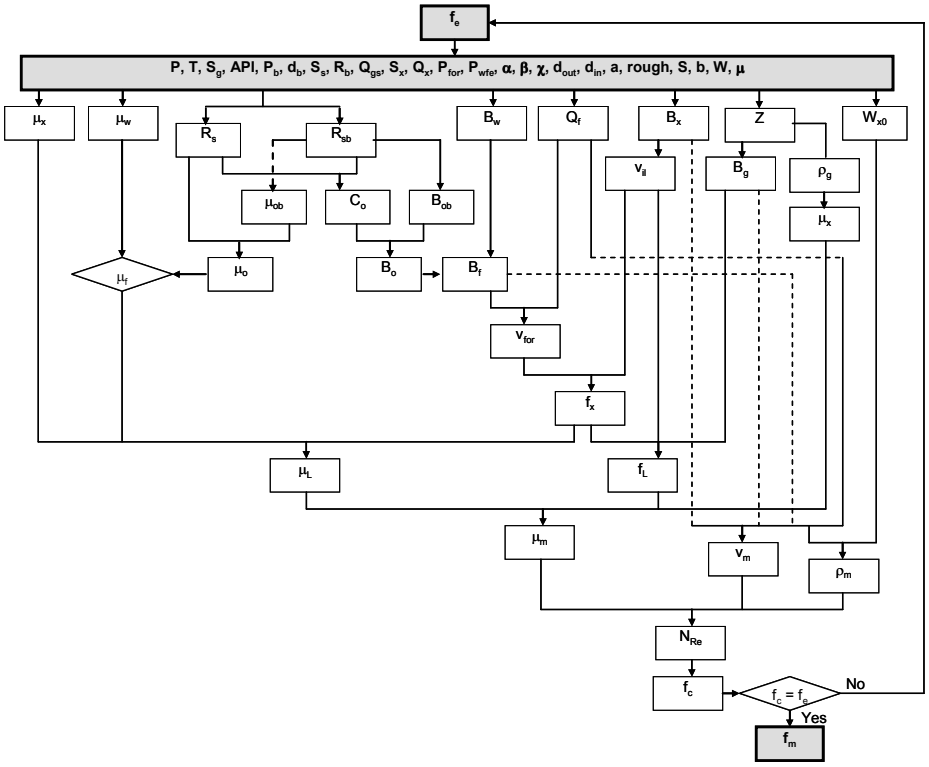

Fig 5.35. *Friction factor in the annulus flowchart*

- *Friction factor in the drillpipe (N_{Re})*

$$f_m = fricfac\_L\_I(P,T,S_g,Q_{gs},S_x,Q_x,d_{in},rough,S,b,W,\mu)$$

The calculation of the friction factor in the drillpipe can also be referred from Eq (3.31) and (3.32).

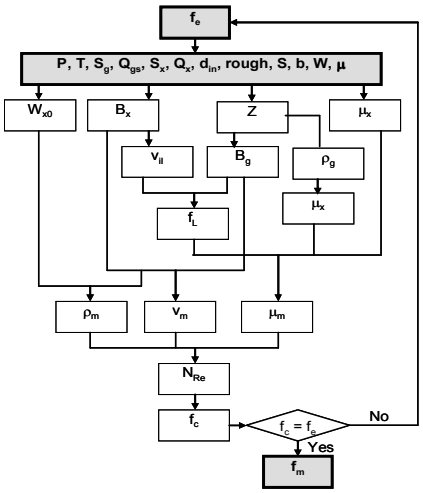

Fig 5.36. *Friction factor in the drillpipe flowchart*

- *Frictional pressure gradient in the annulus (dP/dL_f)*

$$\left(\frac{dP}{dL}\right)_f = friction\_L\_O(P,T,S_g,API,P_b,d_b,S_s,R_b,Q_{gs},S_x,Q_x,P_{for},P_{wfe},\alpha,\beta,\chi,d_{out},d_{in},a,rough,S,b,W,\mu)$$

Frictional pressure gradient in the annulus depends on mixture density, mixture velocity, and friction factor. It is shown by the following flowchart.

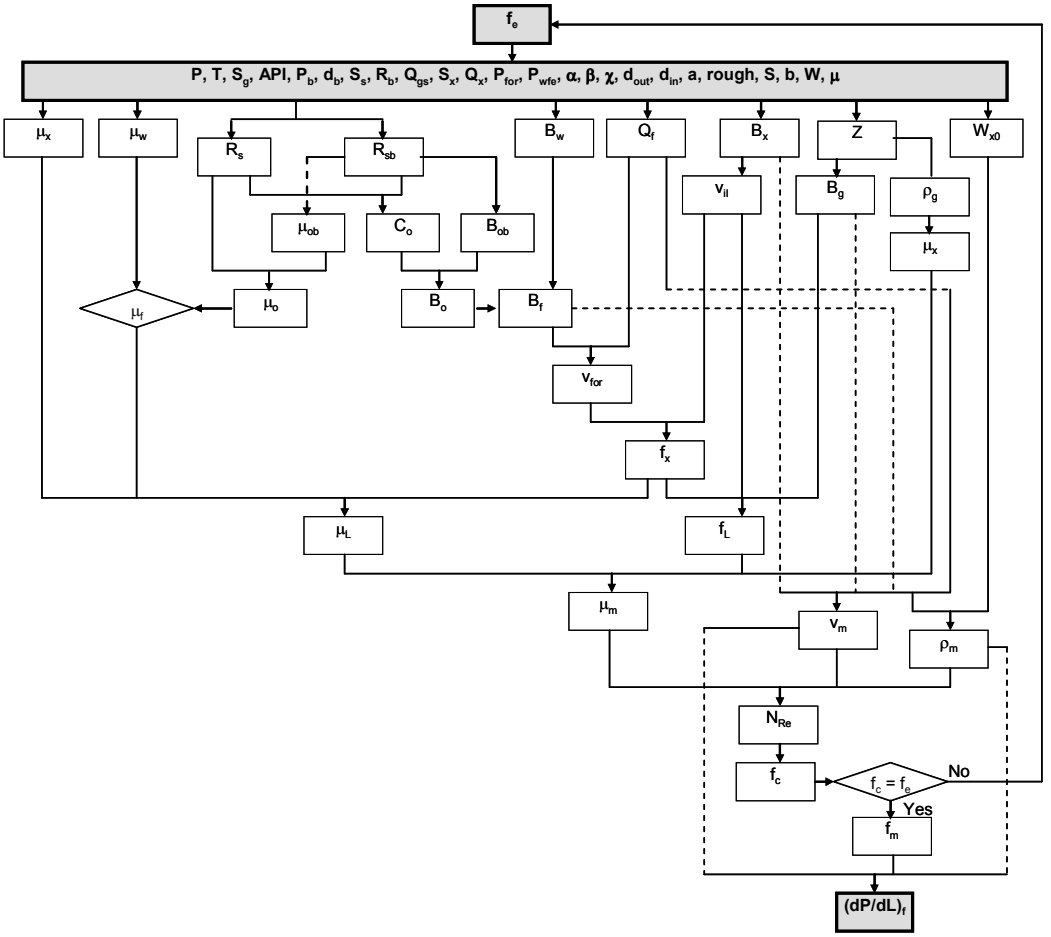

Fig 5.37. *Frictional pressure gradient in the annulus flowchart*

- *Frictional pressure gradient in the drillpipe (dP/dL_f)*

$$\left(\frac{dP}{dL}\right)_f = friction\_L\_I(P,T,S_g,Q_{gs},S_x,Q_x,d_{in},rough,S,b,W,\mu)$$

The flowchart of frictional pressure gradient in the drillpipe can be shown in Fig 5.38.

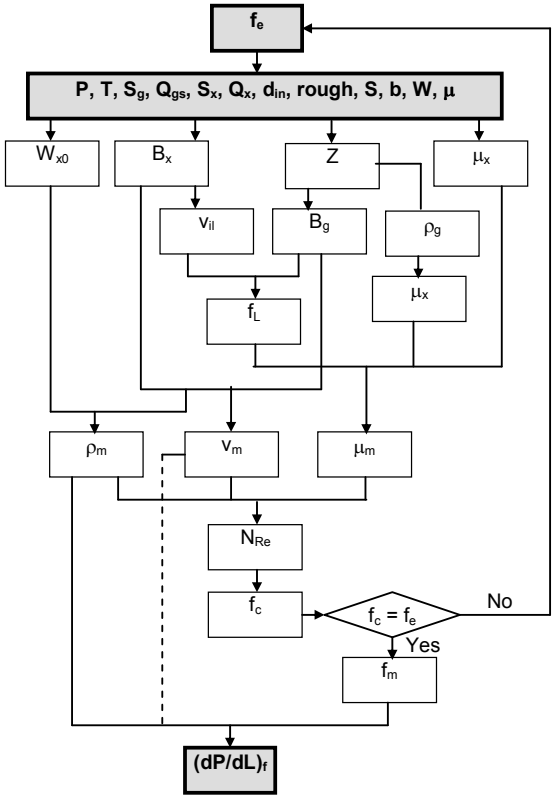

Fig 5.38. *Frictional pressure gradient in the drillpipe flow chart*

- *Hydrostatic pressure gradient in the annulus (dP/dL_{hyd})*

$$\left(\frac{dP}{dL}\right)_{hyd} = hydrostatic\_L\_O(P,T,S_g,API,P_b,d_b,S_s,R_b,Q_{gs},S_x,Q_x,P_{for},P_{wfe},\alpha,\beta,\chi,a,S,b,W,\mu)$$

Hydrostatic pressure in the annulus can be expressed in the following graph.

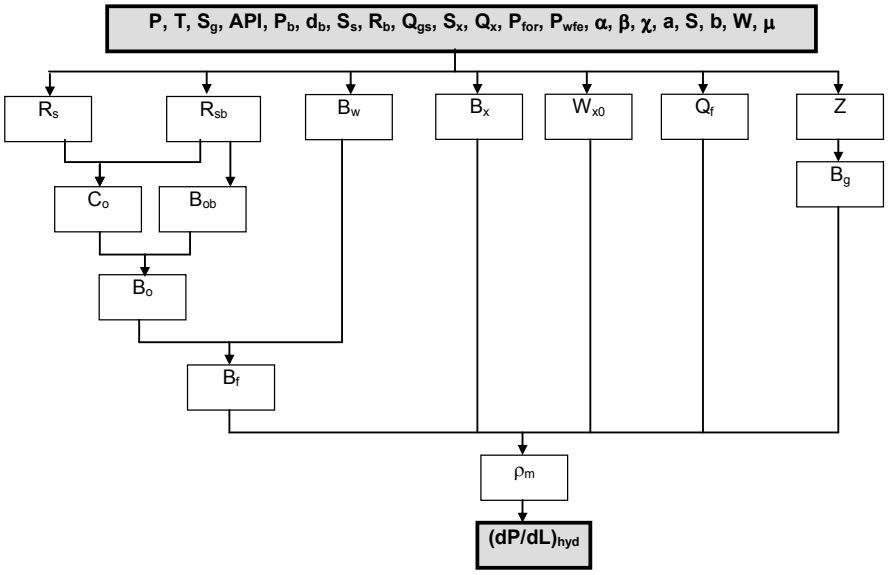

Fig 5.39. *Hydrostatic pressure gradient in the annulus flowchart*

- *Hydrostatic pressure gradient in the drillpipe (dP/dL_{hyd})*

$$\rho_m = mixden\_L\_I(P,T,S_g,API,Q_{gs},S_x,Q_x,S,b,W,\mu)$$

Hydrostatic pressure in the drillpipe can be expressed in the following graph.

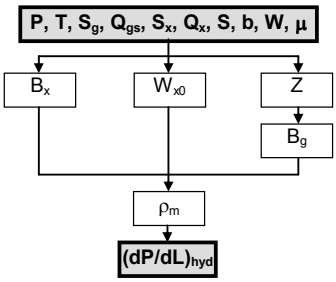

Fig 5.40. *Hydrostatic pressure gradient in the drillpipe flowchart*

- *Total pressure gradient in the annulus (dP/dL)*

$$\left(\frac{dP}{dL}\right) = presgra\_L\_O(P,T,S_g,API,P_b,d_b,S_s,R_b,Q_{gs},S_x,Q_x,P_{for},P_{wfe},\alpha,\beta,\chi,d_{out},d_{in},a,rough,S,b,W,\mu$$

Total pressure gradient is calculated by the Eq (3.4) and includes two parts, the first one is hydrostatic pressure and the last one is frictional pressure.

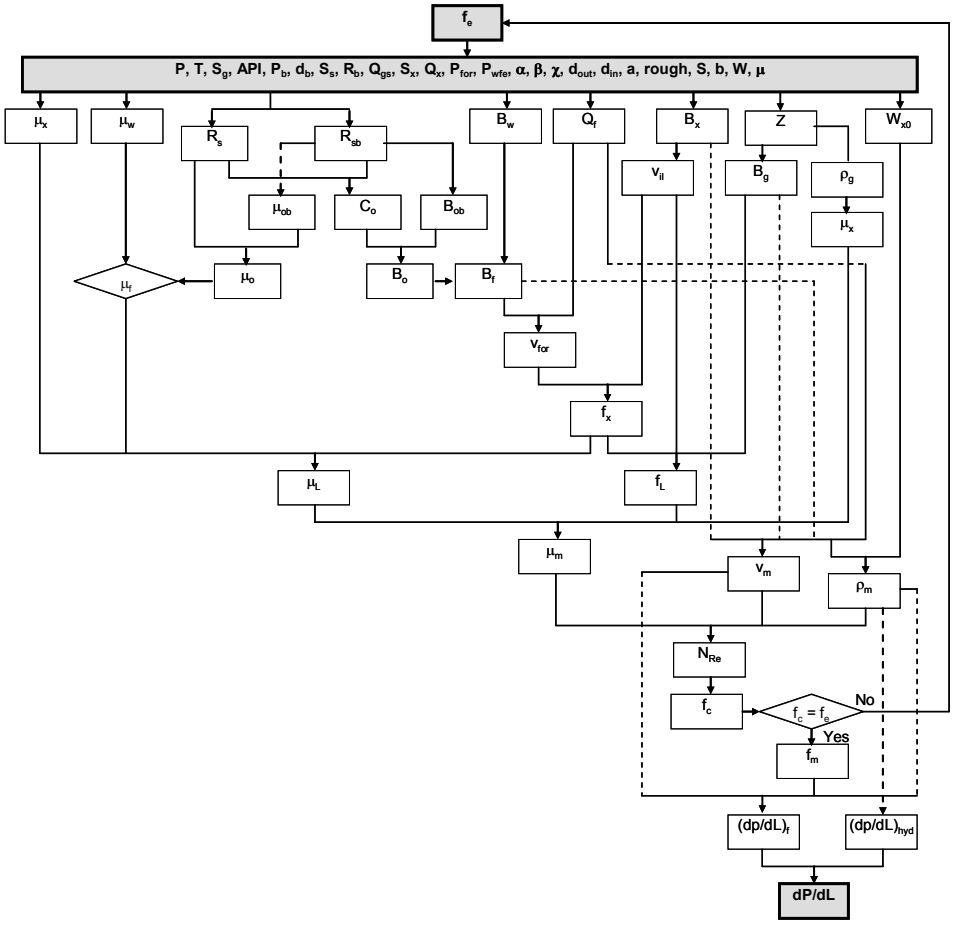

Fig 5.41. *Total pressure gradient in the annulus flowchart*

- *Total pressure gradient in the drillpipe (dP/dL)*

$$\left(\frac{dP}{dL}\right) = pregra\_L\_I(P,T,S_g,Q_{gs},S_x,Q_x,d_{in},rough,S,b,W,\mu)$$

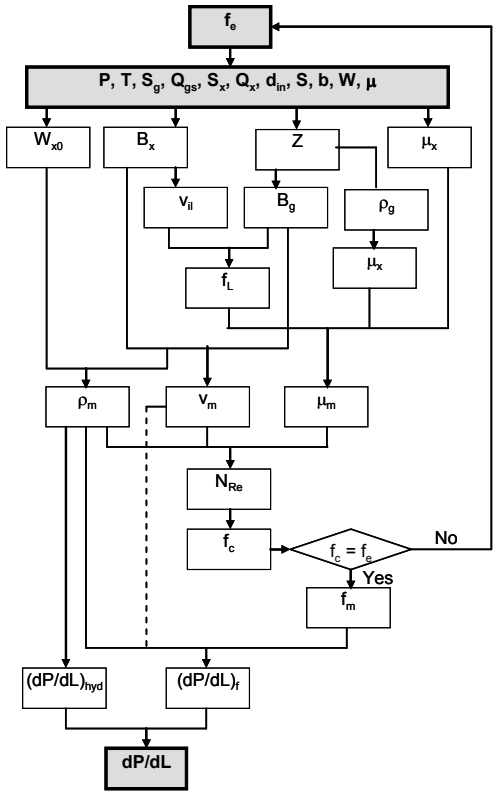

Fig 5.42. *Total pressure gradient in the drillpipe flowchart*

Procedures

The main program includes 7 procedures in which each procedure will use suitable functions above. The main program is expressed in the following structure:

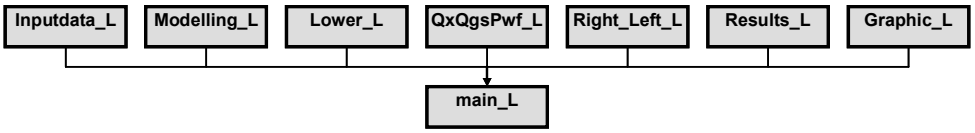

Fig 5.43. *Matlab program*

- *Inputdata_L*

This procedure reads and saves all input data such as drilling, PVT, well structure, IPR data from Excel files.

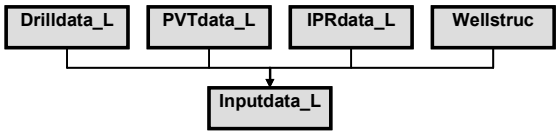

Fig 5.44. *Inputdata_L*

- *Modelling_L*

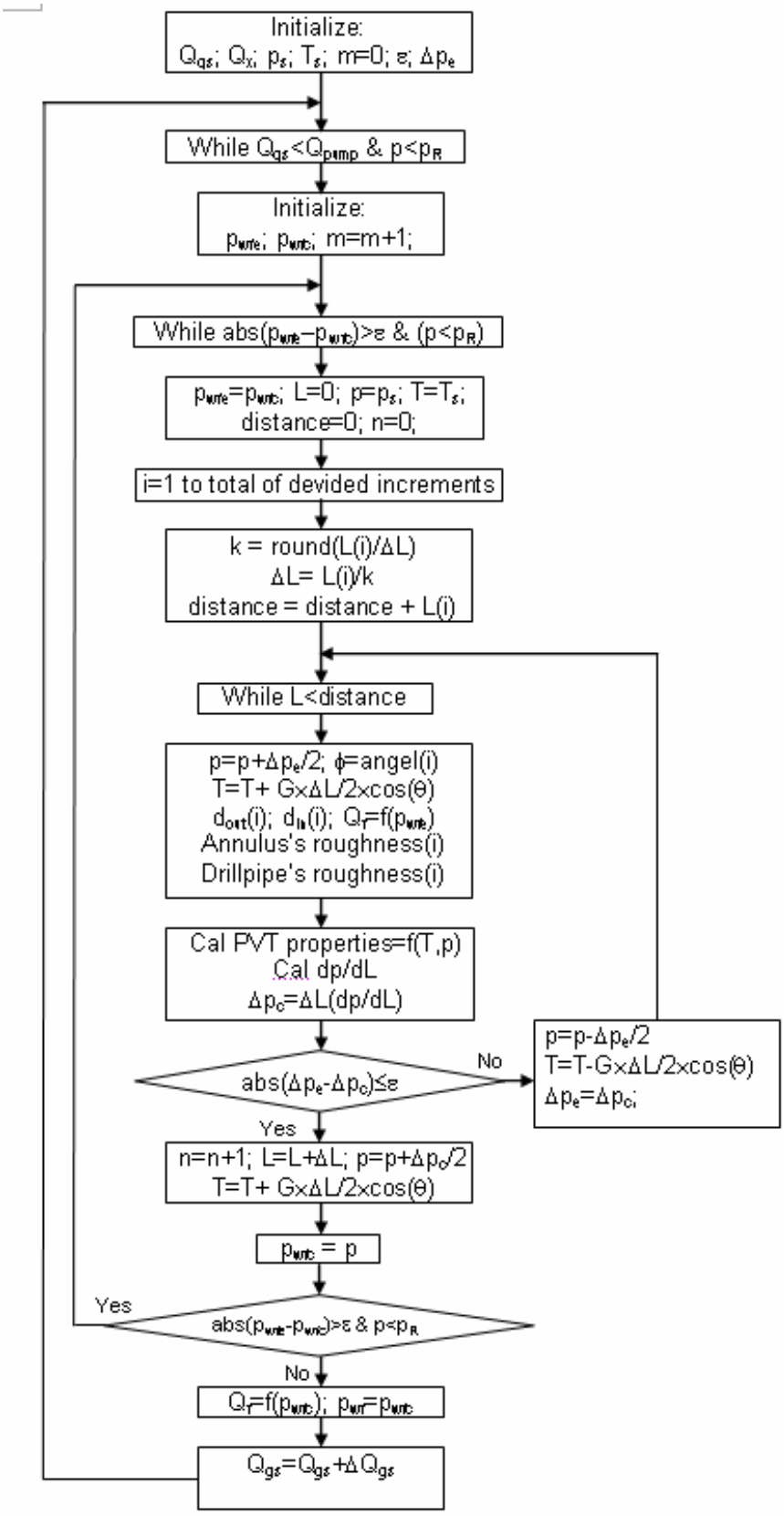

Fig 5.45. *Modelling_L*

Modelling_L establishes the relation between drilling fluid properties such as density, viscosity, velocity, temperature, and pressure corresponding with measured depths. Using this procedure, the length increments can be selected so that their sum is exactly equal to the total conduit length, and interpolation is not required in the last step. This method is always iterative even if temperature and inclination angle are constant, since fluid properties in an increment depend on the unknown pressure.

- *Lower_L*

This procedure was used to calculate the lower boundary of Liquid Gas Rate Window (LGRW). The details of LGRW will be presented in the next chapter.

- *QxQgsPwf_L*

One of the innovative ideas developed in this research is the fact that the formation fluid influx flow rate (Q_f) is not constant, and it depends on BHP (P_{wf}). So, this procedure will help to determine BHP in the static and dynamic condition, and formation fluid influx flow rate corresponding with the given liquid flow rate (Q_x) and gas injection rate (Q_{gs}).

- *Right_Left_L*

The right and left boundary of LGRW can be estimated by this procedure.

- *Results_L*

This procedure saves results solved by Matlab and exported to Excel files for using in other applications. These results include:

- The mixture velocity gradient versus measured depths in the annulus.
- The mixture velocity gradient versus measured depths in the drillpipe.
- The mixture density gradient versus measured depths in the annulus.
- The mixture density gradient versus measured depths in the drillpipe.
- The mixture viscosity gradient versus measured depths in the annulus.
- The mixture viscosity gradient versus measured depth in the drillpipe.
- The gas compressibility factor gradient versus measured depths in the annulus.
- The gas compressibility factor gradient versus measured depths in the drillpipe.
- The gas solution ratio gradient versus measured depths in the annulus.
- The formation fluid volume factor gradient versus measured depths in the annulus.
- The gas formation volume factor gradient versus measured depths in the annulus.

- The gas formation volume factor gradient versus measured depths in the drillpipe.
- The Reynolds number gradient versus measured depths in the annulus.
- The Reynolds number gradient versus measured depths in the drillpipe.
- The friction factor gradient versus measured depths in the annulus.
- The friction factor gradient versus measured depths in the drillpipe.
- The temperature gradient versus measured depths in the annulus.
- The temperature gradient versus measured depths in the drillpipe.
- The pressure gradient versus measured depths in the annulus.
- The pressure gradient versus measured depths in the drillpipe.
- The inflow performance relationship.
- Static bottom hole pressure versus given liquid and gas injection rates.
- Dynamic bottom hole pressure versus given liquid and gas injection rates.
- Formation fluid influx flow rates versus given liquid and gas injection rates.
- Lower boundary of LGRW.
- Right and left boundary of LGRW.

• *Graphic_L*

This plots all calculated output data.

5.2.3. Output data protocol

The output data file is an Excel file including result worksheets. This file is created by the procedure "*results_L*" of Matlab program. Some result worksheets are shown in the following pictures:

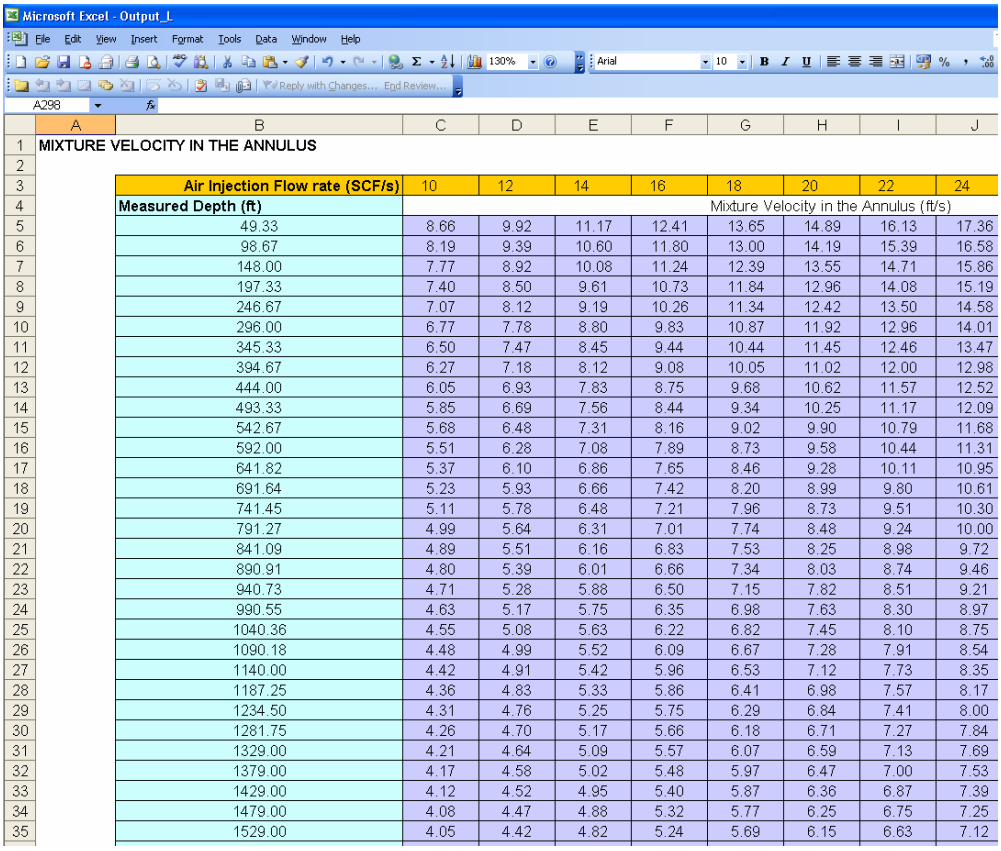

MIXTURE VELOCITY IN THE ANNULUS

Air Injection Flow rate (SCF/s)	10	12	14	16	18	20	22	24
Measured Depth (ft)	Mixture Velocity in the Annulus (ft/s)							
49.33	8.66	9.92	11.17	12.41	13.65	14.89	16.13	17.36
98.67	8.19	9.39	10.60	11.80	13.00	14.19	15.39	16.58
148.00	7.77	8.92	10.08	11.24	12.39	13.55	14.71	15.86
197.33	7.40	8.50	9.61	10.73	11.84	12.96	14.08	15.19
246.67	7.07	8.12	9.19	10.26	11.34	12.42	13.50	14.58
296.00	6.77	7.78	8.80	9.83	10.87	11.92	12.96	14.01
345.33	6.50	7.47	8.45	9.44	10.44	11.45	12.46	13.47
394.67	6.27	7.18	8.12	9.08	10.05	11.02	12.00	12.98
444.00	6.05	6.93	7.83	8.75	9.68	10.62	11.57	12.52
493.33	5.85	6.69	7.56	8.44	9.34	10.25	11.17	12.09
542.67	5.68	6.48	7.31	8.16	9.02	9.90	10.79	11.68
592.00	5.51	6.28	7.08	7.89	8.73	9.58	10.44	11.31
641.82	5.37	6.10	6.86	7.65	8.46	9.28	10.11	10.95
691.64	5.23	5.93	6.66	7.42	8.20	8.99	9.80	10.61
741.45	5.11	5.78	6.48	7.21	7.96	8.73	9.51	10.30
791.27	4.99	5.64	6.31	7.01	7.74	8.48	9.24	10.00
841.09	4.89	5.51	6.16	6.83	7.53	8.25	8.98	9.72
890.91	4.80	5.39	6.01	6.66	7.34	8.03	8.74	9.46
940.73	4.71	5.28	5.88	6.50	7.15	7.82	8.51	9.21
990.55	4.63	5.17	5.75	6.35	6.98	7.63	8.30	8.97
1040.36	4.55	5.08	5.63	6.22	6.82	7.45	8.10	8.75
1090.18	4.48	4.99	5.52	6.09	6.67	7.28	7.91	8.54
1140.00	4.42	4.91	5.42	5.96	6.53	7.12	7.73	8.35
1187.25	4.36	4.83	5.33	5.86	6.41	6.98	7.57	8.17
1234.50	4.31	4.76	5.25	5.75	6.29	6.84	7.41	8.00
1281.75	4.26	4.70	5.17	5.66	6.18	6.71	7.27	7.84
1329.00	4.21	4.64	5.09	5.57	6.07	6.59	7.13	7.69
1379.00	4.17	4.58	5.02	5.48	5.97	6.47	7.00	7.53
1429.00	4.12	4.52	4.95	5.40	5.87	6.36	6.87	7.39
1479.00	4.08	4.47	4.88	5.32	5.77	6.25	6.75	7.25
1529.00	4.05	4.42	4.82	5.24	5.69	6.15	6.63	7.12

Fig 5.46. *Mixture velocity in the annulus*

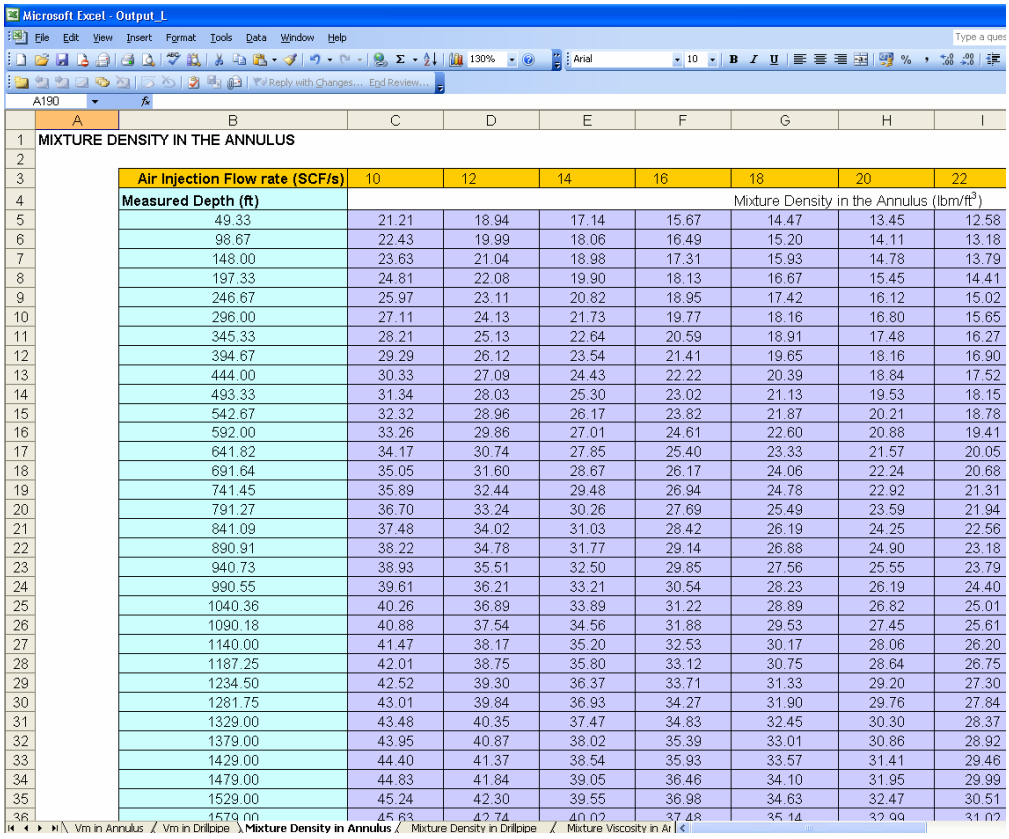

MIXTURE DENSITY IN THE ANNULUS

Air Injection Flow rate (SCF/s)	10	12	14	16	18	20	22
Measured Depth (ft)	Mixture Density in the Annulus (lbm/ft^3)						
49.33	21.21	18.94	17.14	15.67	14.47	13.45	12.58
98.67	22.43	19.99	18.06	16.49	15.20	14.11	13.18
148.00	23.63	21.04	18.98	17.31	15.93	14.78	13.79
197.33	24.81	22.08	19.90	18.13	16.67	15.45	14.41
246.67	25.97	23.11	20.82	18.95	17.42	16.12	15.02
296.00	27.11	24.13	21.73	19.77	18.16	16.80	15.65
345.33	28.21	25.13	22.64	20.59	18.91	17.48	16.27
394.67	29.29	26.12	23.54	21.41	19.65	18.16	16.90
444.00	30.33	27.09	24.43	22.22	20.39	18.84	17.52
493.33	31.34	28.03	25.30	23.02	21.13	19.53	18.15
542.67	32.32	28.96	26.17	23.82	21.87	20.21	18.78
592.00	33.26	29.86	27.01	24.61	22.60	20.88	19.41
641.82	34.17	30.74	27.85	25.40	23.33	21.57	20.05
691.64	35.05	31.60	28.67	26.17	24.06	22.24	20.68
741.45	35.89	32.44	29.48	26.94	24.78	22.92	21.31
791.27	36.70	33.24	30.26	27.69	25.49	23.59	21.94
841.09	37.48	34.02	31.03	28.42	26.19	24.25	22.56
890.91	38.22	34.78	31.77	29.14	26.88	24.90	23.18
940.73	38.93	35.51	32.50	29.85	27.56	25.55	23.79
990.55	39.61	36.21	33.21	30.54	28.23	26.19	24.40
1040.36	40.26	36.89	33.89	31.22	28.89	26.82	25.01
1090.18	40.88	37.54	34.56	31.88	29.53	27.45	25.61
1140.00	41.47	38.17	35.20	32.53	30.17	28.06	26.20
1187.25	42.01	38.75	35.80	33.12	30.75	28.64	26.75
1234.50	42.52	39.30	36.37	33.71	31.33	29.20	27.30
1281.75	43.01	39.84	36.93	34.27	31.90	29.76	27.84
1329.00	43.48	40.35	37.47	34.83	32.45	30.30	28.37
1379.00	43.95	40.87	38.02	35.39	33.01	30.86	28.92
1429.00	44.40	41.37	38.54	35.93	33.57	31.41	29.46
1479.00	44.83	41.84	39.05	36.46	34.10	31.95	29.99
1529.00	45.24	42.30	39.55	36.98	34.63	32.47	30.51
1579.00	45.63	42.74	40.02	37.48	35.14	32.99	31.02

Fig 5.47. *Mixture density in the annulus*

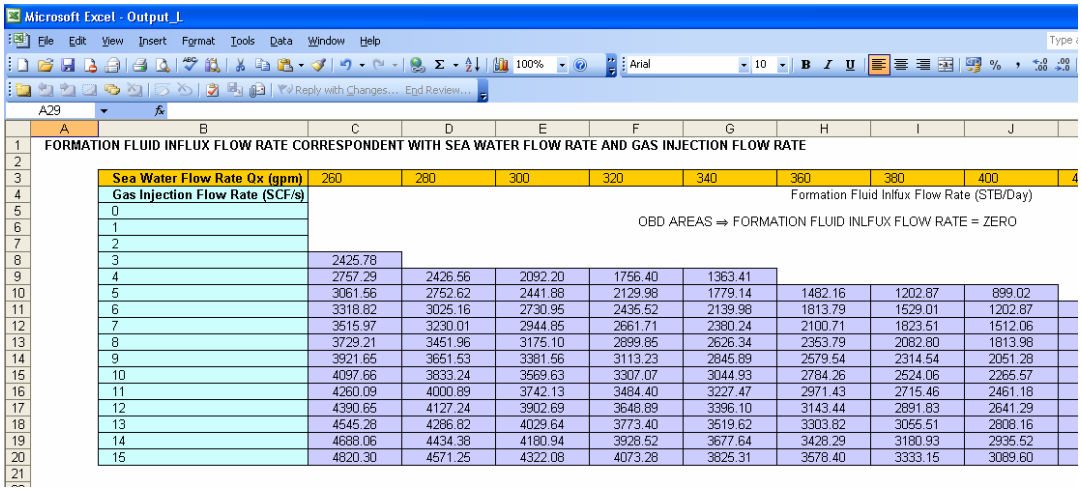

Microsoft Excel - Output_L

File Edit View Insert Format Tools Data Window Help

A29

FORMATION FLUID INFLUX FLOW RATE CORRESPONDENT WITH SEA WATER FLOW RATE AND GAS INJECTION FLOW RATE

Sea Water Flow Rate Qx (gpm)	260	280	300	320	340	360	380	400
Gas Injection Flow Rate (SCF/s)	Formation Fluid Influx Flow Rate (STB/Day)							
0	OBD AREAS ⇒ FORMATION FLUID INLFUX FLOW RATE = ZERO							
1								
2								
3	2425.78							
4	2757.29	2426.56	2092.20	1756.40	1363.41			
5	3061.56	2752.62	2441.88	2129.98	1779.14	1482.16	1202.87	899.02
6	3318.82	3025.16	2730.95	2435.52	2139.98	1813.79	1529.01	1202.87
7	3515.97	3230.01	2944.85	2661.71	2380.24	2100.71	1823.51	1512.06
8	3729.21	3451.96	3175.10	2899.85	2626.34	2353.79	2082.80	1813.98
9	3921.65	3651.53	3381.56	3113.23	2845.89	2579.54	2314.54	2051.28
10	4097.66	3833.24	3569.63	3307.07	3044.93	2784.26	2524.06	2265.57
11	4260.09	4000.89	3742.13	3484.40	3227.47	2971.43	2715.46	2461.18
12	4390.65	4127.24	3902.69	3648.89	3396.10	3143.44	2891.83	2641.29
13	4545.28	4286.82	4029.64	3773.40	3519.62	3303.82	3055.51	2808.16
14	4688.06	4434.38	4180.94	3928.52	3677.64	3428.29	3180.93	2935.52
15	4820.30	4571.25	4322.08	4073.28	3825.31	3578.40	3333.15	3089.60

Fig 5.48. *Formation fluid influx flow rate*

CHAPTER 6 - APPLICATION

The previous chapters presented equations and approaches related to UBD operation from evaluating the wellbore stability in UBD, calculating the hydraulics drilling in UBD, to coupling the productivity in UBD. This chapter will present these applications for granite basement reservoirs in Vietnam. So it will be divided into two parts: (1) wellbore stability evaluation in UBD, and (2) hydraulics drilling analysis in UBD. In each part, field data and experiment data will be used and the results solved by simulators developed in this research such as WELLST and UBDRILL will be analysed and compared to the results of commercial software.

6.1. Wellbore Stability Evaluation in UBD

6.1.1. ABAQUS - a commercial finite element software

Finite elements techniques [84] have proven to be reliable in areas such as mechanics and structure analysis. As a result of this success, researchers have turned their attention to use finite element theory in modelling geomechanical problems and recently in wellbore analysis. This research applies ABAQUS, a commercial finite element software developed by Hibbit, Karlsson, and Sorensen (2000) [85] to model wellbore stability in UBD. Then the results calculated by ABAQUS are compared to that of WELLST.

According to Starfield and Cundall [86], by comparing rock mechanics problems with other areas of mechanics such as aerospace or structural mechanics, rock mechanics falls into the class of problems dealing with limited amount of data. This leads to the question of why mathematical or computational models are considered viable tools to forecast the behaviour of rock in the absence of enough information. One of the reasons to think about computational modelling to simulate rock mechanic problems is accessibility to more versatile and powerful computer packages that have been successfully applied in other areas. As a consequence of this versatility, these computer packages have increased their ability to handle geological detail in construction of appropriate models. Easy access to high-performance computers provides to the modeller an important tool. Although the limited amount of geological data is a concern in modelling process, it is necessary to accept and recognize that to model the real wellbore, it should be necessary to construct a model with the same complexity as reality. An alternative to overcome this situation is simplifying the model by applying appropriate assumptions. [14]

As many of the researchers in wellbore stability mention, strictly there will always be a need to compare the model predictions against laboratory data and calibrate the model if possible. ABAQUS has been developed initially to study problems related to structural analysis. Because of its success, it has become a general purpose modelling software package. ABAQUS is equipped to handle different constitutive models to

represent material behaviour, and as such, it was chosen as the commercial finite element software to conduct this research.

Since ABAQUS is the general purpose finite element software, it allows considering different constitutive models. These models range from the purely elastic model, passing through models that take into account void ratio such as poroelasticity to complex models that incorporate plasticity. In order to analyze and compare rock behaviour with respect to the constitutive model, the following constitutive models elastic, poroelastic, and thermo-poroelastic were discussed. For the simplest case of elasticity, Young's modulus and Poisson's ratio are the required parameters. If a porous medium is considered, then in addition to the elastic parameters, the following parameters are required: bulk modulus of rock and fluid, shear modulus, average rock porosity and average rock permeability, densities of rock and fluid contained.

The linear form of the Mohr-Coulomb failure criterion with no intermediate principal stress effect is used in ABAQUS to forecast the failure of rock around the wellbore. The model assumes non-associated flow. Consequently, the material stiffness matrix is not symmetric. So the use of UNSYMM = YES on the *STEP option improves the convergence of the nonlinear solution significantly. The porous media is assumed saturated with oil.

The permeability in ABAQUS $\bar{k}$ (unit of LT^{-1}) is defined as the hydraulic conductivity of porous medium and a function of permeability k (Darcy or L^2), kinematic viscosity of the wetting liquid ν (the ratio of the liquid's dynamic viscosity to its mass density), and the magnitude of the gravitational acceleration g.

$$\bar{k} = \frac{g}{\nu} k \quad \text{----------} \quad (6.1)$$

So, if permeability is available in this form, it must be converted such that the appropriate values of k are used in ABAQUS. The problem is run in three steps. The first step of the analysis is defining the heat transfer to know the temperature distribution in the model. The second step is a geostatic step to establish the initial distribution of stress state, pore pressure, void ratio, and temperature. The last step of the analysis models the effect of pore pressure, and temperature to stress field around the wellbore in underbalanced drilling to wellbore stability. In this step, all factors such as thermal, pore pressure, stresses will be coupled and the results will be discussed.

6.1.2. WELLST

WELLST, a powerful tool presented in chapter 2, and 5 will be used to solve the 3D directional wellbore stability problem. The results solved by WELLST will be compared to the results of ABAQUS, and the model definition is common to both ABAQUS and WELLST. Mohr-Coulomb failure criteria will be applied to evaluate the wellbore stability.

6.1.3. Model Definition

Although the object of interest in this research is the basement formation, the clastic sections (overburden) has to be drilled through on the way to the basement target. Moreover, the wellbore instability often occurs in clastic sections (overburden) above the basement. Therefore, the investigation of wellbore stability are carried out for both formations, 12 ¼ clastic section and 8 ½ basement section. The well diagram is shown in Fig. 6.1. A 3D model (Fig 6.2) was used to predict the behaviour of rock formation surrounding a directional wellbore through the granite basement formation of Basin X. The cylindrical coordinate system can be set up with the origin at the center of the wellbore (Fig 6.3). Because the initial state of stress is altered over a distance of 5 to 7 times the wellbore radius, the radius of the model should be 1.5 m which is equivalent to 15 radii. However, to avoid the effect of boundary condition at the boundary radius position, the calculated area is divided into two parts. The outside circular region has the radius of 3 m, and the inside is 1.5 m. It will represent better the boundary conditions at infinity.

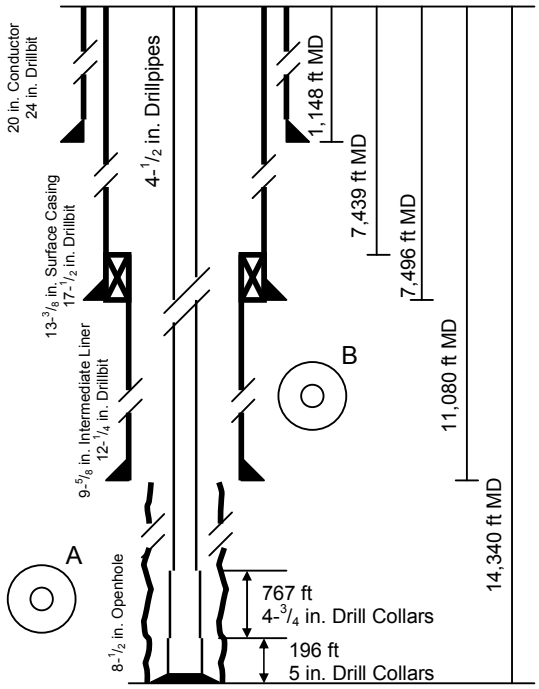

Fig 6.1. *Diagram of a typical well*

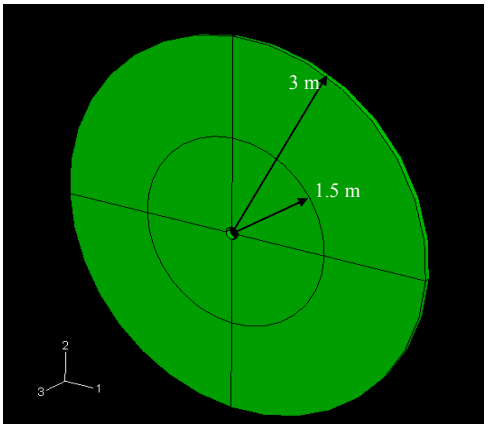

Fig 6.2. *3D - directional wellbore model*

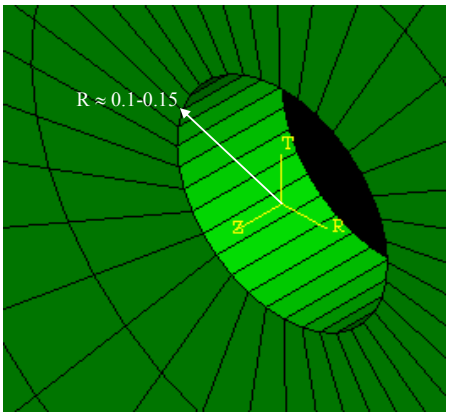

Fig 6.3. *Cylindrical coordinate system*

Based on the available geology overviews, literature and earlier studies, the clastic sections (overburden) above the basement have a very weak shale section in places, interbedded with grain supported rocks with strength varying from 13.2 MPa in high porosity sandstone to more than 103.3 MPa in strongly cemented sanstones and igneous (extrusive) formations (Fig 2.10). The previous computations suggest that shear breakout risk is present in the shale sections of the overburden. In the overburden section, the shales are very weak, have low modulus of elasticity, high Poisson's ratio, and little horizontal stress anisotropy. Because of this, the breakout risk is strongly dependent on wellbore deviation but only weakly dependent on well azimuth. In general, it would be increasingly difficult to drill stable boreholes at deviations over 30^o in the overburden sections but there are specific differences between the fields in the study area. This conclusion will be verified in chapter 6 when the wellbore inclination and azimuth variation effects on the wellbore stability are considered. It was found that mud weight, pore pressure, shale thickness, wellbore deviation and openhole exposure time are important factors for wellbore stability in the overburden, and they are all interdependent.

From the analysis of existing wells and drilling performances, wellbore instability problems in the overburden generally arise in relation with the following factors:

- Wellbore deviation (especially deviations over 30^o seem to carry increased risk). Azimuth is much less important.
- Overpressure (25 MPa).
- Thick shale sections.
- Exposure time of the open hole section.
- Insufficient attention for hole cleaning.

If only one of these problems in encountered, the resulting instability is probably manageable. If two or more of these problems occur however, the situation may become critical. It is therefore recommended to adopt the following general procedures for well and drilling design in the overburden:

- Keep wellbore deviation in this section below 30^o if it is possible. This is

especially important for overpressure and thick shale sections.

- Adapt mud weight to the circumstances, and base it on geomechanical models.
- Plan for an interactive real time stability management approach.
- Plan for contingency measures in case unexpected events happen and in particular if wellbore deviation has to exceed 30^o (contingency casing string, mud supplies).

In the basement, it was assumed that the Basin X is under compression in a strike-slip environment. This would make the overburden stress the intermediate stress. In this calculation, the vertical stress is approximate 85 MPa, maximum horizontal stress is 88 MPa, and minimum horizontal stress is 54 MPa. These data can be referred in Figs 2.5, and 2.6 of chapter 2. Unconfined compressive stress is from 68.9 to 275.6 MPa (see Figs 2.8, 2.9, and 2.10), and frictional angle of rock from 25 to 30 degree. All data of clastic and basement sections are tabulated in Table 6.1.

Table 6.1. *Input data*

Parameters	**Clastic**	**Basement**	**Units**	**Notes**
Young 's modulus (E)	19,872 - 44,712	42,811 - 96,323	MPa	Obtained from 2.3.3 chapter 2
Poison ratio (ν)	0.28	0.28		
Rock density	2600	2800	kg/m^3	
UCS	13.2 – 103.3	68.9 – 275.6	MPa	Obtained from 2.3.3 chapter 2
Cohesion of material (c)	4.20 – 32.90	20.69 – 93.14	MPa	Eq (2.60)
Frictional angle (ϕ)	25 - 30	25 - 30	Degree	
Maximum horizontal stress (σ_H)	43.91	88	MPa	Fig 2.6
Minimum horizontal stress (σ_h)	38.23	54	MPa	Fig 2.6
Vertical stress (σ_V)	56.54	85	MPa	Fig 2.6
Fluid compressibility (C_f)	7.90E-04	7.90E-04	1/MPa	
Void ratio	0.50	0.45		
Oil density	828.4	828.4	kg/m^3	API = 39.3
Fluid thermal expansion coefficient (α_f)	9.00E-04	9.00E-04	$1/^oC$	
Drained thermal expansion coefficient (α_B)	12.5E-06	8.50E-06		
Specific heat of rock (C_ε)	750	750	$J/kg.^oC$	
Permeability (k)	0.0001	0.0005	Darcy	
Oil Viscosity (μ_o)	1	0.5	cp	
Thermal conductivity (κ)	5	5	$W/m.^oC$	
Reservoir Temperature (T_R)	110	131	^oC	
Wellbore Temperature (T_{wf})	85	98	^oC	
Reservoir Pressure (P_R)	25.02	34.45	MPa	
Wellbore Pressure (P_{wf})	19.58	32.34	MPa	
Wellbore Radius (R_w)	0.156	0.108	m	
Boundary Radius (R_e)	1.5	1.5	m	
Number of increments	70	70		Number of elements along the radial direction
Dilation angle (ψ)	0	0	Degree	Nonassociated flow
Biot elastic constraint	1	1		

6.1.4. Results and discussions

Mesh refinement

The analysis assumes a plane stress condition for a vertical well with input data referred from 6.1.3. The mesh will be kept constant (5 elements along the path) at the outside area because only the inside area around the wellbore is interested in the modelling of wellbore stability (Fig 6.4).

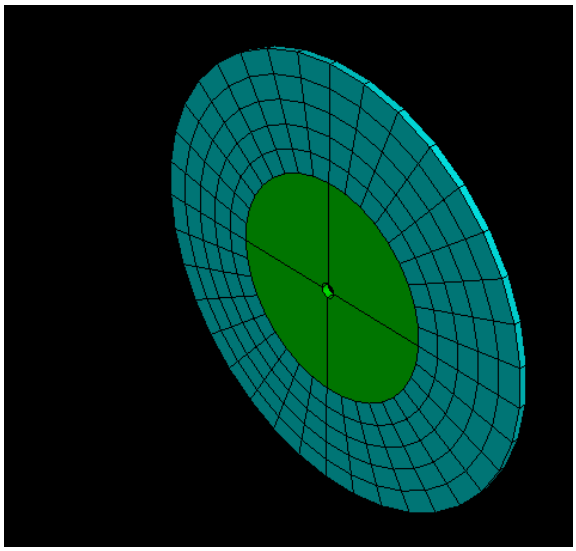

Fig 6.4. *The inside area*

Figs 6.5 and 6.6 show the radial stress and tangential stress as a function of distance from the wellbore varying with the number (N) of spaced quadratic elements along the path stress direction of the inside circular region (see stress path in Fig 6.7).

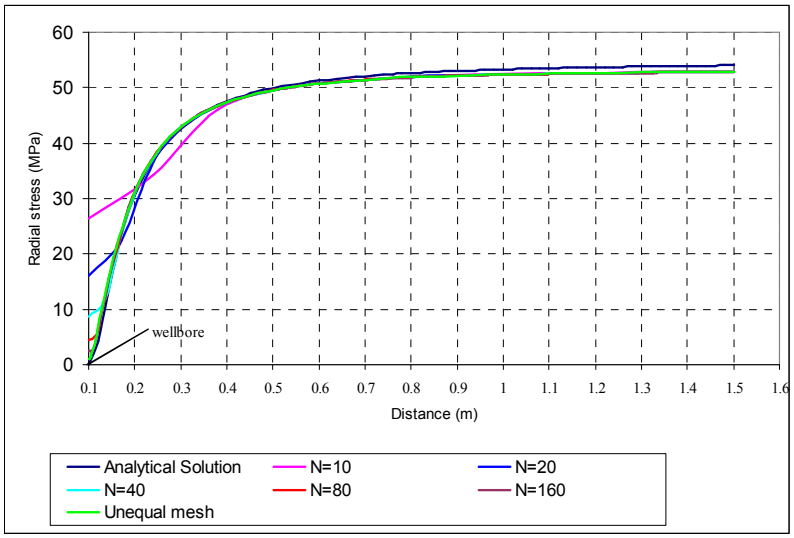

Fig 6.5. *Effect of mesh refinement on the accuracy of radial stress calculations*

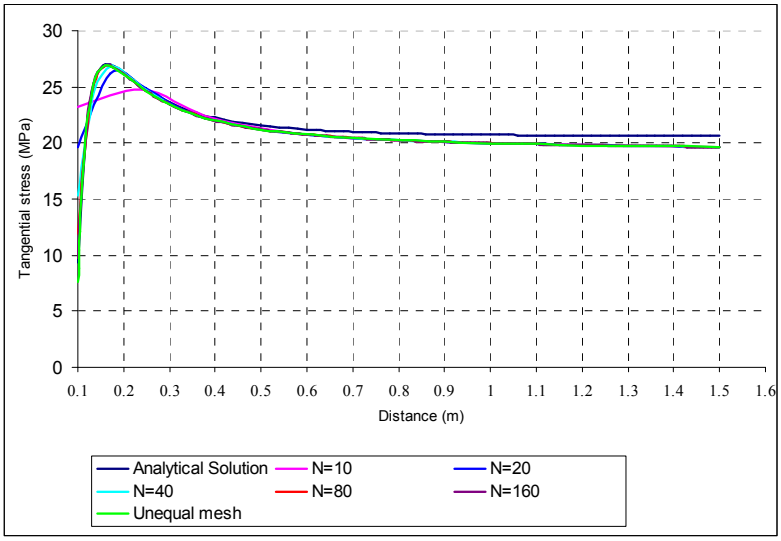

Fig 6.6. *Effect of mesh refinement on the accuracy of tangential stress calculations*

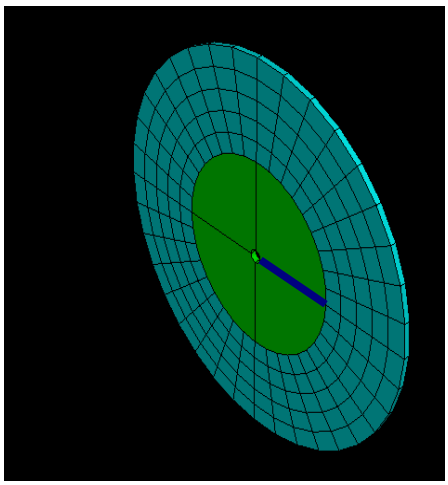

Fig 6.7. *The stress path*

It can be seen that the accuracy of the results approaches the analytical solution as N increases from 10 to 160 elements toward the radial direction (Figs 6.5, and 6.6). These plots show that accuracy of the result is highly sensitive to mesh size in the stress path direction. The relationship between the size of the element nearest the wellbore and the number of elements in the stress path direction (N) is as follows: element size = 0.15 m for N = 10, element size = 0.075 m for N = 20, element size = 0.0375 m for N = 40, element size = 0.01875 m for N = 80, and element size = 0.009375 m for N = 160. The results from Figs 6.4, and 6.5 show that when the number of elements along the stress path increases from 10 to 160, the effective radial stress at the wellbore reduces from 26.37 MPa to 2.57 MPa. So if the mesh size is continued to increase, the better results can be obtained. However, because of the limitation of the computer capacity, the maximum number of elements calculated in this case is 20,000. This result (2.57 MPa) is still quite far from the exact result solved by analytical solution (0 MPa). That is why in order to improve the accuracy of the results in the nearest region to the wellbore; a denser concentration of "unequally spaced" quadratic elements (Figs 6.5, and 6.6) with the size of the nearest wellbore element 0.00138 m was applied instead of "equally

spaced" quadratic elements. And the final solution obtained from the denser mesh near the wellbore has given the better result. These results show that the size of the element nearest the wellbore must be equal or smaller than 0.00138 m to obtain the acceptable result. Fig 6.5 & 6.6 also show that the initial state of stress is altered over a distance of 5 to 7 times the wellbore radius. Beyond this zone, the solution tends to the initial conditions.

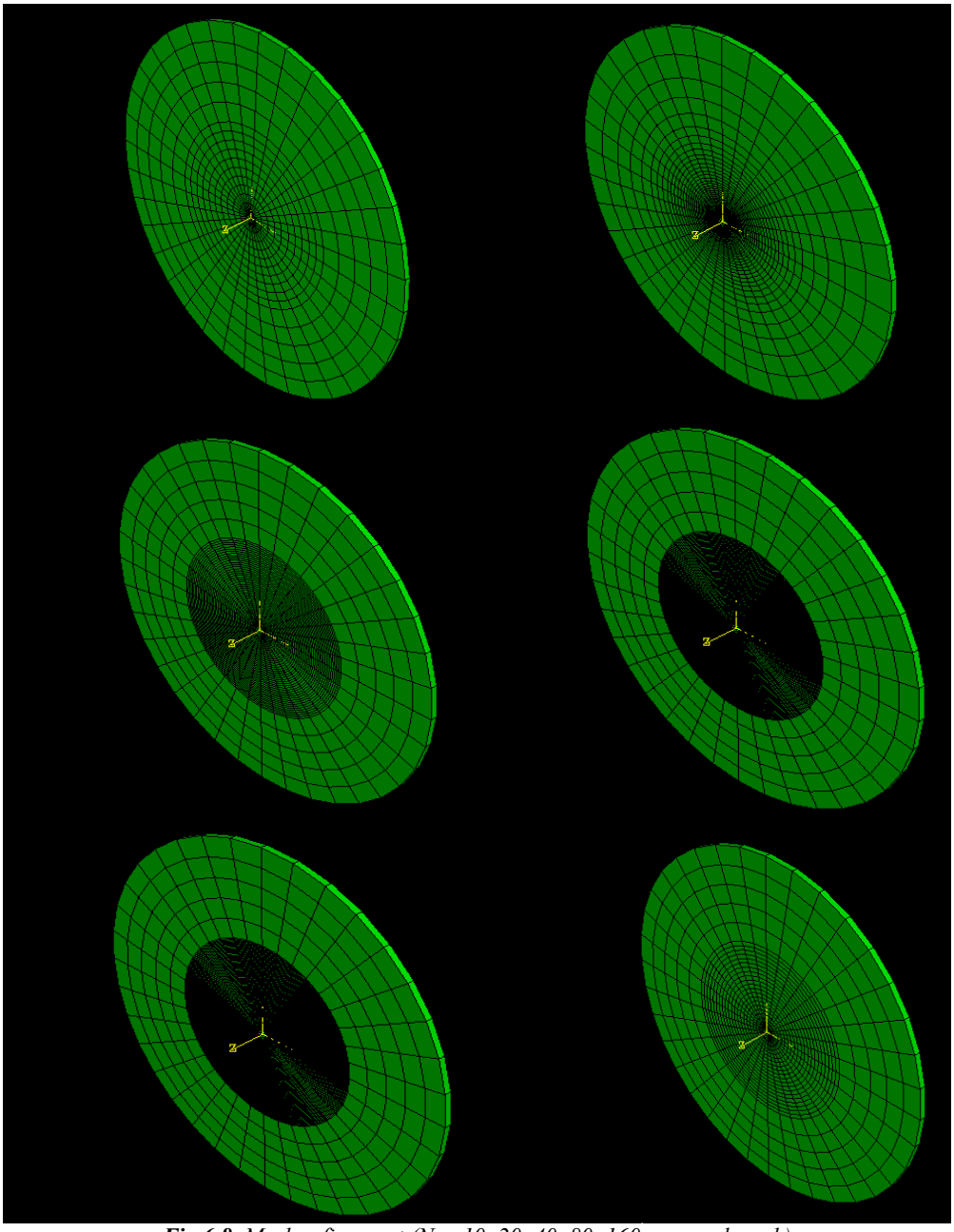

Fig 6.8. *Mesh refinement (N = 10, 20, 40, 80, 160, unequal mesh)*

Time dependent effect

The magnitude of pore pressure has a significant impact on wellbore stability. In general, high pore pressures will lead to wellbore instability, the reducing of pore pressure after the period of drilling or production operation will result in stabilization of

the wellbore. The results solved by WELLST showed that pore pressure profiles have the trend of decrease after the certain exposure drilling time. Fig 6.9 displays the pore pressure conditions as a function of distance from the wellbore for different exposure times. An original wellbore pressure 32.34 MPa lower than the formation pressure 34.45 MPa in UBD operation was assumed. As calculated by WELLST, the pore pressure at a distance 0.5 m from the wellbore drops quickly to 33.56 MPa (after 10 seconds), 32.71 MPa (after 10 minutes), 32.53 MPa (after 1 hour), 32.42 MPa (after 5 hours), and 32.39 (after 10 hours).

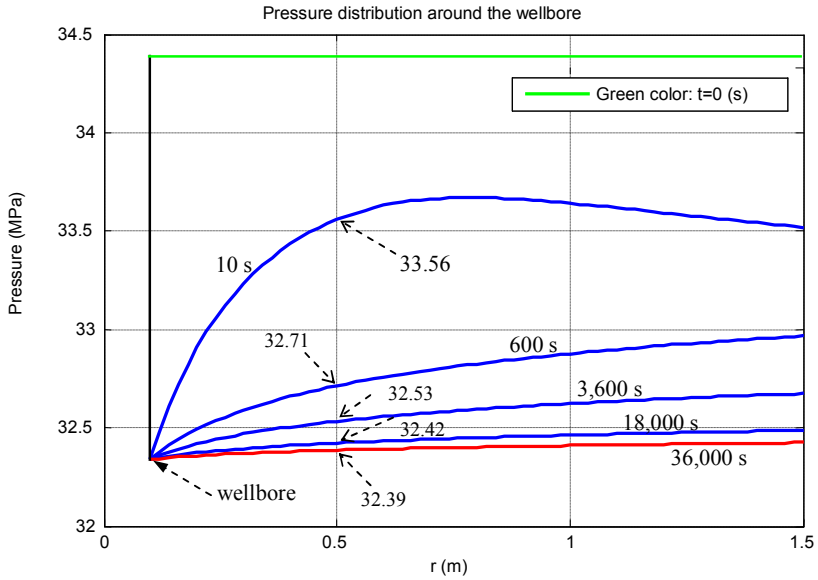

Fig 6.9. *Time dependent pressure profiles*

It can be considered the ratio of pressure reduction with time as the percentage of pressure reduction at a given point and the pressure difference of formation pressure and wellbore pressure. I_P varies from 0 (equivalent to the initial time when the pore pressure is equal formation pressure everywhere in the reservoir) to 1 (when equilibrium is approached and pore pressure around the wellbore is equal to the wellbore pressure).

$$I_P = \frac{P_R - P(r,t)}{P_R - P_{wf}} \quad \text{----------} \quad (6.1)$$

The following figure shows the propagation of pressure into the formation in UBD. After drilling, the wellbore pressure immediately reduced from the initial condition pressure P_R to P_{wf} and the equilibrium was set up after 10 hours (36,000 s). The propagation speed of pressure happens quickly in a short time (0 - 600 s) and slower after that when the equilibrium is nearly established (600 - 36,000 s).

As with the pressure, the temperature also changes with time because of the heat transfer around the wellbore. Although the temperature propagation into the formation is often slower than pressure propagation, the time dependent temperature has influenced particularly to transient stress. The transient temperature profiles are shown in Fig 6.11.

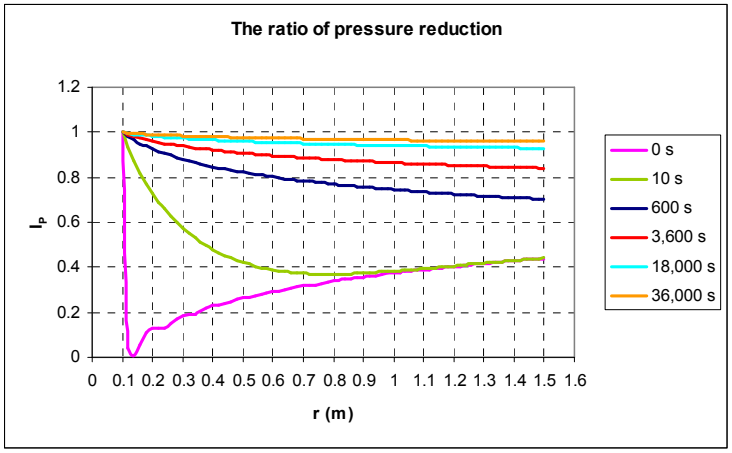

Fig 6.10. *Pressure propagation*

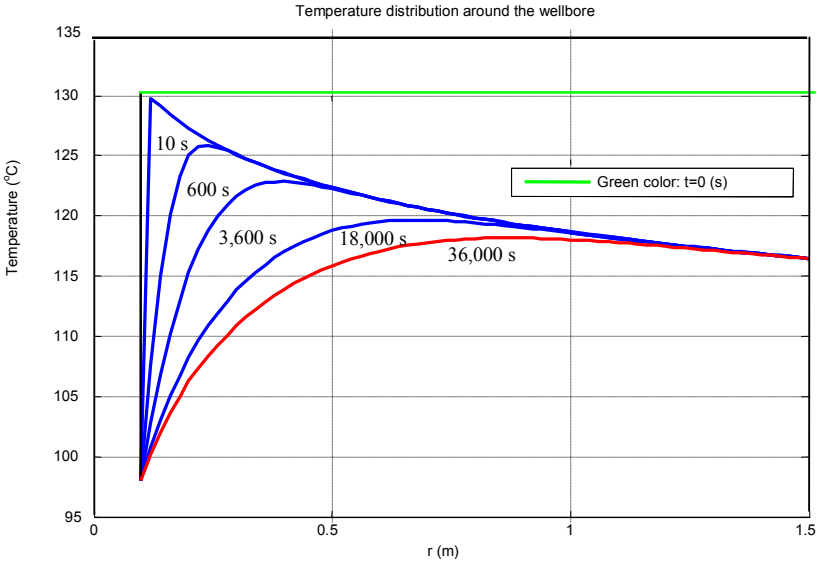

Fig 6.11. *Time dependent temperature profiles*

If considering the varying of temperature with time as the dimensionless ratio,

$$I_T = \frac{T_R - T(r,t)}{T_R - T_w} \qquad \text{----------(6.2)}$$

in which $I_T = 0$ (initial time), and $I_T = 1$ (equilibrium state), the following figure shows the propagation of temperature into the formation.

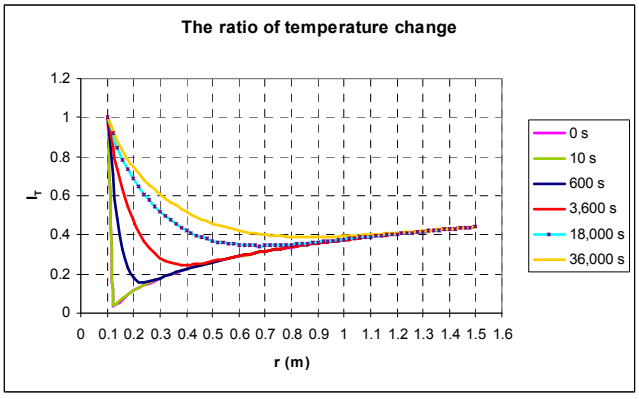

Fig 6.12. *Temperature propagation*

The temperature propagation in comparison to pressure propagation is quite slow. It does not change significantly 10 s after drilling and the temperature equilibrium state around the wellbore is not approached after 10 hours. The propagation of pressure and temperature can be compared by plotting the results of I_P and I_T in the same plot:

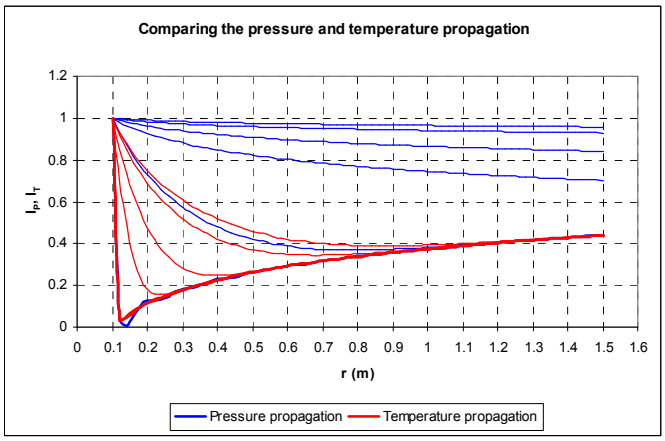

Fig 6.13. *Comparing the pressure and temperature propagation*

The observation from Fig 6.13 shows clearly that progression of thermal front is slower than that of hydraulic front. This can be verified again in the next section "hydraulic and thermal diffusivity effects". The input data for plotting Figs 6.9 to 6.13 is obtained from the basement section and can be referred in table 1, appendix A.

The reduction of pore pressure and temperature from the wellbore to a certain distance (1.5 m) happens whenever the temperature/pressure coupling is taken into account the calculation of hydraulics and thermal diffusivity. This trend can be explain mathematically by Eqs (2.32) and (2.33) of Charlez.

Time dependent effect has not only influenced to pore pressure but also to stress condition. Whenever pore pressure changes with time, the stress distribution around the wellbore changes as well. The formation around the wellbore is considered to be a porous medium saturated with pore fluid. The effect of the pore should be considered in analyzing the behaviour of the rock around the wellbore. For this purpose, the concept of effective stress was introduced and is defined as the overall effects of normal stresses and pore pressure. Pore pressure changes will contribute to the state of effective stresses by two mechanism, redistribution of the pressure profile due to transient regime of pore pressure, and additional stresses on the matrix due to the effect of coupling pore pressure into the calculating stress distribution for poroelastic formation.

In general, the pore pressure around the wellbore will decrease with the time as presented in Fig 6.9. This will lead to the fact that effective stress at a point at given time will be higher than the effective stress value at the time before. This means that the maximum and minimum effective principal stresses are increased with the same amount of pore pressure decreasing.

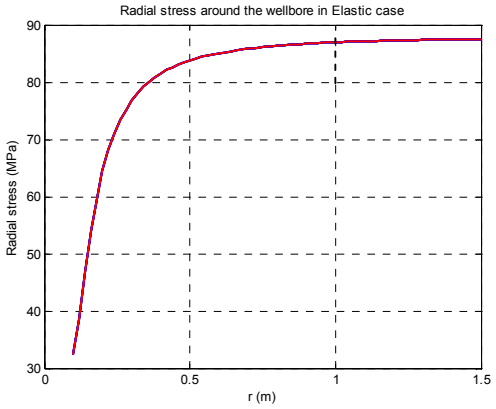

Fig 6.14. *Transient radial stresses*

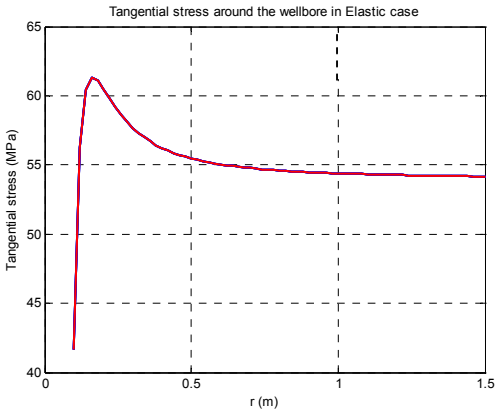

Fig 6.15. *Transient tangential stresses*

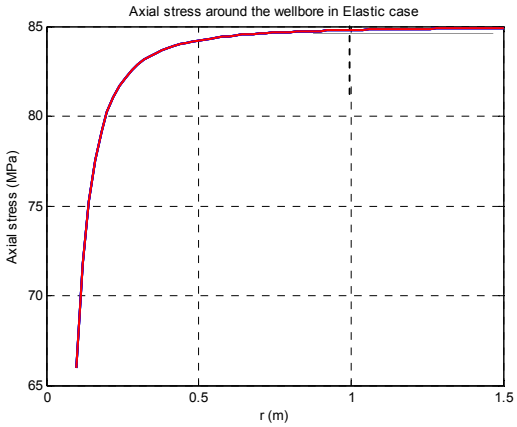

Fig 6.16. *Transient axial stresses*

The above stresses are calculated in elastic case when the transient pore pressure and temperature have not influenced to stress distribution around the wellbore so the state of stress in the difference time is the same.

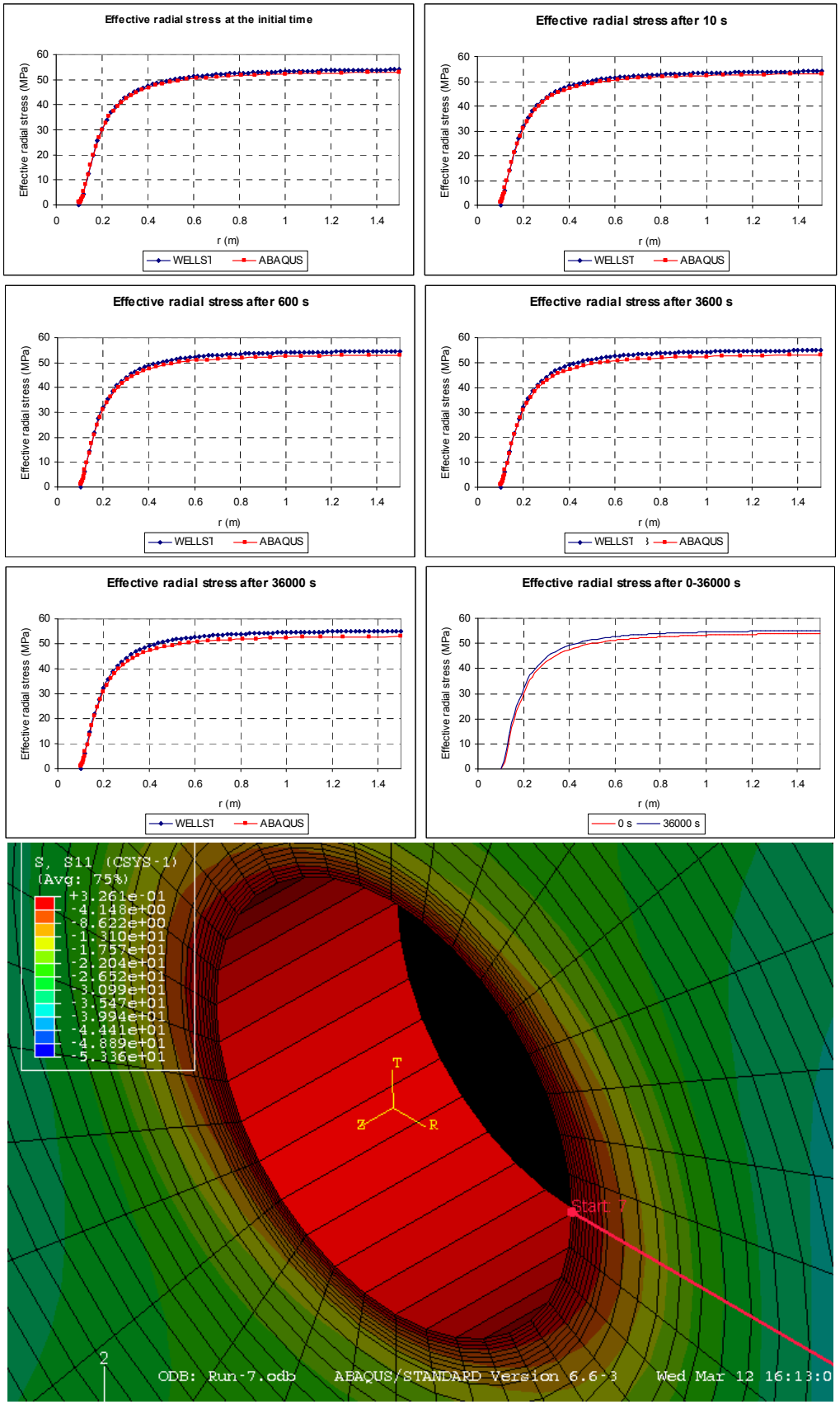

Fig 6.17. *Effective radial stress*

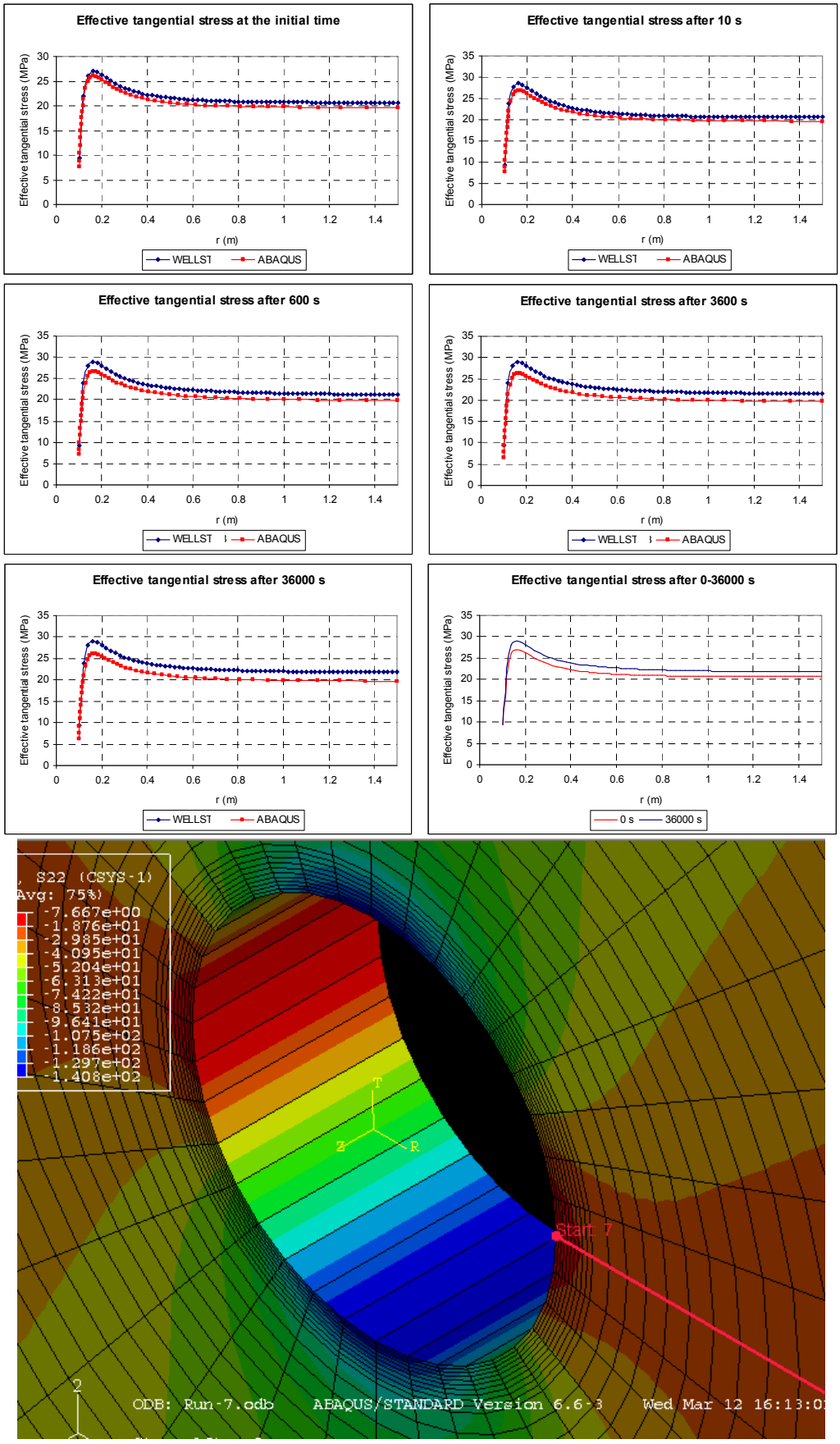

Fig 6.18. *Effective tangential stresses*

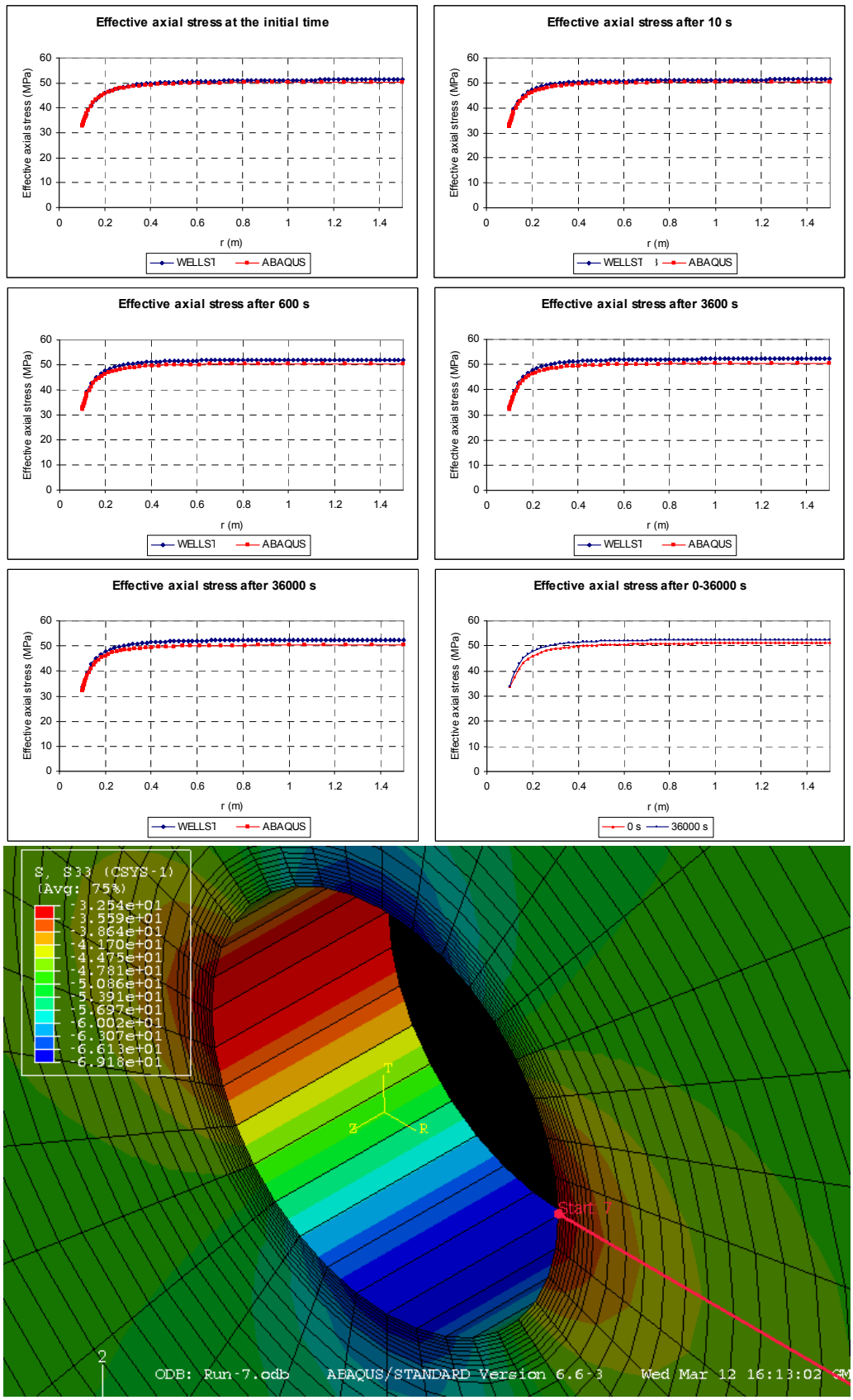

Fig 6.19. *Effective axial stresses*

Figs 6.14 - 6.19 show results of stress distribution around the wellbore after 10 s, 600 s, 3,600 s, and 36,000 s in which all stresses such as radial, tangential stresses, and effective stresses are calculated by WELLST. These results are verified with ABAQUS, and the input data can be referred in Table 2, appendix A.

The total transient stresses (Figs 6.14 - 6.16) are time independent values in elastic case because the transient pressure has not coupled in the calculation of total stresses in elastic case. The total stresses only vary when the coupling pore pressure and temperature were taken into account in the formulation of stress distribution. This one can be explained clearly by looking back Eq (2.7) and (2.47) in which the coupling of pore pressure and temperature have a role in evaluation of total stress in poroelastic and thermo-poroelastic cases. However, because the effective stress is the difference of the total stress and pore pressure, once pore pressure alters with time, the effective stresses change as well, although total stresses is unchanged.

What can be obtained from above recommendations is that the time dependent effect has influence the effective stresses through the varying of pore pressure with time, but it has not affected the total stresses in elastic case. However, in poroelastic and thermo-poroelastic formation, time dependent effect have involved to the alteration of total stresses via the coupling of pore pressure and temperature. The comparison of elastic, poroelastic, and thermo-poro-elastic will be expressed in the section “poroelastic and thermo-poroelastic effects”.

Figs 6.17 - 6.19 show the results of effective stresses solved by WELLST and ABAQUS. These figures prove that there is an approximation of results solved by the two simulators. The negligible difference between two solutions by WELLST and ABAQUS is due to the limitation of the boundary radius of the finite element model solved by ABAQUS (Fig 6.2) when it was set up at 3 m in comparison to the infinite boundary radius of the model solved by WELLST. One more reason causes this difference is the fact that the result calculated by ABAQUS is defined at the center of the element while the result solved by WELLST is calculated at the edge of the element. The observation of these figures showing the effective stresses from 0 s to 36,000 s gives the viewpoint that the effective stresses in this calculation have not changed considerably as time progresses. This point can be explained due to the fact that the difference between the formation pressure (34.45 MPa) and wellbore pressure (32.34 MPa) is not too much, so the transient pore pressure can change maximum about 2 MPa after 10 hours (this value is obtained from the data of Fig 6.9). That is why the maximum alteration of effective stresses is approximately 2 MPa at some positions. Additionally, the trend of tangential stresses is not like as normal, high at the wellbore and lower along the distance far from wellbore because of the stress anisotropy condition. And this can be seen in the section “anisotropic stress effect”. To sum up, the transient stresses depend primarily on the wellbore pressure. This conclusion will be proved clearly in the section “UBD operation”.

Transient pressure and temperature profiles will induce transient stresses. Transient stresses affected to the wellbore stability. Once the changes of pressure and

temperature with time are known, the transient stresses will be evaluated as well. So thermal induced stress and pore pressure induced stress can be calculated for the effects on wellbore stability. To describe the time dependent effect to wellbore stability, the simple following figure is described.

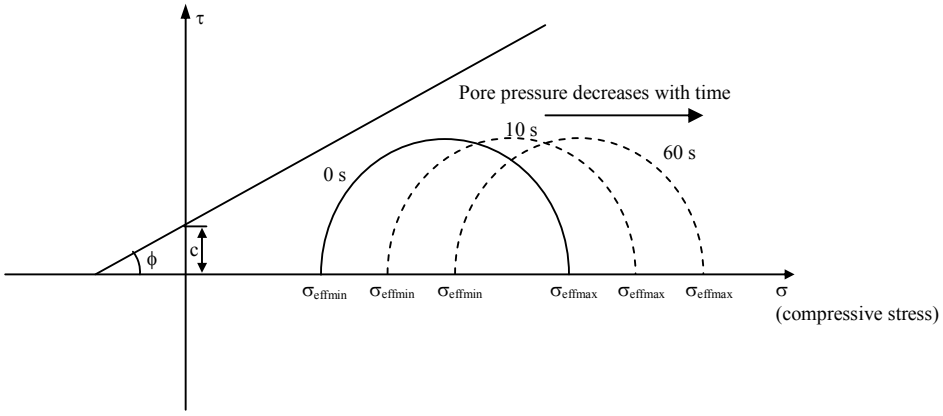

Fig 6.20. *Effect of decreasing pore pressure after drilling – the Mohr-Coulomb moves to the right preserving its shape*

Once pore pressure decreases with time, the shear stress is unaffected. However, the effective minimum and maximum principal stresses are increased by the same amount. This means that the radius of Mohr Circle is unchanged but the center is shifted to the right with time. As shown in the figure, the circle moves far away from the failure line when the pore pressure is reduced for a material obeying the Mohr-Coulomb criterion with a positive friction angle. So, it can conclude that the formation around the wellbore (not at the wellbore wall) will be more stable as time progresses. But it does not mean this stability will happen at the borehole wall because pore pressure at the wellbore is the boundary condition which was kept constant in drilling operation, it is not a time dependent parameter. This conclusion was verified by the solution of WELLST shown in the Figs 6.21 and 6.22.

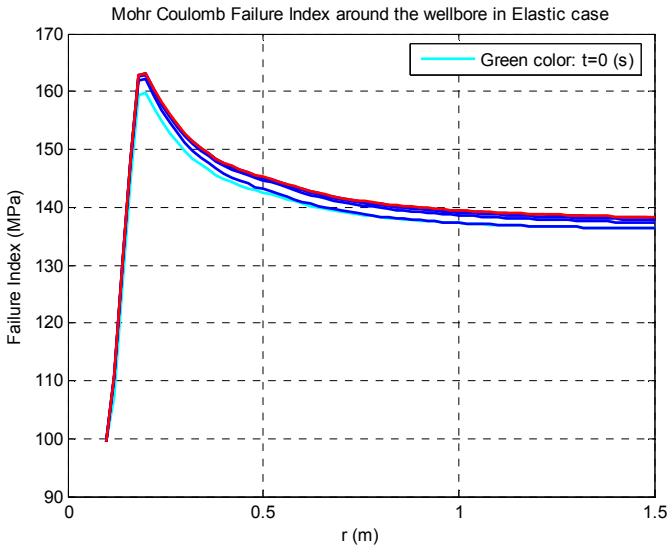

Fig 6.21. *Mohr Coulomb failure index*

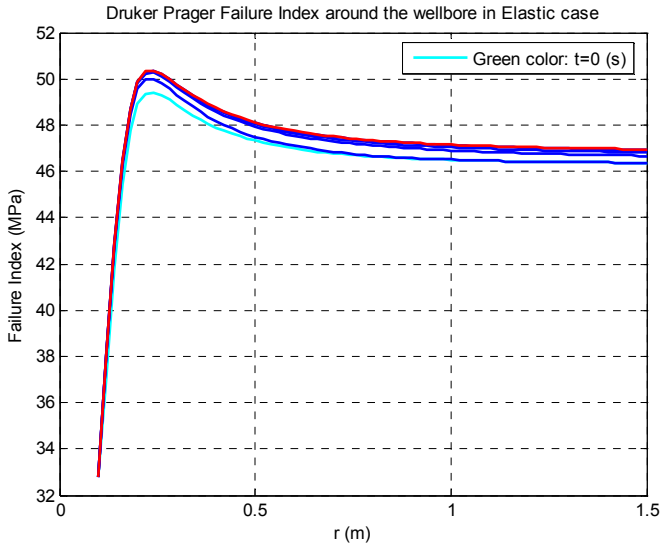

Fig 6.22. *Drucker Prager failure index*

According to results of these figures, both Mohr-Coulomb and Drucker Prager failure indexes which were presented in Eqs 2.61 and 2.62 of section 2.4.2, chapter 2 vary with time at the position around the wellbore but unchangeable at the wellbore wall at anytime. The failure index tends to higher values as time progresses, the green line corresponds to initial time and the red line symbolizes for failure index after 36,000 s (10 hours). The formation is considered unstable whenever the failure index reaches to the negative value. However, with the above calculation, the failure indexes increase with time, so it means that the formation around the wellbore will be more stable with time. In addition, the trend of failure index line also relates to the state of initial stress. The highest failure index in Figs 6.21 and 6.22 is due to the characteristic of the anisotropic stress field. Data for plotting Figs 6.21 and 6.22 are refered from Table 3, appendix A.

Hydraulic and thermal diffusivity effects

The rate of pore pressure and temperature propagation is controlled by the hydraulic diffusion time (t_1) and thermal diffusion time (t_2) (see equation 2.38) of the formation. It clearly shows that the hydraulic diffusivity influences the rate of pressure propagation in response to the hydraulic pressure gradient. In cases where $t_2 >> t_1$, it is seen that hydraulic effects become evident at short times whereas thermal diffusion may require a much longer time. The main purpose of this section is investigating the hydraulic and thermal diffusivity effects to the wellbore stability of the clastic and basement formations, so the range of parameters symbolized hydraulic diffusivity such as rock permeability, and fluid viscosity will be changed from 0.05 to 1 mD (basement), and 0.5 to 1 cP (overburden). Calculated by WELLST with data in table 1, appendix B, pressure will diffuse 134 times faster than temperature at 0.05 mD rock permeability. For the same fluid, diffusion times will increase to approximately 2685 times when permeability is up to 1 mD. The relation between permeability and the ratio of temperature/pressure diffusivity is nearly the linear when the other conditions are kept constant. And this ratio also depends on the fluid viscosity, when increasing the fluid

viscosity from 0.5 to 1 cP, diffusion times through 0.4 mD rock reduces from 1074 to 537 time. In other words, when the medium is highly permeable and the fluid only slightly viscous, pressure diffuses much faster than temperature. The results of ratio of temperature/pressure diffusivity calculated by WELLST are shown on the Fig 6.23 and Table 6.2.

Table 6.2. *Comparing thermal and hydraulic diffusions*

Permeability k (mD)	Ratio of temperature/pressure diffusion time t_2/t_1					
	μ = 0.5 cP	μ = 0.6 cP	μ = 0.7 cP	μ = 0.8 cP	μ = 0.9 cP	μ = 1 cP
0.05	134.31	111.93	95.95	83.96	74.64	67.18
0.1	268.58	223.82	191.85	167.88	149.23	134.31
0.2	537.11	447.60	383.66	335.71	298.41	268.58
0.3	805.64	671.37	575.47	503.54	447.60	402.84
0.4	1074.17	895.15	767.28	671.37	596.78	537.11
0.5	1342.70	1118.92	959.08	839.20	745.96	671.37
0.6	1611.23	1342.70	1150.89	1007.04	895.15	805.64
0.7	1879.76	1566.47	1342.70	1174.87	1044.33	939.90
0.8	2148.29	1790.25	1534.51	1342.70	1193.52	1074.17
0.9	2416.82	2014.02	1726.31	1510.53	1342.70	1208.43
1	2685.35	2237.80	1918.12	1678.36	1491.88	1342.70

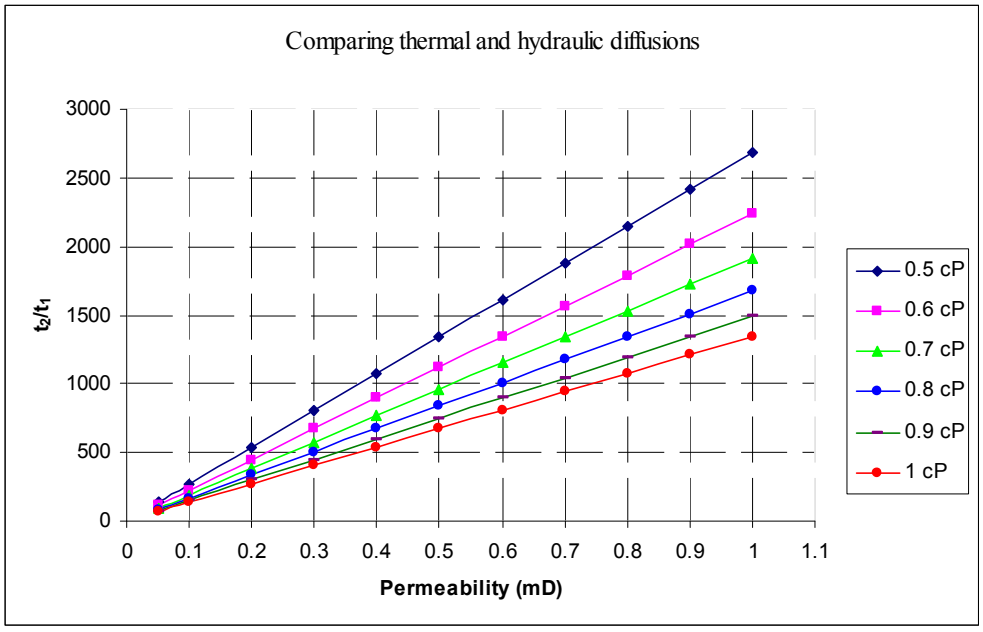

Fig 6.23. *Comparing thermal and hydraulic diffusions*

Faster pressure propagation occurs in formations with higher hydraulic diffusivity [12, 34, 87] which can be calculated by:

$$K_1 = \frac{c_f R^2}{t_1} \text{ ----------} (6.3)$$

The propagation of pressure into the rock is controlled by the hydraulic diffusivity. Fig 6.24 shows simulations run for four different values of K_1 ($m^3/s.kg$) at 10 s. For a large value of K_1, the pore pressure profile approaches equilibrium very quickly. As K_1 decreases, the propagation of pressure is slower. It is clear from these

simulations that the rate of the propagation of pressure is directly related to the magnitude of hydraulic diffusivity.

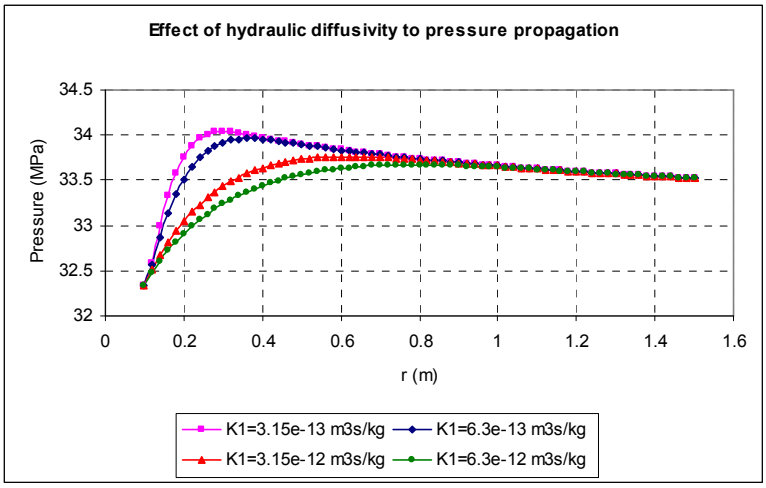

Fig 6.24. *Effect of hydraulic diffusivity on pressure propagation*

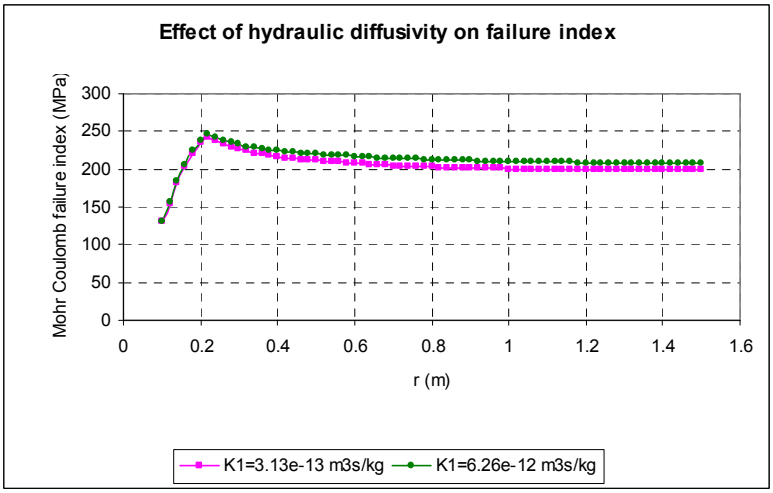

Fig 6.25. *Effect of hydraulic diffusivity on wellbore stability via Mohr Coulomb failure index*

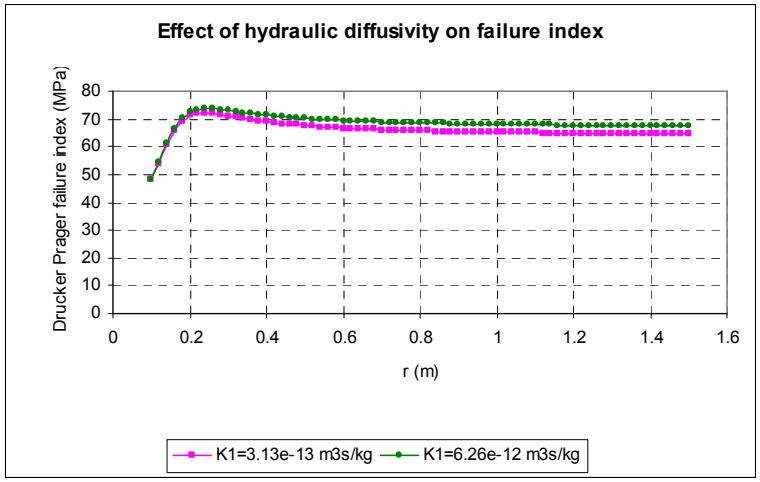

Fig 6.26. *Effect of hydraulic diffusivity on wellbore stability via Drucker Prager failure index*

The effect of thermal and hydraulic diffusivity on wellbore stability is due to the change of pore pressure and temperature on the failure criteria. The results of this influence was shown in Fig 6.24 which show that why sometimes high permeability formation can be drilled with a mud weight lower than that required for low permeability formation. This can be explained that the pressure propagation in the high permeability formation is faster than that of the low permeability formation. So in the same time, the reduction of pore pressure of high permeability formation will be higher than that of the low permeability formation. This leads to an increase in the failure index. As a result, the wellbore in high permeability formation is more stable, so it needs a lower mud weight to be drilled. Figs 6.25 and 6.26 express this viewpoint when evaluating the stability for two formations (clastic and basement) with different permeability. The first one is analyzed with high hydraulic diffusivity (K_1=6.26x10^{-12} m^{3}kg/s), and the second one has low hydraulic diffusivity (K_1=3.13x10^{-13} m^{3}kg/s). The results solved by WELLST show clearly that the formation around the wellbore (not at the wellbore wall) with high hydraulic diffusivity is more stable than another because the failure indexes calculated in Figs 6.25 and 6.26 are higher.

However, the above conclusion is only valuable when the friction angle and cohesion of both formations are the same. It is not a real assumption because the formation with high permeability has often low material cohesion. The observation from Figs 6.27 and 6.28 can explain this point when the failure index of the clastic formation with high permeability (K_1 = 6.26x10^{-12} m^{3}s/kg) and low material cohesion (20.0 MPa) is compared to that of low permeability basement formation (K_1 = 3.15x10^{-13} m^{3}s/kg) and high material cohesion (54.6 MPa). Figs 6.23 – 6.28 are plotted from the input data in table 1, appendix B.

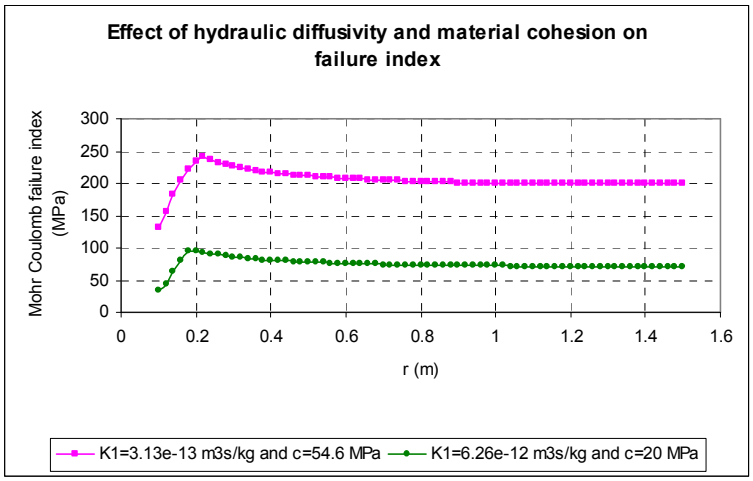

Fig 6.27. *Effect of hydraulic diffusivity and material cohesion on wellbore stability via Mohr Coulomb failure index*

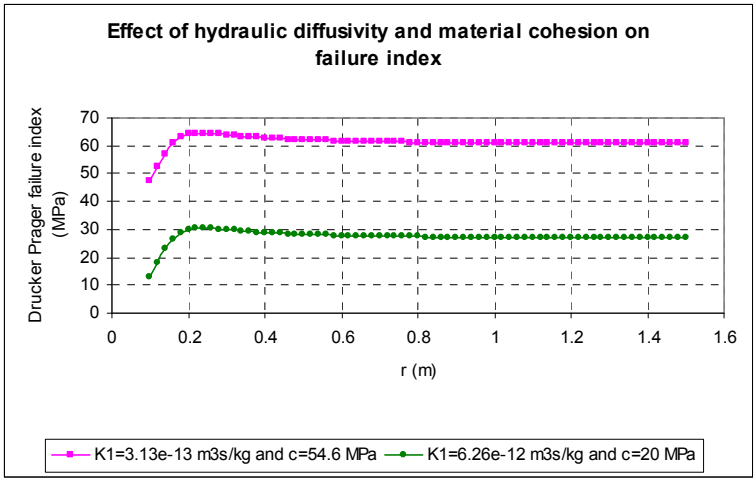

Fig 6.28. *Effect of hydraulic diffusivity and material cohesion on wellbore stability via Drucker Prager failure index*

UBD operation

In UBD operation, the wellbore pressure is always kept below the formation pressure. However, this value is not constant, it changes continually because of a variety of reasons from totally lost circulation ($P_{wf} = 0$), partially lost circulation ($0 < P_{wf} < P_R$) to tripping operations or circulation interruption ($0 < P_{wf} = P_{hyd} < P_R$). In UBD, the wellbore pressure can only change from zero (lost circulation) to P_R (formation pressure), and this trend is shown in the Fig 6.29 (basement section) or Fig 6.45 (clastic section). The results show clearly that pore pressure profile reduces when wellbore pressure reduces. The data used to calculate this section can be referred in Tables 1 and 2, appendix C.

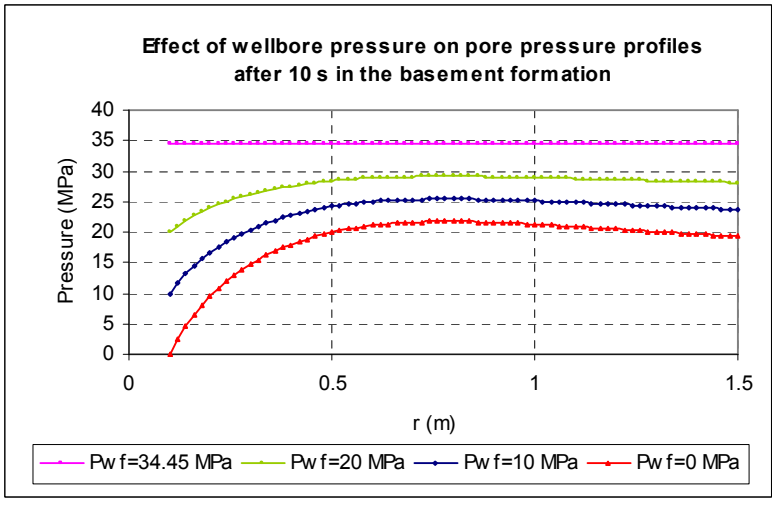

Fig 6.29. *Pore pressure profiles in respond to different wellbore pressures in UBD through the basement formation*

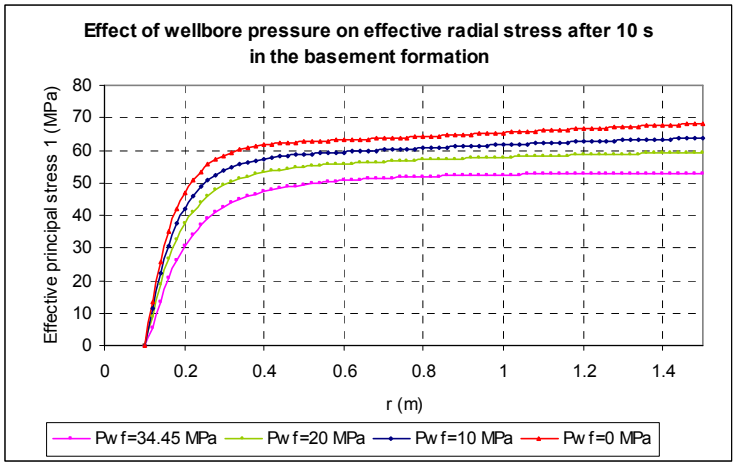

Fig 6.30. *Effective radial stress profiles in respond to different wellbore pressures in UBD*

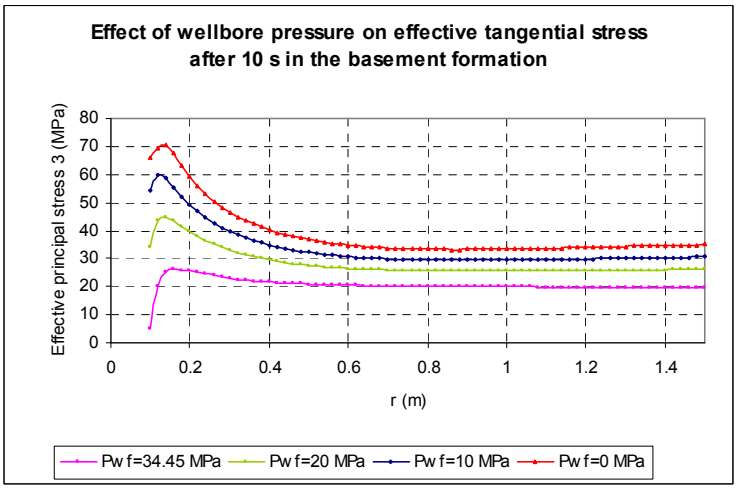

Fig 6.31. *Effective tangential stress profiles in respond to different wellbore pressures in UBD*

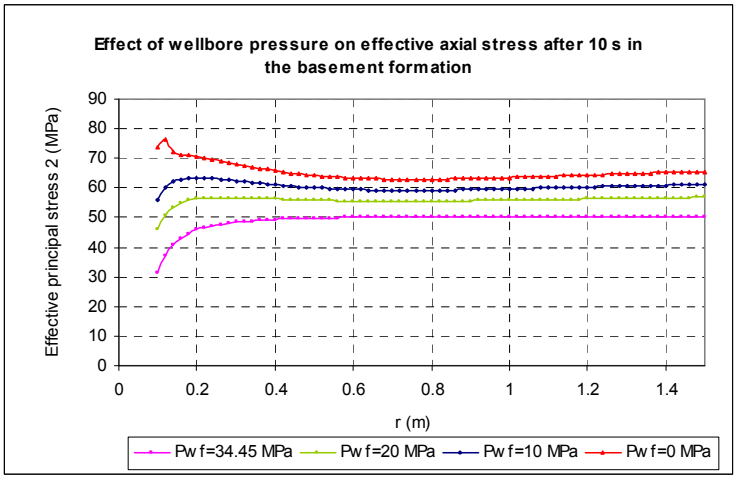

Fig 6.32. *Effective axial stress profiles in respond to different wellbore pressures in UBD*

It is important to distinguish the difference between the changes of pore pressure with time to wellbore pressure changes in drilling operation. In general, when pore pressure reduces as the discussion above (Fig 6.20), the Mohr-Coulomb circle will move to the right so the formation around the wellbore, not at the wall of the wellbore,

is more stable because the circle now goes far from the failure line. While the changes of wellbore pressure will lead the changes of stability condition of the area from the wellbore wall to a certain distance around the wellbore. The behaviour of this area (Fig 6.33) is very difficult to predict because of the effect of a variety of reasons such as initial stress condition, the stress anisotropy, or the wellbore trajectory. Some scenarios of wellbore pressure effect on the stability of the area around the wellbore will be established to define this varying rule.

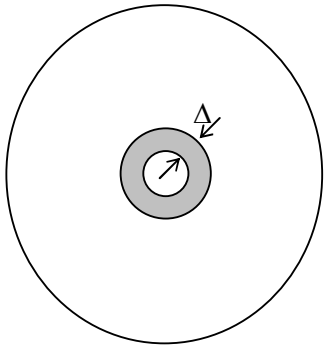

Fig 6.33. *The area of interest*

First of all, assume that the effective radial stress at the wellbore wall of a vertical well is the minimum effective stress. This stress is always unchangeable whenever wellbore pressure changes in UBD because the total radial stress at the wellbore is equal to wellbore pressure, and pore pressure at the wellbore is exactly wellbore pressure as well. That is why the effective radial stress at the wellbore is always zero despite the value of wellbore pressure (Fig 6.30). Continuing to assume that the effective tangential or axial stress is the maximum effective stress at the wall of the borehole, this value will change oppositely with the alteration of wellbore pressure (Figs 6.31 & 6.32). For example, if wellbore pressure decreases due to lost circulation or tripping operations, the minimum effective stress is unchangeable (zero) while the maximum effective stress increases. So, the maximum effective stress position moving to the right results in the Mohr-Coulomb circle becoming larger and approaching the failure line, so the wellbore will be more susceptible to collapse. On the other hand, if wellbore pressure increases that leads to an increase of pore pressure, the maximum effective stress will decrease and move to the left. As a result, the Mohr-Coulomb will be smaller and farther from the failure line making the wellbore more stable. Fig 6.34 with the input data in Table 1, appendix C shows this viewpoint. However, this viewpoint shown in Fig 6.34 is not the general conclusion. It is just a specific case when the following assumptions are correct:

- Effects of induced stress due to pressure and temperature changes are not taken into account.
- Minimum effective stress must be equal to radial effective stress during the period of wellbore pressure varying.
- Mohr-Coulomb failure criterion is applied.

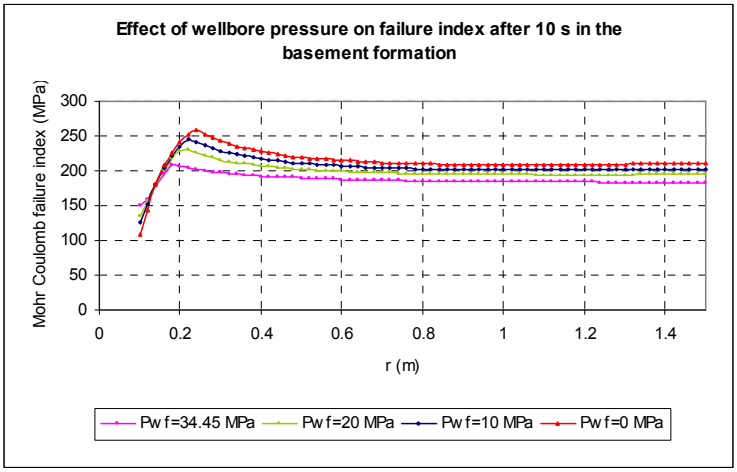

Fig 6.34. *Effect of wellbore pressure on failure index at $\theta = 0^o$ in UBD operations through the basement formation after 10 s*

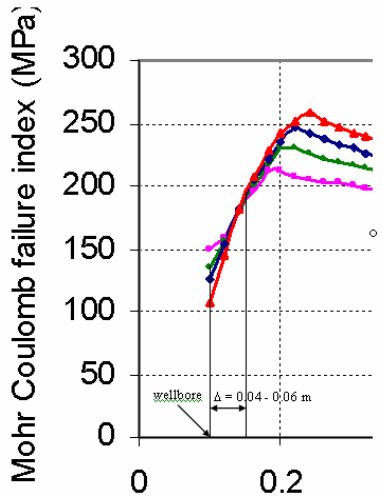

Fig 6.35. *Mohr-Coulomb failure index at the wellbore wall in UBD*

The results of Mohr-Coulomb failure index in Fig 6.34 which was solved by WELLST can also be compared to the results of ABAQUS. The near wellbore area is zoomed in Fig 6.35. The following plot (Fig 6.36) shows the accuracy of two simulators. The small difference between the results of WELLST and ABAQUS is mainly due to the mesh refinement and the error in integral Eq (2.37).

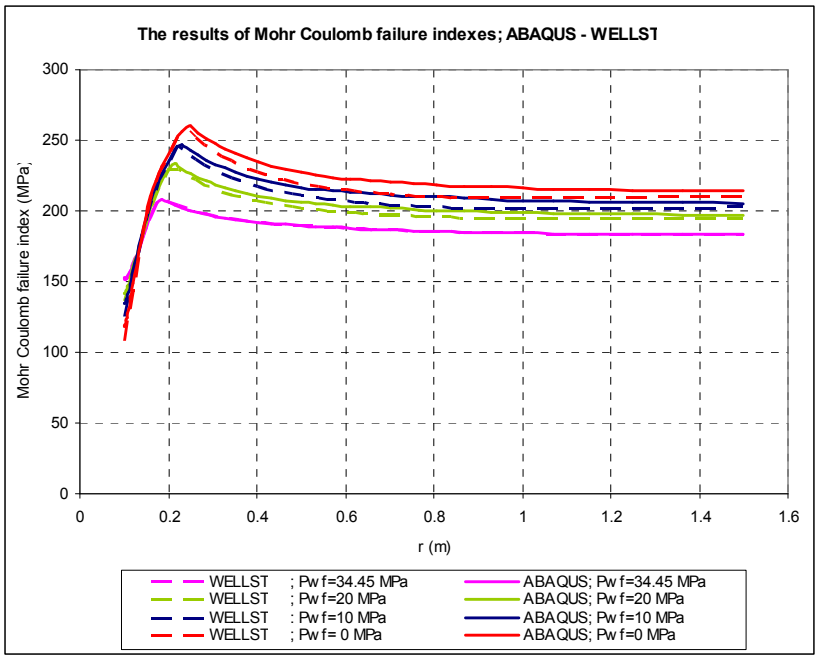

Fig 6.36. *Comparing Mohr-Coulomb failure index around the wellbore in UBD operation solved by WELLST and ABAQUS*

As discussion above, when changing wellbore pressure in UBD, the stability condition of the wellbore is not only affected by this factor but also depends on other factors such as the position around the wellbore, trajectory of the wellbore, the initial stress field. Precisely, the calculated failure index varies from point to point around the wellbore, especially in the anisotropic stress field. Notice that θ is the angle between the interested point and x-axis in the new coordinate system. The following scenario will analyze the influence of two factors, the alteration of wellbore pressure in UBD, and the position around the wellbore, on wellbore stability with the input data referred in table 1, appendix C. To do that, the figures related between wellbore pressures, failure indexes, and the angle θ are plotted.

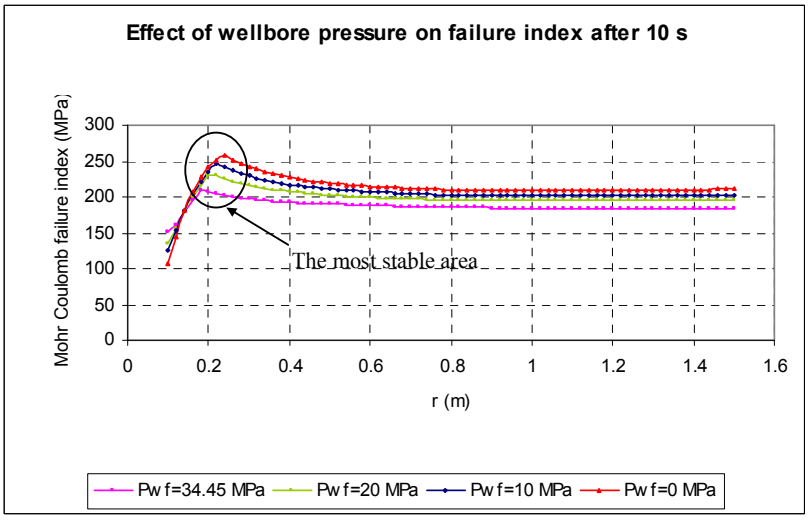

Fig 6.37. *Effect of wellbore pressure on failure index at $\theta = 0^o$ after 10 s*

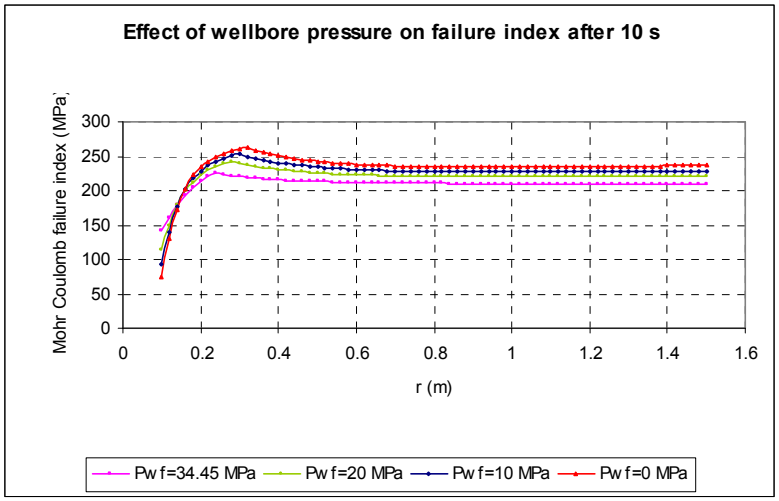

Fig 6.38. *Effect of wellbore pressure on failure index at $\theta = 30^o$ after 10 s*

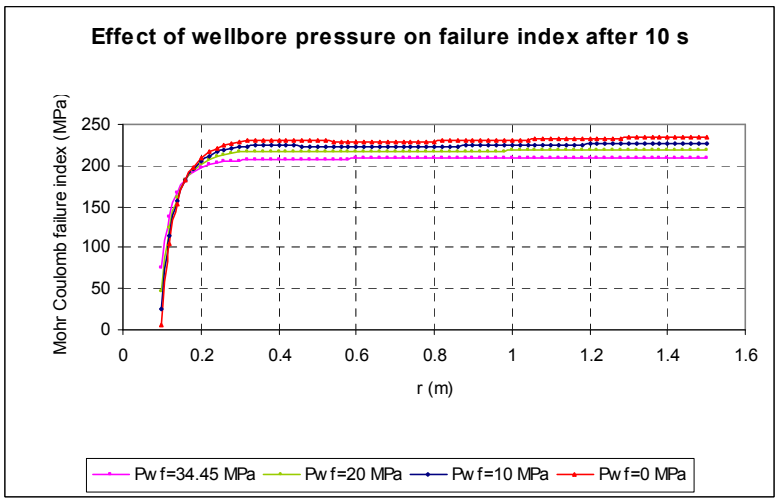

Fig 6.39. *Effect of wellbore pressure on failure index at $\theta = 60^o$ after 10 s*

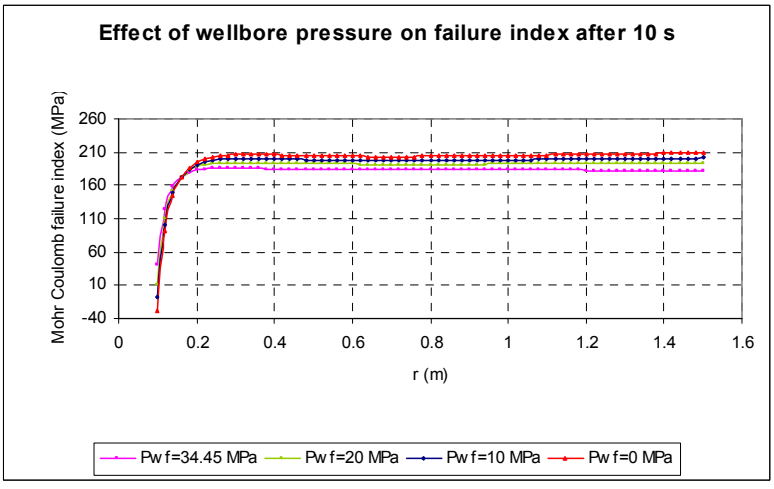

Fig 6.40. *Effect of wellbore pressure on failure index at $\theta = 90^o$ after 10 s*

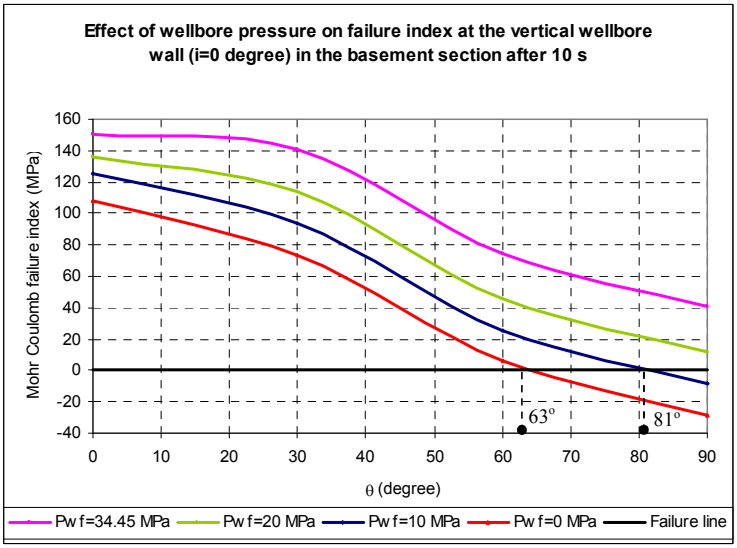

Fig 6.41. *Effect of wellbore pressure on failure index at the vertical wellbore wall in the basement section after 10 s*

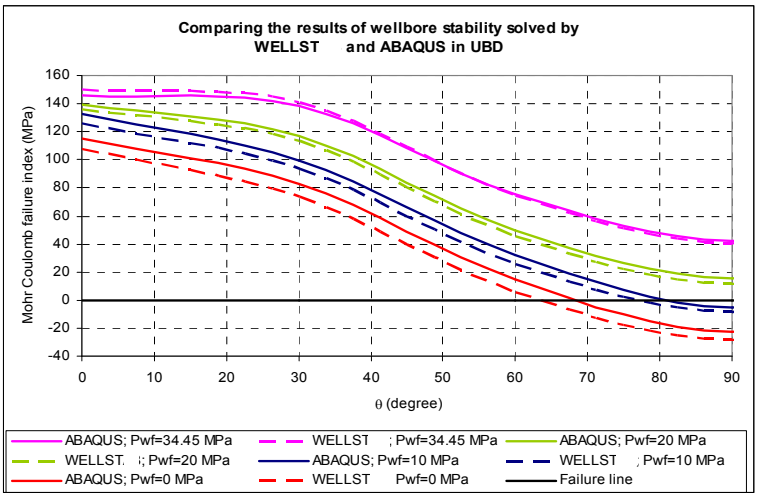

Fig 6.42. *Comparing the results of wellbore stability solved by WELLST and ABAQUS in UBD*

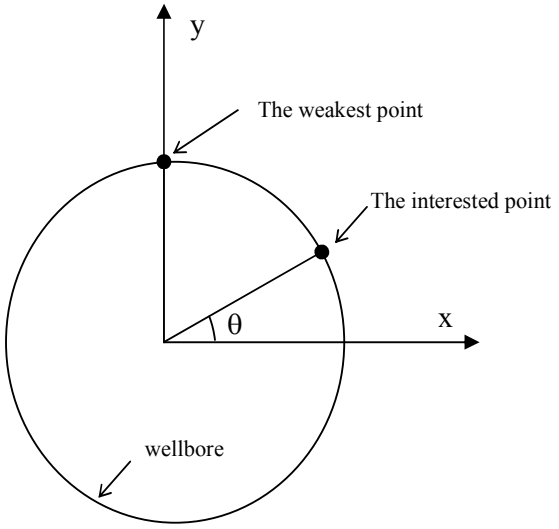

Fig 6.43. *The weakest point on the wellbore wall*

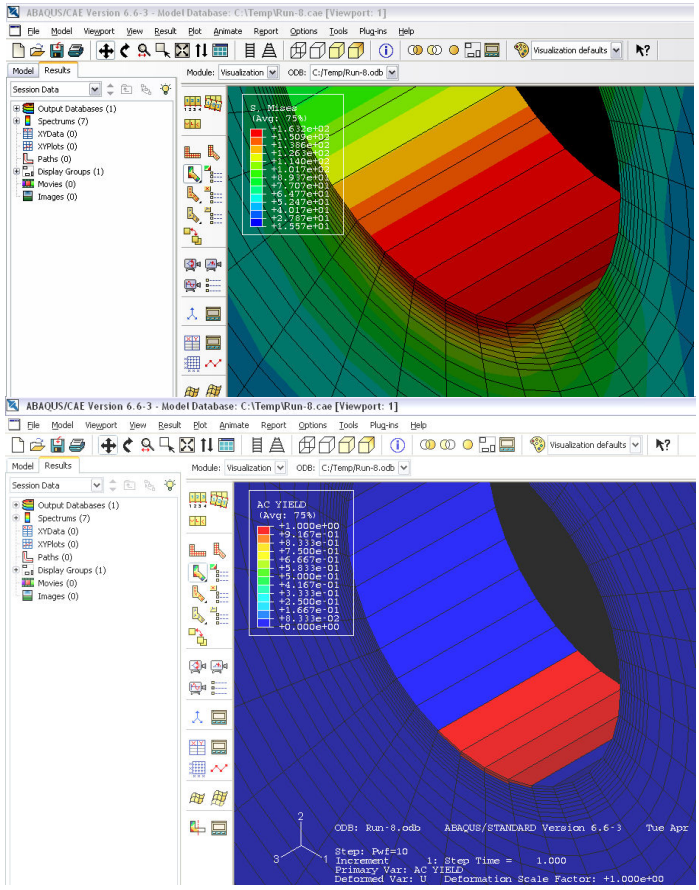

Fig 6.44. *The weakest point on the wellbore wall solved by ABAQUS*

Fig 6.44 can be obtained from section A in Fig 6.1 as a cut of the borehole section along the basement formation. The results from Figs 6.29 to 6.44 are solved from data of the basement of Basin X. According to the clastic section, the following results can be withdrawn with the input data of Table 2, Appendix C.

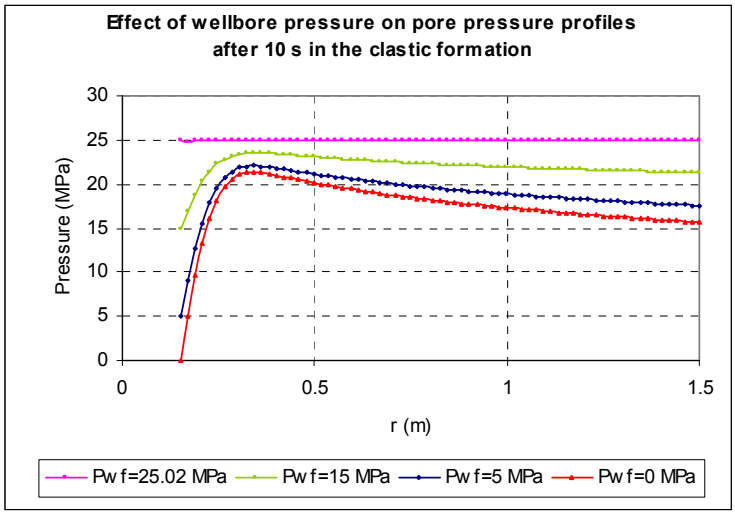

Fig 6.45. *Pore pressure profiles in respond to different wellbore pressures in UBD through the clastic formation*

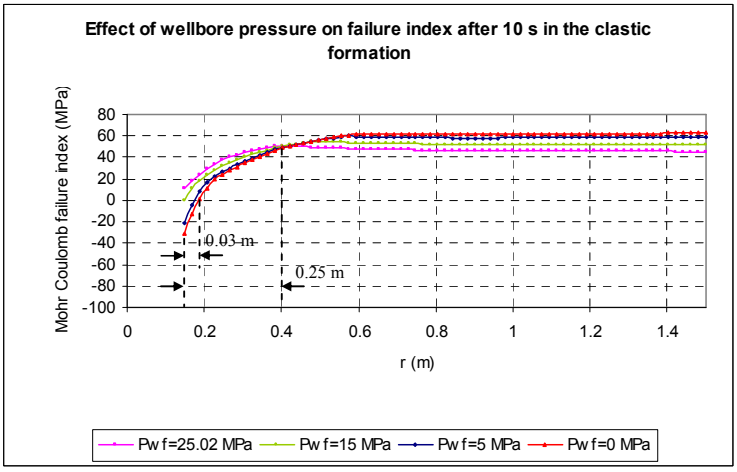

Fig 6.46. *Effect of wellbore pressure on failure index at $\theta = 0^o$ in UBD operations through the clastic formation after 10 s*

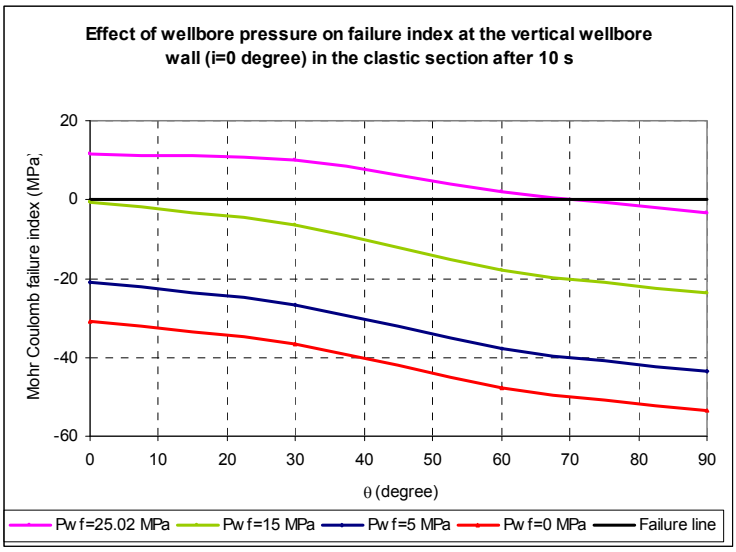

Fig 6.47. *Effect of wellbore pressure on failure index at the vertical wellbore wall in the clastic section after 10 s*

There are two problems need to be interested in the calculated results of clastic sections. Firstly, there is an area with the radius of 0.25 m around the wellbore in which its stability once wellbore pressure reduces behaves differently from the area far from the wellbore. The reason of this behavior can be explained as same as the explanation for the case of basement section above. Secondly, as the calculated results in Fig 6.46 in the case of $\theta=0^o$, the wellbore is collapsed when wellbore pressure decreases lower than 15 MPa. When totally lost circulation happens (P_{wf}=0), the collapsed area is in the range from 0-0.03 m from the wellbore. When considering other positions around the wellbore (Fig 6.47), the collapse actually happened even when wellbore pressure is maintained at 25.02 MPa which is equal to formation pore pressure, and the wellbore is collapsed partially from $\theta=70^o$-90^o. However, this conclusion does not mean that it is impossible to apply UBD to the clastic section because the cohesion of material assumed to calculate in these cases is 12 MPa while the gathered cohesion of material of the clastic section changes from 4.2 to 32.9 MPa (Table 6.1). Therefore, the feasibilities of UBD

application to ensure the wellbore stability in the clastic section depend on the accuracy of the cohesion of material of penetrated formations.

From the results solved by WELLST and ABAQUS shown on Figs 6.37-6.44, the following viewpoints can be obtained for a vertical well drilled through the basement section:

- There is an area around the wellbore within 0.04-0.06 m which becomes less stable when wellbore pressure reduces in UBD, irrespective of the point around the circumference of the well. However, the region far from the wellbore behaves in the opposite way. The formation in this far region will be more stable once wellbore pressure decreases.
- In case of $\theta=0^o$, the position corresponds to the direction of the maximum horizontal stress, the most stable area is located from 0.1 to 0.15 m from the wellbore in the basement section. And this peak will move into the formation when θ increases. This is caused by the anisotropy of stresses (Fig 6.37).
- The weakest point at the vertical wellbore is located on y-axis in the direction of minimum horizontal stress. The wellbore wall will start to collapse when wellbore pressure reduces to 15 MPa. The collapsed point starts at the weakest point ($\theta=90^o$) (Figs 6.41-6.44).
- If wellbore pressure continues to reduce to 10 MPa, the wellbore wall will collapse from $\theta=81^o$ to 90^o. The collapsed area will increase from 63^o to 90^o when wellbore pressure reduces to zero (totally lost circulation). So the wellbore at points in the above area will be collapsed although the rock cohesion is quite hard (54.6 MPa). Figs 6.41-6.42 show the negative values of the failure index at the collapsed points.
- These conclusions are acceptable if it is assumed that effects of induced stress due to pressure and temperature changes are ignored, minimum effective stress is equal to radial effective stress, and the wellbore inclination is zero (vertical well).

According to clastic section, the following conclusions can be obtained:

- There is also an area around the wellbore within 0.25-0.27 m which becomes less stable when wellbore pressure reduces while the region far from the wellbore behaves in the opposite way. This area is larger than the area around the wellbore in the basement because the anisotropy of stresses in clastic section is less than that of the basement section.
- The weakest points are located at the wellbore wall, especially at $\theta=90^o$ and the most stable are is far from the wellbore.
- The wellbore starts to collapse even when the wellbore pressure is as same as formation pore pressure, and the collapsed area is in the range $\theta=70^o$ to 90^o at this wellbore pressure.

- The cohesion of material has an important role in these calculations. Its change will lead to the change of the wellbore stability.

It is necessary to notice again that the result and conclusion of Figs 6.34 and 6.35 is a common case but this does not mean that it always occurs. Once wellbore pressure changes in UBD, it will lead to the changes of radial, tangential and axial stresses as well. This alteration sometimes swaps the role of stress values. The radial effective stress at the wellbore will be constant (zero), and the effective tangential and axial stresses increase when wellbore pressure decreases. Another scenario can be set up as follows. Assume that the minimum effective stress is the axial effective stress; the maximum effective stress is tangential stress in the initial condition. When wellbore pressure reduces, both axial effective stress and tangential effective stress increase. And if the coupling of pore pressure and temperature are ignored in this calculation, the increase of tangential stress is larger than that of axial stress. As a result, Mohr-Coulomb circle will move to the right and has a larger radius (A-B, Fig 6.48). The first change (moving to the right) will help to get a beneficial effect on borehole stability, but the second change (widening the circle) will lead the instability due to the circle approaching to failure line. So, if the first one dominates, the wellbore will be more stable, if the second the wellbore will be more susceptible to collapse. Then, when the axial stress is larger than the intermediate effective stress (radial effective stress in this case), the minimum effective stress will be radial effective stress and this value will remain when wellbore pressure continues to reduce. Therefore, this scenario is the same as the previous scenario meaning that only the maximum effective stress moves to the right widening the Mohr-Coulomb circle and approaching the failure line (B-C, Fig 6.48). These explanations once again show the complication of stability analyses around the wellbore. What can be concluded in this scenario? The wellbore may be more stable or unstable when wellbore pressure reduces. The exact answer can not be obtained if only the changes of wellbore pressure are known without the other parameters such as the stress anisotropy, or the wellbore trajectory, being known.

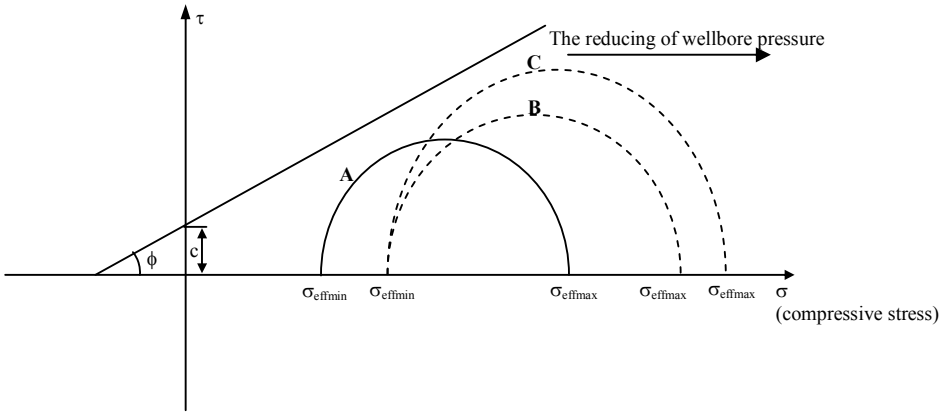

Fig 6.48. *The stability at the wellbore wall when wellbore pressure reduces*

To sum up, there are totally 6 scenarios of this problem ($\sigma_\theta \geq \sigma_z \geq \sigma_r$, $\sigma_z \geq \sigma_\theta \geq \sigma_r$, $\sigma_z \geq \sigma_r \geq \sigma_\theta$, $\sigma_r \geq \sigma_z \geq \sigma_\theta$, $\sigma_r \geq \sigma_\theta \geq \sigma_z$, $\sigma_\theta \geq \sigma_r \geq \sigma_z$). For each case there are a set of stability criteria that can be calculated. In this calculation with given data in Tables 1, 2 appendix C, the formation within 0.04-0.06 m (basement) and 0.25-0.27 m (clastic) of

the wellbore are of interest in cases of reduced wellbore pressure such as lost circulation or tripping operations.

Wellbore inclination and azimuth variation effects

The effects of wellbore inclination and azimuth variation on wellbore stability have been widely discussed in literature. Bradley (1979) [16] concluded that in normally stress regions ($\sigma_V > \sigma_H = \sigma_h$), vertical wellbore are more stable to collapse than inclined wellbores. Aadnoy and Chenevert [21] agreed with Bradley's conclusion when they reported that isotropic formations become more sensitive towards collapse the higher the wellbore inclination.

Assume that the well is drilled through the basement formation with the inclination of 30^o, 60^o, and 90^o in comparison to the vertical direction and the azimuth is zero, the following results can be solved by WELLST with the input data following Table 1, appendix D.

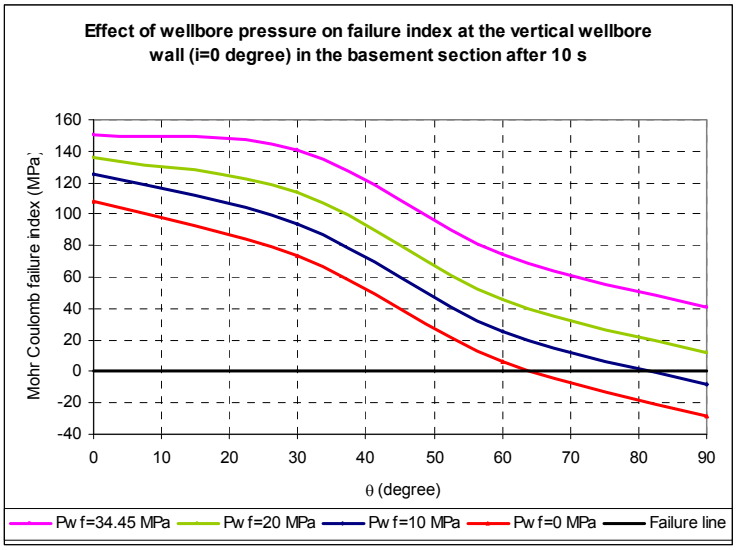

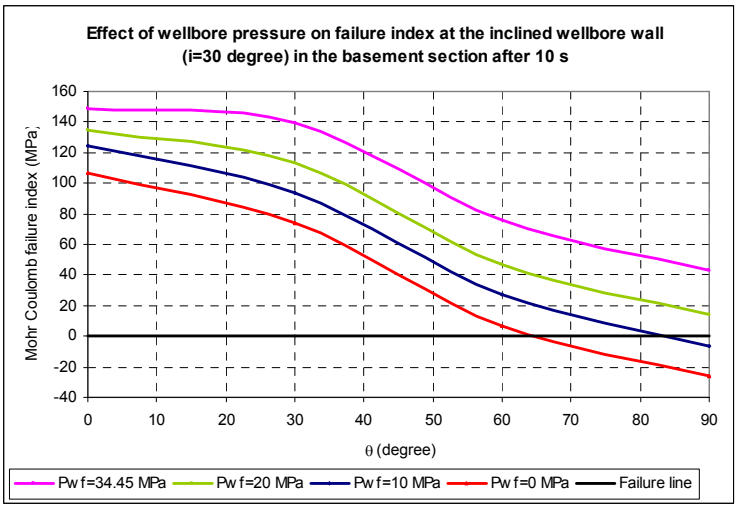

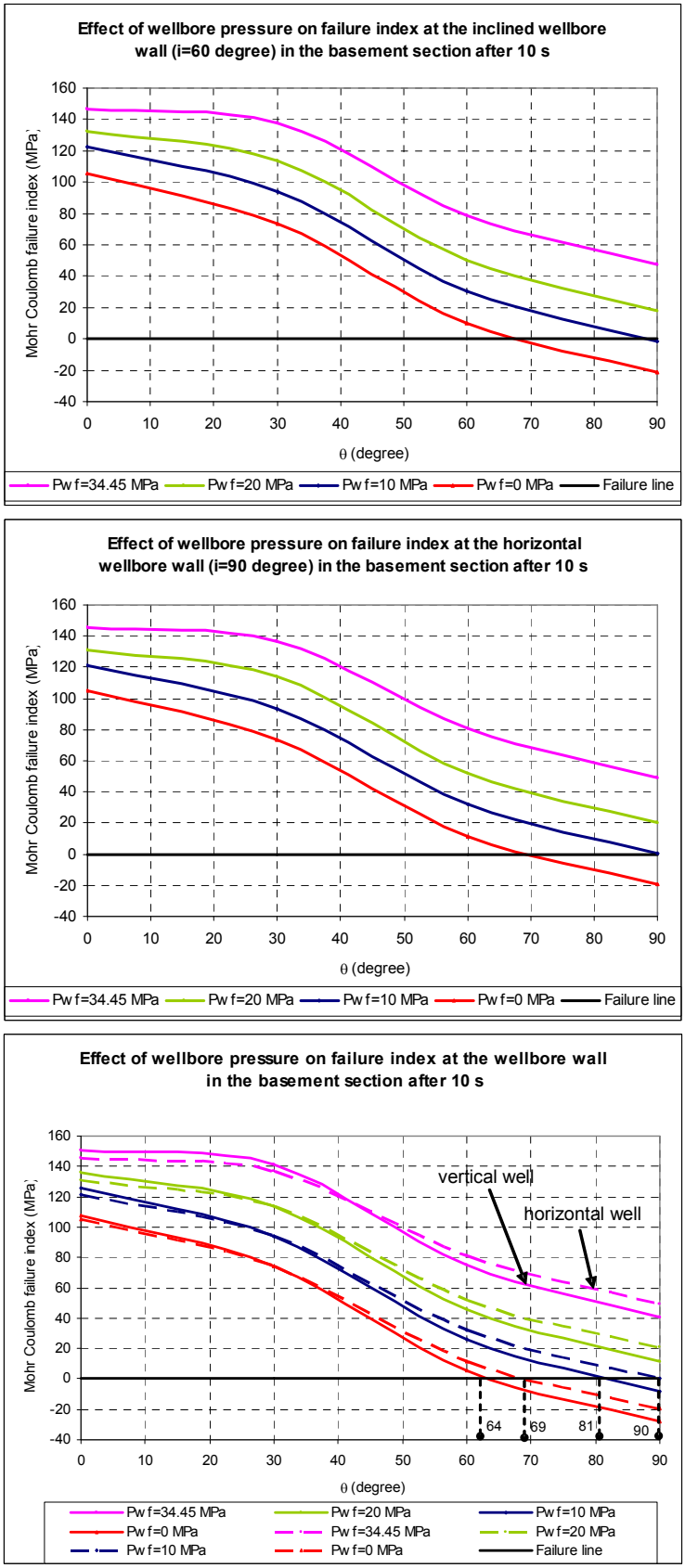

Fig 6.49. *Effect of wellbore pressure and wellbore inclination on failure index at the wellbore wall in the basement section after 10 s*

In this calculation the horizontal wellbore wall in the basement section begins to collapse when wellbore pressure reduces to 10 MPa instead of 15 MPa in case of vertical wells. When P_{wf} equals 10 MPa, the horizontal well starts to collapse but the vertical well has collapsed from the position $\theta=81^o$ to 90^o. Moreover, if lost circulation happens ($P_{wf}=0$ MPa), the collapsed range of the vertical wellbore (64^o-90^o) will be larger than the horizontal wellbore (69^o-90^o). All above calculations show that in the basement, the horizontal wells in comparison to the vertical wells seem to be more stable because the failure index in the same position at the wellbore wall is higher. If changing the inclination from zero (vertical well) to 90^o (horizontal well) and keeping the azimuth of the wellbore zero, the wellbore will more stable. This conclusion is opposite to the research of Bradley due to the difference of the initial stress condition. Notice that the initial stresses in these calculations are not as normal ($\sigma_V > \sigma_H = \sigma_h$) but in the strike-slip compression condition ($\sigma_H > \sigma_V > \sigma_h$). So it can be understood that once the inclination increases, the minimum principal stress (54 MPa) is unchanged but there is an exchange between other principal stresses. As a result, horizontal well is more stable than vertical well in the same condition due to the Basin X is under compression in a strike-slip environment. From the results obtained in this calculation, it can be concluded that drilling the horizontal well in Basin X will give a benefit to the wellbore stability than drilling the vertical well (Fig 6.50).

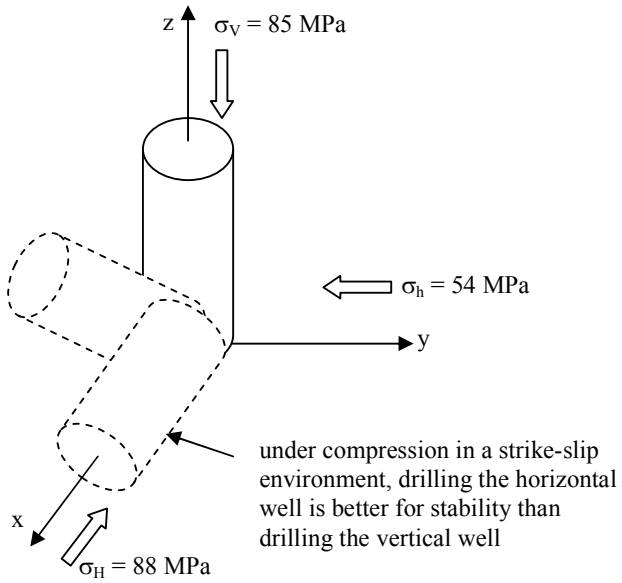

Fig 6.50. *The best inclination to drill in strike-slip formation*

As the conclusion above, when the wellbore azimuth (a) is zero, drilling the horizontal well in the basement of Basin X is better for wellbore stability than drilling the vertical well. However, it is necessary to consider this conclusion in case of azimuth variation. To do that, the azimuth of the wellbore is varied from 0 to 90^o and the alteration of failure index in these calculations is investigated case by case.

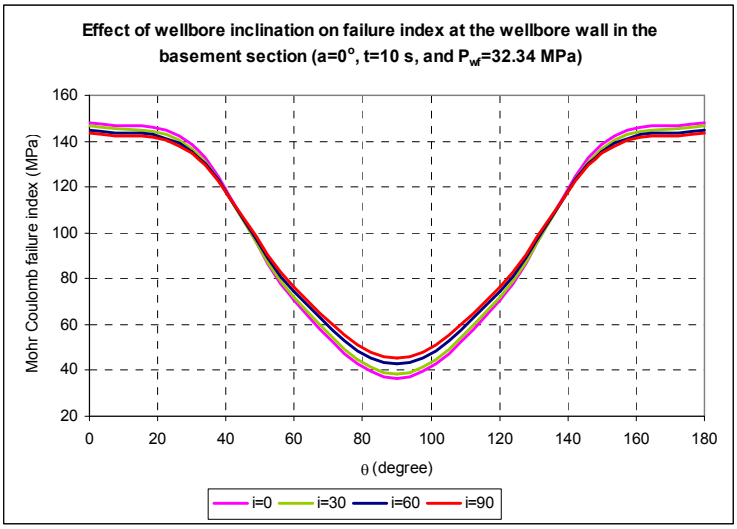

Fig 6.51. *Effect of wellbore inclination on failure index at the wellbore wall in the basement section ($a=0^o$, $t=10$ s, and $P_{wf}=32.34$ MPa)*

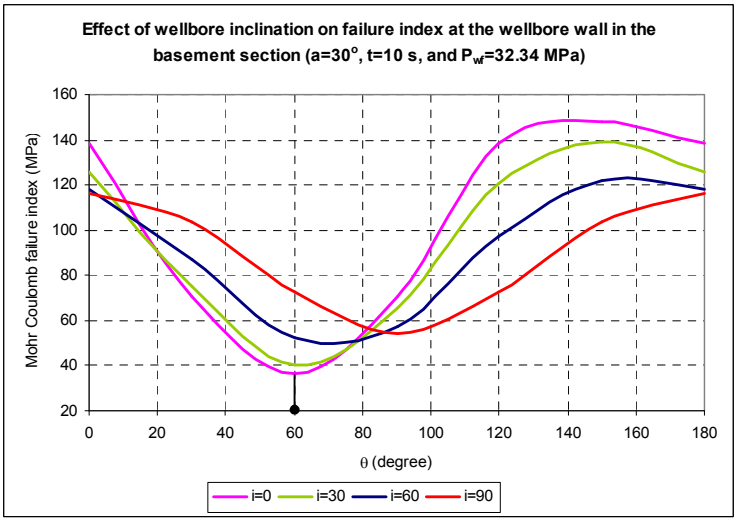

Fig 6.52. *Effect of wellbore inclination on failure index at the wellbore wall in the basement section ($a=30^o$, $t=10$ s, and $P_{wf}=32.34$ MPa)*

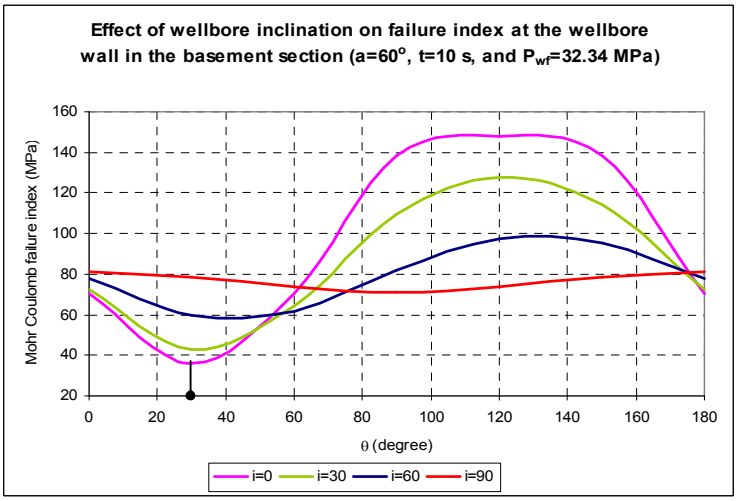

Fig 6.53. *Effect of wellbore inclination on failure index at the wellbore wall in the basement section ($a=60^o$, $t=10$ s, and $P_{wf}=32.34$ MPa)*

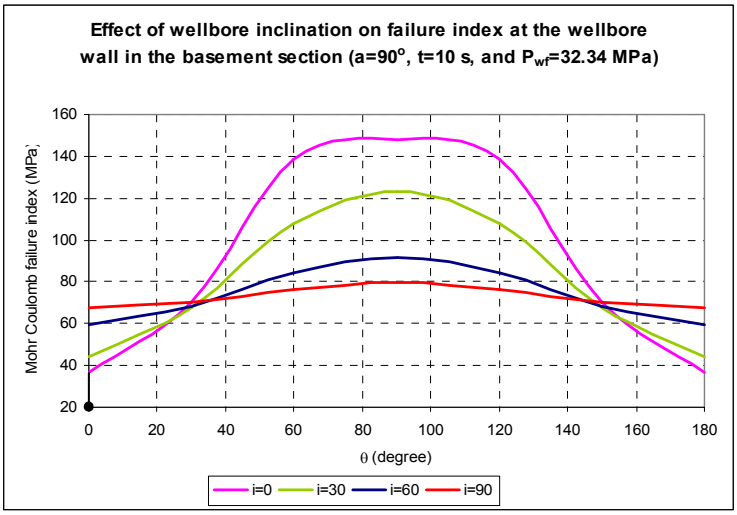

Fig 6.54. *Effect of wellbore inclination on failure index at the wellbore wall in the basement section ($a=90^o$, $t=10$ s, and $P_{wf}=32.34$ MPa)*

For a deviated wellbore in a strike-slip stress formation oriented with azimuth zero degree ($a = 0^o$), parallel to the direction of the maximum horizontal stress, Fig 6.51 shows that the weakest point at the wellbore is located on y-axis in the direction of minimum horizontal stress ($\theta=90^o$) and the increasing of inclination angle (i) in the range from 0^o to 90^o will increase the stability of this point. However, at this direction ($a = 0^o$), the influence of the inclination to wellbore stability can be ignored because the difference of failure indexes as calculated in the Fig 6.51 is insignificant.

When the wellbore drilled with azimuth 30^o of the direction of the maximum horizontal stress, the weakest position at the wellbore is defined at $\theta = 60^o$. And Fig 6.52 also shows that a deviated wellbore in a strike-slip compression formation is more stable towards collapse than a vertical well because the Mohr Coulomb failure index at the same weakest point increases when the inclination increases. Besides, it is clear that the wellbores with inclinations up to 30^o in this case can be treated as vertical wellbore which was suggested by Aadnoy and Chenevert [21]. Fig 6.53 shows how failure behaviors changes as inclination angle increases from 0 to 90^o when $a = 60^o$. These behaviors indicate that increasing the inclination angle will help the wellbore more stable, especially at the weakest position ($\theta = 30^o$). In case of azimuth angle 90^o, the weakest point at the wellbore is located at $\theta = 0^o$, and in this direction drilling horizontal wells also improves the wellbore stability more than drilling vertical wells. Moreover, the failure index lines between the inclination 60^o and horizontal wells in Fig 6.54 have inconsiderable difference, so wellbores with inclination more than 60^o can be treated as horizontal wells in case of $a = 90^o$.

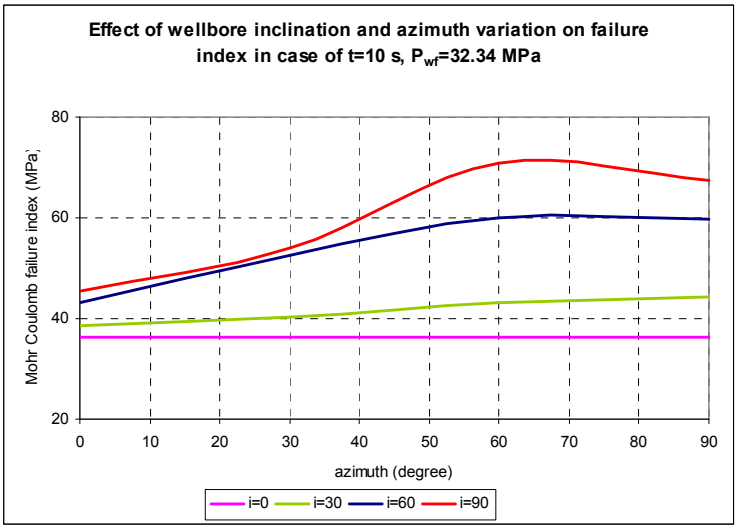

Fig 6.55. *Effect of wellbore inclination and azimuth variation on failure index at the weakest point of the wellbore wall when P_{wf}=32.34 MPa, t= 10 s*

Fig 6.55 indicates the conclusion that azimuth angle has not impacted to stability of vertical wells (i = 0^o). However, according to wellbores with inclination over 60^o, the failure index gets the highest value as azimuth (a = 60-75^o), and lowest once a = 0^o. It means that the wellbore with high inclination (>60^o) should be drilled in the direction of azimuth angle 60-75^o and the stability of the wellbore will increase when the inclination angle increases.

In summary, the results obtained in studying the effect of wellbore inclination and azimuth variation on the wellbore stability in the basement formation of Basin X can be summarized as follows:

- The weakest point at the wellbore wall will vary mostly depending on azimuth angle. For a = 0^o, θ = 90^o; a = 30^o, θ = 60^o; a = 60^o, θ = 30^o; and a = 90^o, θ = 0^o.
- In the strike-slip compression formation where the maximum horizontal stress is higher than vertical stress like Basin X, drilling a horizontal well will improve the stability of the wellbore more than drilling a vertical well. This conclusion remains valid in any case of azimuth angle.
- When drilling the horizontal well in Basin X, the best direction is oriented with azimuth angle a = 60-75^o.

The similar calculations are also carried out in the case of the clastic formation. The following results can be obtained from the input data of Table 2, Appendix D.

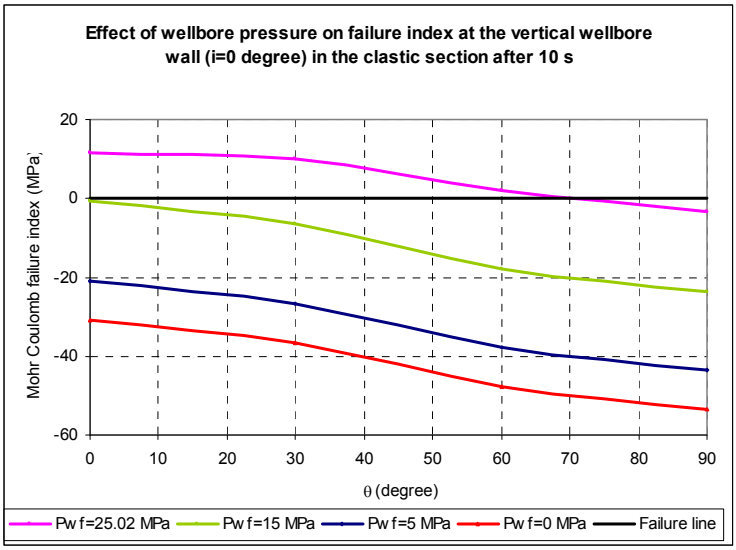
Effect of wellbore pressure on failure index at the vertical wellbore wall (i=0 degree) in the clastic section after 10 s
Mohr Coulomb failure index (MPa)
20
0
-20
-40
-60
0
10
20
30
40
50
60
70
80
90
θ (degree)
Pw f=25.02 MPa
Pw f=15 MPa
Pw f=5 MPa
Pw f=0 MPa
Failure line

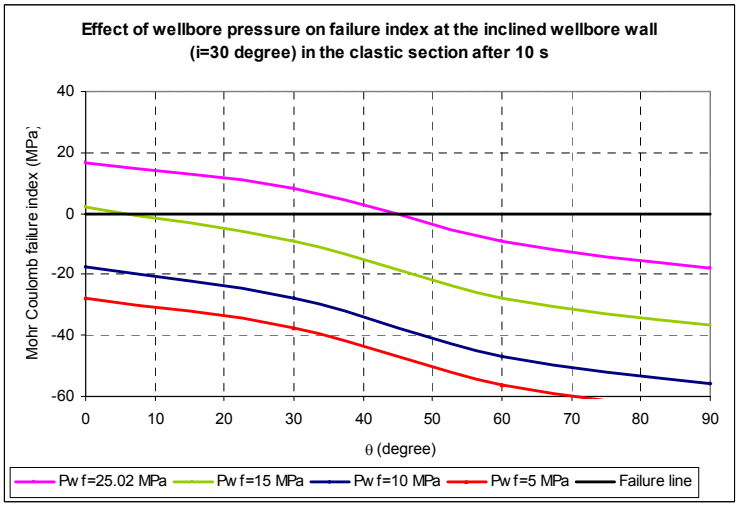
Effect of wellbore pressure on failure index at the inclined wellbore wall (i=30 degree) in the clastic section after 10 s
Mohr Coulomb failure index (MPa)
40
20
0
-20
-40
-60
0
10
20
30
40
50
60
70
80
90
θ (degree)
Pw f=25.02 MPa
Pw f=15 MPa
Pw f=10 MPa
Pw f=5 MPa
Failure line

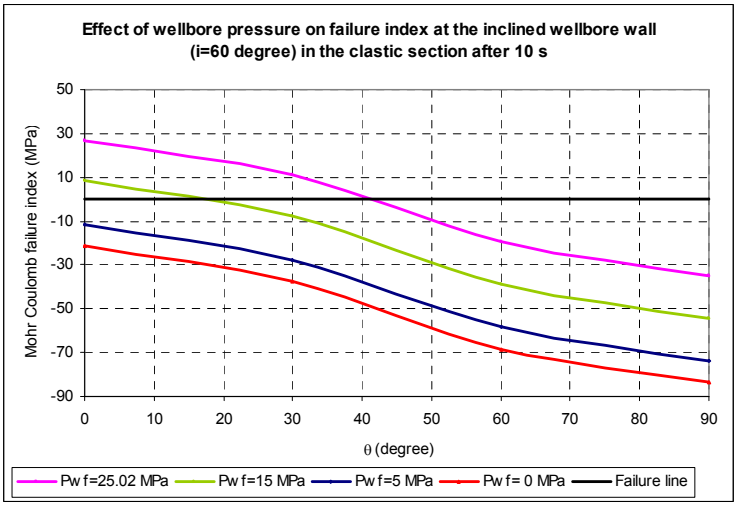
Effect of wellbore pressure on failure index at the inclined wellbore wall (i=60 degree) in the clastic section after 10 s
Mohr Coulomb failure index (MPa)
50
30
10
-10
-30
-50
-70
-90
0
10
20
30
40
50
60
70
80
90
θ (degree)
Pw f=25.02 MPa
Pw f=15 MPa
Pw f=5 MPa
Pw f= 0 MPa
Failure line

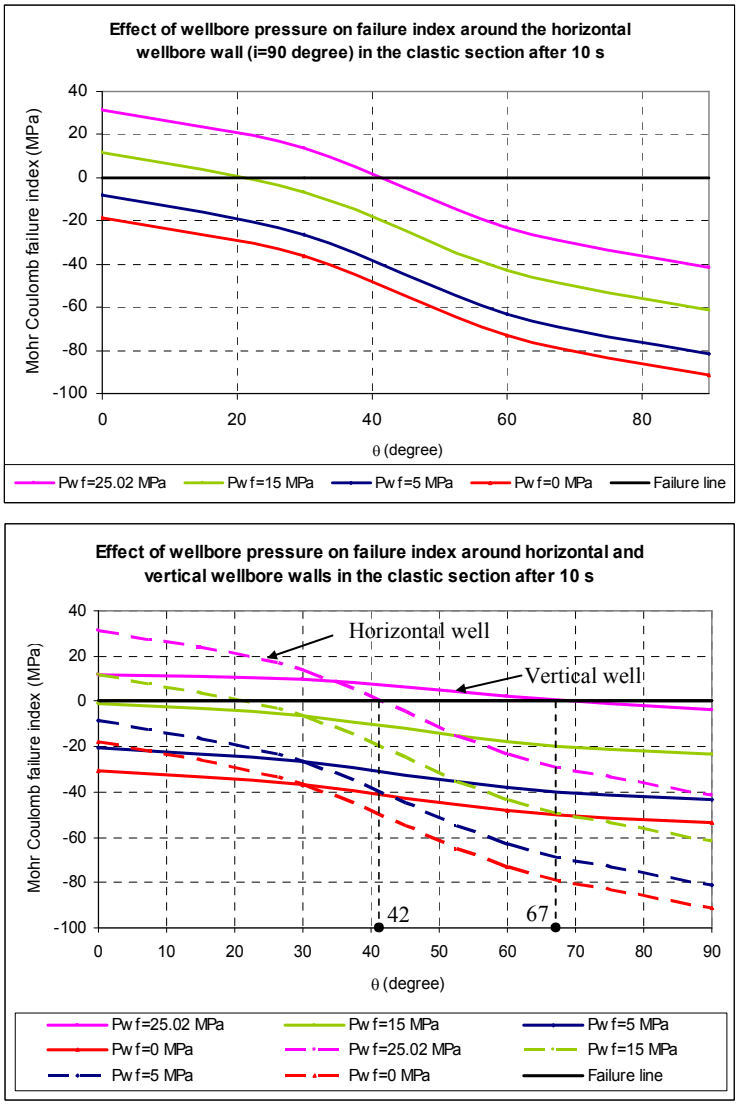

Fig 6.56. *Effect of wellbore pressure and wellbore inclination on failure index around the wellbore wall in the clastic section after 10 s*

In clastic section, the wellbore instability happens even when the wellbore pressure is maintained in the balance to formation pore pressure (25.02 MPa). The wellbore partially collapses at this wellbore pressure. According the calculated results, the collapsed area of the horizontal wellbore in this formation ($\theta = 67^o$ to 90^o) is larger than that of the vertical wellbore ($\theta = 42^o$ to 90^o). All above calculations show the horizontal wells in comparison to the vertical wells in the clastic formation seem to be less stable because the failure index in the same position at the wellbore wall is lower. This conclusion is opposite to the case of the basement section due to the difference of the initial stress condition. It means that if changing the inclination from zero (vertical well) to 90^o (horizontal well) and keeping the azimuth of the wellbore zero, the wellbore will less stable.

As the conclusion above, when the wellbore azimuth (a) is zero, drilling the vertical well in the clastic section of Basin X is better for wellbore stability than drilling the horizontal well (Fig 6.57). However, it is necessary to consider this conclusion in

case of azimuth variation. To do that, the alteration of failure index in these calculations is investigated case by case when the azimuth of the wellbore is varied from 0 to 90^o and the wellbore pressure is kept at 21.58 MPa (500 psi lower than formation pressure).

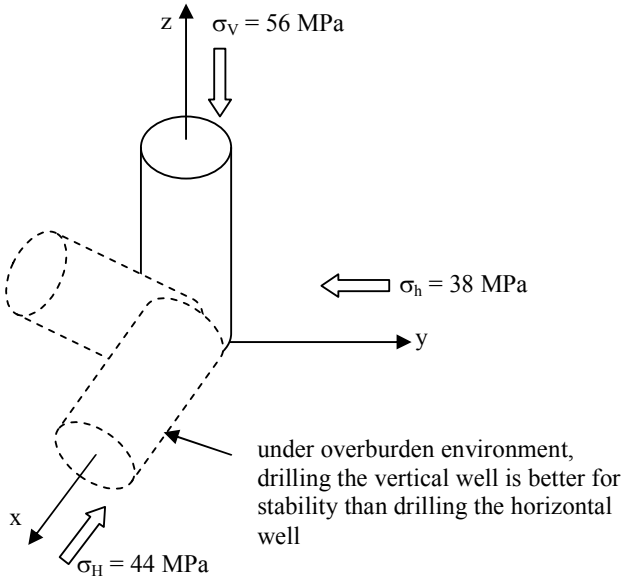

Fig 6.57. *The best inclination to drill in the clastic formation*

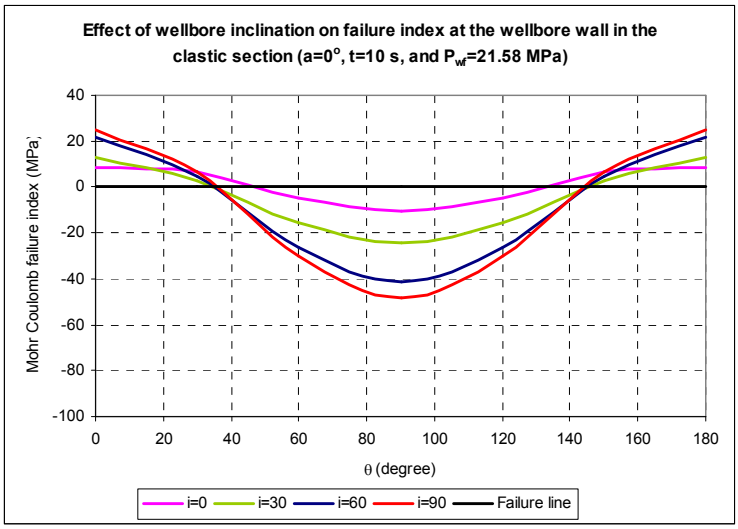

Fig 6.58. *Effect of wellbore inclination on failure index at the wellbore wall in the clastic section (a=0^o, t=10 s, and P_{wf}=32.34 MPa)*

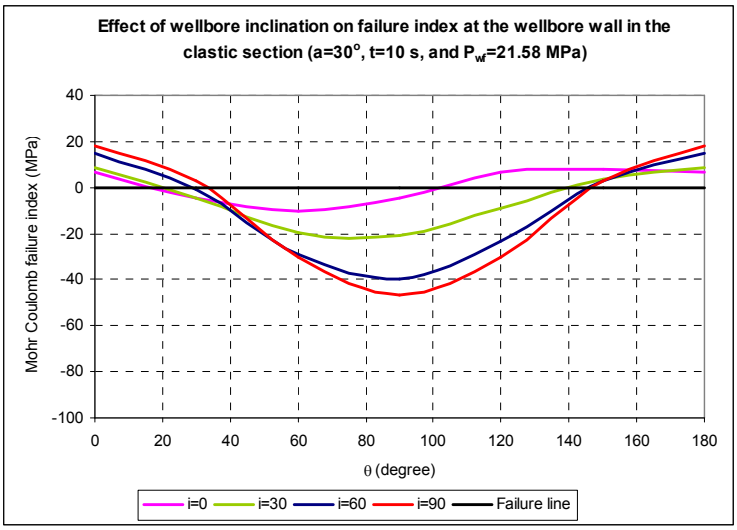

Fig 6.59. *Effect of wellbore inclination on failure index at the wellbore wall in the clastic section (a=30°, t=10 s, and P_{wf}=32.34 MPa)*

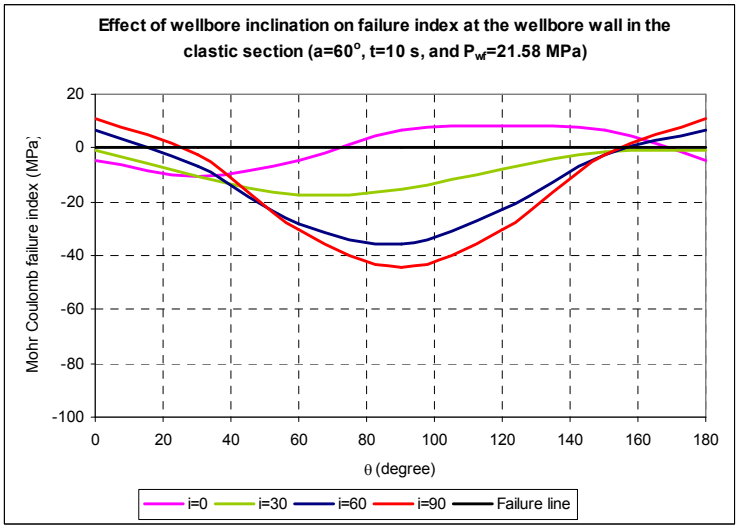

Fig 6.60. *Effect of wellbore inclination on failure index at the wellbore wall in the clastic section (a=60°, t=10 s, and P_{wf}=32.34 MPa)*

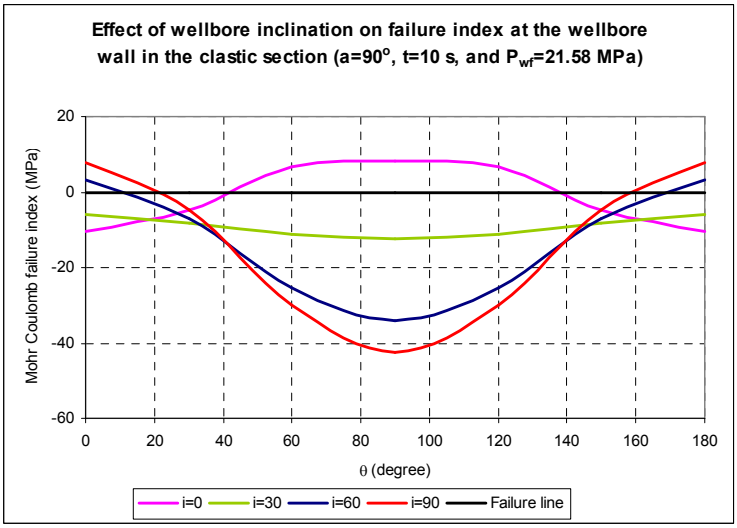

Fig 6.61. *Effect of wellbore inclination on failure index at the wellbore wall in the clastic section (a=90°, t=10 s, and P_{wf}=32.34 MPa)*

For a deviated wellbore in a clastic formation (overburden) oriented with azimuth zero degree (a = 0^o), parallel to the direction of the maximum horizontal stress, Fig 6.58 shows that the weakest point at the wellbore is located on y-axis in the direction of minimum horizontal stress (θ = 90^o) and the increase of inclination angle (i) in the range from 0^o to 90^o will decrease the stability of this point. This is contrary to the calculation of the wellbore stability in the basement. Moreover, while the influence of the inclination to wellbore stability in the basement section at this direction (a = 0^o) can be ignored, this affect contributes significantly in the clastic section because the difference of failure indexes as calculated in Fig 6.58 is considerable.

All of cases of the azimuth variation, it is shown in Figs 6.59, 6.60, and 6,61 that that a deviated wellbore in an overburden formation is less stable towards collapse than a vertical well because the Mohr Coulomb failure index at the same weakest point decreases when the inclination increases. Besides, it is clear that the wellbores with inclinations more than 60^o can be treated as horizontal wellbores which was suggested by Aadnoy and Chenevert [21].

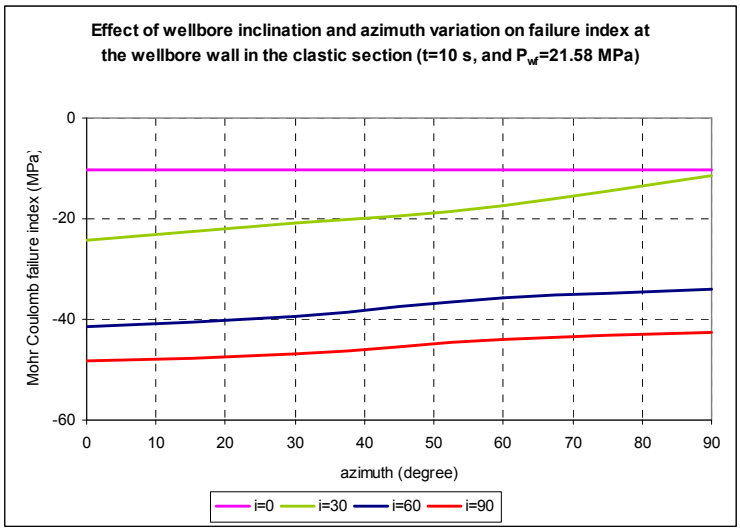

Fig 6.62. *Effect of wellbore inclination and azimuth variation on failure index at the weakest point of the wellbore wall when P_{wf}=32.34 MPa, t= 10 s*

Fig 6.62 indicates that azimuth angle has not impacted to the wellbore stability of all vertical or horizontal wells. However, according to wellbores with inclination over 30^o, the failure index gets the highest value as azimuth (a = 90^o), and lowest once a = 0^o. It means that the wellbore with inclination (>30^o) should be drilled in the direction of azimuth angle 90^o and the stability of the wellbore will decrease when the inclination angle increases.

To sum up, the results obtained in studying the effect of wellbore inclination and azimuth variation on the wellbore stability in the clastic formation of Basin X can be summarized as follows:

- The wellbores with inclinations over 30^o in the clastic section should be drilled in the minimum horizontal stress direction (a=90^o).

- The wellbores with inclinations more than 60^o can be treated as horizontal wellbores.

- In the overburden formation where the vertical stress is largest, drilling a vertical well will improve the stability of the wellbore more than drilling a horizontal well. The opposite conclusion is applied to basement formation of Basin X.

Poroelastic and thermo-poroelastic effects

All the simulations presented earlier have been for elastic case when pore pressure and temperature have not been coupled in calculation of the total stresses. The following results show a general case for the poroelastic and thermo-poroelastic formation. Figs 6.63 through 6.70, and Tables 6.3 - 6.10 display the difference of elastic, poroelastic and thermo-poroelastic formation to wellbore stability once wellbore trajectory changes. The input data is obtained from the basement section (Table 1, appendix E), and the clastic section (Table 2, appendix E). The wellbore pressures are assumed 500 psi lower than formation pressures (a range of 300 - 500 psi is commonly assumed in the literature [44]) in both cases, drilling through the clastic section and basement section.

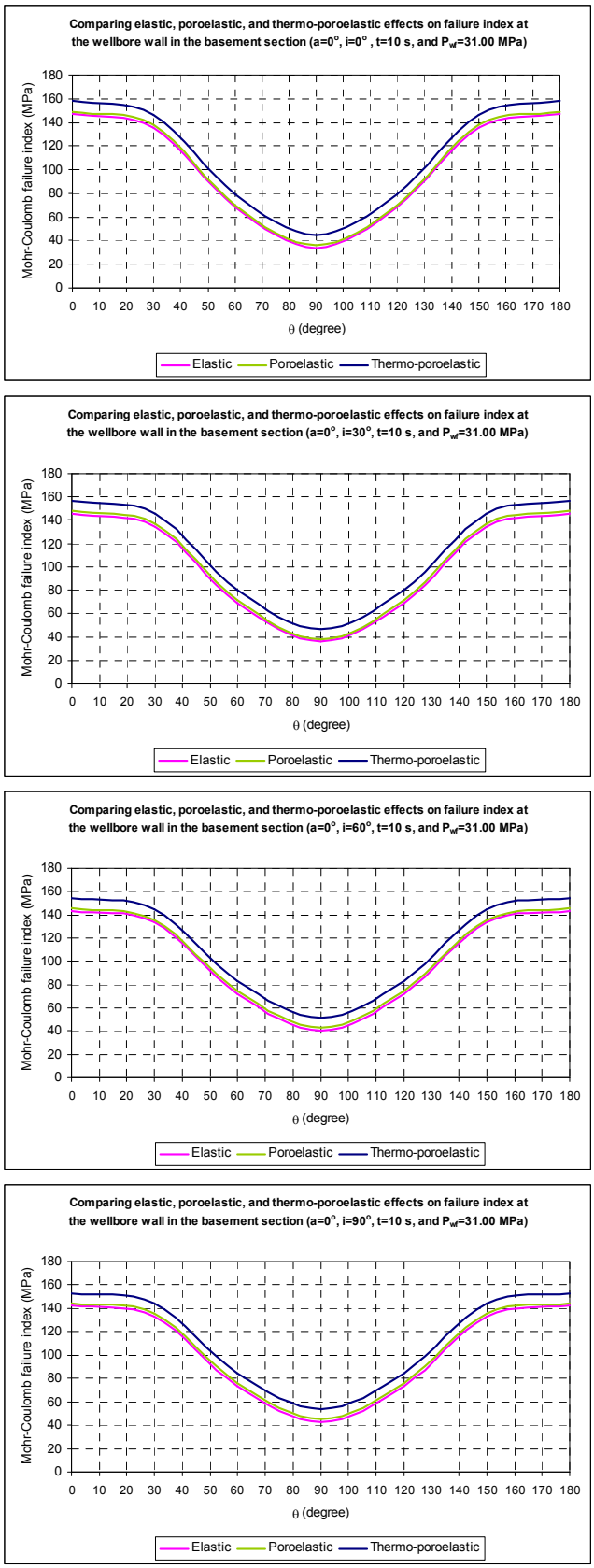

Fig 6.63. *The difference in elastic, poroelastic and thermo-poroelastic formation effects to wellbore stability in the basement section (a = 0^o, t=10 s, and P_{wf} = 31 MPa)*

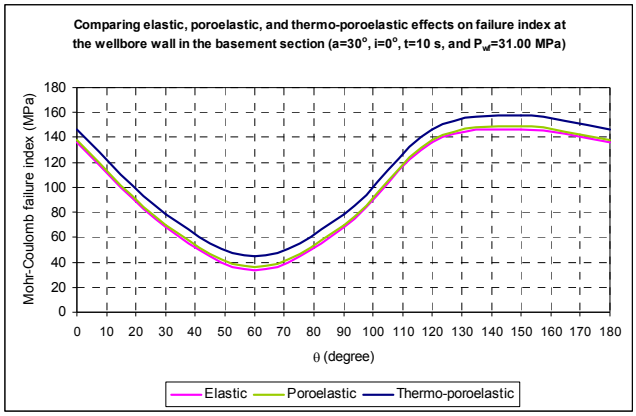

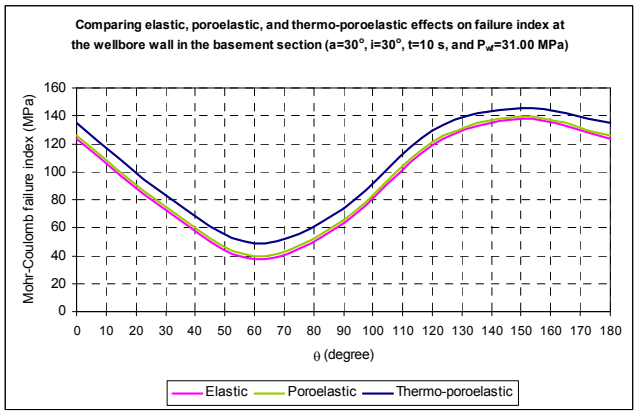

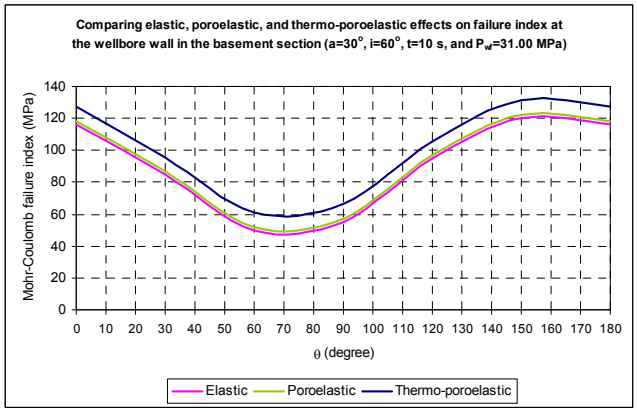

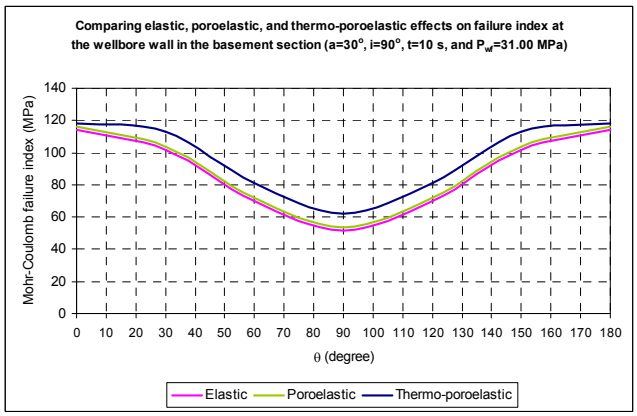

Fig 6.64. *The difference in elastic, poroelastic and thermo-poroelastic formation effects to wellbore stability in the basement section (a = 30°, t=10 s, and P_{wf} = 31 MPa)*

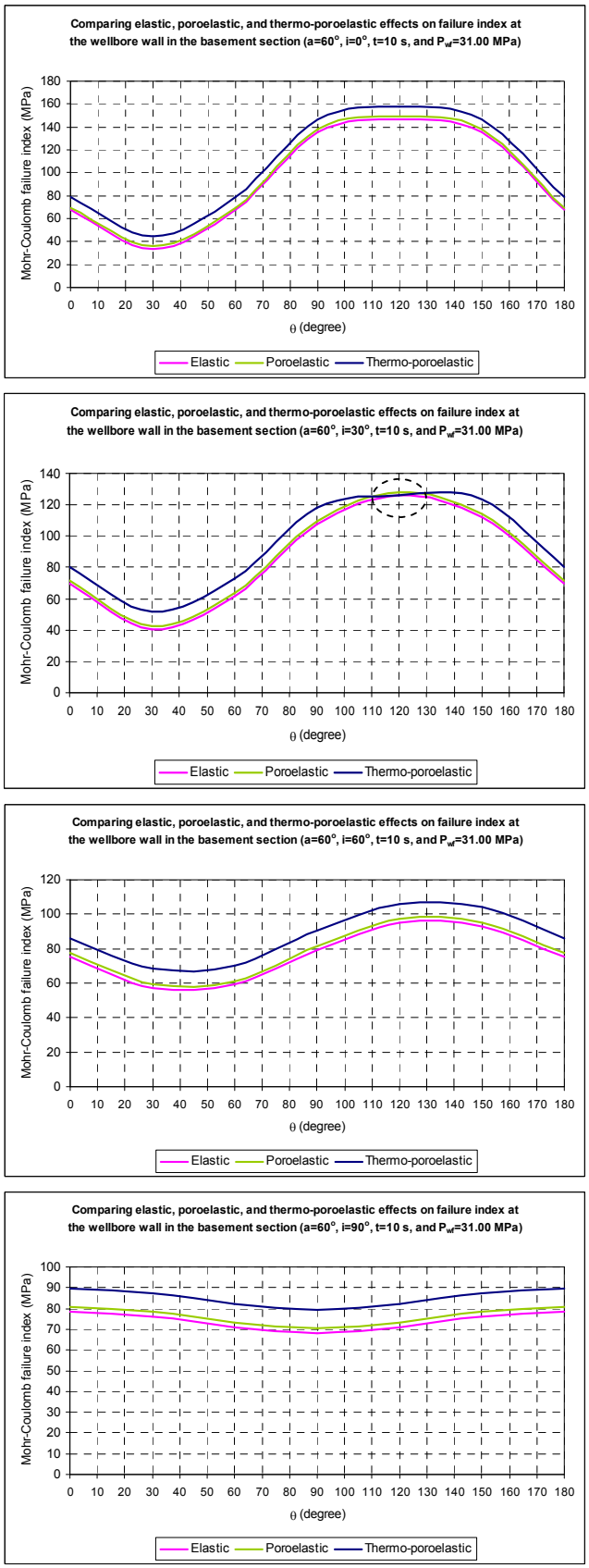

Fig 6.65. *The difference in elastic, poroelastic and thermo-poroelastic formation effects to wellbore stability in the basement section ($a = 60^o$, t=10 s, and $P_{wf} = 31$ MPa)*

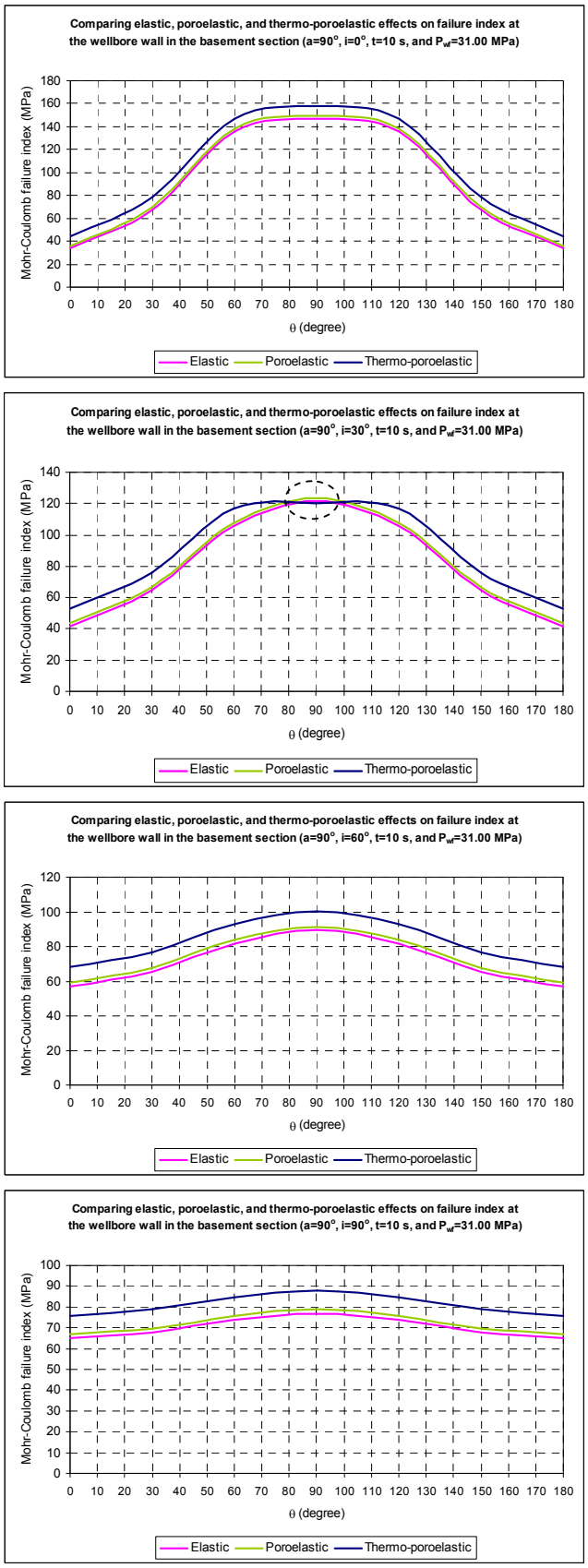

Fig 6.66. *The difference in elastic, poroelastic and thermo-poroelastic formation effects to wellbore stability in the basement section (a = 90^o, t=10 s, and P_{wf} = 31 MPa)*

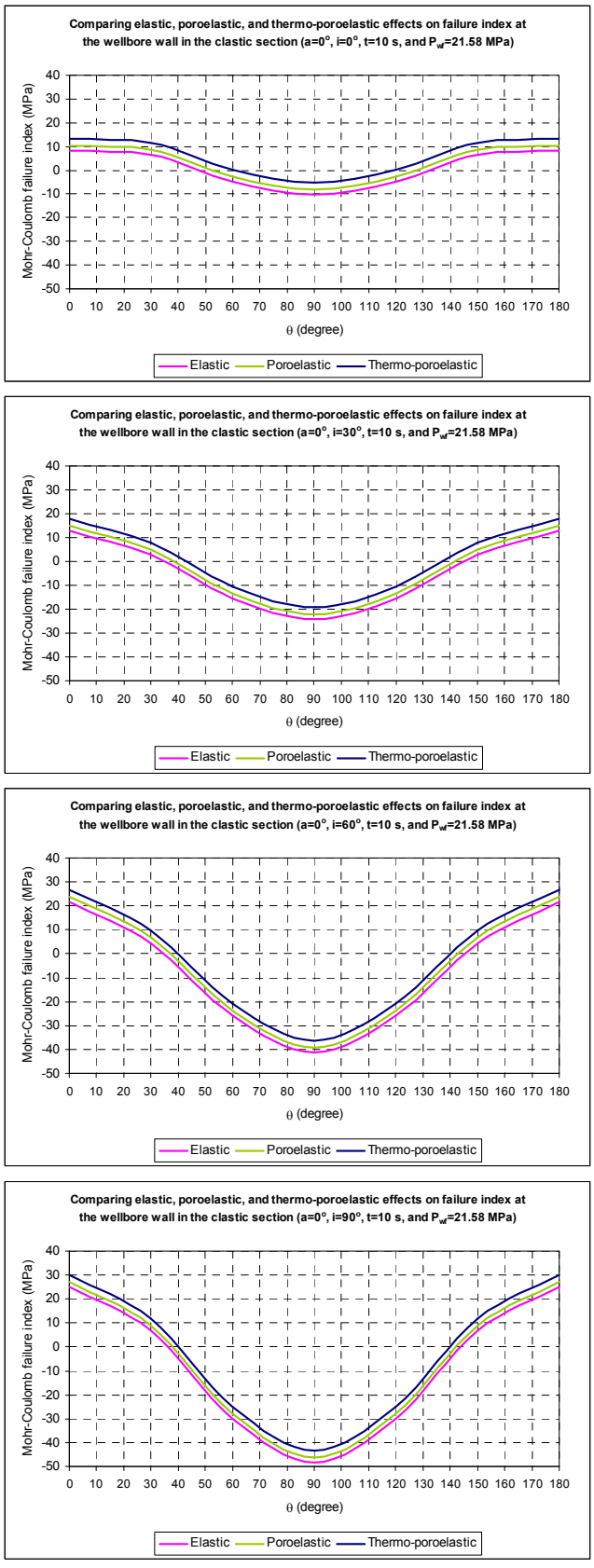

Fig 6.67. *The difference in elastic, poroelastic and thermo-poroelastic formation effects to wellbore stability in the clastic section ($a = 0^o$, t=10 s, and $P_{wf} = 21.58$ MPa)*

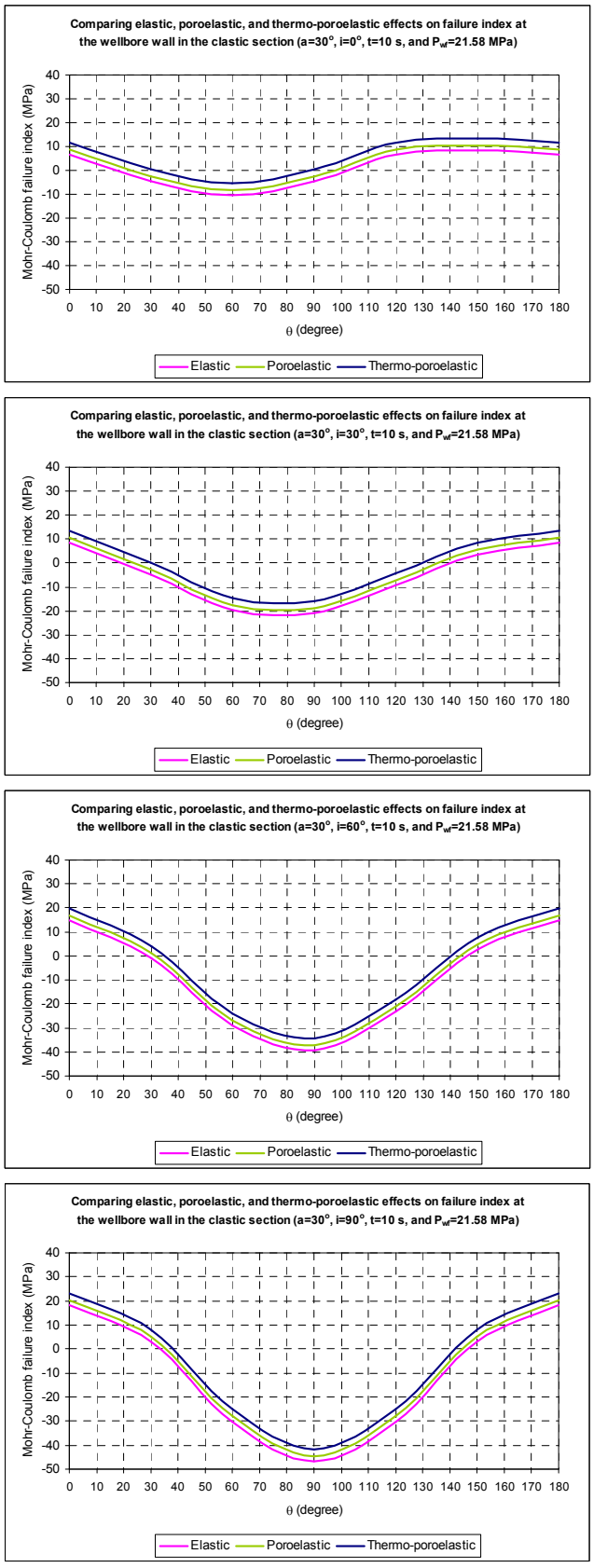

Fig 6.68. *The difference in elastic, poroelastic and thermo-poroelastic formation effects to wellbore stability in the clastic section ($a = 30^o$, $t=10$ s, and $P_{wf} = 21.58$ MPa)*

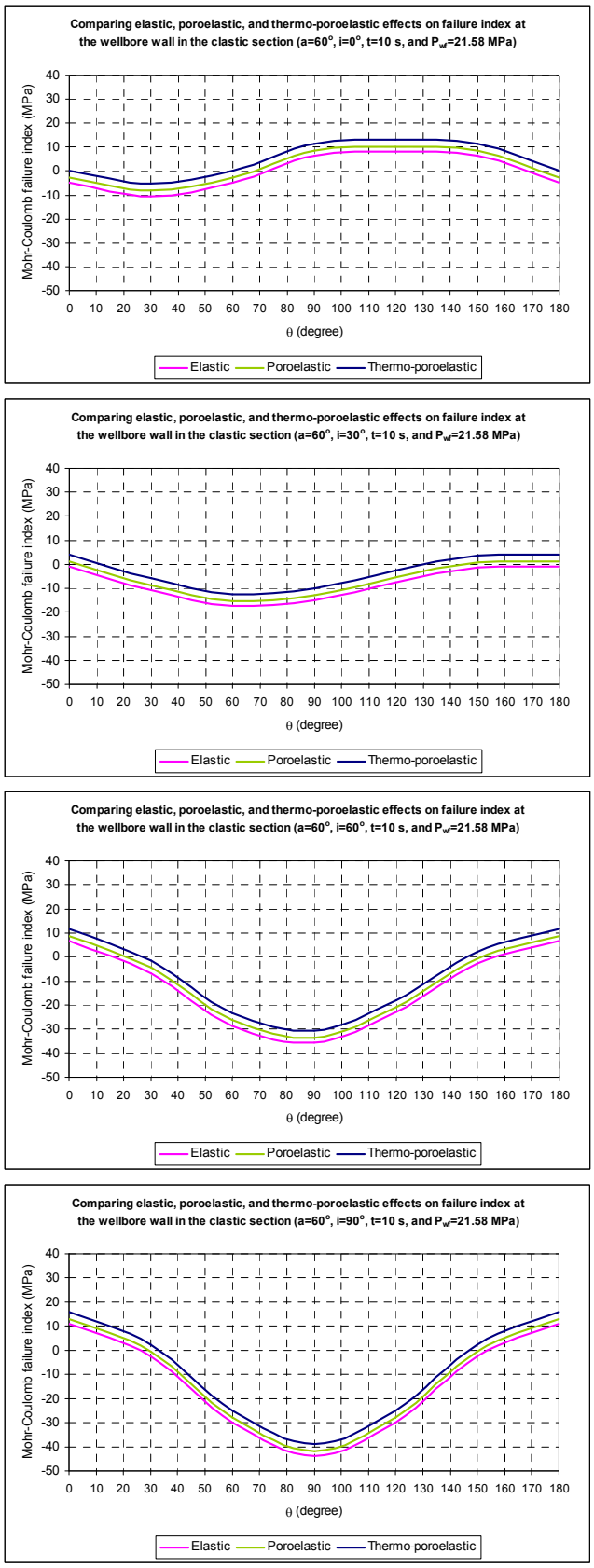

Fig 6.69. *The difference in elastic, poroelastic and thermo-poroelastic formation effects to wellbore stability in the clastic section ($a = 60^o$, t=10 s, and $P_{wf} = 21.58$ MPa)*

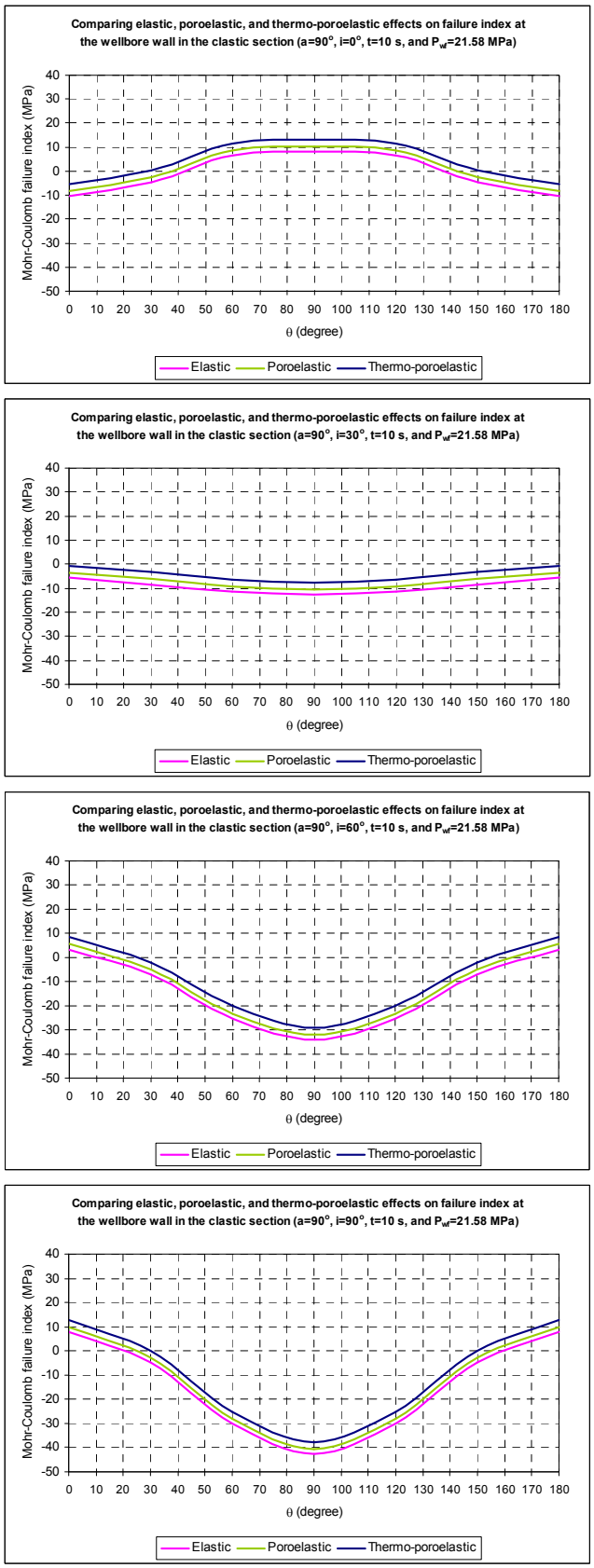

Fig 6.70. *The difference in elastic, poroelastic and thermo-poroelastic formation effects to wellbore stability in the clastic section ($a = 90^o$, t=10 s, and $P_{wf} = 21.58$ MPa)*

Table 6.3. *The difference in elastic, poroelastic and thermo-poroelastic formation effects to wellbore stability in the basement section (a = 0°, t=10 s, and P_{wf} = 31 MPa)*

Formation	Inclination (degree)	Mohr Coulomb failure index (MPa)						
		θ = 0°	θ = 30°	θ = 60°	θ = 90°	θ = 120°	θ = 150°	θ = 180°
Elastic	i = 0°	146.78	135.74	67.74	33.74	67.74	135.74	146.78
	i = 30°	145.61	134.69	69.14	35.90	69.14	134.69	145.61
	i = 60°	143.27	133.59	72.13	40.39	72.13	133.59	143.27
	i = 90°	142.10	133.42	73.74	42.74	73.74	133.42	142.10
Poroelastic	i = 0°	148.89	137.85	69.85	35.85	69.85	137.85	148.89
	i = 30°	147.72	136.80	71.24	38.00	71.24	136.80	147.72
	i = 60°	145.38	135.70	74.23	42.50	74.23	135.70	145.38
	i = 90°	144.21	135.53	75.85	44.85	75.85	135.53	144.21
Thermo-poroelastic	i = 0°	157.81	146.77	78.77	44.77	78.77	146.77	157.81
	i = 30°	156.64	145.72	80.16	46.92	80.16	145.72	156.64
	i = 60°	154.30	144.62	83.15	51.41	83.15	144.62	154.30
	i = 90°	153.13	144.45	84.77	53.77	84.77	144.45	153.13

Table 6.4. *The difference in elastic, poroelastic and thermo-poroelastic formation effects to wellbore stability in the basement section (a = 30°, t=10 s, and P_{wf} = 31 MPa)*

Formation	Inclination (degree)	Mohr Coulomb failure index (MPa)						
		θ = 0°	θ = 30°	θ = 60°	θ = 90°	θ = 120°	θ = 150°	θ = 180°
Elastic	i = 0°	135.74	67.74	33.74	67.74	135.74	146.78	135.74
	i = 30°	123.49	72.40	37.68	63.21	118.68	137.58	123.49
	i = 60°	116.21	84.78	49.91	55.02	94.59	120.11	116.21
	i = 90°	114.00	101.60	69.94	51.24	69.94	101.60	114.00
Poroelastic	i = 0°	137.85	69.85	35.85	69.85	137.85	148.89	137.85
	i = 30°	125.60	74.51	39.79	65.31	120.79	139.69	125.60
	i = 60°	118.32	86.88	52.02	57.12	96.70	122.22	118.32
	i = 90°	116.11	103.71	72.05	53.35	72.05	103.71	116.11
Thermo-poroelastic	i = 0°	146.77	78.77	44.77	78.77	146.77	157.81	146.77
	i = 30°	134.52	83.43	48.71	74.23	129.71	145.19	134.52
	i = 60°	127.23	95.80	60.94	66.04	105.62	131.14	127.23
	i = 90°	118.49	112.63	80.96	62.27	80.96	112.63	118.49

Table 6.5. *The difference in elastic, poroelastic and thermo-poroelastic formation effects to wellbore stability in the basement section (a = 60°, t=10 s, and P_{wf} = 31 MPa)*

Formation	Inclination (degree)	Mohr Coulomb failure index (MPa)						
		θ = 0°	θ = 30°	θ = 60°	θ = 90°	θ = 120°	θ = 150°	θ = 180°
Elastic	i = 0°	67.74	33.74	67.74	135.74	146.78	135.74	67.74
	i = 30°	69.59	40.46	61.87	107.20	**126.01**	112.22	69.59
	i = 60°	75.23	57.34	59.27	79.31	95.03	92.99	75.23
	i = 90°	78.63	76.14	70.95	68.24	70.95	76.14	78.63
Poroelastic	i = 0°	69.85	35.85	69.85	137.85	148.89	137.85	69.85
	i = 30°	71.70	42.56	63.98	109.30	**128.12**	114.33	71.70
	i = 60°	77.34	59.45	61.38	81.42	97.14	95.10	77.34
	i = 90°	80.74	78.25	73.06	70.35	73.06	78.25	80.74
Thermo-poroelastic	i = 0°	78.77	44.77	78.77	146.77	157.81	146.77	78.77
	i = 30°	80.61	51.48	72.90	118.22	**126.38**	123.25	80.61
	i = 60°	86.26	68.36	70.30	90.33	106.05	104.02	86.26
	i = 90°	89.66	87.17	81.98	79.27	81.98	87.17	89.66

Table 6.6. *The difference in elastic, poroelastic and thermo-poroelastic formation effects to wellbore stability in the basement section (a = 90°, t=10 s, and P_{wf} = 31 MPa)*

Formation	Inclination (degree)	Mohr Coulomb failure index (MPa)						
		θ = 0°	θ = 30°	θ = 60°	θ = 90°	θ = 120°	θ = 150°	θ = 180°
Elastic	i = 0°	33.74	67.74	135.74	146.78	135.74	67.74	33.74
	i = 30°	41.49	64.89	105.69	**121.43**	105.69	64.89	41.49
	i = 60°	56.99	65.55	81.76	89.34	81.76	65.55	56.99
	i = 90°	64.74	67.74	73.74	76.74	73.74	67.74	64.74
Poroelastic	i = 0°	35.85	69.85	137.85	148.89	137.85	69.85	35.85
	i = 30°	43.60	67.00	107.80	**123.54**	107.80	67.00	43.60
	i = 60°	59.10	67.66	83.87	91.45	83.87	67.66	59.10
	i = 90°	66.85	69.85	75.85	78.85	75.85	69.85	66.85
Thermo-poroelastic	i = 0°	44.77	78.77	146.77	157.81	146.77	78.77	44.77
	i = 30°	52.52	75.92	116.71	**119.89**	116.71	75.92	52.52
	i = 60°	68.02	76.58	92.78	100.36	92.78	76.58	68.02
	i = 90°	75.77	78.77	84.77	87.77	84.77	78.77	75.77

Table 6.7. *The difference in elastic, poroelastic and thermo-poroelastic formation effects to wellbore stability in the clastic section (a = 0°, t=10 s, and P_{wf} = 21.58 MPa)*

Formation	Inclination (degree)	Mohr Coulomb failure index (MPa)						
		θ = 0°	θ = 30°	θ = 60°	θ = 90°	θ = 120°	θ = 150°	θ = 180°
Elastic	i = 0°	8.16	6.57	-4.72	-10.40	-4.72	6.57	8.16
	i = 30°	13.09	2.81	-15.31	-24.23	-15.31	2.81	13.09
	i = 60°	21.80	4.53	-26.13	-41.34	-26.13	4.53	21.80
	i = 90°	24.95	6.64	-29.98	-48.29	-29.98	6.64	24.95
Poroelastic	i = 0°	10.27	8.68	-2.62	-8.30	-2.62	8.68	10.27
	i = 30°	15.19	4.91	-13.21	-22.13	-13.21	4.91	15.19
	i = 60°	23.90	6.63	-24.03	-39.24	-24.03	6.63	23.90
	i = 90°	27.05	8.74	-27.88	-46.19	-27.88	8.74	27.05
Thermo-poroelastic	i = 0°	13.16	11.57	0.28	-5.40	0.28	11.57	13.16
	i = 30°	18.08	7.81	-10.31	-19.24	-10.31	7.81	18.08
	i = 60°	26.79	9.53	-21.14	-36.35	-21.14	9.53	26.79
	i = 90°	29.95	11.64	-24.98	-43.29	-24.98	11.64	29.95

Table 6.8. *The difference in elastic, poroelastic and thermo-poroelastic formation effects to wellbore stability in the clastic section (a = 30°, t=10 s, and P_{wf} = 21.58 MPa)*

Formation	Inclination (degree)	Mohr Coulomb failure index (MPa)						
		θ = 0°	θ = 30°	θ = 60°	θ = 90°	θ = 120°	θ = 150°	θ = 180°
Elastic	i = 0°	6.57	-4.72	-10.40	-4.72	6.57	8.16	6.57
	i = 30°	8.47	-4.78	-19.82	-20.97	-9.22	3.53	8.47
	i = 60°	14.93	-0.76	-29.00	-39.45	-23.14	2.69	14.93
	i = 90°	18.31	2.93	-30.11	-46.87	-30.11	2.93	18.31
Poroelastic	i = 0°	8.68	-2.62	-8.30	-2.62	8.68	10.27	8.68
	i = 30°	10.57	-2.68	-17.72	-18.87	-7.11	5.63	10.57
	i = 60°	17.04	1.34	-26.90	-37.35	-21.03	4.79	17.04
	i = 90°	20.42	5.03	-28.01	-44.77	-28.01	5.03	20.42
Thermo-poroelastic	i = 0°	11.57	0.28	-5.40	0.28	11.57	13.16	11.57
	i = 30°	13.46	0.22	-14.83	-15.97	-4.22	8.52	13.46
	i = 60°	19.93	4.23	-24.00	-34.45	-18.14	7.68	19.93
	i = 90°	23.31	7.93	-25.12	-41.87	-25.12	7.93	23.31

Table 6.9. *The difference in elastic, poroelastic and thermo-poroelastic formation effects to wellbore stability in the clastic section (a = 60°, t=10 s, and P_{wf} = 21.58 MPa)*

Formation	Inclination (degree)	Mohr Coulomb failure index (MPa)						
		θ = 0°	θ = 30°	θ = 60°	θ = 90°	θ = 120°	θ = 150°	θ = 180°
Elastic	i = 0°	-4.72	-10.40	-4.72	6.57	8.16	6.57	-4.72
	i = 30°	-1.04	-10.73	-17.43	-15.11	-7.67	-1.35	-1.04
	i = 60°	6.84	-6.65	-28.43	-35.82	-22.89	-2.62	6.84
	i = 90°	10.89	-2.52	-30.10	-44.03	-30.10	-2.52	10.89
Poroelastic	i = 0°	-2.62	-8.30	-2.62	8.68	10.27	8.68	-2.62
	i = 30°	1.06	-8.63	-15.33	-13.01	-5.57	0.75	1.06
	i = 60°	8.94	-4.54	-26.33	-33.72	-20.79	-0.52	8.94
	i = 90°	12.99	-0.42	-28.00	-41.93	-28.00	-0.42	12.99
Thermo-poroelastic	i = 0°	0.28	-5.40	0.28	11.57	13.16	11.57	0.28
	i = 30°	3.95	-5.73	-12.43	-10.12	-2.68	3.64	3.95
	i = 60°	11.83	-1.65	-23.43	-30.82	-17.89	2.38	11.83
	i = 90°	15.88	2.48	-25.11	-39.03	-25.11	2.48	15.88

Table 6.10. *The difference in elastic, poroelastic and thermo-poroelastic formation effects to wellbore stability in the clastic section (a = 90°, t=10 s, and P_{wf} = 21.58 MPa)*

Formation	Inclination (degree)	Mohr Coulomb failure index (MPa)						
		θ = 0°	θ = 30°	θ = 60°	θ = 90°	θ = 120°	θ = 150°	θ = 180°
Elastic	i = 0°	-10.40	-4.72	6.57	8.16	6.57	-4.72	-10.40
	i = 30°	-5.82	-8.30	-11.39	-12.50	-11.39	-8.30	-5.82
	i = 60°	3.34	-6.97	-25.33	-34.08	-25.33	-6.97	3.34
	i = 90°	7.91	-4.72	-29.98	-42.61	-29.98	-4.72	7.91
Poroelastic	i = 0°	-8.30	-2.62	8.68	10.27	8.68	-2.62	-8.30
	i = 30°	-3.72	-6.20	-9.28	-10.40	-9.28	-6.20	-3.72
	i = 60°	5.44	-4.87	-23.23	-31.98	-23.23	-4.87	5.44
	i = 90°	10.01	-2.62	-27.88	-40.51	-27.88	-2.62	10.01
Thermo-poroelastic	i = 0°	-5.40	0.28	11.57	13.16	11.57	0.28	-5.40
	i = 30°	-0.82	-3.30	-6.39	-7.50	-6.39	-3.30	-0.82
	i = 60°	8.33	-1.97	-20.34	-29.09	-20.34	-1.97	8.33
	i = 90°	12.91	0.28	-24.98	-37.61	-24.98	0.28	12.91

In examining all results described above, it can be found that when poroelastic and thermo-poroelastic effects have been taken into account the investigation of wellbore stability, the failure index in case of coupling pressure and temperature will be higher than that of elastic case. This can be explained that coupling pore pressure and temperature in UBD will reduce the total tangential stress and axial stress while maintain the total radial stress at the wellbore. In the case of total radial stress is smallest, the reduction of tangential stress and axial stress will help the wellbore to be more stable because the Mohr Coulomb circle now will be smaller. However, if the reduction of hoop stress and axial stress makes them smaller than the radial stress, the above comment is not valid because the Mohr Coulomb circle will move to the left approaching the failure line and the wellbore wall becomes unstable. This can be observed on Figs 6.65-6.66 at inclination angle equal 30°. Briefly, analyzing wellbore stability regarding collapse in the elastic case is pessimistic in comparison to the poroelastic and thermo-poroelastic cases. It means that the wellbore wall which was supposed to be collapsed in elastic formation can be still stable in poroelastic or thermo-poroelastic formation. This conclusion is valid to both clastic and basement formations.

The second part of the result analysis in this section is considering which of the following has the main influence on wellbore stability: pressure coupling or temperature coupling. The results calculated for the basement section from Figs 6.63-6.66 show clearly that the temperature coupling is the main influence on wellbore stability while the effect of pore pressure coupling can be ignored because the difference between the failure line of elastic formation and poroelastic formation is negligible. This conclusion can be applied for granite basements. In other cases, this will depend on magnitude of each parameter. However, notice that this conclusion is obtained when the difference of wellbore pressure (31.00 MPa) and formation pressure (34.45 MPa) is 3.45 MPa (500 psi). So, it is important to take into account wellbore pressure variation when analysing poroelastic and thermo-poroelastic effects to wellbore stability. Figs 6.71 - 6.72 display the difference of elastic, poroelastic and thermo-poroelastic effects on wellbore stability when wellbore pressure decreases 10 MPa. It is clear that once reducing the wellbore pressure from 31.00 MPa to 10 MPa, the difference between wellbore pressure and formation pressure will increase. So, Mohr Coulomb failure index in this case has been affected remarkably by pore pressure coupling. Figs 6.71 and 6.72 can be plotted from the input data referred to in Table 3, appendix E.

In contrast the basement section, the results calculated for the clastic section (Figs 6.67-6.70) show that both temperature and pressure coupling have influenced equally on wellbore stability even the differenent of wellbore pressure and formation pressure in this calculation is just 500 psi which is the same as the pressure difference applied to basement section's calculation.

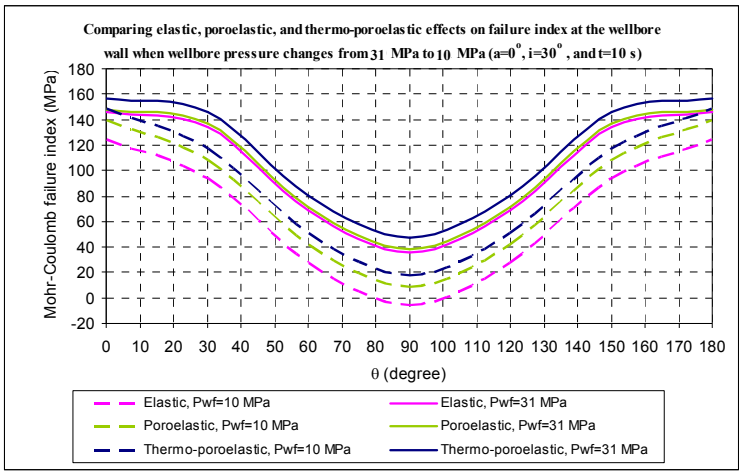

Fig 6.71. *Elastic, poroelastic, and thermo-poroelastic effects on wellbore stability when wellbore pressure changes from 31 MPa to 10 MPa ($a=0^o$, $i=30^o$, and t = 10 s)*

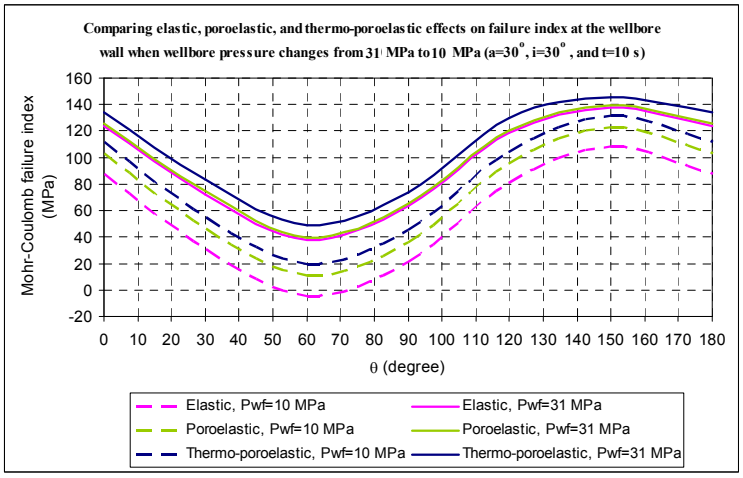

Fig 6.72. *Elastic, poroelastic, and thermo-poroelastic effects on wellbore stability when wellbore pressure changes from 31 MPa to 10 MPa ($a=30^o$, $i=30^o$, and $t = 10$ s)*

To sum up, the following conclusion can be obtained:

- The wellbore stability will get beneficial effects when the coupling of pore pressure and temperature has been taken into account, and these effects depend mainly on the difference between wellbore pressure and temperature with formation pressure and temperature.
- In basement section, the effect of temperature coupling dominates the effect of pressure coupling to the wellbore stability. In the clastic section, both factors have the equal influence to the wellbore stability.

As discussion in "Time dependent effect" section, this effect has influenced to effective stresses through the varying of pore pressure with time, but it has not affected to the total stresses in the elastic case. However, in poroelastic and thermo-poro-elastic formation, time dependent effects have involved the alteration of total stresses via the coupling of pore pressure and temperature. The comparison of elastic, poroelastic, and thermo-poro-elastic was expressed in Figs 6.73 - 6.75 which calculate the Mohr Coulomb failure index of elastic, poroelastic, thermo-poroelastic formation at 10 s and 3,600 s as a = 30^o, i = 60^o, θ = 60^o, and wellbore pressure P_{wf} = 10 MPa. See Table 4, appendix E to obtain the necessary data.

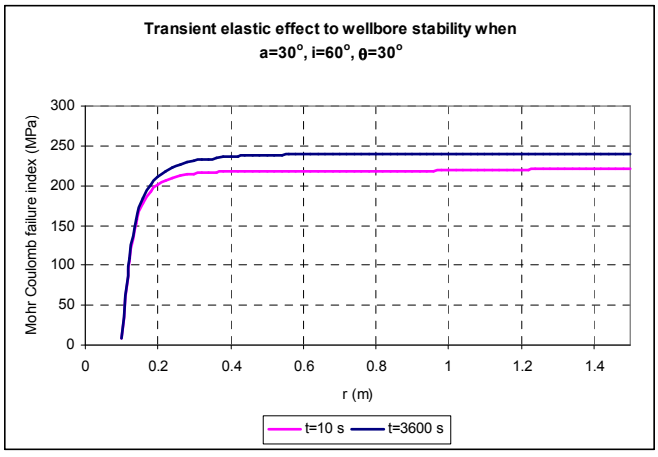

Fig 6.73. *Transient elastic effect to wellbore stability when $a = 30^o$, $i = 60^o$, $\theta = 60^o$*

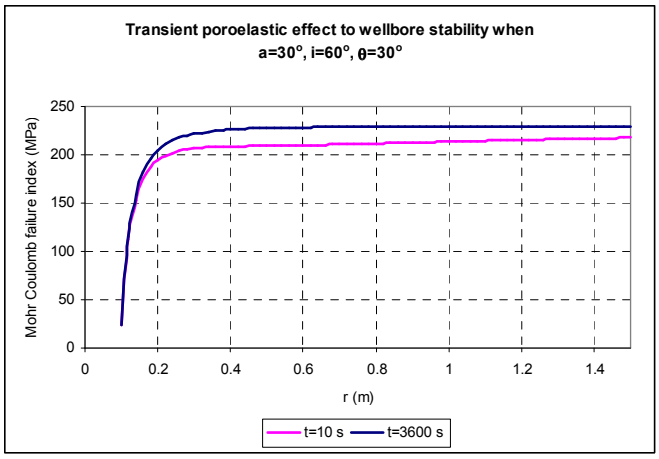

Fig 6.74. *Transient poroelastic effect to wellbore stability when a = 30°, i = 60°, θ = 60°*

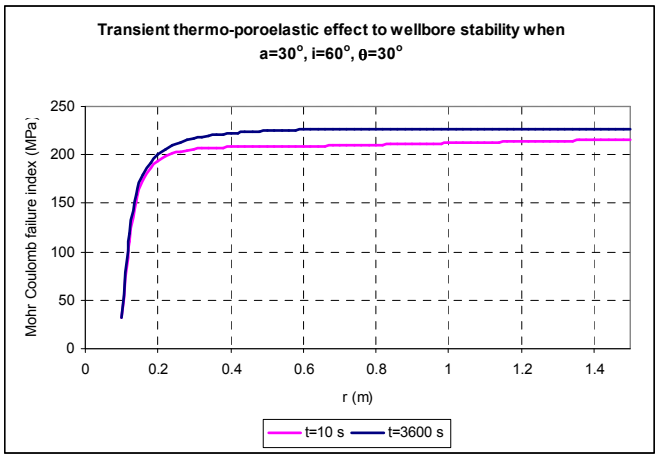

Fig 6.75. *Transient thermo-poroelastic effect to wellbore stability when a = 30°, i = 60°, θ = 60°*

Figs 6.73 - 6.75 shows Mohr Coulomb failure index in the elastic, poroelastic, and thermo-poroelastic formation at different time. These results emphasize that the time dependent effects only influence the wellbore stability of the formation around the wellbore but not at the wellbore wall in all cases, elastic, poroelastic, thermo-poroelastic formation.

Cooling and heating effects

The drilling fluid often has a temperature different from the formation due to thermal gradient down the borehole, or a borehole may be heated up to enhance production in heavy oil exploitation. In these cases, temperature difference exists between drilling fluid and the formation. As a result, heat transfer between the two media will occur. Changes in volume of the rock matrix and pore fluid induced by changes in temperature will depend on the thermal expansion of the rock matrix and pore fluid. They will result in changes in effective stresses and pore pressure which may lead to borehole failure. Hence, cooling or heating effect is a fundamental factor which needs to be taken into account in predicting time dependent wellbore stability. To determine the thermal effect on stability of the borehole, first, the distribution of the varied temperature around the wellbore has to be set up. Then, the stress distribution near the hole is established from equations in chapter 2. Finally, its effect on the

stability is analyzed. Therefore, the analysis in this section expresses the effect of cooling or heating wellbore temperature to wellbore stability in UBD. Figs 6.76 and 6.77 present evolution of temperature when the drilling fluid is heated from 131 ^{o}C in the initial condition to 150 ^{o}C then reduced to 98 ^{o}C.

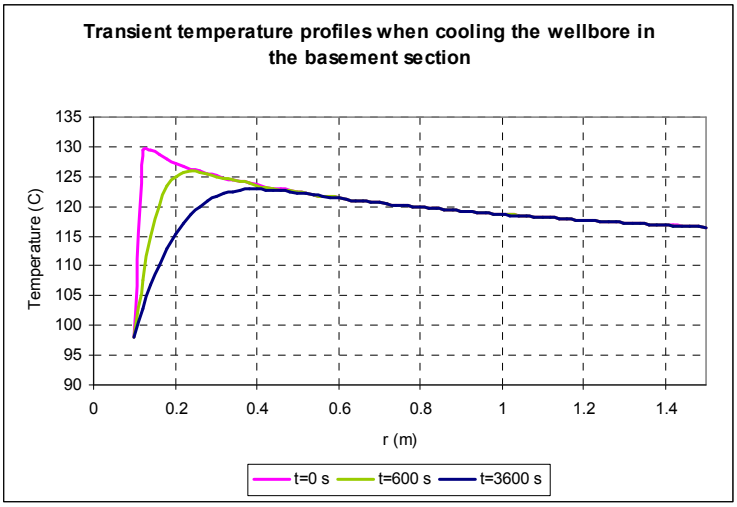

Fig 6.76. *Transient temperature profiles when cooling the wellbore in the basement section*

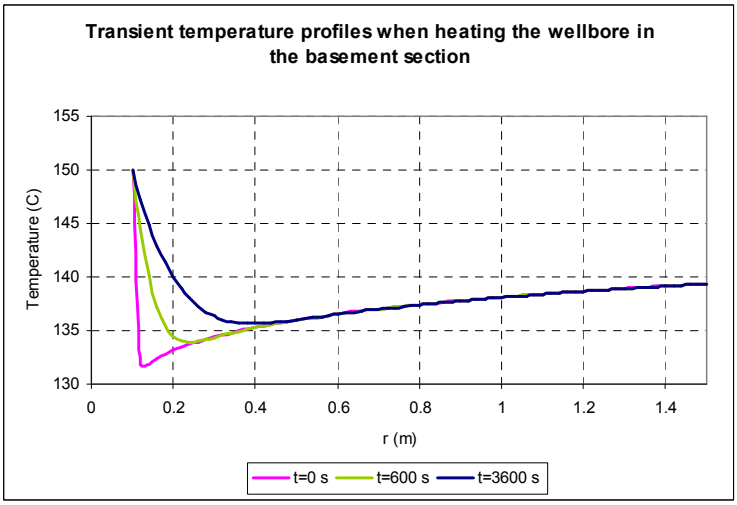

Fig 6.77. *Transient temperature profiles when heating the wellbore in the basement section*

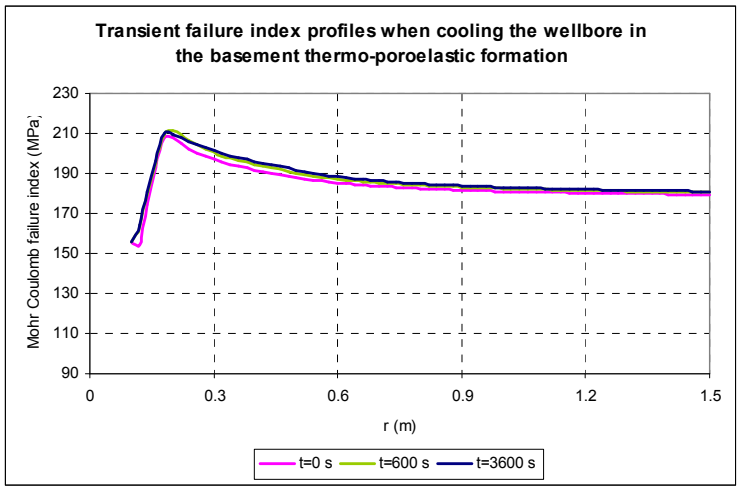

Fig 6.78. *Transient failure index profiles when cooling the wellbore in the basement thermo-poroelastic formation*

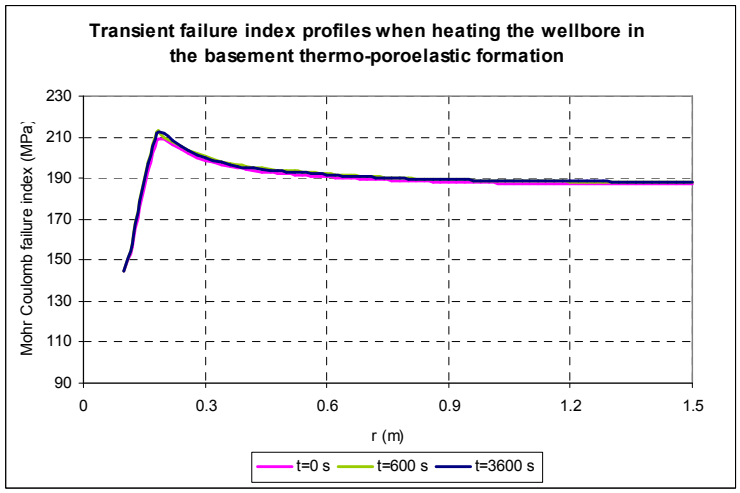

Fig 6.79. *Transient failure index profiles when heating the wellbore in the basement thermo-poroelastic formation*

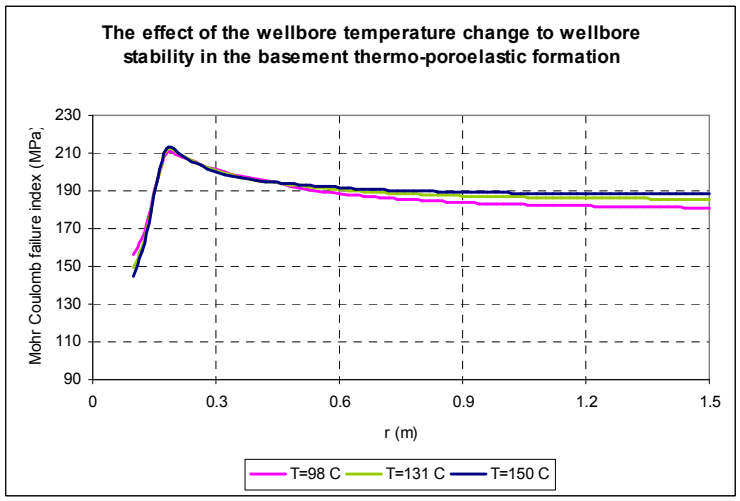

Fig 6.80. *The effect of wellbore temperature change to wellbore stability in the basement thermo-poroelastic formation*

Figs 6.78, and 6.79 show the transient wellbore stability profiles in thermo-poroelastic formation when cooling or heating the wellbore. It can be observed from the above figures that the difference between failure index profiles with time is quite small so the time dependent effects on wellbore stability in these calculations can be ignored and it can be acceptable to choose any given time after drilling to calculate the effect of wellbore temperature change to wellbore stability. For example, consider a geothermal temperature of 131 ^{o}C at a depth of 11,610 ft and assume that drilling fluid will have a temperature of 150 ^{o}C when it reaches that depth. If the wellbore temperature is kept constant for one hour (3,600 s) and then decreased to 98^{o} C, failure index around the wellbore will be simulated. The effect of this temperature change on wellbore stability can be seen in Fig 6.80. The result shows that cooling the wellbore temperature tends to increase the wellbore stability while the reverse applies to heating of the formation. Nevertheless, this conclusion remains valid for the formation within 0.1 m around the wellbore. Hence, when concerned with compressive failure preventions which was considered in UBD, heavier drilling fluid is need when it is at higher temperatures than the formation and lighter drilling fluid can be used when it is at lower temperatures than the formation. As a result, cooling of the drilling fluid may be used as an effective option to manage the wellbore stability, especially when the use of high mud weight is not feasible. Figs 6.76-6.80 are plotted from the input data of the basement section (Table 1, appendix F).

Figs 6.81-6.85 show the same analysis of the transient wellbore stability when heating or cooling the wellbore. However, the input data in these calculations is obtained from the clastic section (Table 2, appendice F).

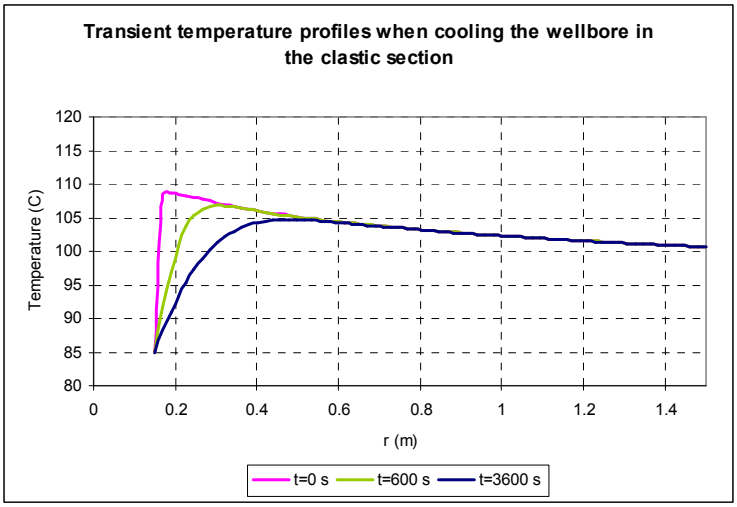

Fig 6.81. *Transient temperature profiles when cooling the wellbore in the clastic section*

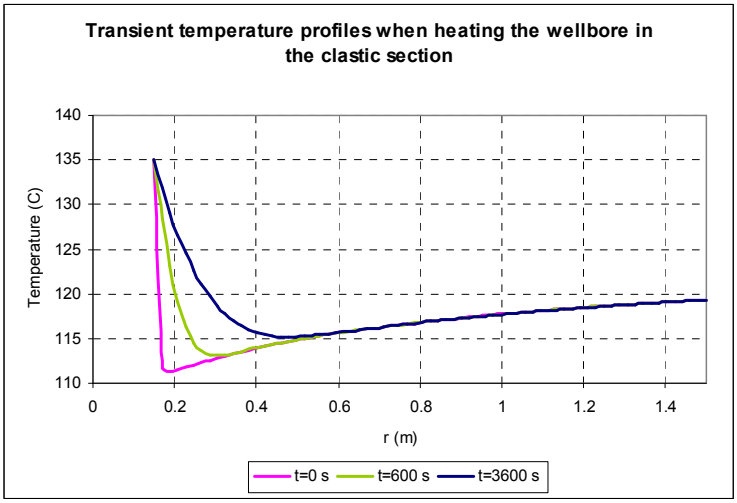

Fig 6.82. *Transient temperature profiles when heating the wellbore in the clastic section*

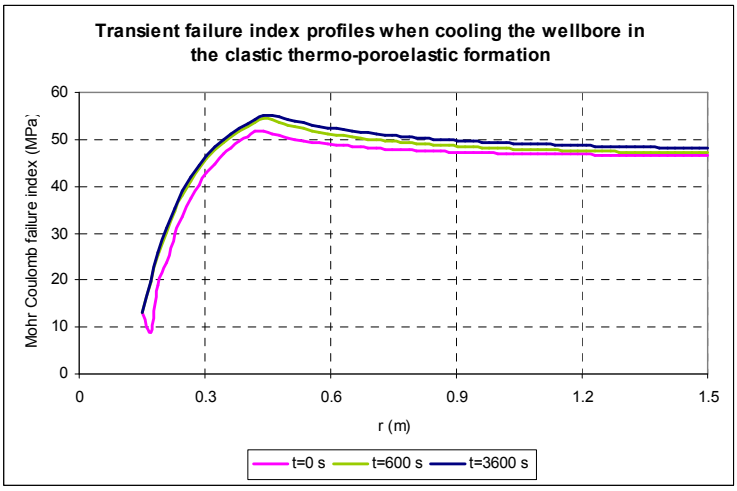

Fig 6.83. *Transient failure index profiles when cooling the wellbore in the clastic thermo-poroelastic formation*

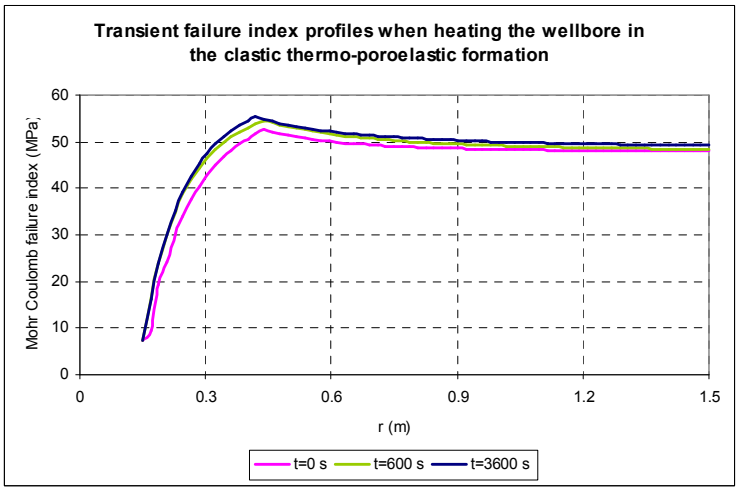

Fig 6.84. *Transient failure index profiles when heating the wellbore in the clastic thermo-poroelastic formation*

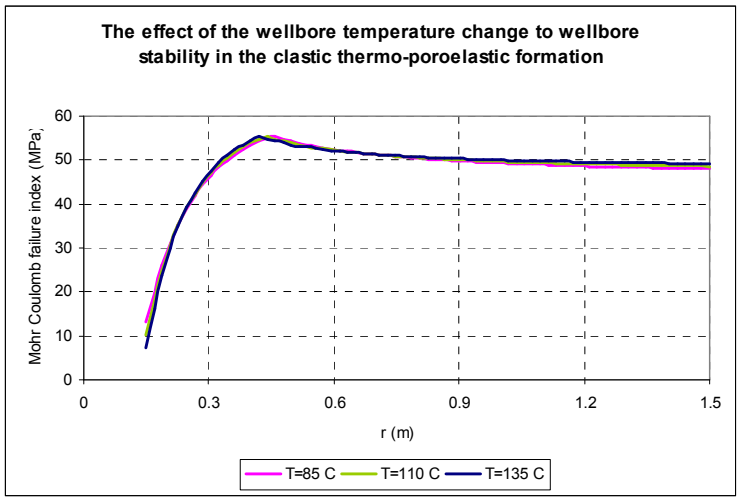

Fig 6.85. *The effect of wellbore temperature change to wellbore stability in the clastic thermo-poroelastic formation*

The same conclusions can be obtained for the effect of cooling or heating on the wellbore stability of the well drilled through the clastic section. The wellbore becomes more stable with the time because the failure index around the wellbore at the initial time is lower than the failure index after that although this increase of failure index with the time is quite small (Figs 6.81-6.84). As same as the basement section, cooling the wellbore temperature in the clastic section also tends to improve the wellbore stability and heating the wellbore will lead to the instability of the borehole (Fig 6.85). However, this recommendation is also accepted for the formation within 0.1 m around the wellbore not so far from the wellbore.

The result from Figs 6.80 and 6.85 also show that the weakest points are located at the wellbore wall because the failure index is lowest at these points, so it is important to verify the stability of the wellbore wall when changing the wellbore temperature. The following figures analyse the stability at the wellbore wall of a well with any inclination angle when heating or cooling the wellbore.

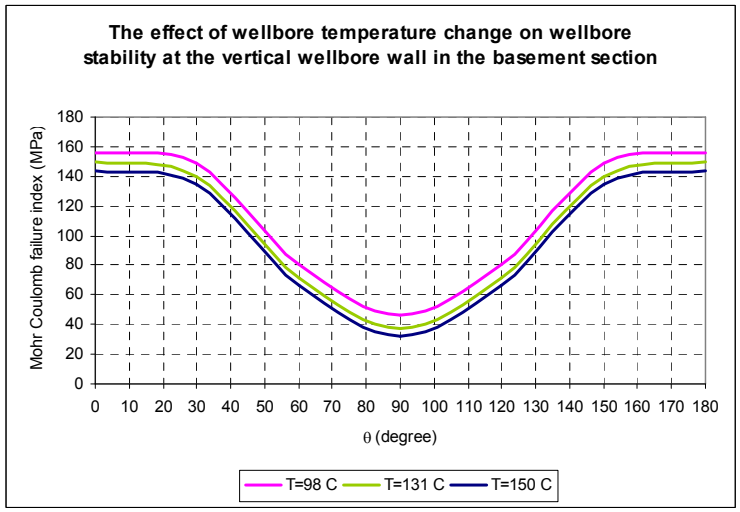

Fig 6.86. *The effect of wellbore temperature change to wellbore stability at the vertical wellbore wall in the basement section*

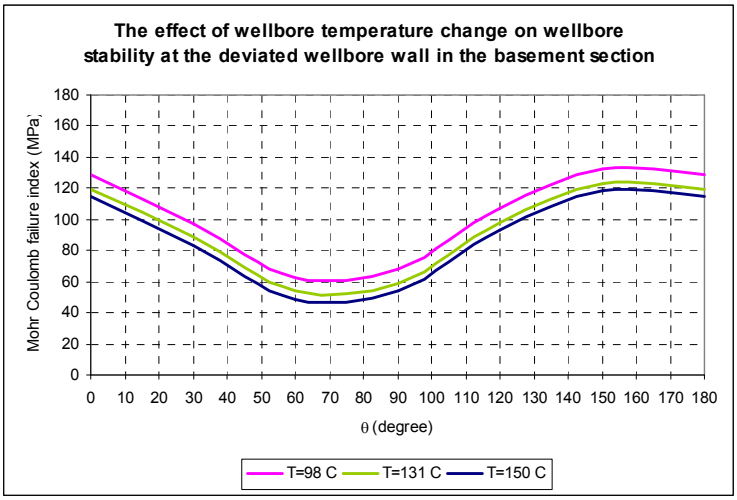

Fig 6.87. *The effect of wellbore temperature change to wellbore stability at the deviated wellbore wall in the basement section*

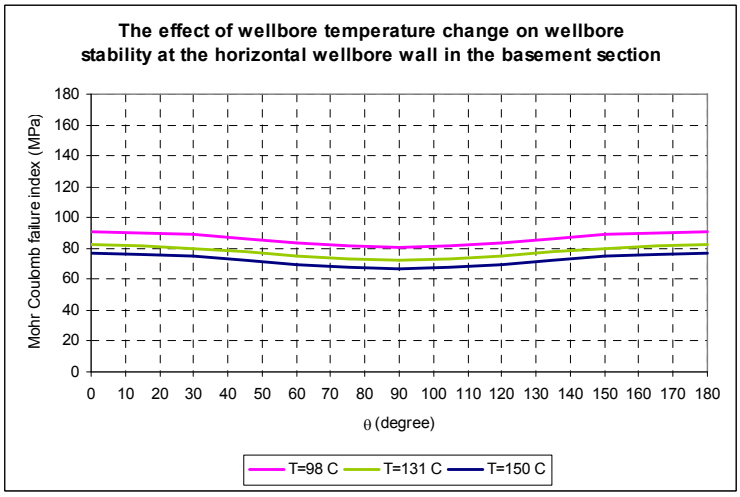

Fig 6.88. *The effect of wellbore temperature change to wellbore stability at the horizontal wellbore wall in the basement section*

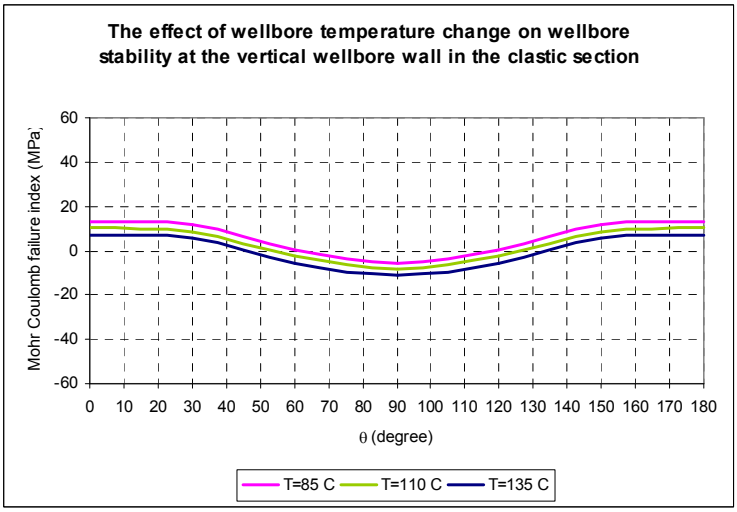

Fig 6.89. *The effect of wellbore temperature change to wellbore stability at the vertical wellbore wall in the clastic section*

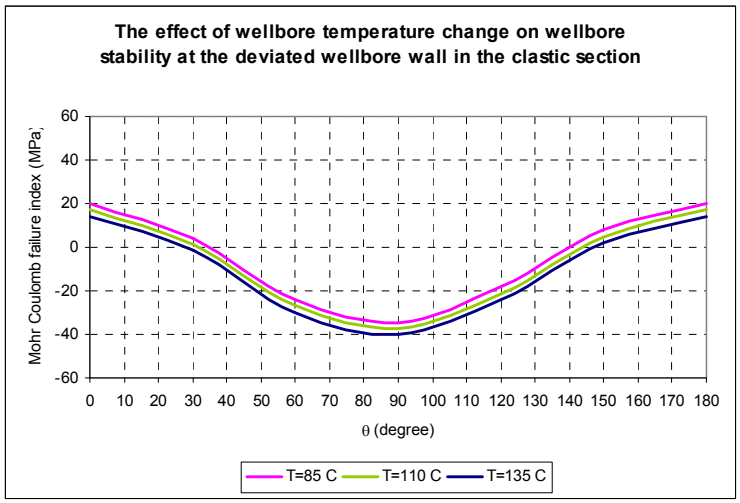

Fig 6.90. *The effect of wellbore temperature change to wellbore stability at the deviated wellbore wall in the clastic section*

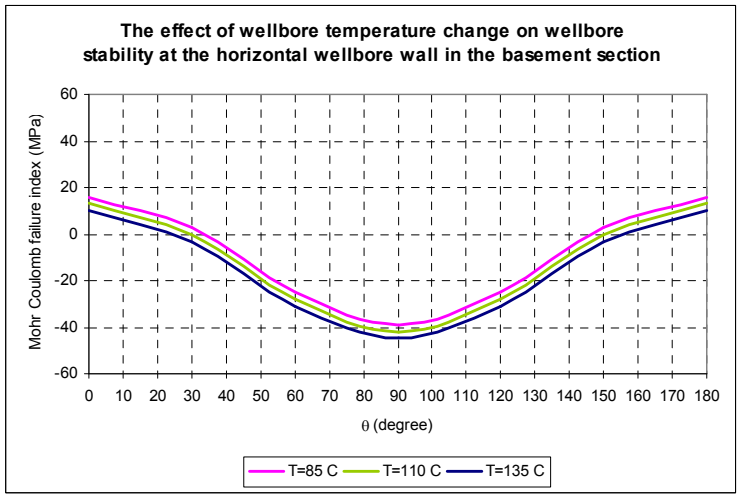

Fig 6.91. *The effect of wellbore temperature change to wellbore stability at the horizontal wellbore wall in the clastic section*

Figs 6.86 through 6.91 show that, cooling the wellbore in both basement and clastic formations will help the wellbore more stable despite the wellbore trajectory. This conclusion remains valid for any directional well. See Table 3, and 4, appendix F to get the input data to plot Figs 6.86 to 6.91.

To sum up, cooling improves the stability of the wellbore while heating reduces the failure index (Figs 6.86-6.91), and can induce wellbore instability. This conclusion remains valid for any directional well and not depends on the wellbore trajectory. However, this opinion can only be applied for the formation within 0.1 m around the wellbore not for the region so far from the wellbore. When the time dependent effect is taken into account the calculation of wellbore stability, the alteration of failure index is insignificant with different time.

Effect of thermal expansion coefficients

Volumetric expansion coefficients of granite rocks range from $5x10^{-6}$ $^{o}C^{-1}$ to $10x10^{-6}$ $^{o}C^{-1}$ [89]. Fig 6.92 shows that for a vertical well the failure index increases very

little for an increase of the thermal expansion coefficient. Thus, the effect of thermal expansion on the wellbore stability is insignificant. However, formations, in general, with higher thermal expansion coefficients (blue line in Fig 6.92) are less stable than the formations with lower thermal expansion coefficient (pink line) because the higher thermal expansion coeficients of material will suggests more strains, and displacements when temperature alters. The input data for Fig 6.92 is from Table 1, appendix G.

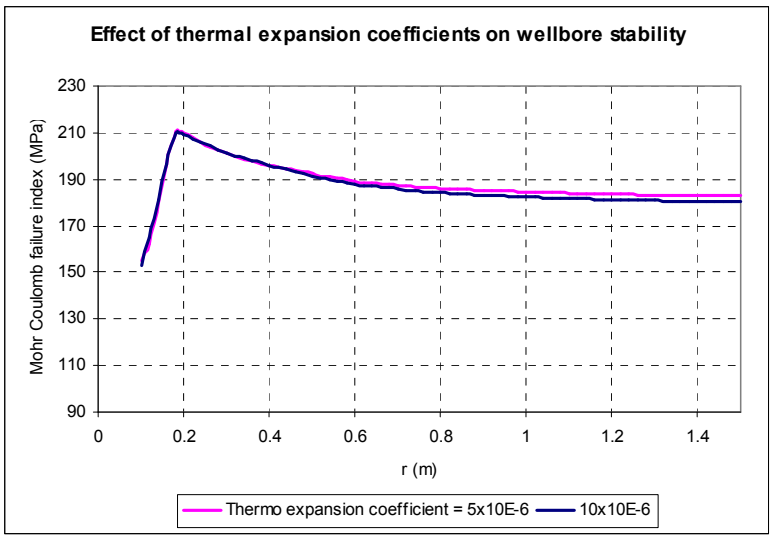

Fig 6.92. *Effect of thermal expansion coefficients on wellbore stability*

Estimating wellbore collapse pressure for horizontal wells in thermo-poroelastic formations

Wellbore collapse pressure is one of the most important parameters used to build up the Liquid Gas Rate Window (LGRW) that can be constructed based on formation pore pressure, wellbore collapse pressure, cuttings carrying capacity of the fluid mixture, and wellbore washout criteria. And it gives the field engineers flexibility in selection of liquid and gas injection rates on the drilling site. This study used Mohr Coulomb failure criterion for estimating formation collapse pressure. Assume that a deviated well is drilled with the inclination of 17 degree through the clastic interval and 90 degree (horizontal) through the basement interval. The following results solved by WELLST show values of collapse pressure of the wellbore when azimuth angle varies from 0 to 90^{o}. The poroelastic and thermo-poroelastic effect are taken into account the calculated results. The input data can be referred in Table 1 (basement), and Table 2 (clastic), appendix H.

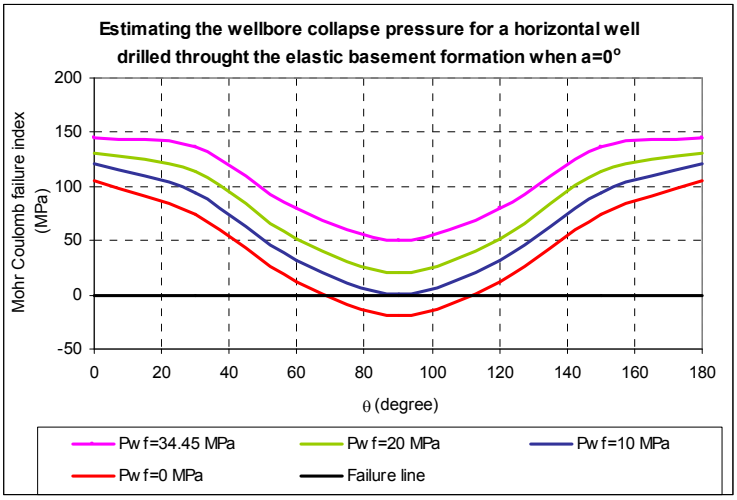

Fig 6.93. *Wellbore collapse pressure of a horizontal well interval drilled through the basement formation in elastic case, and a=0°*

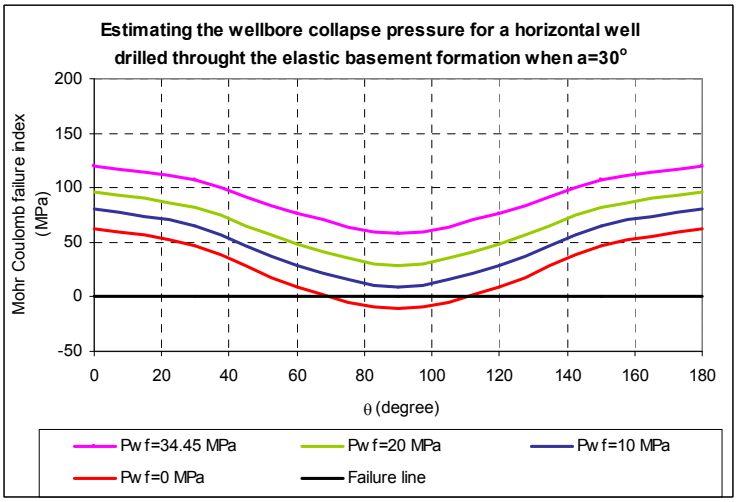

Fig 6.94. *Wellbore collapse pressure of a horizontal well interval drilled through the basement formation in elastic case, and a=30°*

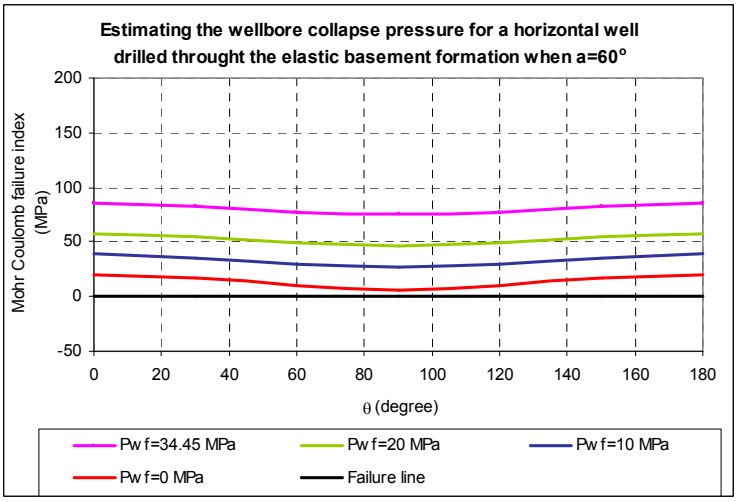

Fig 6.95. *Wellbore collapse pressure of a horizontal well interval drilled through the basement formation in elastic case, and a=60°*

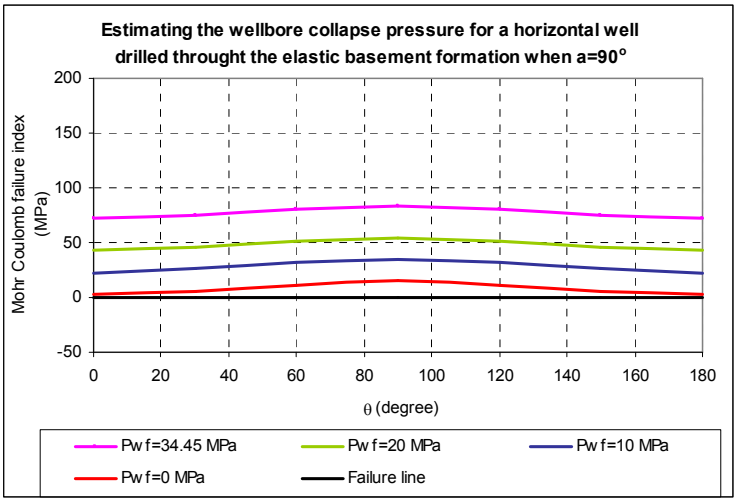

Fig 6.96. *Wellbore collapse pressure of a horizontal well interval drilled through the basement formation in elastic case, and a=90°*

It can be observed from Fig 6.93 that the wellbore of horizontal well drilled through the basement in the direction of maximum horizontal stress (a=0°) begins to collapse when wellbore pressure reduces to 10 MPa. However, the wellbore collapse pressure tends to decrease when azimuth angle increases. So the best direction to drill a horizontal well in the basement of Basin X is of 60°-90° azimuth in comparison to maximum horizontal stress direction. And the well drilled in this direction is stable even when the wellbore pressure decreases to zero. These results are solved when the rock behavior of penetrated formation is considered elastic. When the poroelastic and thermo-poroelastic effects are accounted into the solution, the following results can be obtained:

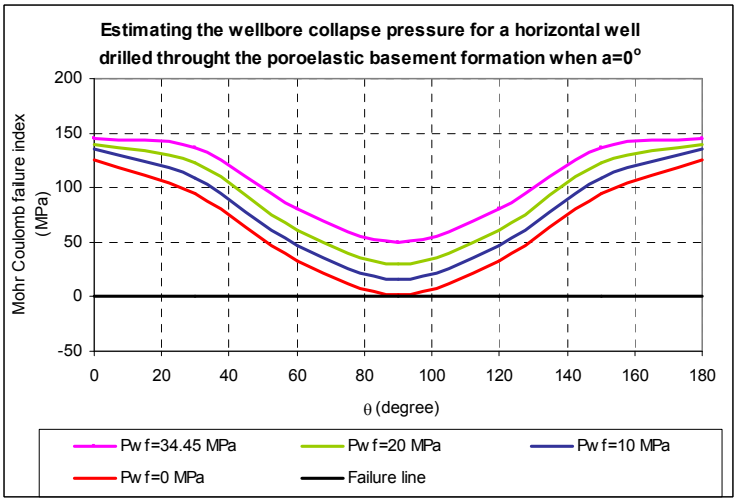

Fig 6.97. *Wellbore collapse pressure of a horizontal well interval drilled through the basement formation in poroelastic case, and a=0°*

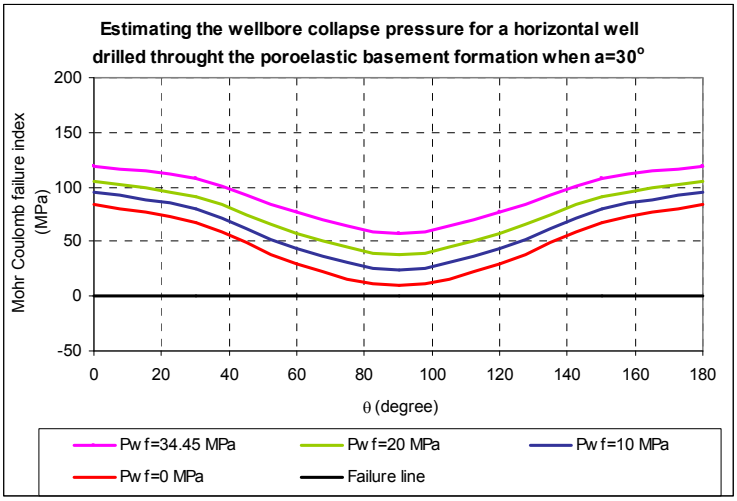

Fig 6.98. *Wellbore collapse pressure of a horizontal well interval drilled through the basement formation in poroelastic case, and a=30°*

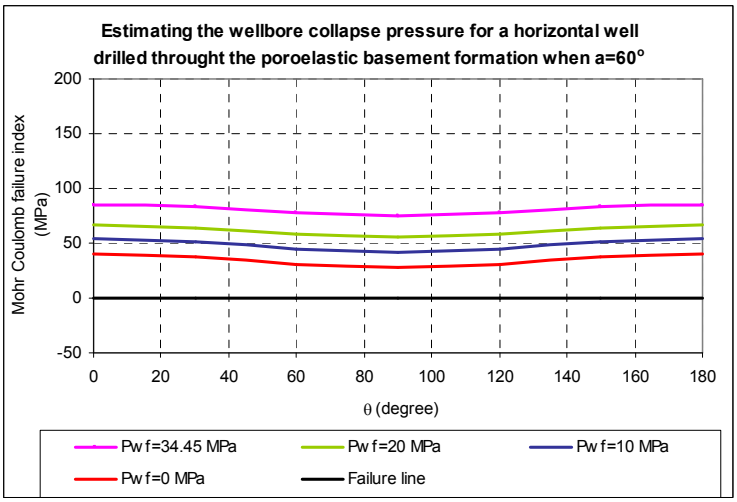

Fig 6.99. *Wellbore collapse pressure of a horizontal well interval drilled through the basement formation in poroelastic case, and a=60°*

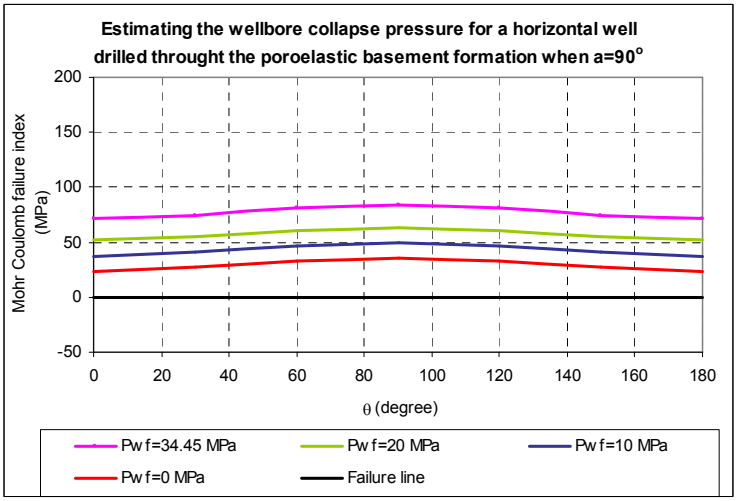

Fig 6.100. *Wellbore collapse pressure of a horizontal well interval drilled through the basement formation in poroelastic case, and a=90°*

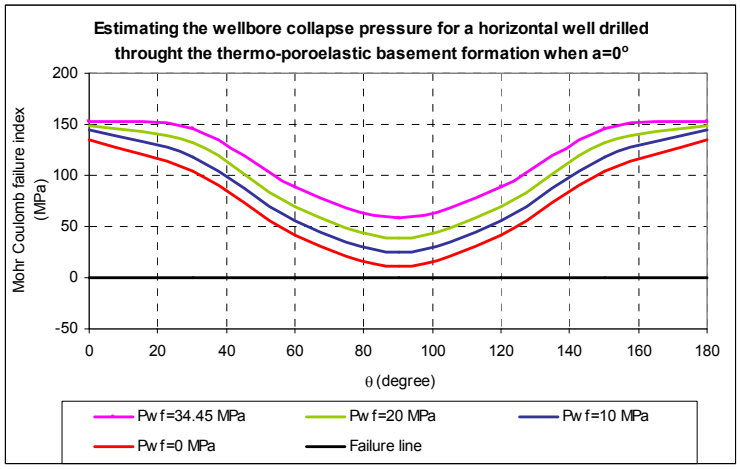

Fig 6.101. *Wellbore collapse pressure of a horizontal well interval drilled through the basement formation in thermo-poroelastic case, and a=0°*

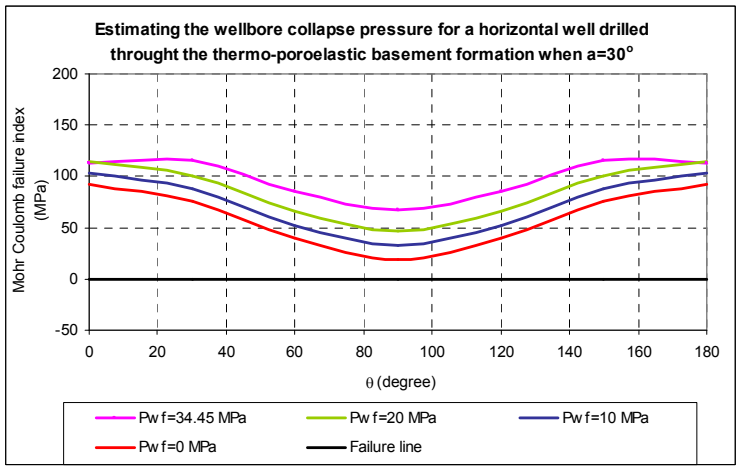

Fig 6.102. *Wellbore collapse pressure of a horizontal well interval drilled through the basement formation in thermo-poroelastic case, and a=30°*

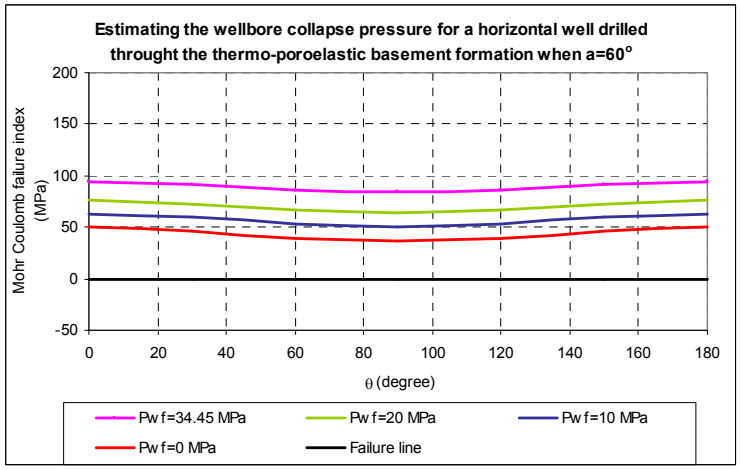

Fig 6.103. *Wellbore collapse pressure of a horizontal well interval drilled through the basement formation in thermo-poroelastic case, and a=60°*

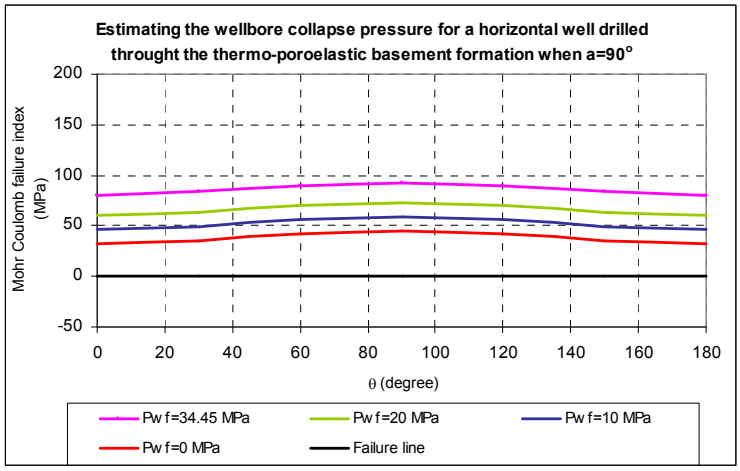

Fig 6.104. *Wellbore collapse pressure of a horizontal well interval drilled through the basement formation in thermo-poroelastic case, and a=90°*

As results shown in Figs 6.97-6.104, the poroelastic and thermo-poroelastic effects have positive roles on the wellbore stability. In elastic case, the wellbore collapse pressure was calculated around 10 MPa (Fig 6.93). It means that the wellbore starts to collapse when wellbore pressure reduces to 10 MPa. This value decreases to zero in poroelastic case (Fig 6.97). In thermo-poroelstic case, the wellbore is still stable even when wellbore pressure reduces to zero. Therefore, wellbore instability is considered insignificant when drilling UBD through the basement. However, it should be checked the solution with the other values of material cohesion because the cohesion of material used to calculate results from Figs 6.93 to 6.104 is quite high (54.6 MPa) while the collected data is in range from 20.69 to 93.14 MPa (Table 6.1). The following result depends on the input data from Table 1, appendix H in which the material cohesion of 30 MPa is used instead of 54.6 MPa as the above calculation.

When the cohesion of material of 30 MPa is used instead of 54.6 MPa, it is clear that the failure index reaches a negative value even when the wellbore pressure is mainained the same as the formation pore pressure so the wellbore will be collapsed in UBD operations due to the fact that the wellbore pressure is lower than pore pressure. These verifications are valid for three cases elastic, poroelastic, and thermo-poroelastic.

The results from Figs 6.93-6.107 used to estimate the collapse pressure of the wellbore in basement formation while the collapse pressure calculated for the wellbore interval drilled through the clastic section can be shown in Figs 6.108-6.122.

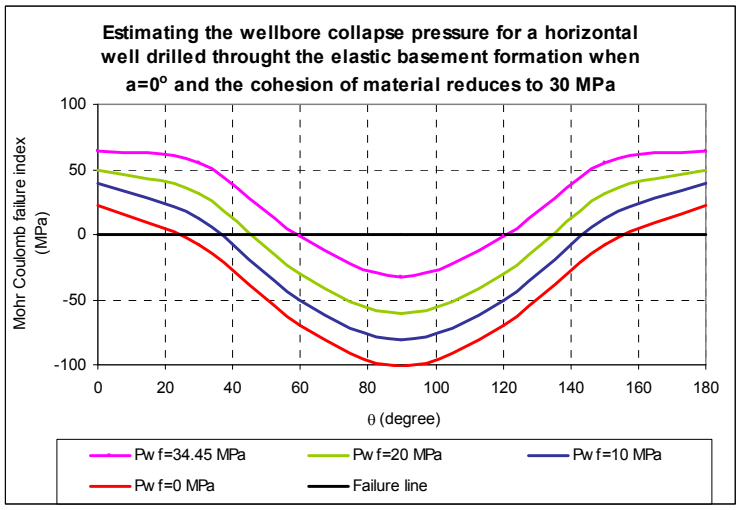

Fig 6.105. *Wellbore collapse pressure of a horizontal well interval drilled through the basement formation in elastic case, c=30 MPa, and a=0°*

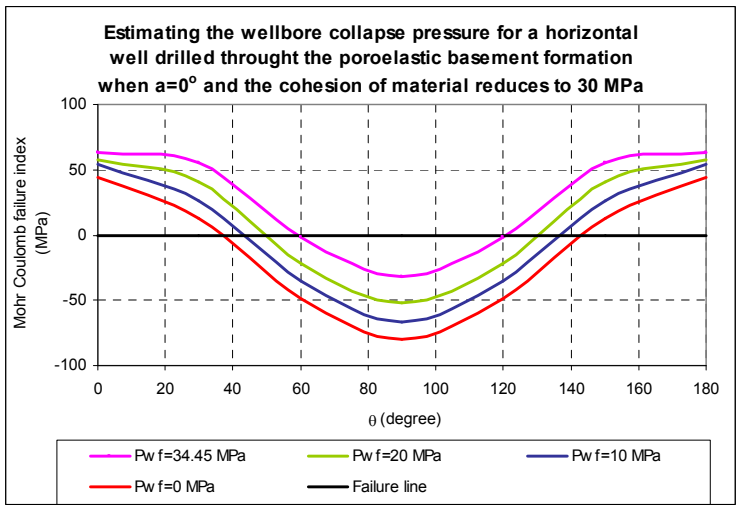

Fig 6.106. *Wellbore collapse pressure of a horizontal well interval drilled through the basement formation in poroelastic case, c=30 MPa, and a=0°*

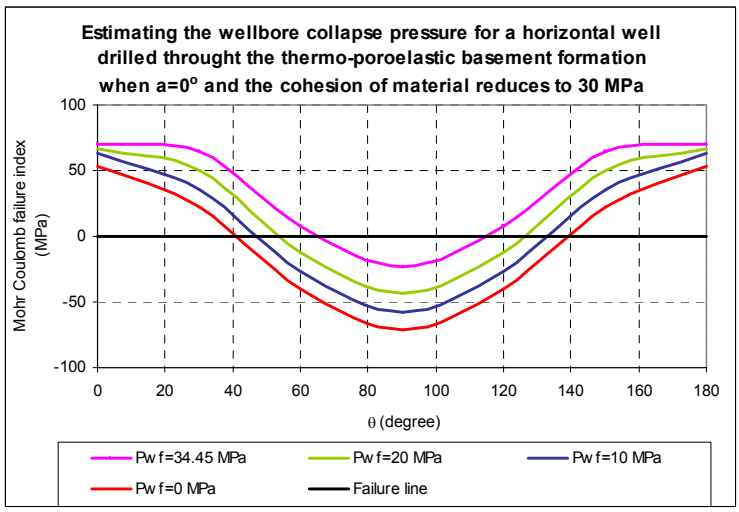

Fig 6.107. *Wellbore collapse pressure of a horizontal well interval drilled through the basement formation in thermo-poro elastic case, c=30 MPa, and a=0°*

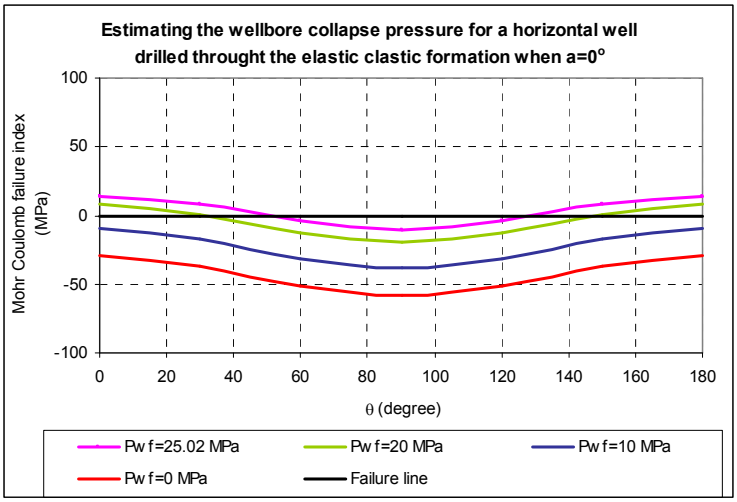

Fig 6.108. *Wellbore collapse pressure of a deviated well interval drilled through the clastic formation in elastic case, and a=0°*

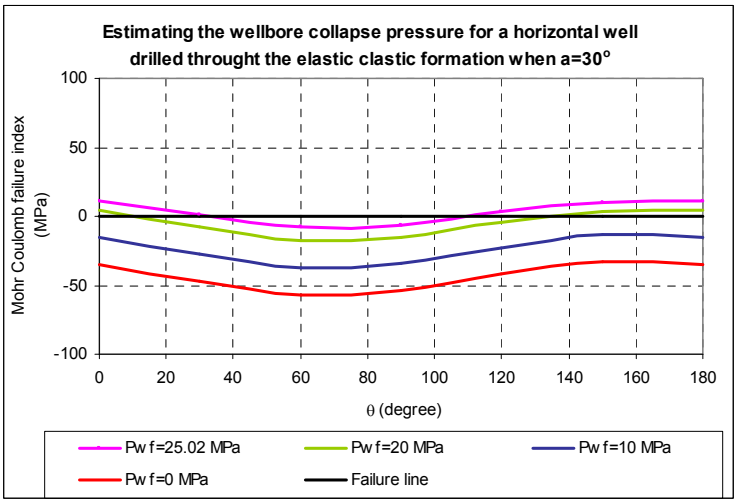

Fig 6.109. *Wellbore collapse pressure of a deviated well interval drilled through the clastic formation in elastic case, and a=30°*

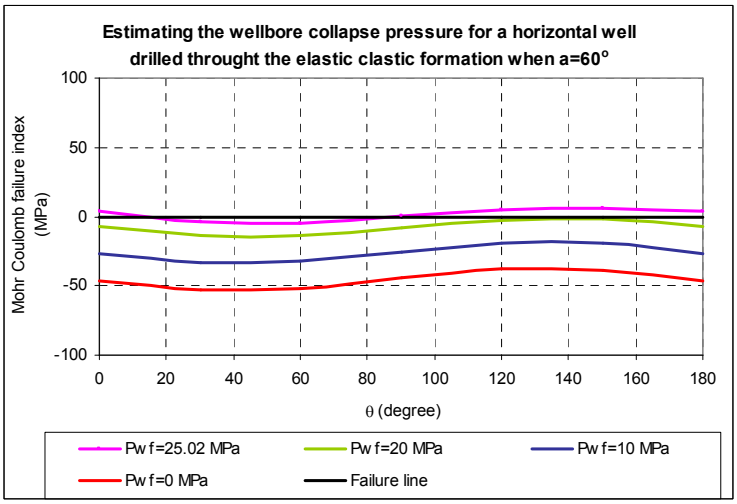

Fig 6.110. *Wellbore collapse pressure of a deviated well interval drilled through the clastic formation in elastic case, and a=60°*

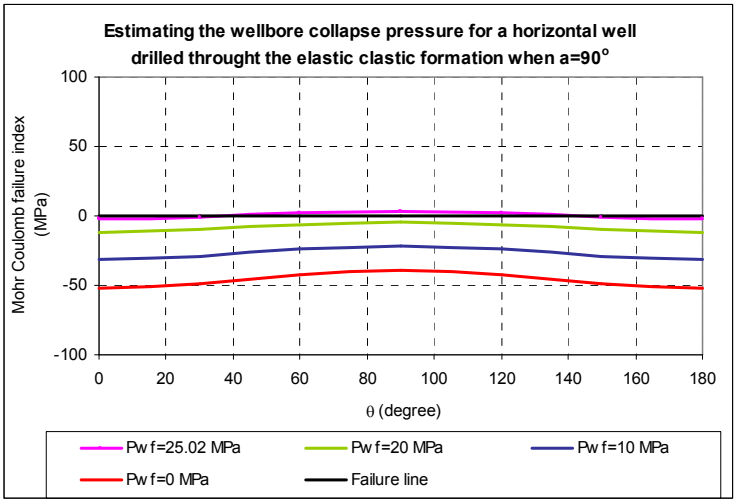

Fig 6.111. *Wellbore collapse pressure of a deviated well interval drilled through the clastic formation in elastic case, and a=90°*

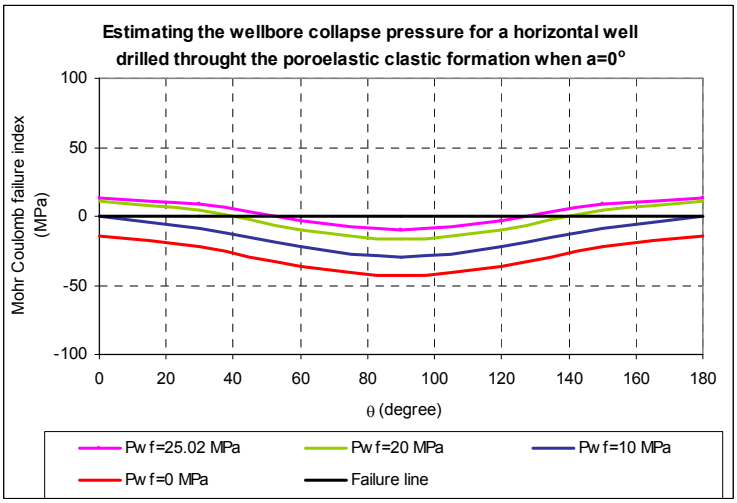

Fig 6.112. *Wellbore collapse pressure of a deviated well interval drilled through the clastic formation in poroelastic case, and a=0°*

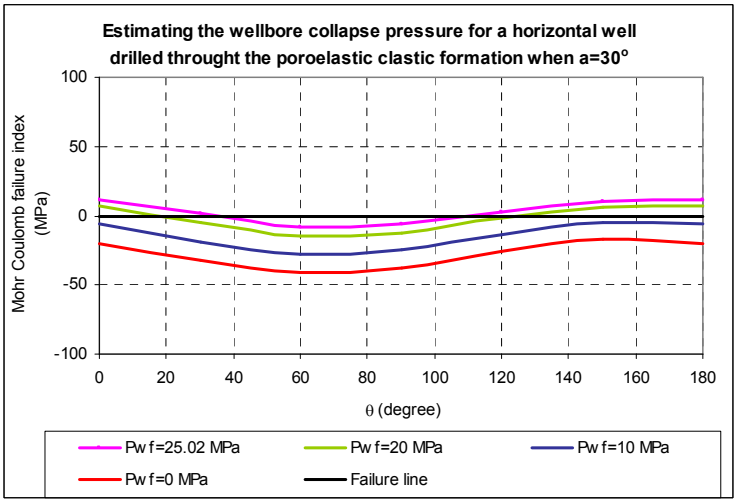

Fig 6.113. *Wellbore collapse pressure of a deviated well interval drilled through the clastic formation in poroelastic case, and a=30°*

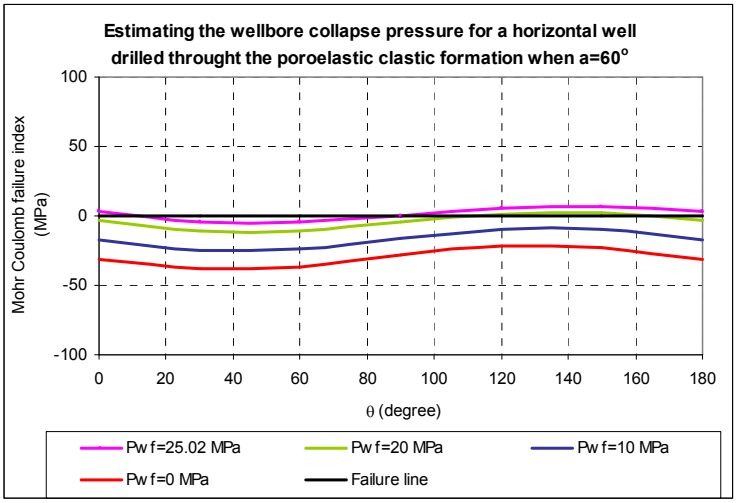

Fig 6.114. *Wellbore collapse pressure of a deviated well interval drilled through the clastic formation in poroelastic case, and a=60°*

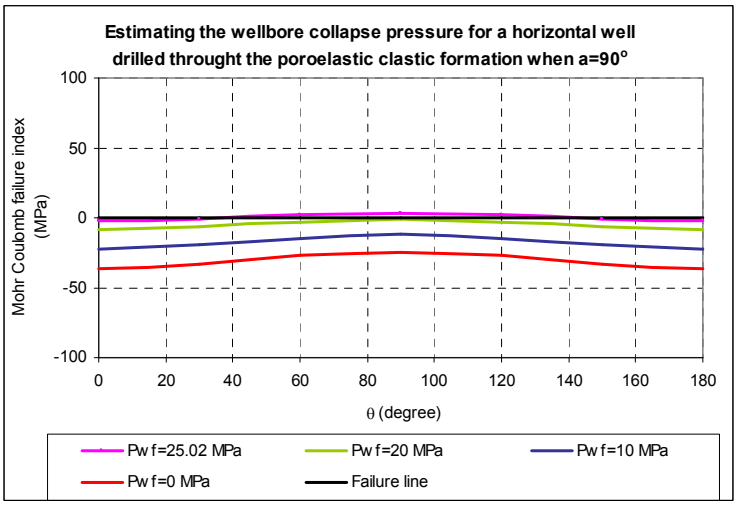

Fig 6.115. *Wellbore collapse pressure of a deviated well interval drilled through the clastic formation in poroelastic case, and a=90°*

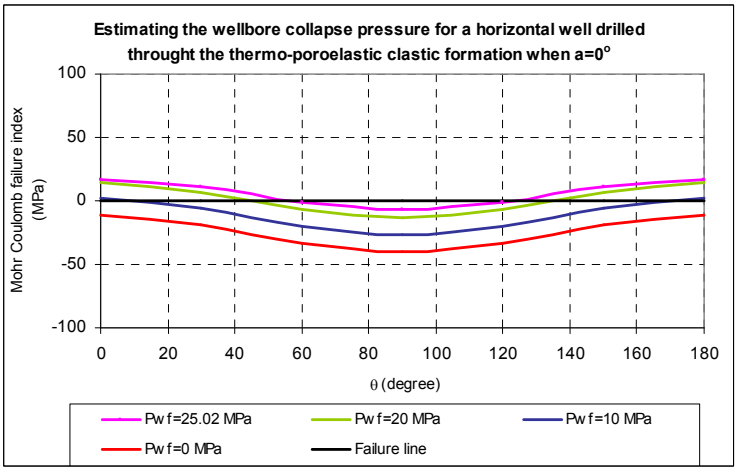

Fig 6.116. *Wellbore collapse pressure of a deviated well interval drilled through the clastic formation in thermo-poroelastic case, and a=0°*

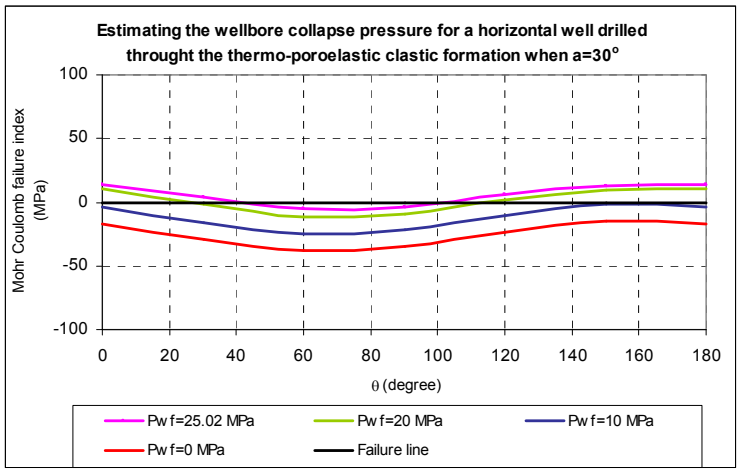

Fig 6.117. *Wellbore collapse pressure of a deviated well interval drilled through the clastic formation in thermo-poroelastic case, and a=30°*

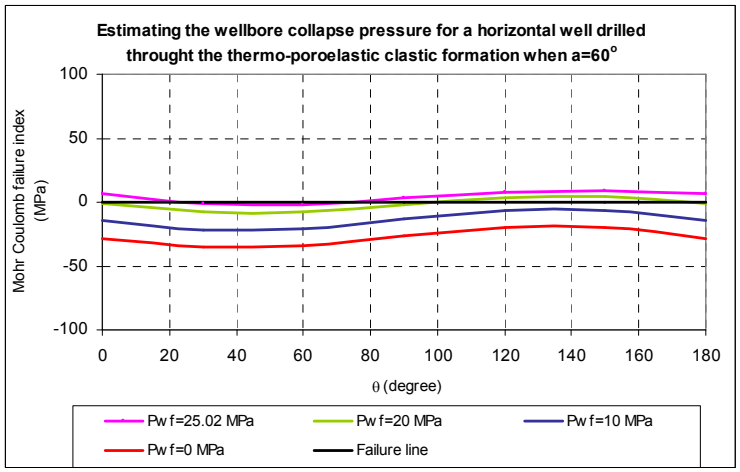

Fig 6.118. *Wellbore collapse pressure of a deviated well interval drilled through the clastic formation in thermo-poroelastic case, and a=60°*

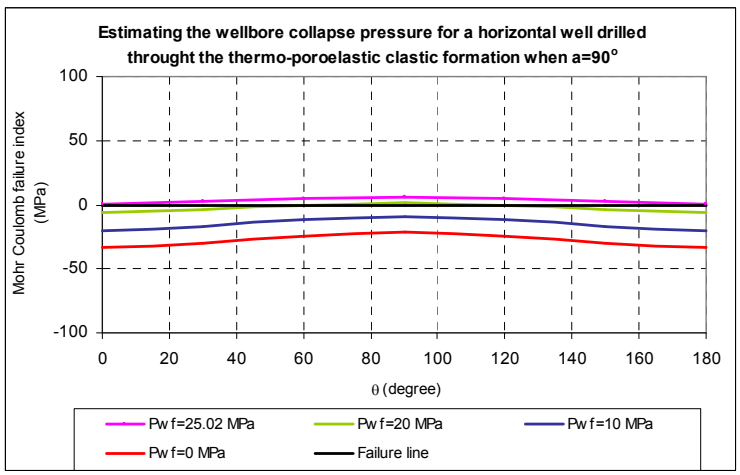

Fig 6.119. *Wellbore collapse pressure of a deviated well interval drilled through the clastic formation in thermo-poroelastic case, and a=90°*

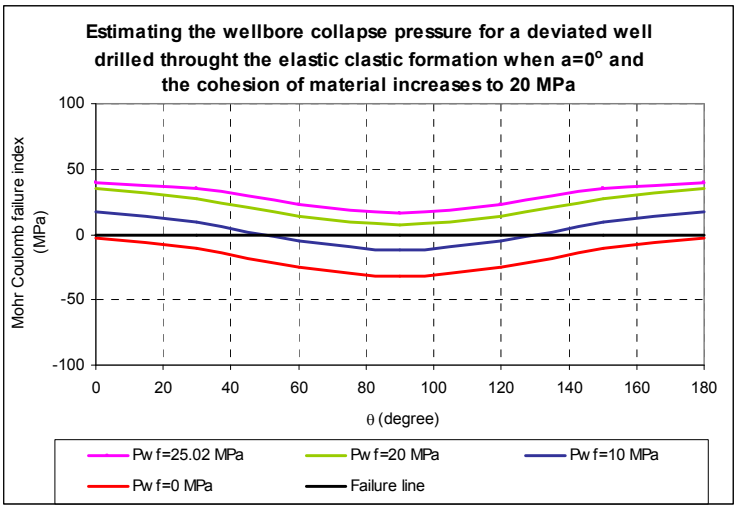

Fig 6.120. *Wellbore collapse pressure of a deviated well interval drilled through the clastic formation in elastic case, c=20 MPa, and a=0°*

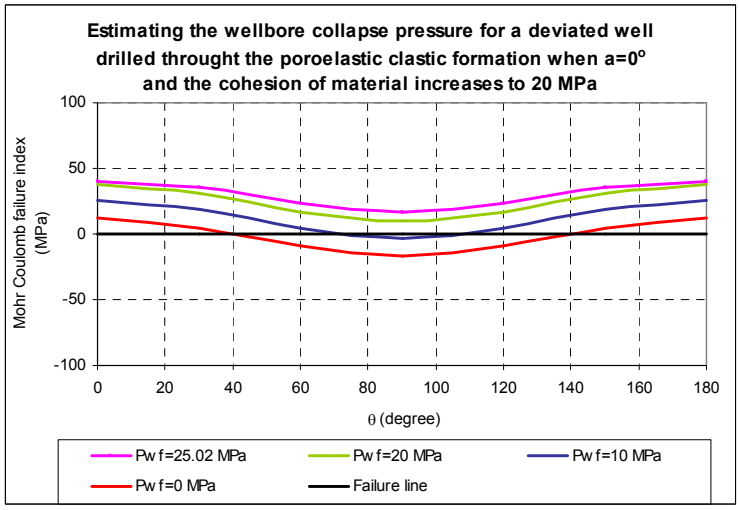

Fig 6.121. *Wellbore collapse pressure of a deviated well interval drilled through the clastic formation in poroelastic case, c=20 MPa, and a=0°*

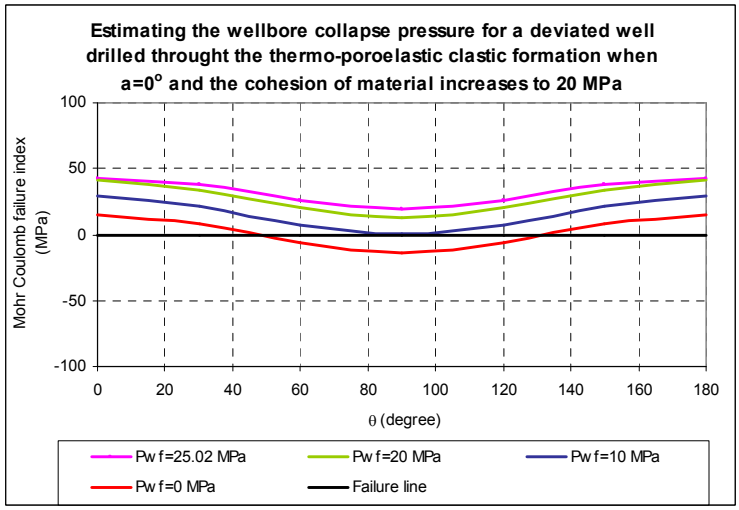

Fig 6.122. *Wellbore collapse pressure of a deviated well interval drilled through the clastic formation in thermo-poro elastic case, c=20 MPa, and a=0°*

The following conclusions can be withdrawn in the estimation of wellbore collapse pressure for the wellbore interval penetrated through the clastic section:

- The failure occurs on the wellbore wall even though the well is drilled in the balanced condition ($P_{wf}=P_R$). In the above calculations, the wellbore becomes unstable because the assumed cohesion material of clastic interval is 12 MPa while the initial stress environment is in a highly compressive condition. Therefore, to conclude the possiblity of UBD in the clastic interval, it is necessary to verify the accuracy of the collected cohesion of material. The higher cohesion of material is, the more stable wellbore is. This was verified in Figs 6.120-6.122 when increasing the cohesion of material from 12 MPa to 20 MPa. The results show that the wellbore just starts to collapse when the wellbore pressure drops approximately to 15 MPa in elastic case (Fig 6.120), or 10 MPa in thermo-poroelastic case (Fig 6.122).

- Similar to the wellbore in the clastic interval is also more stable when poroelastic, and thermo-poroelastic effects was accounted in the calculation. However, this influence hasn't contributed clearly to wellbore stability as the former one.

- The wellbore azimuth variation has an insignificant influence to wellbore stability in the clastic section (Fig 6.62).

To sum up, this section analyzed the effects of all factors as time dependent, thermal and hydraulic diffusivity, wellbore pressure changing, inclination and azimuth variation, poroelastic and thermo-poroelastic, cooling and heating effects to wellbore stability in UBD. It helps to qualify these influences, decide which drilling direction is the best for improving stability, and estimate wellbore collapse pressure which is used to set up Liquid gas rate window (LGRW) in the next section.

6.2. Gasified Liquid Drilling Analysis in UBD

One of the important tasks in UBD design is to model multiphase flow in the well under given drilling conditions. Due to the complex nature of multiphase flow including water, oil, gas, and solid in the UBD systems, numerous runs of sophisticated computer programs are required to calculate the distribution of drilling fluid properties along the wellbore and in the drillpipe. According to engineers who are in charge of UBD designs and operations, it is highly desirable to have a program that can accurately perform such predictions. This research applies UBDRILL to calculate all hydraulics drilling parameters in UBD such as the distribution of pressure, temperature, drilling fluid properties in the annulus, and in the drillpipe of the directional well. UBDRILL also helps to estimate the production flow rate in UBD and set up quickly Liquid gas rate window (LGRW) for drilling engineers.

6.2.1. UBDRILL

UBDRILL has been codified based on the IFDM method and equations

presented in chapter 3, 4 and 5.

6.2.2. Input data

The following data of a typical well were collected from Basin X of South Vietnam and UBDRILL program was used to model multiphase flow in the well, couple productivity in UBD, and plan LGRW of the directional well in UBD. The drilling fluid is gasified sea water.

Table 6.11. *Drilling data*

Parameters	Input Data	Units	Notes
Bit Diameter (d_b)	8.5	inch	
Specific Gravity of Solid Phase (S_s)	2.8		Equivalent to the granite density of 2800 kg/m^3
Rate of Penetration (R_p)	30	ft/hr	
Rotary Speed (Rot)	120	rpm	
Bit Nozzle Diameter (d_n)	0.625	inch	20/32 equi

Table 6.12. *PVT data*

	Input Data	Units	Notes
Formation Pressure (P_R)	5000	psia	34.45 MPa
Bubble Point Pressure (P_b)	4678	psia	
Collapse Pressure (P_{col})	1450	psia	10 MPa
Wellhead Pressure (P_{wh})	80	psia	
Surface Temperature (T_{wh})	139	^oF	
Gas Gravity (S_g)	0.65		
API Gravity (API)	39.3		
Specific Gravity of Liquid Injection (S_x)	1.02		
Maximum Compressor Flow Rate(Q_{pumb})	40	SCF/s	
Formation Influx Fluid (a)	1		Oil a = 1; Water a = 2;
Drilling Fluid (b)	2		b=1: drilling with gasified mud, so the mud weight and mud viscosity must be input b=2: drilling with gasified sea water, so only the sea water salinity is input
Mud Weight (W_x)	8.2	ppg	
Mud Viscosity (μ_x)	6	cp	
Sea Water Salinity	35	$^o/_{oo}$	

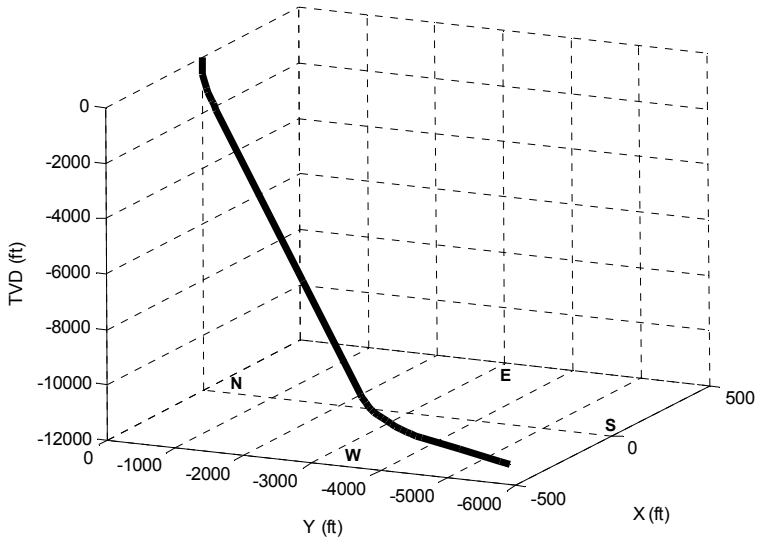

Fig 6.123. *Well trajectory*

Table 6.13. *Well structure*

MD (ft)	Angle (degrees)	Azimuth (Degrees)	Well Diameter (inch)	OD (inch)	ID (inch)	Annulus's Roughness (inch)	Drillpipe's Roughness (inch)
592	0	0	12.615	4.5	3.826	0.0018	0.0018
1148	2.4	225	12.615	4.5	3.826	0.0018	0.0018
1329	2.4	225	12.615	4.5	3.826	0.0018	0.0018
1629	10.61	180	12.615	4.5	3.826	0.0018	0.0018
1729	13.6	177	12.615	4.5	3.826	0.0018	0.0018
1945	17.09	175.32	12.615	4.5	3.826	0.0018	0.0018
7439	17.26	175.4	12.615	4.5	3.826	0.0018	0.0018
11080	17.26	175.4	8.681	4.5	3.826	0.0018	0.0018
11142	21.81	175.42	8.5	4.5	3.826	0.197	0.0018
11342	26.36	175.42	8.5	4.5	3.826	0.197	0.0018
11442	30.91	175.43	8.5	4.5	3.826	0.197	0.0018
11542	35.46	175.43	8.5	4.5	3.826	0.197	0.0018
11642	40.02	175.44	8.5	4.5	3.826	0.197	0.0018
11742	44.57	175.44	8.5	4.5	3.826	0.197	0.0018
11842	49.12	175.44	8.5	4.5	3.826	0.197	0.0018
11942	53.67	175.44	8.5	4.5	3.826	0.197	0.0018
12042	58.22	175.45	8.5	4.5	3.826	0.197	0.0018
12142	62.78	175.45	8.5	4.5	3.826	0.197	0.0018
12242	67.33	175.45	8.5	4.5	3.826	0.197	0.0018
12342	71.88	175.45	8.5	4.5	3.826	0.197	0.0018
12442	76.43	175.45	8.5	4.5	3.826	0.197	0.0018
12542	80.98	175.45	8.5	4.5	3.826	0.197	0.0018
12642	85.54	175.45	8.5	4.5	3.826	0.197	0.0018
13377	90	175.46	8.5	4.5	3.826	0.197	0.0018
14144	90	175.46	8.5	4.75	2.25	0.193	0.0018
14340	90	175.46	8.5	5	2.25	0.190	0.0018

Referring to the stress map of Basin X (Fig 2.7, chapter 2), the direction of maximum horizontal stress is in the range SE-NW (130^o – 310^o). And the azimuth of typical horizontal section can be referred in table 6.13 where it was 175^o. So the direction of the horizontal wellbore to the maximum horizontal stress direction in this example is around 45^o (=175 – 130). This can be explained in the following figure:

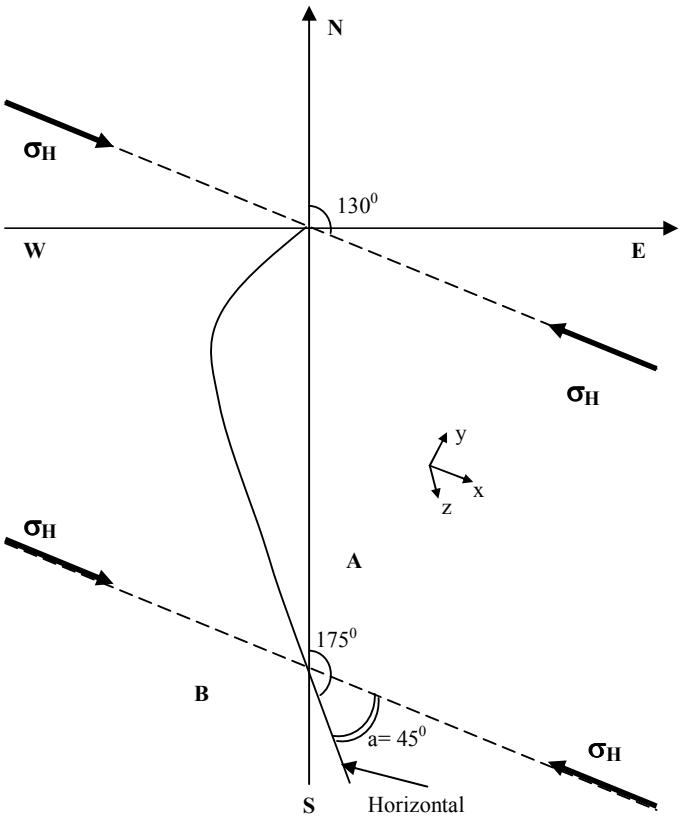

Fig 6.124. *The wellbore azimuth of a typical well in Basin X*

Table 6.14. *Inflow Performance Relationship*

Flow Rate (STB/D)	Pressure (psia)
0	5000
988	4750
1963	4500
2894	4250
3777	4000
4613	3750
5403	3500
6145	3250
6840	3000
7488	2750
8089	2500
8643	2250
9150	2000
9610	1750
10023	1500
10388	1250
10707	1000
10979	750
11203	500
11381	250
11505	15

Fig 6.124 shows that the well is drilled in the prevailing fracture direction (45^o) which is the best direction toward getting the highest wel productivity when it intersects as many fautlts in the basement as possible. However, the best direction to drill a well

for the wellbore stability purpose as calculated above is from 60-75^{o}. Although there is not a compromise between two directions, we should notice that drilling the horizontal well in the direction of 45^{o} of azimuth still maintain the well in the stability condition. Therefore, drilling the horizontal well with the azimuth of 45^{o} in the basement will satisfy two conditions, the wellbore stability and the highest productivity.

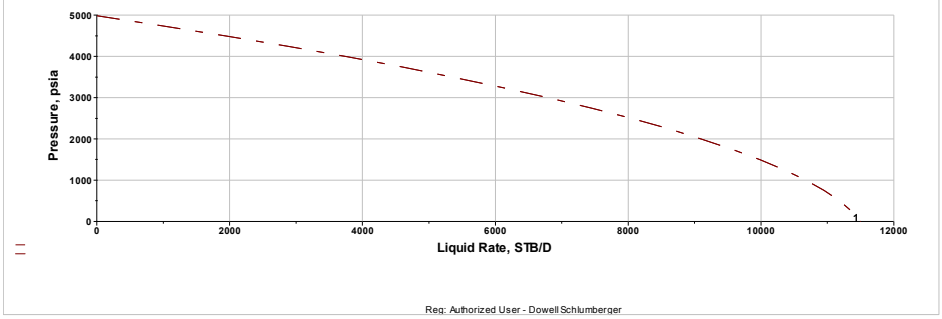

Fig 6.125. *IPR solving by PERFORM 3.0 [80]*

6.2.3. Results of modelling gasified flow

Modelling gasified flow in UBD is a key tool for the UBD engineer who must identify a target BHP and access how to achieve this target. To do that, they must know the distribution of fluid properties inside drillpipes and in the annular space between the drillpipe and the wellbore. This section shows these results.

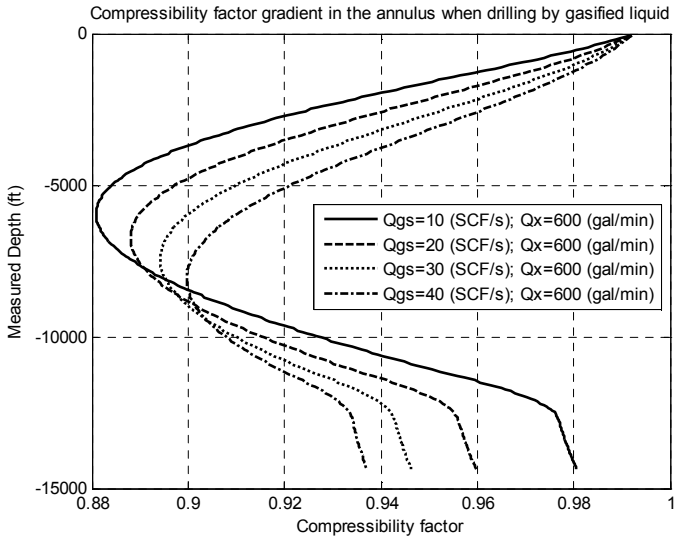

Fig 6.126. *Gas compressibility factor gradient in the annulus when drilling by gasified liquid*

Gas compressibility factor (Z) varies complexly with the varying of pressure and temperature. This relationship was shown in Eq 3.22, chapter 3 (Fig 3.1). At the first time, Z decreases from 0.99 to 0.88 due to the calculation of Z in this section (0-6,500 ft) drops into the top-left of Fig 3.1. Then, Z increases from 0.88 to 0.98 in the next section 6,500-12,642 ft when the calculation of Z is referred by the top-right of Fig 3.1. However, the varying of Z in horizontal section (12,642-14,340 ft) is insignificant (0.975-0.980) because the temperature is unchangeable, and pressure increases lightly due to the friction in this section (see Figs 6.140, and 6.141).

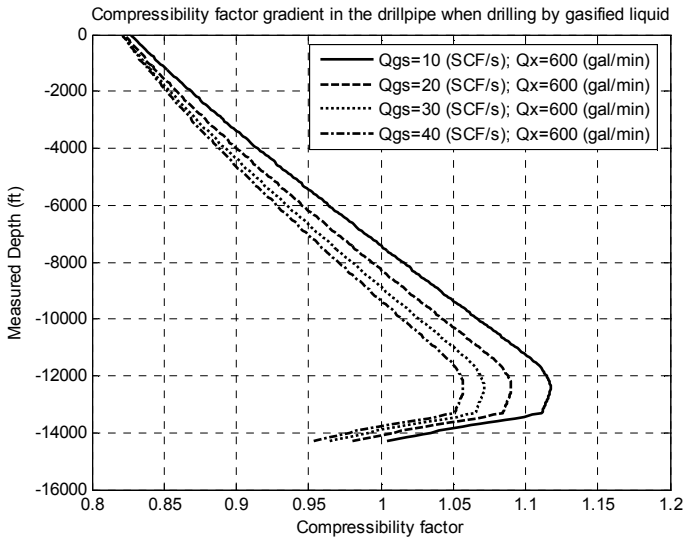

Fig 6.127. *Gas compressibility factor gradient in the drillpipe when drilling by gasified liquid*

It is explained in the same way for the alteration of Z in the drillpipe. From 0-12,642 ft, Z increases from 0.83 to 1.12 when pressure and temperature in the drillpipe increase and the calculation of Z is referred to in the top-right of Fig 3.1. However, when temperature becomes constant, and pressure decreases lightly due to the friction (see Figs 6.140, 6.141) in horizontal section (12,642-14,340 ft), Z begins to reduce from 1.12 to 1.02.

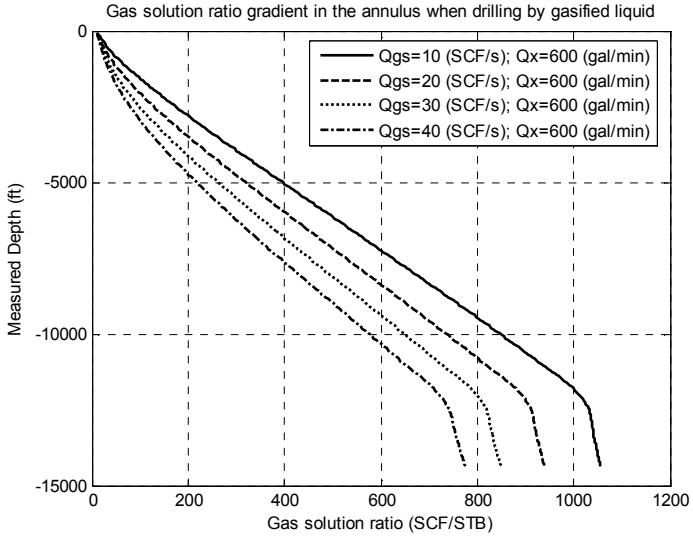

Fig 6.128. *Gas solution ratio when drilling by gasified liquid*

There are two sections that need to be noticed in this plot. The first one is from 0-12,642 ft and the second one is the horizontal section from 12,642-14,340 ft. In both sections, gas solution ratio increases with the increase of pressure from the surface to the bottom hole. However, this development is slightly in the horizontal section because hydrostatic pressure is maintained constant and the variation of frictional pressure is negligible when the annulus diameters of this section reduce just from 4 to 3.75, and 3.5.

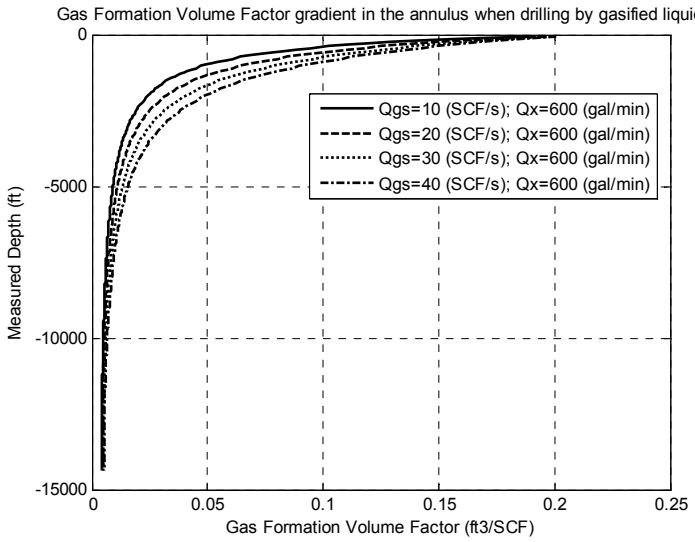

Fig 6.129. *Gas formation volume factor gradient in the annulus when drilling by gasified liquid*

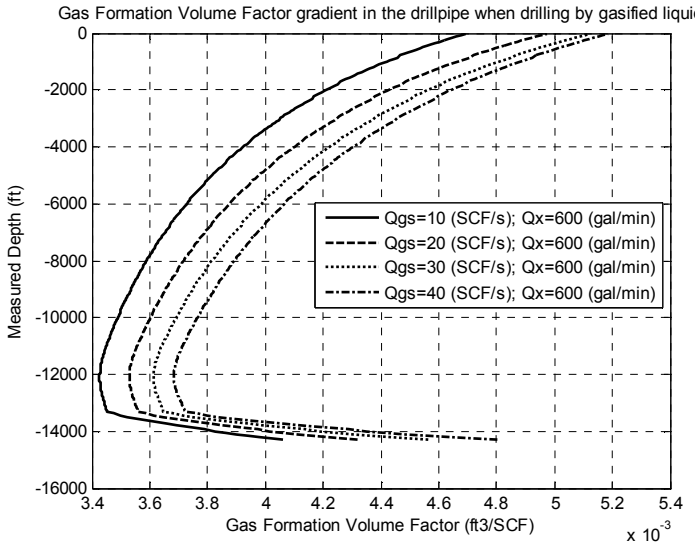

Fig 6.130. *Gas formation volume factor gradient in the drillpipe when drilling by gasified liquid*

The formation volume factor of a gas (B_g), oil (B_o), or fluid (B_f) is a convenient parameter to use for converting from standard volumes to actual or in-situ volumes existing at any pressure and temperature. In this computation, gas formation volume factor (B_g) in the annulus reduces from the surface to the bottom hole because of the compression of gas at the high pressure condition when pressure increases from the surface to the bottomhole in the annulus. Gas formation volume factor equals one at standard condition of 60^{o}F, and 14.7 psia. In these results, when surface pressure is controlled in 80 psia, and surface temperature 139 ^{o}F, the calculated value of B_g is about 0.2 ft^3/SCF at the surface and 0.0043 ft^3/SCF at the bottomhole. It means that one ft^3 at the bottomhole condition approximates 233 ft^3 of gas at the standard condition. So it should be careful in UBD when there is a signal of inflow gas in the annulus because this gas volume can expand uncontrollably when reaching to the surface. Controlling wellhead pressure is one of the effective methods to guarantee the safety in UBD. For example, the gas volume only reaches to 5 ft^3 at surface condition (80 psia, 139 ^{o}F) from

1 ft^3 at reservoir condition. According to gas formation volume factor in the drillpipe, this value decreases from the surface to the depth of 12,642 ft, then increases in the horizontal section (12,642-14,340 ft). The first trend can be explained by the increase of pressure in this section, and the second trend is caused by the decrease of pressure in horizontal drillpipe section (refer Fig 6.142).

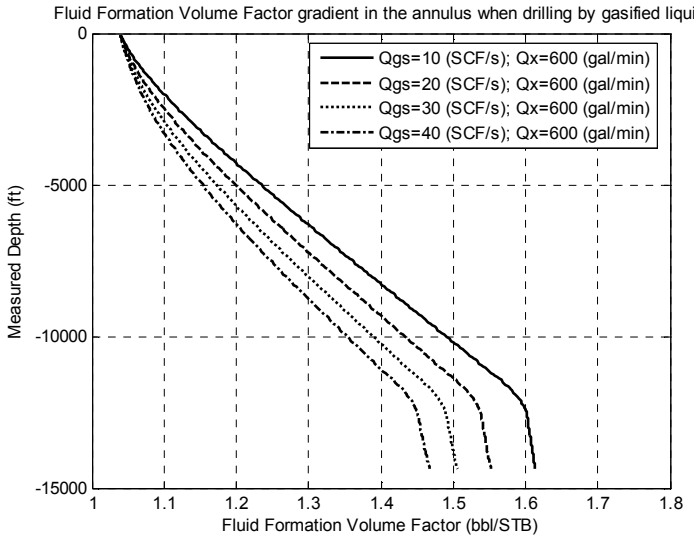

Fig 6.131. *Fluid formation volume factor gradient in the annulus when drilling by gasified liquid*

In contrast gas formation volume factor (B_g), fluid formation volume factor (B_f) increases with depth. This is due to the fact that when pressure increases from the surface to the bottomhole, solution gas ratio also increases, gas was dissolved into fluid phase so one ft^3 of fluid at the bottomhole condition will be compressed at the surface condition. That is the reason B_f develops with depth. In this calculation, B_f is about 1.05 bbl/STB at the surface condition when surface pressure and temperature is 80 psia and 139 ^oF (B_f equals 1 at the standard condition 14.7 psia and 60 ^oF). Near the bottom hole, the evolution of B_f is different from the previous sections because of the alteration of well trajectory (horizontal) and well diameter (drill collar instead of drillpipe).

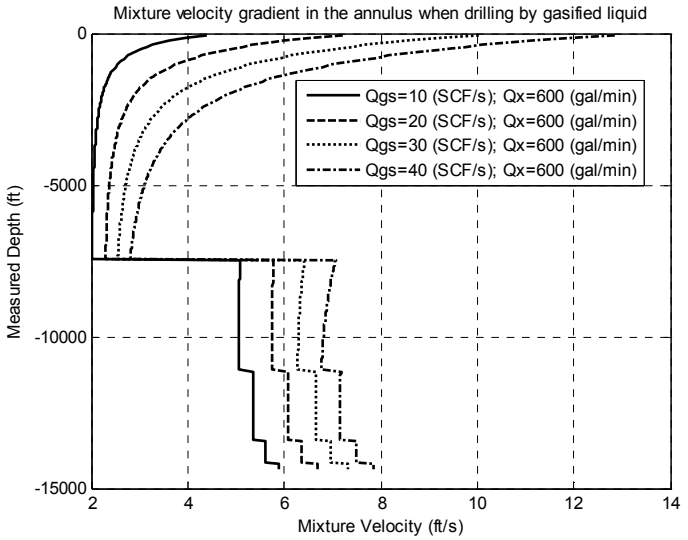

Fig 6.132. *Mixture velocity gradient in the annulus when drilling by gasified liquid*

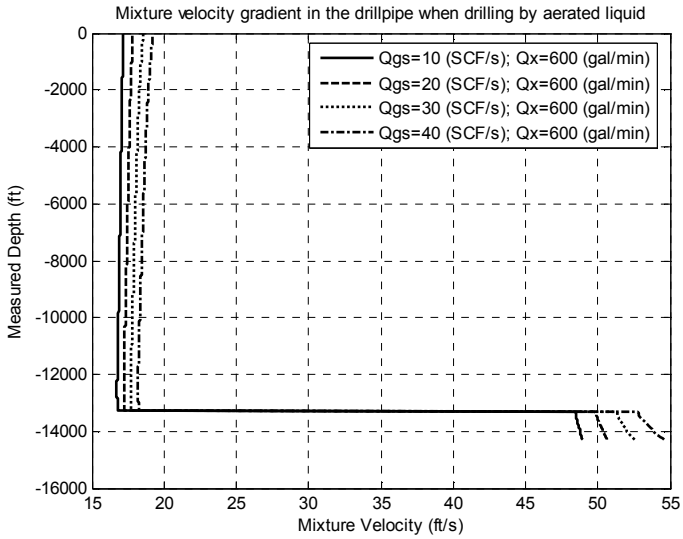

Fig 6.133. *Mixture velocity gradient in the drillpipe when drilling by gasified liquid*

There are three remarkable changes of mixture velocity in the annulus. The first one is from surface to 3000 ft. In this section, mixture velocity reduces considerably because the reduction of gas formation volume factor (see Fig 6.129) makes the gas volume in mixture decrease as well. In the second section (7,439-11,080 ft), and the last sections (11,080-14,340 ft), mixture velocity changes because the well diameter varies from 12.615 to 8.681 inch, and drillpipe (4.5 inch OD) was replaced by drill collars (4.75, and 5 inch OD).

The mixture velocity in the drillpipe increases significantly from 13,640 ft in depth to the bottomhole when a "jump" can be observed in this section due to the change of well diameters.

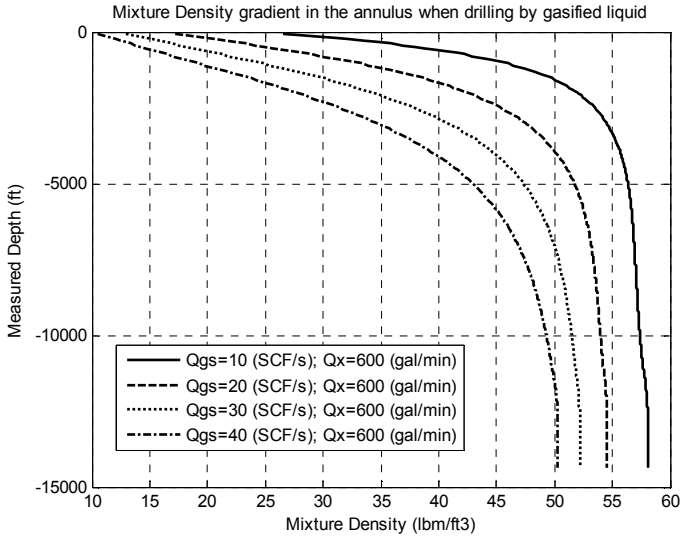

Fig 6.134. *Mixture density gradient in the annulus when drilling by gasified liquid*

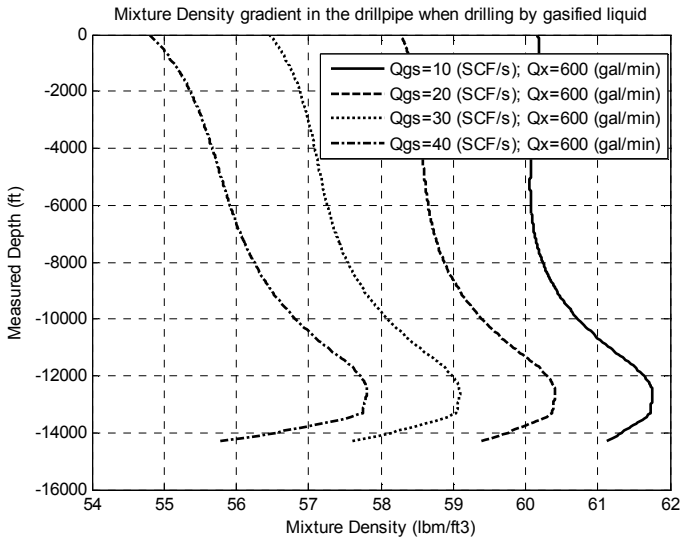

Fig 6.135. *Mixture density gradient in the drillpipe when drilling by gasified liquid*

Another important term in the pressure drop calculation is the mixture density. The general trend of this parameter is that the mixture density increases from the surface to the bottomhole because of the development of pressure in the anulus. And the variation of mixture density is inversely proportional to that of gas injection rates. So increasing gas injected volume into drilling fluid in UBD can be carried out to reduce the mixture density in UBD. The mixture density in the drillpipe of the horizontal interval reduces because of the reduction of pressure in this interval (Fig 6.142).

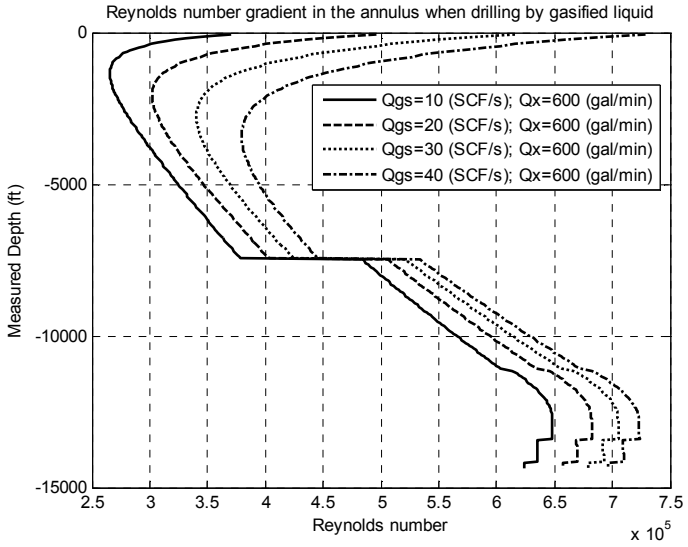

Fig 6.136. *Reynolds number gradient in the annulus when drilling by gasified liquid*

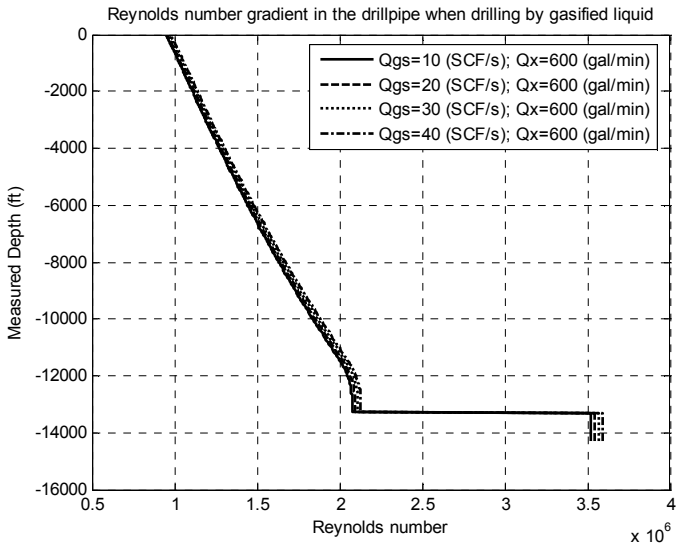

Fig 6.137. *Reynolds number gradient in the drillpipe when drilling by gasified liquid*

Reynolds number alters significantly in last sections once the well is drilled in horizontal direction and the well diameter is narrowed.

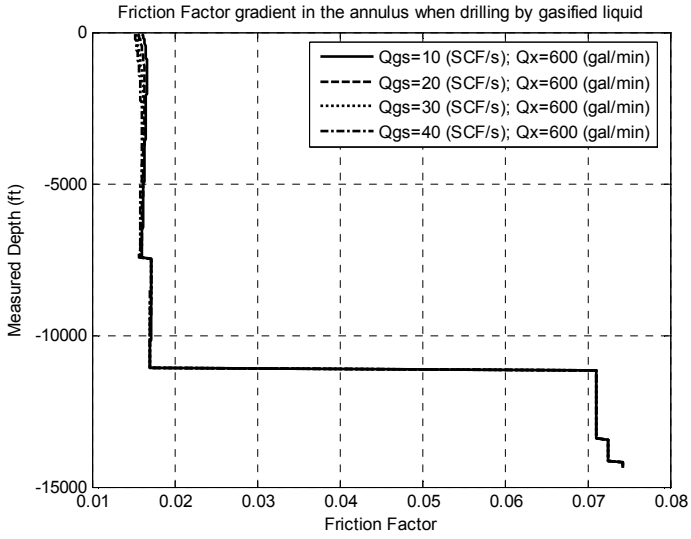

Fig 6.138. *Friction factor gradient in the annulus when drilling by gasified liquid*

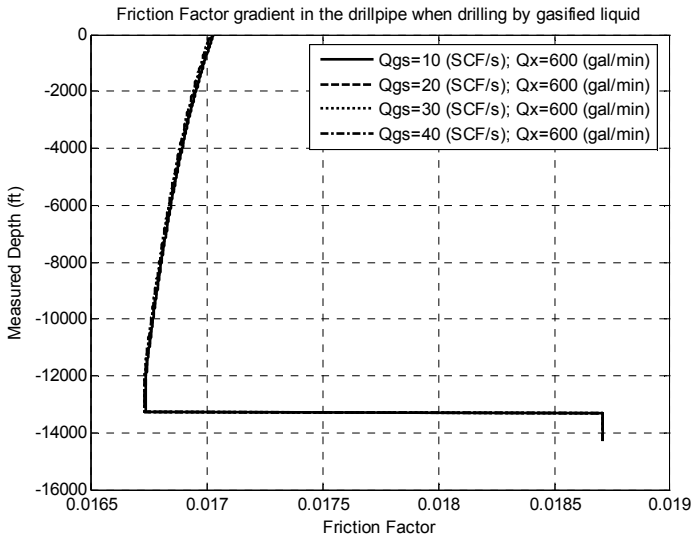

Fig 6.139. *Friction factor gradient in the drillpipe when drilling by gasified liquid*

Friction factor can be estimated from Reynolds numbers (Eq 3.31). Once Reynolds numbers reaches to a certain value which is quite large, its contribution to friction factor will become inconsiderable. And this is the reason why friction factors have not depended a lot on injection gas flow rates (Q_{gs}) in this calculation. All curves in Figs 6.138 and 6.139 tend to the same.

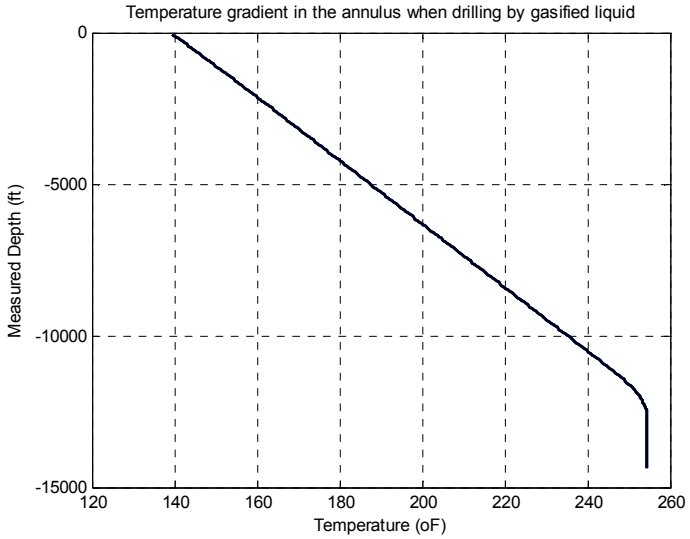

Fig 6.140. *Temperature gradient in the annulus when drilling by gasified liquid*

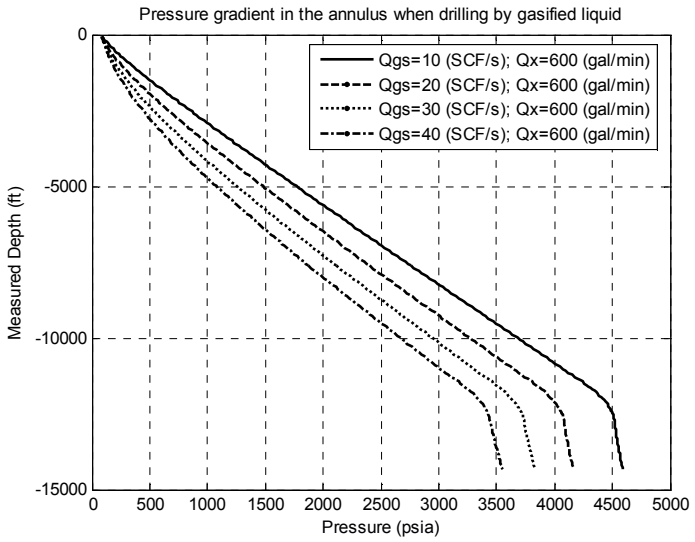

Fig 6.141. *Pressure gradient in the annulus when drilling by gasified liquid*

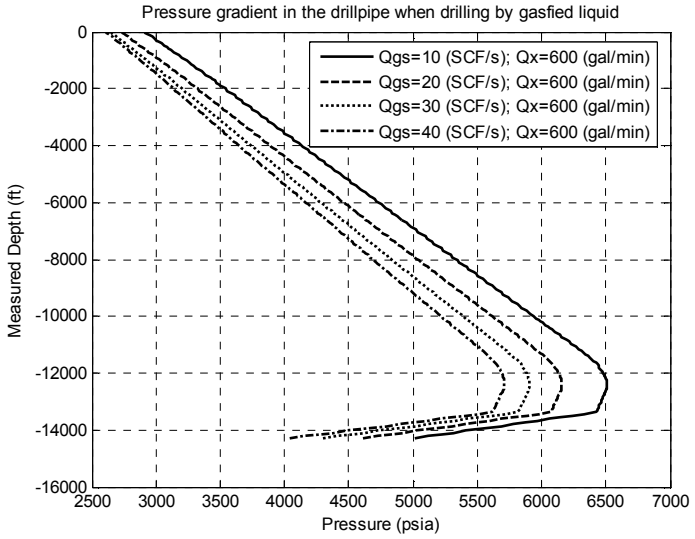

Fig 6.142. *Pressure gradient in the drillpipe when drilling by gasified liquid*

At the end, pressure gradient profiles were set up as observed in Figs 6.141, and 6.142. The pressure distribution along the wellbore is contributed significantly by wellhead pressure, liquid and gas injection flow rates, and drilling fluid density. Any change of these will make the alteration of wellbore pressure which will affect to the wellbore stability and productivity in UBD. The pressure gradient in the annulus increases with depth However, although the pressure gradient in drillpipe increases in the inclined section (0-12,642 ft), it reduces along the horizontal section (12,642-14,340 ft) because the increase of hydrostatic pressure (zero in the horizontal section) can not cover the drop of frictional pressure due to friction when the wellbore diameter is narrowed in the last sections.

The graphical results above show clearly the properties of drilling fluid in the wellbore and in the drillpipe while underbalanced drilling and this is an intermediate step in which results of pressure distribution and BHP will be used to calculate LGRW in UBD optimization and couple productivity with UBD parameters. Moreover, these

results are also exported to Excel files containing the information of pressure, density, velocity of drilling fluids versus measured depths. Table 6.15 displays the results of pressure distribution in the annulus from the surface to the bottomhole when fluid injection rate equals 600 gal/min and gas injection rate varies from 10 to 40 SCF/s.

Table 6.15. *Pressure distribution in the annulus*

Air Injection Flow rate (SCF/s)	10	20	30	40
Measured Depth (ft)	Wellbore Pressure in the Annulus (psia)			
59.20	90.72	87.08	85.43	84.50
118.40	102.19	94.57	91.13	89.18
177.60	114.38	102.48	97.09	94.05
236.80	127.25	110.81	103.32	99.11
296.00	140.76	119.56	109.83	104.36
355.20	154.88	128.74	116.62	109.81
414.40	169.57	138.33	123.70	115.47
473.60	184.80	148.34	131.06	121.33
532.80	200.52	158.75	138.72	127.39
592.00	216.71	169.57	146.66	133.67
653.78	234.04	181.26	155.25	140.44
715.56	251.80	193.38	164.15	147.45
777.33	269.97	205.90	173.38	154.69
839.11	288.51	218.82	182.91	162.17
900.89	307.40	232.12	192.76	169.90
962.67	326.61	245.79	202.92	177.86
1024.44	346.11	259.83	213.39	186.07
1086.22	365.90	274.21	224.17	194.51
1148.00	385.94	288.93	235.24	203.21
1208.33	405.74	303.62	246.34	211.93
1268.67	425.76	318.61	257.73	220.88
1329.00	445.98	333.88	269.38	230.07
…	…	…	…	…
13436.00	4546.18	4113.03	3773.12	3485.84
13495.00	4548.88	4116.29	3776.85	3489.99
13554.00	4551.58	4119.55	3780.58	3494.14
13613.00	4554.27	4122.81	3784.31	3498.29
13672.00	4556.97	4126.07	3788.03	3502.45
13731.00	4559.67	4129.33	3791.76	3506.60
13790.00	4562.36	4132.59	3795.49	3510.75
13849.00	4565.06	4135.86	3799.22	3514.90
13908.00	4567.76	4139.12	3802.95	3519.05
13967.00	4570.45	4142.38	3806.67	3523.20
14026.00	4573.15	4145.64	3810.40	3527.35
14085.00	4575.85	4148.90	3814.13	3531.50
14144.00	4578.54	4152.16	3817.86	3535.65
14209.33	4582.17	4156.55	3822.88	3541.24
14274.67	4585.80	4160.94	3827.89	3546.82
14340.00	4589.43	4165.33	3832.91	3552.40

6.2.4. Results of planning LGRW

The LGRW is the window that can be constructed based on formation pore pressure, wellbore collapse pressure, cuttings carrying capacity of the fluid mixture, and wellbore washout criteria. And it gives the field engineers flexibility in selection of liquid and gas injection rates on the drilling site.

For a given hole geometry (hole and pipe sizes and depth) and fluid properties, the surface choke pressure, liquid flow rate, and gas injection rate are three major parameters that effect BHPs during drilling and circulation breaking conditions. The liquid flow rate and gas injection rate should be carefully designed to ensure underbalanced drilling and wellbore integrity. The LGRW described defines the margins of useable liquid and gas flow rates in underbalanced drilling.

A typical LGRW is illustrated in the Fig 6.143. [45] It can be prepared using equations developed in chapter 3. The procedure is demonstrated as follow:

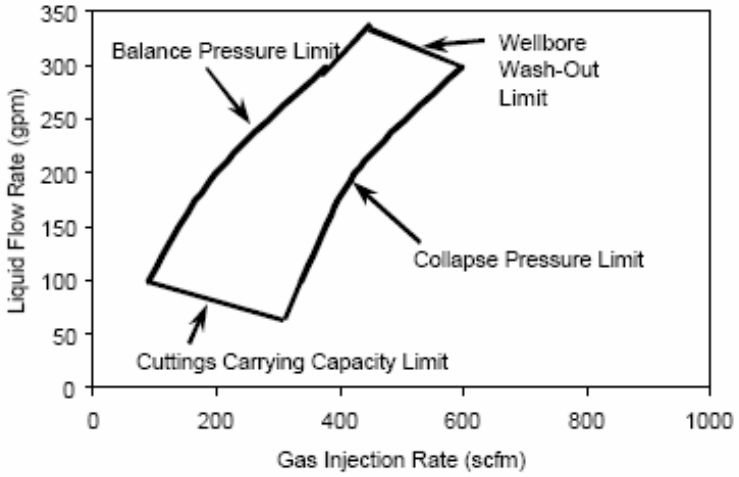

Fig 6.143. *A typical Gas-Liquid Flow Rate Window (GLRW) [45]*

Right boundary

The right boundary of the LGRW is defined by a locus of liquid-gas rate combinations that yield a hydrostatic bottomhole pressure developed during circulation breaks equal to the formation collapse pressure at different liquid injection rates. The combinations of liquid and gas flow rates that yield the formation collapse pressure can be determined by reading pressure values from the pressure curves. Equations in a previous chapter can be used to calculate the hydrostatic bottomhole pressure in stable foam/gasified liquid drilling, with friction factor being zero. While the bottomhole pressure during circulation break can be predicted, estimating wellbore collapse pressure is not easy. There are several methods that can be used for estimating formation collapse pressure such as Von Mises, Drucker Prager, this study used Mohr Coulomb failure criterion for estimating formation collapse pressure.

Wellbore collapse pressure is defined as the critical wellbore pressure. The hydrostatic bottomhole pressure should be higher than the wellbore collapse pressure in order to prevent the wellbore from collapse.

Left boundary

The left boundary of the LGRW is also defined by a locus of liquid-gas rate combinations. To determine this locus, the dynamic bottomhole pressure curves are plotted as a function of gas injection rate for different liquid injection rates. The

combinations of liquid and gas flow rates that yield the formation pore pressure can be determined by reading pressure values from the pressure curves. The flowing BHP is equal to circulation break BHP plus pressure loss due to friction. Equations in chapter 3 are also used.

Lower boundary

The lower boundary of the LGRW can be defined based on the cuttings carrying capacity of the fluid mixture as presented in chapter 3. Different criteria for cuttings transport can be used, depending on fluid type. A conservative criterion for gasified liquid is minimum kinetic energy. The minimum kinetic energy assumes that a minimum kinetic energy of 3 lb-ft/ft^3 is required for drilling fluids to effectively carry cuttings up to the surface under normal drilling conditions. In some previous research of other authors, it is safe to assume that the gas phase does not contribute to the carrying capacity of the mixture for calculation simplicity. This means that the minimum kinetic energy of a gasified fluid can be estimated conservatively based on liquid flow rate. However, in this research, instead of using only the velocity and density of liquid phase to calculate the minimum kinetic energy, the mixture (liquid and gas) density and mixture velocity were used.

Upper boundary

The upper boundary of the LGRW can be defined based on wellbore washout constraint. Since no design method is available for this issue, a good practice is to look at capiler logs and use experience gained from local drilling operations.

Results

The following results with the input data referred from 6.2.2 were produced by UBDRILL.

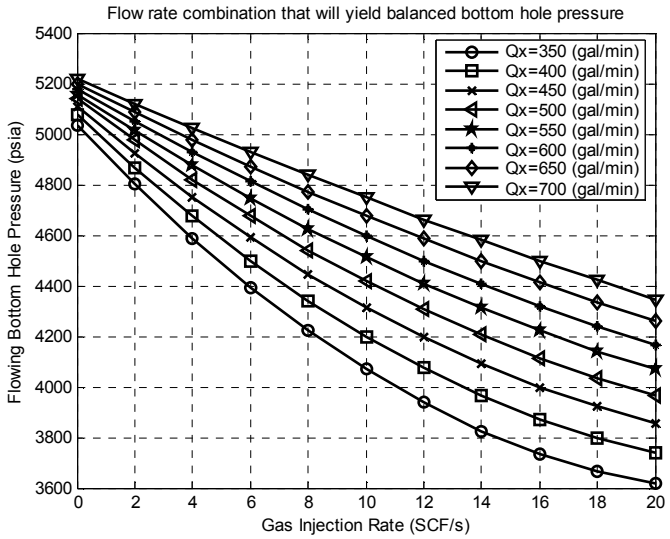

Fig 6.144. *Dynamic BHP*

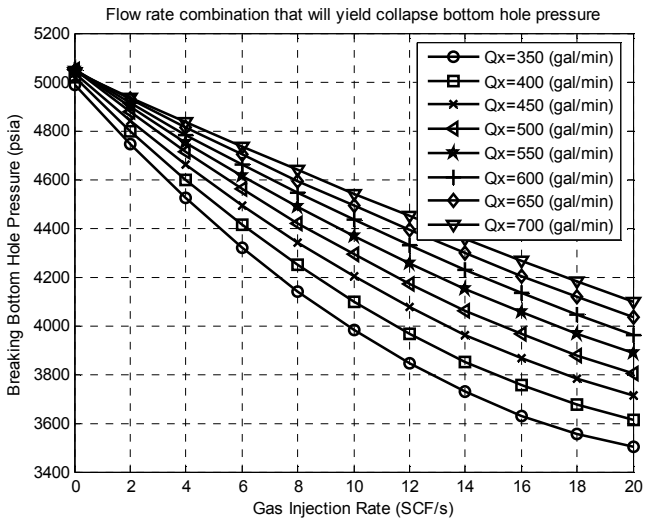

Fig 6.145. *Hydrostatic BHP*

Table 6.16. *Dynamic BHP*

Sea Water Flow Rate Qx (gal/min)	350	400	450	500	550	600	650	700
Gas Injection Flow Rate (SCF/s)	Dynamic Bottom Hole Pressure (psia)							
0	5035.34	5077.17	5109.66	5139.40	5157.79	5177.37	5198.79	5218.40
2	4800.99	4867.99	4923.58	4974.01	5012.39	5049.59	5086.07	5119.00
4	4587.17	4675.59	4751.02	4819.30	4875.11	4927.74	4977.49	5022.31
6	4393.89	4499.98	4591.97	4675.28	4745.96	4811.81	4873.05	4928.35
8	4221.14	4341.14	4446.46	4541.93	4624.92	4701.80	4772.76	4837.10
10	4068.93	4199.08	4314.46	4419.27	4512.01	4597.71	4676.62	4748.56
12	3937.25	4073.81	4195.98	4307.28	4407.21	4499.54	4584.62	4662.74
14	3826.10	3965.32	4091.03	4205.98	4310.54	4407.29	4496.77	4579.64
16	3735.49	3873.61	3999.60	4115.37	4221.99	4320.97	4413.06	4499.26
18	3665.41	3798.68	3921.68	4035.43	4141.56	4240.56	4333.49	4421.59
20	3615.86	3740.53	3857.29	3966.18	4069.26	4166.08	4258.08	4346.63

Table 6.17. *Hydrostatic BHP*

Sea Water Flow Rate Qx (gal/min)	350	400	450	500	550	600	650	700
Gas Injection Flow Rate (SCF/s)	Hydrostatic Bottom Hole Pressure (psia)							
0	4988.62	5018.38	5036.59	5050.10	5049.33	5047.89	5046.50	5040.58
2	4744.82	4799.87	4841.49	4876.16	4896.05	4913.14	4927.78	4936.37
4	4522.18	4598.66	4660.30	4713.13	4750.99	4784.20	4812.89	4834.35
6	4320.72	4414.75	4493.02	4561.03	4614.12	4661.08	4701.84	4734.53
8	4140.42	4248.15	4339.66	4419.86	4485.47	4543.76	4594.62	4636.90
10	3981.29	4098.84	4200.20	4289.60	4365.03	4432.26	4491.24	4541.47
12	3843.33	3966.84	4074.66	4170.27	4252.79	4326.56	4391.69	4448.23
14	3726.53	3852.15	3963.03	4061.87	4148.76	4226.68	4295.97	4357.19
16	3630.90	3754.75	3865.31	3964.39	4052.94	4132.61	4204.09	4268.34
18	3556.44	3674.66	3781.51	3877.83	3965.32	4044.36	4116.05	4181.69
20	3503.15	3611.87	3711.61	3802.19	3885.91	3961.91	4031.83	4097.24

Flowing BHPs at various sea water and gas injection flow rates are plotted in Fig 6.144. If a horizontal line of 5000 psia which symbolizes for formation pressure is drawn in the figure, it will intersect pressure curves at points which are shown in left boundary (balanced pressure limit) of Table 6.18, Fig 6.146. It can be observed from contours of Fig 6.144 that when increasing fluid flow rates and reducing gas injection rates, the BHPs develop because the mixture density increases.The BHP therefore can be controlled by altering the fluid or gas flow rates. The right boundary can be set up similarly. Hydrostatic bottomhole pressure at various sea water and gas injection flow rates are plotted in Fig 6.145. If a horizontal line of the collapse pressure is drawn in the figure at 1450 psia, this line will intersect pressure curves at points which are shown on the right boundary (collapse pressure limit) of Table 6.18, Fig 6.146.

There are significant observations from these results. The LGRW calculated for real data in Fig 6.146 is not smooth and closed as the ideal LGRW in Fig 6.143. First of all, the upper limit in the calculated LGRW is not defined because there is no UBD working carried out in Vietnam so there was no experience gained in the previous drilling operations. Secondly, the left boundary curve does not intersect the lower boundary due to the fact that the dynamic BHP, at values of liquid flow rates below 350 gal/min, is always lower than reservoir pressure (5000 psia) even gas injection rate equals zero. So the horizontal line which is used to define the left boundary can not intersect the corresponding BHP curve. Finally, the right boundary curve in this calculation is quite difficult to define because calculated collapse pressure in previous section is just 1450 psia, so this horizontal line has not intersected with any BHP curves in Fig 6.145 in range of given gas injection rates and liquid flow rates. So the left boundary in Fig 6.146 is only defined when increasing the gas injection rate or lowering fluid flow rate. However, even when the gas injection rate has been increased to the maximum capacity of compressor (40 SCF/s), BHP curves have still been higher than collapse pressure (1450 psia). It means that the right boundary should have moved to the right until gas injection rate reaches to 40 SCF/s. This is out of the compressor capacity, so the well can be drilled safely without reference to the right boundary. This is mainly caused by a calculated collapse pressure that is low.

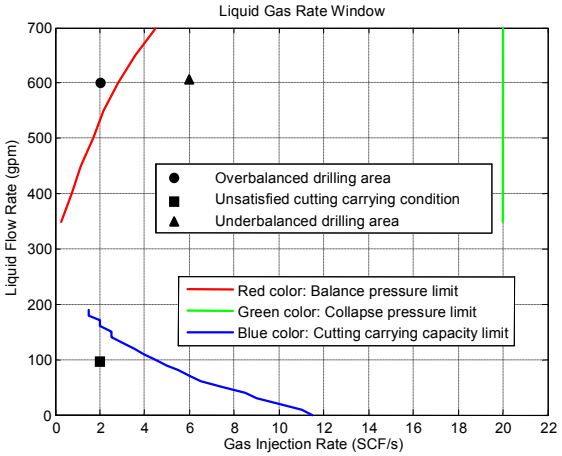

Fig 6.146. *Liquid Gas Rate Window (LGRW)*

To sum up, the combinations of gas injection rates and sea water flow rates must be in the range that liquid flow rate is above the blue line and gas injection rates must be chosen between red line (Fig 6.146) and maximum compressor flow rate.

Table 6.18. *Liquid Gas Rate Window (LGRW)*

	Right Boundary (Collapse Pressure Limit)									
Sea Water Flow Rate (gal/min)	350	400	450	500	550	600	650	700		
Gas Injection Rate (SCF/s)	20	20	20	20	20	20	20	20		
	Left Boundary (Balance Pressure Limit)									
Sea Water Flow Rate (gal/min)	350	400	450	500	550	600	650	700		
Gas Injection Rate (SCF/s)	0.29	0.72	1.16	1.68	2.18	2.80	3.58	4.47		
	Lower Boundary (Cuttings Carrying Capacity Limit)									
Sea Water Flow Rate (gal/min)	0	10	20	30	40	50	60	70	80	90
Gas Injection Rate (SCF/s)	11.5	11	10	9	8.5	7.5	6.5	6	5.5	5
Sea Water Flow Rate (gal/min)	100	110	120	130	140	150	160	170	180	190
Gas Injection Rate (SCF/s)	4.5	4	3.5	3	2.5	2.5	2	2	1.5	1.5

6.2.5. Results of coupling productivity in UBD

During UBD, proper flow monitoring of the produced fluids and drilling records at surface can provide a good indication of productive zones of the reservoir and using the information of produced fluids, reservoir properties and productivity will be qualified. Conversely, during conventional drilling, the overbalance pressure prevents formation inflows; hydrocarbon-bearing zones have to be identified from cuttings, core analysis, logging or drill stem testing.

However, in some areas where UBD has not been applied such as Vietnam, estimating how much oil can be obtained from the reservoir while UBD has always been a difficult question for drilling engineers. If this information is known, the advantage of UBD compared with OBD will be estimated. And this is the important factor for operators to decide whether UBD should be applied or not. Hence, the coupling productivity in UBD work will be carried out by the opposite approach in which well data and reservoir data are collected from historical conventional wells. An estimate of how much oil can be produced by applying UBD can be made. The answer is shown in the following calculated results by using UBDDRILL with the input data from 6.2.2 to solve.

Combinations of sea water flow rates and gas injection rates will give different values of formation influx fluid flow rates. In the figure above, the OBD area in the data table is the area in which the OBD situation occurs. For example, if the sea water flow

rate is 600 gal/min and gas injection rate is 2 SCF/s, the formation influx fluid flow rate will equal zero, it means that the UBD condition does not remain.

In another combination of sea water and air flow rate, 100 gal/min and 2 SCF/s, this combination is out of LGRW because it is located under lower boundary so it can not satisfy cutting carrying capacity condition. In this case, sea water flow rate and gas injection rate needs to be increased to improve the transportion of cuttings to the surface.

Table 6.19. *Formation fluid influx flow rate*

Sea Water Flow Rate (gal/min)	350	400	450	500	550	600	650	700
Gas Injection Flow Rate (SCF/s)	Formation Fluid Inlfux Flow Rate (STB/Day)							
0	OBD Region ⇒ Formation Fluid Influx Flow Rate = 0							
2	861.78	480.76	187.06					
4	1761.27	1345.25	1066.43	756.61	445.57	195.86		
6	2440.03	2018.32	1611.80	1263.10	1038.74	738.48	486.24	199.69
8	2986.92	2554.62	2163.05	1777.08	1461.59	1153.67	893.06	630.77
10	3447.83	3011.75	2612.71	2210.97	1875.95	1563.62	1251.22	1014.49
12	3827.73	3386.82	2980.03	2604.29	2255.04	1927.96	1619.06	1302.25
14	4200.46	3758.75	3346.89	2962.95	2603.52	2265.26	1944.77	1638.90
16	4532.25	4093.78	3680.37	3291.56	2925.17	2578.55	2248.96	1933.74
18	4834.03	4397.81	3985.41	3594.21	3223.24	2870.54	2534.02	2211.15
20	5102.46	4678.57	4265.64	3874.16	3500.54	3143.59	2801.60	2472.76

Continuing to consider 600 gal/min sea water flow rate and 6 SCF/s gas injection rate, dynamic BHP will be 4811.81 psia (see table 6.16) lower than reservoir pressure (5000 psia) so it satisfies the UBD condition. And hydrostatic BHP will be 4661 psia (see table 6.17) higher than collapse pressure (1450 psia) so it also satisfies the collapse pressure limit criterion. As a result, two values (600 gal/min, 6 SCF/s) located between the red and green lines, above the blue line, inside LGRW, gives a considerable rate of production oil in the UBD case (738 STB/Day). However, if sea water flow rate still remains as 600 gal/min and gas injection rate decreases too much, for example 2 SCF/s, the dynamic BHP will increase to 5049 psia (higher than reservoir pressure (5000 psia)). Therefore, the oil influx flow rate in this case will be zero as the well will not be underbalanced.

In summary, coupling drilling parameters and inflow performance parameters such as surface choke pressure, gas injection rates, and liquid flow rates in UBD design can help to calculate the production in UBD operations. These production oil values corresponding to the given sea water rates and gas injection rates then must be checked to be sure that they satisfy conditions of LGRW (UBD condition, cuttings carrying capacity criterion, and collapse pressure limit criterion). At the end, satisfied values will be compared to select the maximum values of formation influx fluid (oil). And the combination of gas injection rate and sea water flow rate which gives this maximum oil production is the optimum combination.

6.2.6. Comparing the results produced by UBDRILL and the analytical solution of Guo and Ghalambor

An Excel spreadsheet is used to solve the same problem with the same input data in 6.2.2. However, in the calculation of Guo and Ghalambor, the formation fluid influx flow rate is considered constant instead of changing to BHP as presented in chapter 4. So the results can be compared in the following way.

- Selecting one value of formation fluid influx flow rate from Table 6.19, for example 2440 STB/Day corresponding to 350 gal/min sea water flow rate and 6 SCF/s gas injection rate.
- Using the analytical solution of Guo and Ghalambor presented in chapter 2 with values of flow rates (Q_f = 2440 STB/Day, Q_x = 350 gal/min, and Q_{gs} = 6 SCF/s = 360 SCF/min) and input data in 6.2.2 to calculate the BHP.
- The BHP solved by Guo and Ghalambor method then will be compared with the BHP result (4393 psia) (see table 6.16) produced by UBDRILL.
- Note that the comparison between two methods is just to verify the difference, not the error of them because these methods have been developed based on two different assumptions. One is taken into account the coupling of inflow performance relationship (UBDRILL), the other one considers Q_f as a constant (Boyun and Ghalambor).

Table 6.20. *Comparing results produced by UBDRILL and the analytical solution of Guo and Ghalambor*

Q_x = gal/min	**400**	**500**	**600**	**650**	**350**	**700**
Q_{gs} = SCF/s	**2**	**4**	**8**	**12**	**6**	**20**
Q_f = STB/Day	**480.76**	**756.61**	**1153.66**	**1619.06**	**2440.03**	**2472.76**
	BHP (psia)					
UBDRILL	4867.99	4819.30	4701.80	4584.62	4393.89	4346.63
Boyun and Ghalambor	5306.64	5298.30	5239.21	5189.90	5095.00	5071.84
Difference (%)	8.27	9.04	10.26	11.66	13.76	14.29

The difference of BHP produced by UBDRILL and the solution of Guo and Ghalambor in the example above is in the range from 8.27% to 14.29%. There is a general trend in these results that when the formation fluid influx flow rate (Q_f) increases, the difference between two method increases as well. This is explained by the fact that, Q_f is assumed constant in the analytical solution of Guo and Ghalambor, and only depends on the drilling operation and independent of reservoir parameters. When Q_f changes, its affect on BHP is negligible because BHP mainly depends on hydrostatic pressure. And hydrostatic pressure depends on mixture density. So when Q_f changes, mixture density changes slightly. As a result, BHP in the analytical solution of Guo and Ghalambor is influenced not much by Q_f. However, in IFDM method, Q_f is a parameter decided by two factors. The first one is UBD parameters, and the second one is the IPR. And it is only calculated through the iterative method. So the higher Q_f, the lower BHP, the higher difference between two approaches.

In summary, the difference of results produced by UBDRILL and the analytical solution of Guo and Ghalambor is caused by:

- IFDM method is used to calculate the results in UBDRILL instead of the analytical solution of Guo and Ghalambor.
- The modification of some parameters in IFDM method such as formation volume factor (oil, sea water), friction factor.
- The coupling productivity in UBD is applied to the solution of UBDRILL so the formation fluid influx flow rate depends on BHP while this flow rate is considered constant in the analytical solution of Guo and Ghalambor.

6.2.7. Analyzing the sensitivity of input data

Sometimes, it is difficult to know which data have the significant influence to the obtained results. Altering the input data and evaluating the output which is called sensitivity analysis is the effective approach to evaluate the important role of collected data. Some following data will be analyzed their sensitivities:

Wellhead pressure

Wellhead pressure is controlled in drilling operation and it helps to maintain BHP at required values. The estimation of the wellhead pressure sensitivity can be carried out by changing the wellhead pressure from 60 to 100 psia (40%) while all other input data are described in 6.2.2. Comparing the alteration of wellhead and corresponding results then will help to define the sensitivity of wellhead pressure in this case.

The results on Table 6.21 show that when the wellhead pressure changes 40% (from 60 to 100 psia), the BHP only changes from 1.09% to 3.52%, so it means that the wellhead pressure is not an important input data because its influence on the calculated results is unremarkable. So the wellhead pressure is not a sensitive parameter.

Table 6.21. *Sensitivity Analysis of wellhead pressure*

Sea Water Flow Rate Qx (gal/min)		350	400	450	500	550	600	650	700
Gas Injection Flow Rate (SCF/s)	**Sensitivity of Wellhead Pressure**	Dynamic BHP (psia)							
0	P_{wh} = 60 psia	4998	5041	5076	5106	5134	5155	5176	5199
	P_{wh} = 100 psia	5074	5116	5146	5163	5181	5200	5218	5237
	Sensitivity (%)	$\frac{1}{n}\sum_{i=1}^{n}\frac{P_{wh(100)}-P_{wh(60)}}{P_{wh(100)}} = \mathbf{1.09}$							
2	P_{wh} = 60 psia	4756	4823	4881	4932	4978	5017	5053	5090
	P_{wh} = 100 psia	4846	4913	4967	5007	5045	5081	5114	5146
	Sensitivity (%)	1.47							
4	P_{wh} = 60 psia	4534	4623	4701	4770	4832	4885	4936	4985
	P_{wh} = 100 psia	4637	4726	4800	4860	4916	4967	5013	5057
	Sensitivity (%)	1.83							
6	P_{wh} = 60 psia	4334	4441	4535	4619	4694	4761	4823	4883
	P_{wh} = 100 psia	4449	4555	4646	4723	4794	4857	4916	4970
	Sensitivity (%)	2.17							
8	P_{wh} = 60 psia	4155	4276	4383	4479	4566	4644	4716	4785
	P_{wh} = 100 psia	4280	4400	4504	4596	4679	4753	4821	4884
	Sensitivity (%)	2.48							
10	P_{wh} = 60 psia	3998	4129	4246	4352	4447	4535	4615	4691
	P_{wh} = 100 psia	4131	4261	4376	4478	4570	4654	4730	4800
	Sensitivity (%)	2.76							
12	P_{wh} = 60 psia	3862	4000	4124	4236	4338	4432	4518	4600
	P_{wh} = 100 psia	4003	4138	4260	4369	4469	4559	4642	4718
	Sensitivity (%)	3.00							
14	P_{wh} = 60 psia	3748	3888	4015	4132	4238	4336	4427	4513
	P_{wh} = 100 psia	3894	4032	4157	4271	4375	4469	4557	4638
	Sensitivity (%)	3.20							
16	P_{wh} = 60 psia	3655	3794	3922	4039	4147	4248	4341	4430
	P_{wh} = 100 psia	3804	3941	4067	4182	4287	4385	4475	4560
	Sensitivity (%)	3.36							
18	P_{wh} = 60 psia	3583	3718	3842	3958	4065	4166	4261	4351
	P_{wh} = 100 psia	3735	3867	3989	4102	4207	4305	4396	4483
	Sensitivity (%)	3.47							
20	P_{wh} = 60 psia	3533	3659	3778	3889	3993	4092	4186	4275
	P_{wh} = 100 psia	3685	3809	3924	4032	4133	4230	4321	4408
	Sensitivity (%)	**3.52**							

Rate of penetration

Rate of penetration is a parameter of drilling operation. The higher rate of penetration is, the lower drilling cost is spent. However, in some hard rock formations in Vietnam, rate of penetration in the conventional drilling is only from 10-15 ft/hr. So when applying UBD this parameter can reach to 30 ft/hr. The purpose of its sensitivity analysis is to evaluate the influence of penetration rate to BHP which is an important factor in maintaining UBD condition.

To investigate the sensitivity of the rate of penetration, it can be carried out by changing its value from 20 to 40 ft/hr and still using other input data of 6.2.2. This result of sensitivity analysis can be expressed in the following table:

Table 6.22. *Sensitivity Analysis of Rate of Penetration*

Sea Water Flow Rate Qx (gal/min)		350	400	450	500	550	600	650	700
Gas Injection Flow Rate (SCF/s)	**Sensitivity of Wellhead Pressure**	Dynamic BHP (psia)							
0	R_p = 20 ft/hr	5015	5059	5095	5126	5149	5169	5191	5212
	R_p = 40 ft/hr	5054	5095	5126	5150	5167	5186	5206	5225
	Sensitivity (%)	$\frac{1}{n}\sum_{i=1}^{n}\frac{R_{p(40)}-R_{p(20)}}{R_{p(40)}} = \mathbf{0.47}$							
2	R_p = 20 ft/hr	4783	4851	4910	4961	5003	5041	5077	5112
	R_p = 40 ft/hr	4818	4885	4939	4985	5022	5058	5094	5126
	Sensitivity (%)	0.48							
4	R_p = 20 ft/hr	4571	4660	4738	4807	4865	4918	4969	5015
	R_p = 40 ft/hr	4603	4691	4765	4831	4885	4937	4985	5030
	Sensitivity (%)	0.48							
6	R_p = 20 ft/hr	4379	4486	4580	4663	4736	4802	4864	4921
	R_p = 40 ft/hr	4408	4514	4605	4686	4756	4821	4881	4936
	Sensitivity (%)	0.48							
8	R_p = 20 ft/hr	4208	4328	4435	4530	4615	4692	4764	4829
	R_p = 40 ft/hr	4234	4354	4459	4553	4635	4711	4781	4845
	Sensitivity (%)	0.47							
10	R_p = 20 ft/hr	4057	4187	4304	4408	4502	4588	4668	4741
	R_p = 40 ft/hr	4081	4211	4326	4430	4522	4607	4685	4756
	Sensitivity (%)	0.46							
12	R_p = 20 ft/hr	3926	4063	4186	4297	4398	4491	4576	4655
	R_p = 40 ft/hr	3948	4085	4207	4317	4417	4508	4593	4671
	Sensitivity (%)	0.45							
14	R_p = 20 ft/hr	3816	3956	4082	4197	4302	4399	4489	4572
	R_p = 40 ft/hr	3836	3975	4101	4215	4320	4416	4505	4587
	Sensitivity (%)	0.43							
16	R_p = 20 ft/hr	3726	3865	3991	4107	4214	4313	4405	4492
	R_p = 40 ft/hr	3745	3883	4008	4124	4230	4329	4421	4506
	Sensitivity (%)	0.40							
18	R_p = 20 ft/hr	3657	3790	3914	4028	4134	4233	4327	4415
	R_p = 40 ft/hr	3674	3807	3930	4043	4149	4248	4341	4428
	Sensitivity (%)	0.38							
20	R_p = 20 ft/hr	3608	3733	3850	3959	4063	4160	4252	4340
	R_p = 40 ft/hr	3624	3748	3864	3973	4076	4173	4264	4353
	Sensitivity (%)	**0.34**							

Rate of penetration has not interfered a lot in calculation of BHP because it causes a slight change of BHP. The estimated sensitivity is only from 0.34% to 0.47%. It means that when the rate of penetration changes 50% (20 ft/hr – 40 ft/hr), the results of the BHP just varies from 0.34% to 0.47% so it can be increased to save drilling time without influencing a lot to UBD condition. To sum up, the rate of penetration is not a sensitive parameter.

Mud density

Mud density has an important role in maintaining hydrostatic pressure in the wellbore. The input data is the same as 6.2.2 except that replacing gasified sea water by gasified mud with mud density in a range of 9-10 ppg. Comparing the variation of mud

density and the alteration of results will help to evaluate the sensitivity of mud density in this case.

Table 6.23. *Sensitivity Analysis of Mud density*

Sea Water Flow Rate Qx (gal/min)		350	400	450	500	550	600	650	700
Gas Injection Flow Rate (SCF/s)	**Sensitivity of Wellhead Pressure**	Dynamic BHP (psia)							
0	W_x = 9 ppg	5653	5641	5635	5638	5648	5668	5694	5726
	W_x = 10 ppg	6180	6191	6220	6246	6268	6294	6322	6353
	Sensitivity (%)	$\frac{1}{n}\sum_{i=1}^{n}\frac{W_{x(10)}-W_{x(9)}}{W_{x(10)}} = \mathbf{9.53}$							
2	W_x = 9 ppg	5420	5460	5491	5520	5548	5578	5610	5645
	W_x = 10 ppg	6028	6058	6091	6125	6159	6193	6230	6267
	Sensitivity (%)	9.93							
4	W_x = 9 ppg	5200	5284	5346	5399	5445	5486	5525	5564
	W_x = 10 ppg	5869	5920	5962	6005	6050	6094	6138	6182
	Sensitivity (%)	10.31							
6	W_x = 9 ppg	4991	5113	5203	5277	5339	5392	5439	5483
	W_x = 10 ppg	5702	5777	5832	5886	5942	5995	6047	6098
	Sensitivity (%)	10.68							
8	W_x = 9 ppg	4795	4946	5059	5153	5231	5295	5351	5402
	W_x = 10 ppg	5529	5630	5702	5768	5835	5897	5957	6014
	Sensitivity (%)	11.04							
10	W_x = 9 ppg	4611	4783	4916	5027	5119	5196	5261	5320
	W_x = 10 ppg	5348	5478	5571	5652	5729	5800	5867	5931
	Sensitivity (%)	11.37							
12	W_x = 9 ppg	4438	4625	4773	4899	5005	5094	5170	5239
	W_x = 10 ppg	5161	5322	5440	5537	5624	5704	5778	5849
	Sensitivity (%)	11.69							
14	W_x = 9 ppg	4278	4471	4631	4768	4888	4990	5078	5157
	W_x = 10 ppg	4966	5161	5308	5422	5520	5608	5690	5767
	Sensitivity (%)	11.98							
16	W_x = 9 ppg	4130	4322	4488	4636	4768	4884	4985	5075
	W_x = 10 ppg	4764	4995	5176	5309	5417	5513	5602	5686
	Sensitivity (%)	12.24							
18	W_x = 9 ppg	3994	4176	4346	4502	4645	4775	4890	4993
	W_x = 10 ppg	4555	4825	5043	5197	5315	5419	5516	5605
	Sensitivity (%)	12.46							
20	W_x = 9 ppg	3870	4036	4205	4366	4519	4663	4794	4911
	W_x = 10 ppg	4338	4650	4910	5087	5213	5326	5429	5525
	Sensitivity (%)	**12.64**							

It is recognized that when mud density alters 10% (from 9 ppg to 10 ppg), the BHP changes from 9.53% to 12.64%, so this parameter (mud density) needs to be controlled carefully to maintain the pressure condition at the bottom hole satisfying UBD criteria in UBD (cutting carrying capacity, wellbore stability, and under pore formation pressure). The influence of mud density to the results is remarkable so it is really a sensitive parameter.

Gas gravity

To estimate the sensitivity of gas gravity, the input data is as same as 6.2.2, and gas gravity was changed from 0.65 (natural gas) to 1 (air). Comparing the changing of

the gas gravity and the changing of results will help to calculate the sensitivity of gas gravity in this case.

Table 6.24. *Sensitivity Analysis of Gas gravity*

Sea Water Flow Rate Qx (gal/min)		350	400	450	500	550	600	650	700
Gas Injection Flow Rate (SCF/s)	**Sensitivity of Wellhead Pressure**	Dynamic BHP (psia)							
0	gg = 0.65	5035	5077	5110	5139	5158	5177	5199	5218
	gg = 1.00	4954	5025	5113	5151	5174	5198	5215	5231
	Sensitivity (%)	$\frac{1}{n}\sum_{i=1}^{n}\frac{gg_{(1.00)}-gg_{(0.65)}}{gg_{(1.00)}}=\mathbf{0.14}$							
2	gg = 0.65	4801	4868	4924	4974	5012	5050	5086	5119
	gg = 1.00	4702	4798	4902	4967	5015	5063	5101	5136
	Sensitivity (%)	0.40							
4	gg = 0.65	4587	4676	4751	4819	4875	4928	4977	5022
	gg = 1.00	4477	4593	4711	4797	4868	4936	4992	5043
	Sensitivity (%)	0.61							
6	gg = 0.65	4394	4500	4592	4675	4746	4812	4873	4928
	gg = 1.00	4278	4410	4538	4642	4731	4816	4887	4952
	Sensitivity (%)	0.77							
8	gg = 0.65	4221	4341	4446	4542	4625	4702	4773	4837
	gg = 1.00	4106	4250	4385	4502	4605	4703	4786	4863
	Sensitivity (%)	0.85							
10	gg = 0.65	4069	4199	4314	4419	4512	4598	4677	4749
	gg = 1.00	3960	4111	4251	4377	4490	4597	4690	4776
	Sensitivity (%)	**0.87**							
12	gg = 0.65	3937	4074	4196	4307	4407	4500	4585	4663
	gg = 1.00	3841	3995	4137	4267	4387	4499	4599	4691
	Sensitivity (%)	0.80							
14	gg = 0.65	3826	3965	4091	4206	4311	4407	4497	4580
	gg = 1.00	3749	3901	4041	4172	4294	4408	4512	4608
	Sensitivity (%)	0.65							
16	gg = 0.65	3735	3874	4000	4115	4222	4321	4413	4499
	gg = 1.00	3683	3830	3965	4092	4212	4324	4429	4527
	Sensitivity (%)	0.40							
18	gg = 0.65	3665	3799	3922	4035	4142	4241	4333	4422
	gg = 1.00	3644	3781	3907	4027	4141	4248	4351	4448
	Sensitivity (%)	0.06							
20	gg = 0.65	3616	3741	3857	3966	4069	4166	4258	4347
	gg = 1.00	3632	3753	3869	3977	4081	4179	4277	4371
	Sensitivity (%)	0.37							

The increase of gas gravity from 0.65 to 1.00 (35%) almost does not affect to BHP (only change from 0.14 to 0.87%). So it is concluded that gas gravity is not too important to focus in the input data.

6.2.8. Verifying the influence of solid phase

As discussed in chapter 3 (3.2.1, 3.2.2), the volumetric flow rate of a solid in the calculation of mixture density is usually negligible (less than 5% of the total volumetric flow rate) in gasified fluid. So this will be verified in the following results.

Table 6.25. *Influence of solid phase*

Gas Injection Rate Q_{gs} (SCF/s)		10	20	30	40
Measured Depth (ft)	**Mixture Density (lbm/ft^3)**	Mixture density (lbm/ft^3)			
59.2	with Q_s	26.80	17.40	13.07	10.57
	without Q_s	27.10	17.62	13.25	10.71
	Error (%)	$\frac{1}{n}\sum_{i=1}^{n}\frac{\rho_{m(withQ_s)}-\rho_{m(withoutQ_s)}}{\rho_{m(withQ_s)}}=1.26$			
592	with Q_s	39.78	26.58	19.36	15.11
	without Q_s	40.51	27.21	19.83	15.46
	Error (%)	2.20			
1329	with Q_s	48.42	36.66	27.95	21.92
	without Q_s	49.43	37.86	28.98	22.75
	Error (%)	3.11			
4692	with Q_s	56.20	51.33	46.66	42.04
	without Q_s	56.70	52.47	48.50	44.36
	Error (%)	3.02			
7,439	with Q_s	56.96	53.33	50.28	47.35
	without Q_s	56.62	53.21	50.82	48.60
	Error (%)	**0.70**			
11,072	with Q_s	57.67	54.24	51.84	49.80
	without Q_s	56.38	52.61	50.52	48.98
	Error (%)	2.42			
12,642	with Q_s	58.04	54.52	52.18	50.27
	without Q_s	56.51	52.51	50.36	48.85
	Error (%)	3.26			
14,430	with Q_s	58.03	54.51	52.18	50.31
	without Q_s	56.45	52.39	50.22	48.71
	Error (%)	**3.51**			

The difference of mixture density in the case of modifying Q_s to calculate mixture density and negligible Q_s is only from 0.7 to 3.51%. So, this proved that the affection of cutting volume (Q_s) on the annulus mixture density and pressure is inconsiderable and can be ignored.

6.2.9. Selecting compressor

The process of compressor unit selection requires that the borehole requirements be compared to the capabilities of the available compressor units. These comparisons are made between (a) the volumetric flow rate required by the borehole and the volumetric capability of the compressor unit and (b) the injection pressure required by the borehole (calculated based on the compressor volumetric flow rate) and the pressure capability of the compressor unit.

The selected compressor is decided depending on the combination of gas flow rate and liquid injection rate which satisfy cutting carrying capacity requirements, balance pressure limit, and collapse pressure limit. For example, from the previous section (6.2.4) and LGRW (Fig 6.146), it can be observed that the combination of gas flow rate of 10 SCF/s and 600 gal/min will meet all UBD conditions. Therefore, the compressor in this case should be sized based on this gas injection rate value of 10 SCF/s and approximately required injection pressure of 2890 psia which can be referred in following figure.

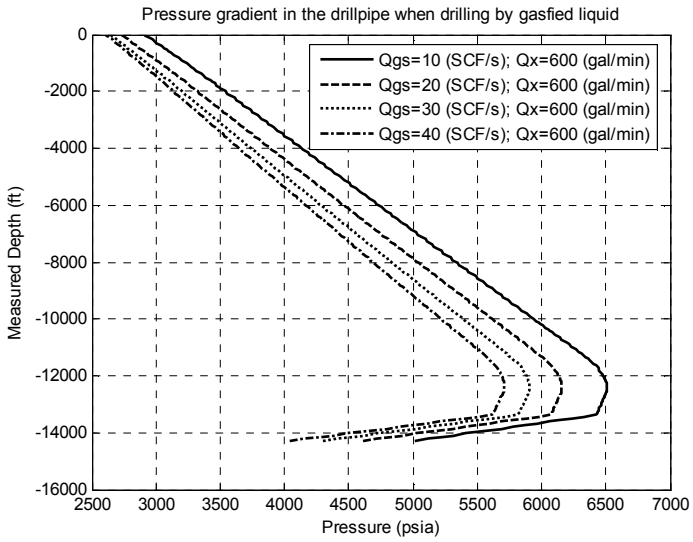

Fig 6.147. *Pressure gradient in the drillpipe*

6.2.10. Comparing UBDRILL and HYDMOD

Keep all input data as same as 6.2.2 except that sea water is replaced by mud which is not gasified, has a weight of 8.2 ppg, and pumped with the flow rate of 400 gal/min. Then, using HYDMOD software of Maurer Engineering Ltd to calculate the results of pressure and compare to the results produced by UBDRILL to withdraw the error between two simulators.

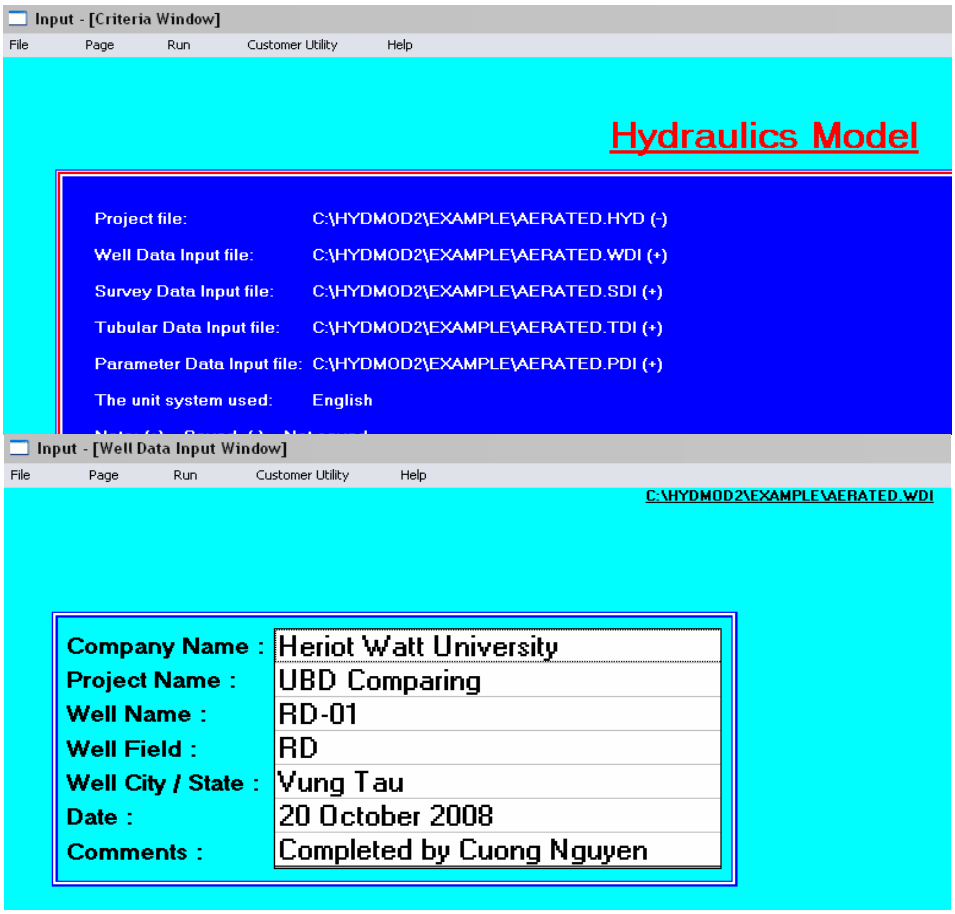

Fig 6.148. *HYDMOD software*

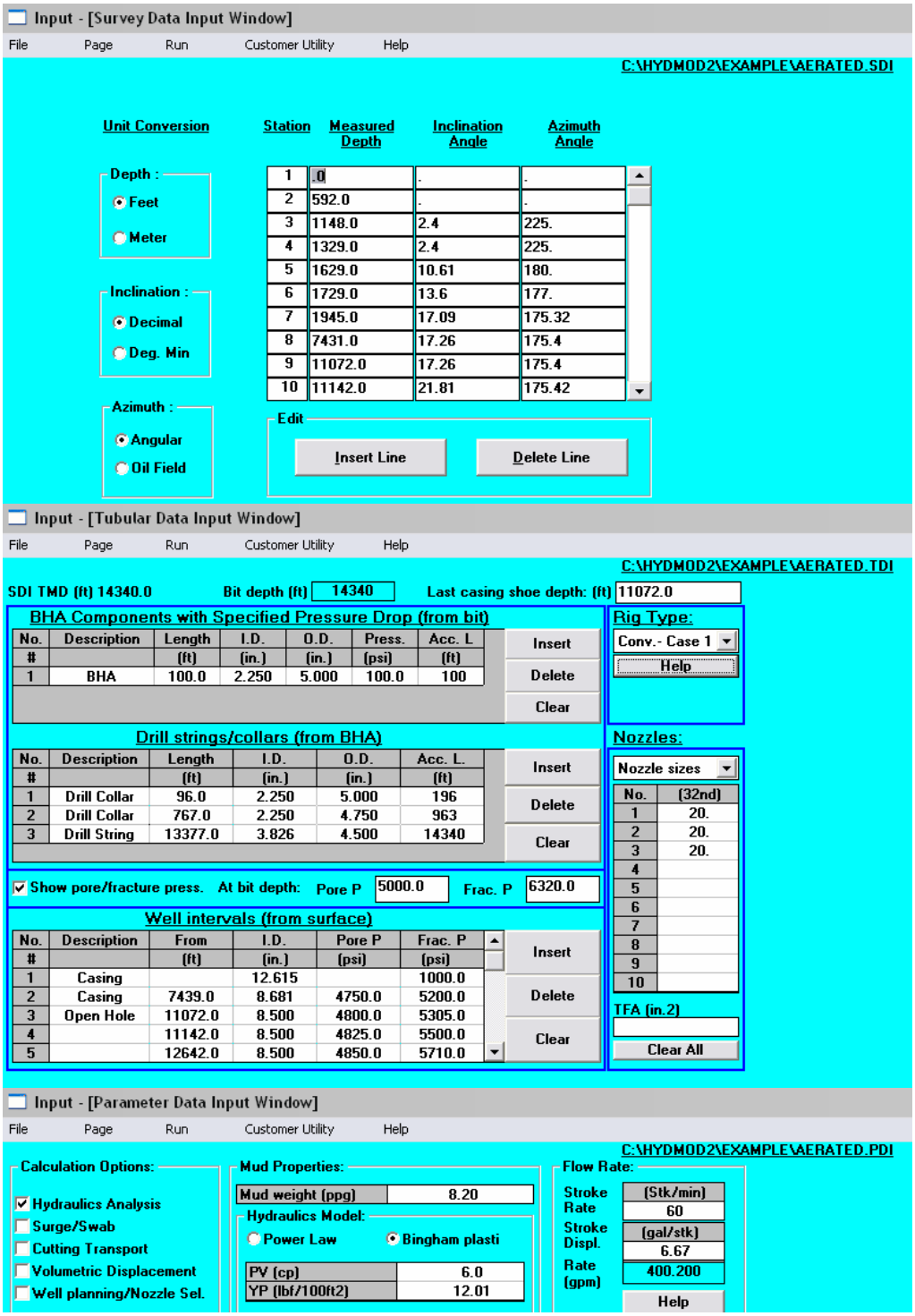

Fig 6.149. *Input data in HYDMOD software*

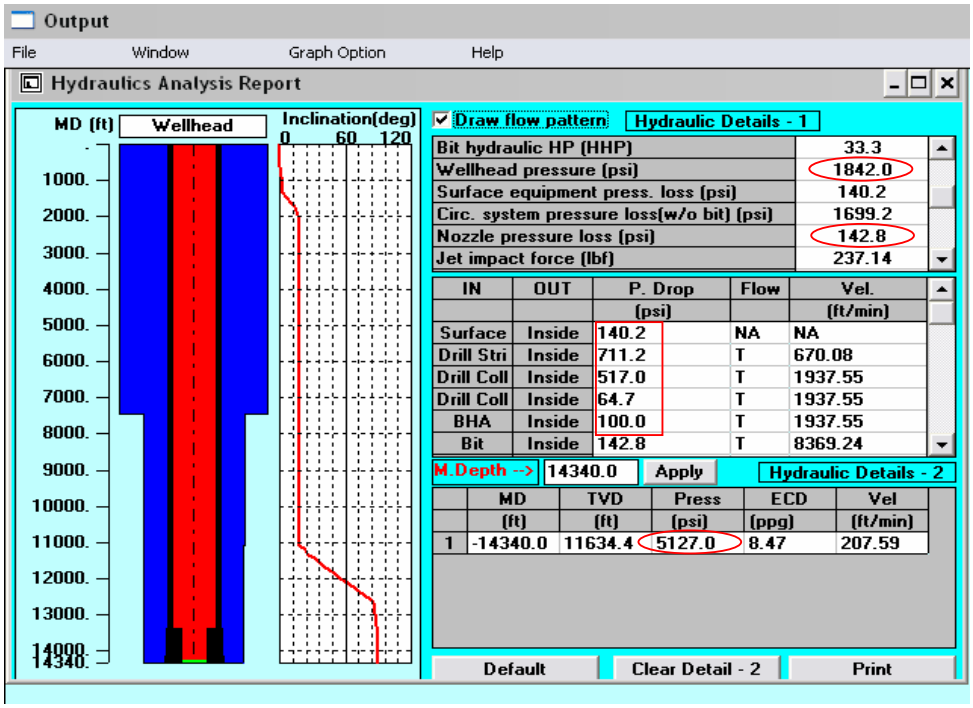

Fig 6.150. *Results produced by HYDMOD software*

The results of UBDRILL and HYDMOD can be summarized as follow:

Table 6.26. *Comparing results produced by UBDRILL and HYDMOD*

Parameters	UBDRILL	HYDMOD	Error (%)
BHP (psia)	5063.9	5127.0	1.23
Nozzle pressure loss (psi)	142.6	142.8	0.14
Pressure loss in drillpipes due to friction (psi)	1482.8	1533.1	3.28
Required compressure pressure (psia)	1824.5	1842.0	0.95

6.2.11. Estimating the convergence

The calculation of a multi-phase flowing pressure distribution involves use of an iterative or trial-and-error procedure if temperatures or wellbore inclination change with location or distance. The flow conduit in this calculation was divided into a number of length increments, and the fluid properties and pressure gradient are evaluated at average conditions of pressure, temperature and wellbore inclination in the increment. The accuracy of calculated result increases when the number of increments increases. However, the time involved may be significant for. Estimating the convergence will help to get good results in the shortest time, and this is one of the most important requirements which software production and user are interested in. Keep the input data as same as 6.2.2 and change divided increments in one section to keep track the varying of BHP results. The BHPs corresponding to 400 gal/min liquid flow rate and 10 SCF/s gas injection rate in the cases increment length = 5-100 ft are shown in the following table:

Table 6.27. *The result of convergence analysis*

Length of Increment (ft)	5	10	15	20	25	30	35	40	45	50
BHP (psia)	4229	4229	4229	4229	4229	4230	4231	4229	4230	4229
Length of Increment (ft)	55	60	65	70	75	80	85	90	95	100
BHP (psia)	4231	4234	4236	4229	4229	4229	4233	4236	4239	4232

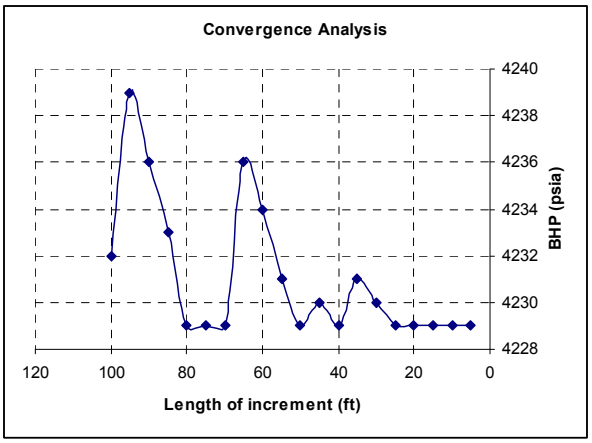

Fig 6.151. *The result of convergence analysis*

The above graph shows that the result converges when the length of each increment is about 25 ft. It means that the better results can be obtained when the more increments corresponding with the smaller length of each increment are divided in each section.

6.3. Foam Drilling Analysis in UBD

Foams have been used as circulating fluid in workover and drilling operation for more than 30 years. They are used in deep drilling mainly for oil and gas producing wells to minimize formation damage and lost circulation in depleted reservoirs. For reservoirs with unconsolidated formation and easy to collapse, foams are not good candidates because its low density will make a low BHP which can not guarantee the wellbore stability. However, for hard rock reservoirs with low collapse pressure like Basin X which approximates 1450 psia as calculated in previous sections, stable foam may be an attractive circulating fluid because the density of foam is quite low.

This section outlines results of foam drilling analysis which includes the minimum required gas volume in planning a successful UBD operation, the LGRW planning results, and estimated production capacity in UBD by foam.

6.3.1. Input data

Table 6.28. *PVT data*

	Input Data	**Units**	**Notes**
Formation Pressure (P_R)	5000	psia	34.45 MPa
Bubble Point Pressure (P_b)	4678	psia	
Collapse Pressure (P_{col})	1450	psia	10 MPa
Wellhead Pressure (P_{wh})	80	psia	
Surface Temperature (T_{wh})	139	^oF	
Gas Gravity (S_g)	0.65		
API Gravity (API)	39.3		
Specific Gravity of Liquid Injection (S_x)	1.02		
Liquid viscosity (μ_x)	1	Cp	
Maximum Compressor Flow Rate(Q_{pumb})	40	SCF/s	
Formation Influx Fluid (a)	1		Oil a = 1; Water a = 2;

According to the input data for the calculation of foam drilling, assuming the wellbore trajectory and IPR are unchangeable and referred in Table 6.13, and 6.14. While the foam drilling parameters have a change in comparison to gasified sea water drilling (Table 6.11) when the rate of penetration is 50 ft/hr instead of 30 ft/hr. PVT data is shown on the above table.

6.3.2. Results of modelling foam flow

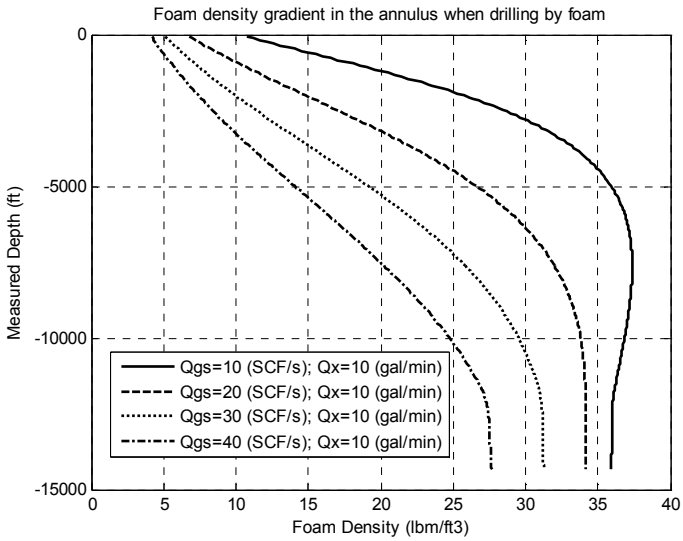

Fig 6.152. *Foam density in the annulus*

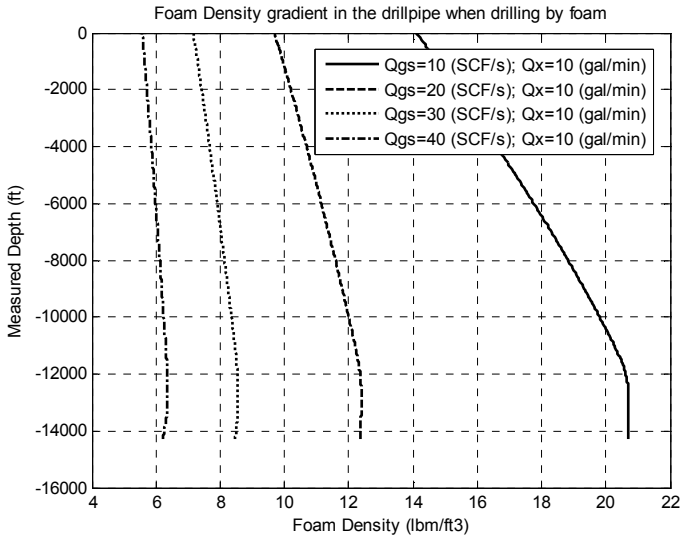

Fig 6.153. *Foam density in the drillpipe*

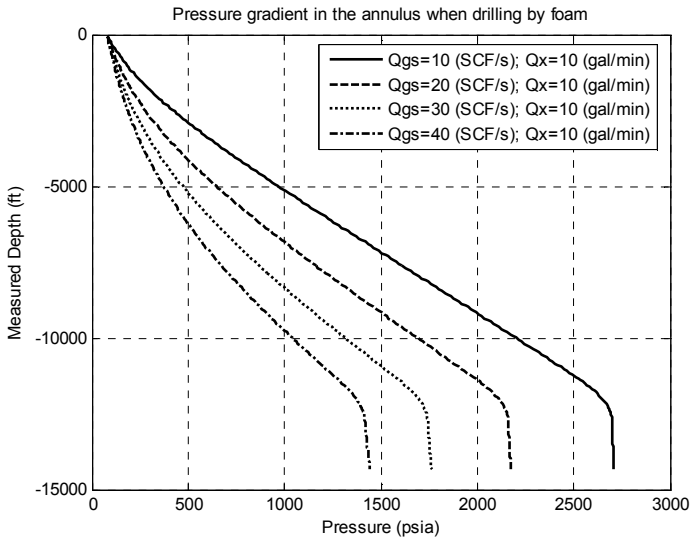

Fig 6.154. *Pressure gradient in the annulus when drilling by foam*

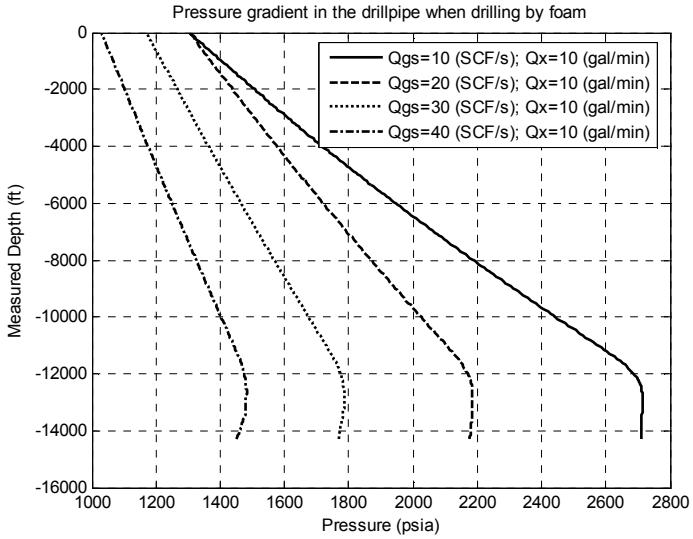

Fig 6.155. *Pressure gradient in the drillpipe when drilling by foam*

Figs 6.151, and 6.152 display foam density gradient in the annulus and the drillpipe when gas injection rate varies from 10 to 40 SCF/s and liquid flow rate is 10 gal/min. According to these results, the foam density at the bottomhole in the annulus is higher than that in the drillpipe caused by the influx of formation fluids into the annulus of the wellbore in UBD.

6.3.3. Results of planning LGRW

The LGRW is the window that can be constructed based on formation pore pressure, wellbore collapse pressure, cuttings carrying capacity of the fluid mixture, and wellbore washout criteria. And it gives the field engineers flexibility in selection of liquid and gas injection rates on the drilling site. The following results with the input data referred from 6.3.1 were produced by UBDRILL.

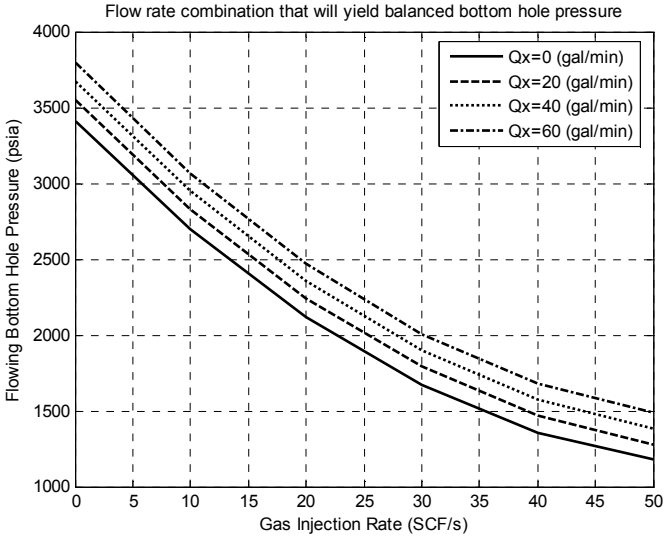

Fig 6.156. *Dynamic BHP*

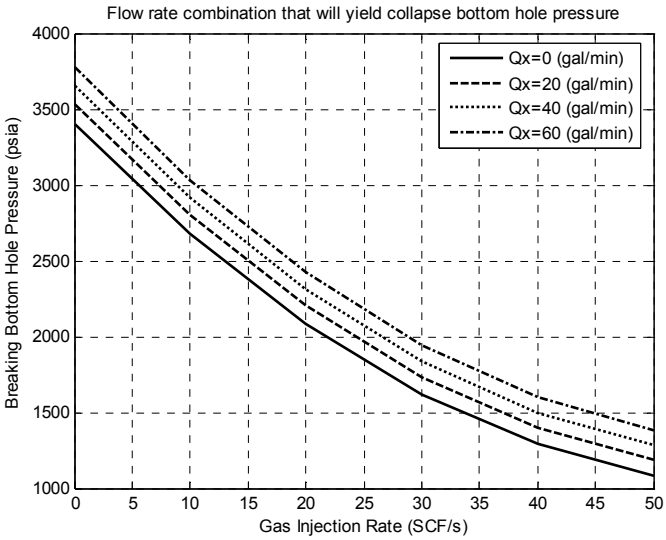

Fig 6.157. *Hydrostatic BHP*

Table 6.29. *Dynamic BHP*

Liquid Flow Rate Qx (gal/min)	0	20	40	60
Gas Injection Flow Rate (SCF/s)	Dynamic Bottom Hole Pressure (psia)			
0	3410.75	3544.30	3671.98	3796.36
10	2700.09	2828.15	2948.79	3065.52
20	2121.30	2243.49	2358.18	2468.97
30	1674.36	1790.32	1900.14	2006.70
40	1359.29	1468.63	1574.66	1678.71
50	1176.08	1278.42	1381.75	1485.00

Table 6.30. *Hydrostatic BHP*

Liquid Flow Rate Qx (gal/min)	0	20	40	60
Gas Injection Flow Rate (SCF/s)	Hydrostatic Bottom Hole Pressure (psia)			
0	3397.46	3529.61	3655.73	3778.68
10	2675.93	2801.42	2919.39	3033.32
20	2084.15	2203.00	2314.24	2421.27
30	1622.12	1734.35	1840.27	1942.54
40	1289.85	1395.47	1497.50	1597.12
50	1087.33	1186.37	1285.92	1385.01

Flowing BHPs at various liquid and gas injection flow rates are plotted in Fig 6.156. A horizontal line is drawn in the figure at a flowing bottom hole reservoir pressure of 5000 psia. This horizontal line has not intersected any pressure curves because the BHP caused by foam drilling has not reached to the formation pressure at any calculated gas and injection rates so the left boundary (balanced pressure limit) in Fig 6.158 can be ignored. Similar to the left boundary, the right boundary can be set up similarly. Hydrostatic bottomhole pressure at various liquid water and gas injection flow rates are plotted in Fig 6.157. A horizontal line is drawn in the figure at the collapse pressure of 1450 psia. This horizontal line intersects pressure curves at points which are shown in right boundary (collapsed pressure limit) of Table 6.31, Fig 6.158.

Table 6.31. *Liquid Gas Rate Window (LGRW)*

	Right Boundary (Collapse Pressure Limit)					
Liquid Flow Rate (gal/min)	0	20	40	60		
Gas Injection Rate (SCF/s)	34.69	38.09	41.79	46.19		
	Left Boundary (Balance Pressure Limit)					
Liquid Flow Rate (gal/min)	0	20	40	60		
Gas Injection Rate (SCF/s)	0	0	0	0		
	Lower Boundary (Cuttings Carrying Capacity Limit)					
Liquid Flow Rate (gal/min)	0	5	10	15	20	25
Gas Injection Rate (SCF/s)	2.57	2.38	2.00	1.81	1.62	1.44
Liquid Flow Rate (gal/min)	30	35	40	45	50	55
Gas Injection Rate (SCF/s)	1.27	1.10	0.95	0.81	0.69	0.57

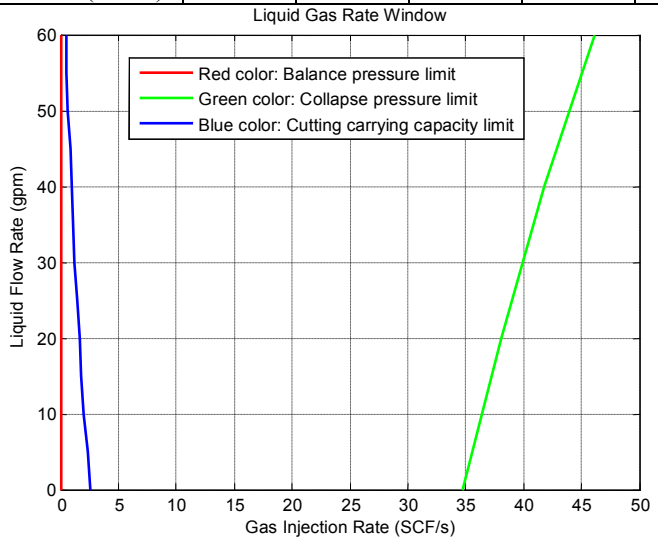

Fig 6.158. *Liquid Gas Rate Window (LGRW)*

6.3.4. Results of coupling productivity in UBD

Oil produced using foam drilling can be estimated by using UBDRILL to solve with the input data from 6.3.2. The observation from Table 6.32 showed that the OBD areas have not existed when drilling by foam. It means that BHP is always less than formation pressure while drilling. That is why the left boundary in Fig 6.158 can not be evaluated.

However, there is one more important question that is what happened to the foam quality when there is a large amount of formation fluid flowing into the wellbore in UBD. This should be checked to ensure that the foam structure is still remained during drilling operation.

Table 6.32. *Formation fluid influx flow rate*

Liquid Flow Rate Qx (gal/min)	0	20	40	60
Gas Injection Flow Rate (SCF/s)	Formation Fluid Influx Flow Rate (STB/Day)			
0	5522.56	5106.70	4714.43	4280.14
10	7671.46	7373.74	7083.59	6799.97
20	8863.91	8626.87	8364.58	8135.78
30	9629.15	9421.79	9213.29	9018.61
40	10138.08	9967.19	9792.36	9614.46
50	10481.59	10331.77	10188.52	10055.14

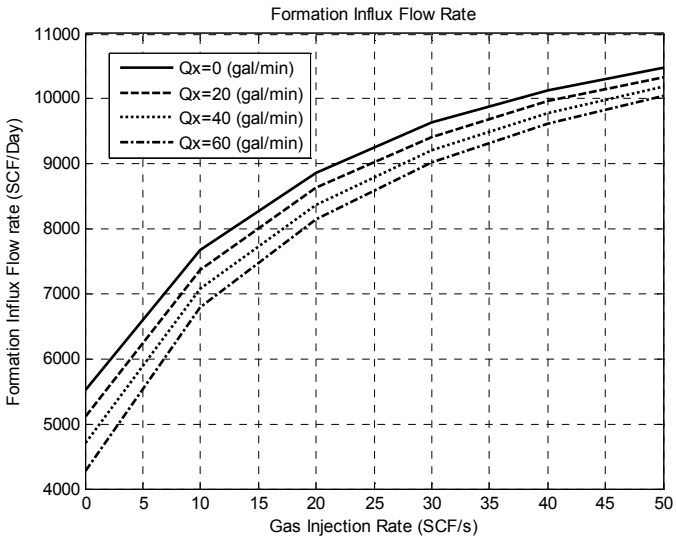

Fig 6.159. *Liquid Gas Rate Window (LGRW)*

6.3.5. Results of foam quality in UBD

Because foam is a compressible and inhomogeneous fluid, special care needs to be taken in foam drilling design and operations. Foam is stable only when its gas content (foam quality) is within a certain range (typically 0.75-0.97, depending on foam agent used, although stable foams have been observed with quality as low as 0.55). The in-situ pressures must be controlled to maintain the foam quality in the range. These pressure requirements are achieved using a wellhead choke (back pressure valve). Because the back pressure is greater than the atmospheric pressure in the annulus, special equipment called a rotating head is a must for foam drilling operations. With the

calculated pressure gradients shown in Figs 6.154, and 6.155, the foam quality in the annulus is very low at the bottomhole is very low as shown in the following results.

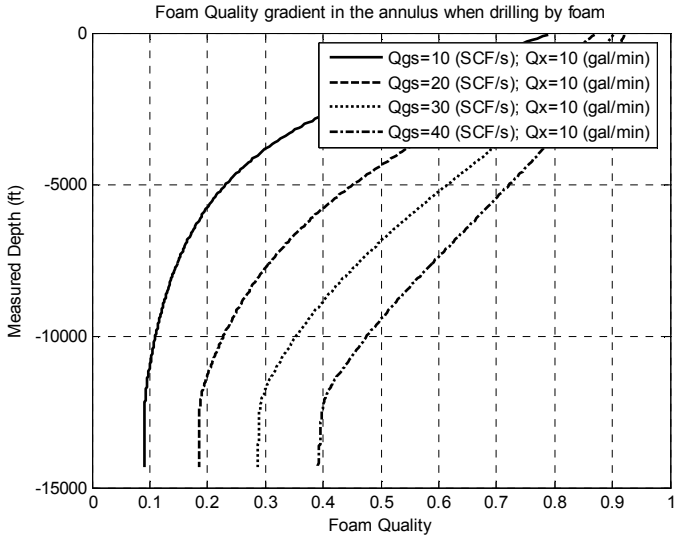

Fig 6.160. *Foam quality in the annulus*

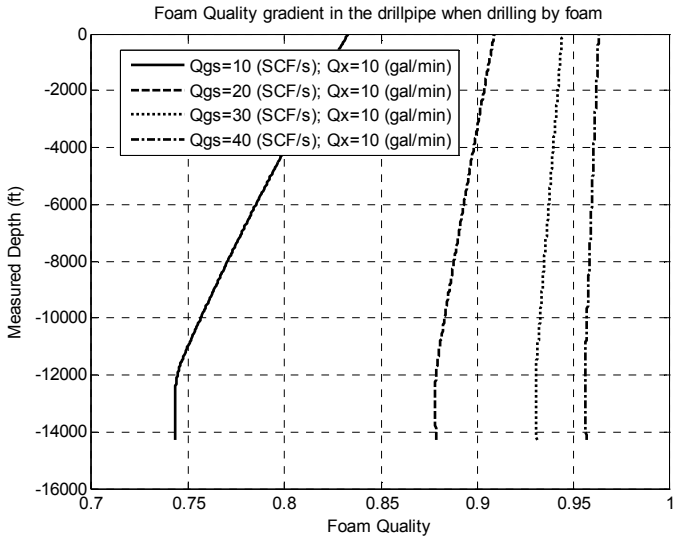

Fig 6.161. *Foam quality in the drillpipe*

According to the calculated results, the foam quality in the drillpipe is still kept in range of stability. However, the foam structure tends to break down in the annulus when the foam quality is less than 0.55 (see Guo et al. [45]). This will lead to the instability of foam when gas forms isolated bubbles that are independent of the liquid phase to the extent that the two phases can move with different velocities. This situation occurs because of the influx of formation fluids into the wellbore while UBD which increases the liquid volume and reduces the foam quality. The collapse of foam structure at the bottomhole has a significant influence to cutting carrying capacity and the rate of penetration which are unwanted things in UBD. So increasing the gas injection rate may be a solution. However, it should be noticed that even increasing the gas injection rate to maximum compressor flow rate (40 SCF/s), foam quality still lower than the expected value to guarantee the stability. Moreover, increasing the gas injection

rate will reduce the BHP and lead to the instability of the wellbore. It can be seen in Fig 6.158 when a combination of gas injection rate and liquid flow rate which ensures the foam quality over 0.55, for example 10 gal/min and 60 SCF/s, is out of LGRW. The BHP in this case is lower than collapse pressure so the wellbore will collapse.

Briefly, UBD by foam is impossible for wells in Basin X due to the fact that the potential production capacity of Basin X is very high which was displayed through IPR in 6.2.2. There is a large amount of formation fluid flowing into the wellbore while UBD which makes the foam quality reduce when the fluid content develops quickly at the bottomhole. This disadvantage can be recovered by controlling the wellhead pressure or raising gas injection volume. Unfortunately, this possibility can not carried out in anytime because of the limitation of compressor capacity.

Low collapse pressure is an advantage of Basin X for applying foam drilling because the widening of LGRW to the right boundary. However, the potential capacity of the reservoir in Basin X is a disadvantage for foam drilling because the formation influx fluid breaks down foam structures. In this calculation, the disadvantage has dominated so applying foam in UBD for Basin X is not a good choice.

CHAPTER 7 - CONCLUSIONS AND RECOMMENDATIONS

7.1. Conclusions

The analysis of wellbore stability in UBD in general cases led to the following conclusions:

- The rate of pore pressure and temperature propagation into the formation is controlled by the hydraulic diffusivity and thermal diffusivity. When the rock is highly permeable and the fluid only slightly viscous, pressure diffuses much faster than temperature.
- Time dependent effect influences effective stresses through the variation of pore pressure with time, but it has not affected on the total stresses in elastic case. However, time dependent effects in poroelastic and thermo-poro-elastic formation have involved the alteration of total stresses via the coupling of pore pressure and temperature.
- The formation around the wellbore (not at the wellbore wall) will be more stable as time progresses as the failure index tends to higher values with time. But it does not mean this stability will happen at the borehole wall because pore pressure at the wellbore is the boundary condition which was kept constant in drilling operation, it is not a time dependent parameter.
- The time dependent effects only influence the wellbore stability of the formation around the wellbore but not at the wellbore wall in all cases, elastic, poroelastic, thermo-poroelastic formation.
- When poroelastic and thermo-poroelastic effects have been taken into account the investigation of wellbore stability, the failure index in case of coupling pressure and temperature will be higher than that of elastic case. Analyzing wellbore stability regarding collapse in elastic case is pessimistic in comparison to coupling the poroelastic and thermo-poroelastic effects. It means that the wellbore wall which was supposed to be collapsed in elastic formation can be still stable in poroelastic or thermo-poroelastic formation. To sum up, the modelling of wellbore stability will give the more optimistic results when the coupling of pore pressure and temperature has been taken into account. The difference between the results of elastic, poroelastic, thermo-poroelastic cases depend mainly on the difference between wellbore pressure and temperature with formation pressure and temperature.
- Cooling the wellbore improves the stability while heating reduces the factor of safety (Mohr-Coulomb failure index), so induces wellbore instability. This conclusion remains valid for any directional well and does not depend on the wellbore trajectory.

The analysis of wellbore stability in UBD of a directional well in strike-slip

compression stress field in the basement of Basin X led to the following conclusions:

- The three dimensional model used for computations of stresses and failure criteria around a single wellbore in this study is reliable for the analysis of the stability of a wellbore, especially when it is oriented in a deviated direction and the initial stress condition is anisotropic. The formation stress field in this study is anisotropic: vertical stress, minimum and maximum horizontal stresses are different. Moreover, the influence of pore pressure and temperature were taken into account the calculation when thermo-poroelastic formation is supposed.

- Pressure propagation calculated by WELLST with data in Table 1, appendix B of this study will diffuse 134 times faster than temperature when the permeability of rock is 0.05 mD. The relation between permeability and the ratio of temperature/pressure diffusivity is nearly linear when the other conditions are kept constant. And this ratio also depends on the fluid viscosity.

- There is an area around the wellbore within 0.04-0.06 m which becomes less stable when the wellbore pressure reduces in UBD. However, the region far from the wellbore behaves in the opposite way. The formation in this far region will be more stable once wellbore pressure decreases. At the position corresponds to the direction of maximum horizontal stress, the most stable area is located from 0.1 to 0.15 m from the wellbore. And this peak will move into the formation when the angle between the point of interest and x-axis increases. This is caused by the anisotropy of stresses.

- The weakest point in a vertical wellbore is located on the direction of minimum horizontal stress. The wellbore wall began to collapse when wellbore pressure reduced to 15 MPa. The collapsed point starts at the weakest point ($\theta=90^o$). If wellbore pressure continues to reduce to 10 MPa, the wellbore wall will collapse from $\theta=80^o$ to 90^o. And the collapsed area will develope from 64^o to 90^o when wellbore pressure reduces to zero (totally lost circulation). So the wellbore at points in the above area will collapse although the rock cohesion is quite high in this calculation (54.6 MPa).

- In the strike-slip compression formation where the maximum horizontal stress is higher than vertical stress like Basin X, horizontal wellbores are more stable to collapse than vertical wellbores. This conclusion remains valid in any case of azimuth angle.

- The effect of thermal expansion on the wellbore stability is insignificant.

- In basement section of Basin X, the wellbore stability is dominated by the effect of temperature coupling.

- A horizontal well drilled in the direction of maximum horizontal stress ($a=0^o$) begins to collapse when wellbore pressure reduces to 10 MPa (Fig 6.93). The wellbore collapse pressure tends to decrease when increasing

azimuth angle to 75^o. So the best direction to drill a horizontal well in Basin X is of 60^o-75^o azimuth in comparison to maximum horizontal stress direction. And in this direction the well is stable even the wellbore pressure decreases to zero.

According to the analysis of wellbore stability in UBD of a directional well in the clastic layer above the basement of Basin X, the following conclusions can be obtained:

- Although the clastic interval has permeability higher than the basement interval, the formation around the wellbore drilled through the clastic section is less stable than that of the basement section. This reason is maily caused by the different of material cohesions between two intervals (54 MPa, and 20 MPa).
- The area around the wellbore within 0.25-0.27 m becomes less stable when wellbore pressure reduces while the region far from the wellbore behaves in the opposite way.
- The weakest point is located at the wellbore wall in the direction of minimum horizontal stress.
- The failure occurs on the wellbore wall even though the well is drilled in the balanced condition ($P_{wf}=P_R$), and the collapsed area is in the range $\theta=70^o$-90^o at this wellbore pressure. However, this conclusion is obtained when the cohesion of material is estimated around 12 MPa. The cohesion of material has an important role in these calculations. Its change will lead to the change of the wellbore stability. The higher cohesion of material is, the more stable wellbore is.
- The horizontal wells in comparison to the vertical wells in the clastic formation seem to be less stable because the collapsed area at the wellbore of the horizontal well in the similar calculation is larger than that of the vertical well.
- The wellbore with inclination over 30^o should be drilled in the direction of azimuth angle 90^o. The stability of the wellbore will decrease when the inclination angle increases. The wellbore azimuth variation has a negligible influence on wellbore stability in the clastic section (Fig 6.62).
- Analyzing wellbore stability regarding collapse in the elastic case is pessimistic in comparison to the poroelastic and thermo-poroelastic cases. Similar to the wellbore drilled through the basement interval, the wellbore in the clastic interval is also more stable when poroelastic, and thermo-poroelastic effects was accounted in the calculation. However, this influence hasn't contributed clearly to wellbore stability as the former one.
- In the clastic section, both temperature and pressure coupling have the equal influence to the wellbore stability.

The following conclusions can be obtained from the analysis of drilling hydraulics in UBD of a directional well:

- Most of UBD applications such as controlling the well in drilling, evaluating the production capacity, selecting the compressor in UBD, monitoring the fluid properties in UBD require multiphase flow modelling.

- A new method (IFDM) is suggested to solve gradient pressure equations by combining the iterative method and finite differential method in which variables of these equations such as the weight of the mixture, mixture velocity, friction factor were modified by adding parameters such as formation volume factor to consider the change of fluid volume along the wellbore, Z factor to calculate the compressibility of gas, and sea water properties to apply to gasified sea water drilling (sea water drilling has often been applied in Vietnam).

- Calculating the pressure distribution along the wellbore is a key factor in controlling wellbore integrity in UBD operations. The pressure is mainly dominated by the combination of gas and liquid flow rates. These results can be used as the boundary condition to estimate stress-strain around the wellbore, model wellbore stability, and help to design LGRW in UBD.

- The optimum combinations of gas and liquid flow rates in UBD can be selected in a LGRW. The window can be constructed based on formation pore pressure, wellbore collapse pressure, cuttings carrying capacity of fluid mixture, and wellbore washout criterion. The LGRW gives field engineers flexibility in selection of liquid and gas injection rates on the drilling site.

- Designing LGRW helps the drilling engineers to be sure that the BHP will be within the safe operation limits during the UBD operation, and to determine the optimal circulation rate to guarantee adequate hole cleaning and ensure vertical transport of cuttings in annular zones. The LGRW calculated for real data from the granite basement reservoir in South of Vietnam is not smooth and closed as the ideal LGRW due to the fact that the upper limit in the calculated LGRW is not defined because there is no previous UBD working to develop experience.

- The right boundary of LGRW in gasified drilling can be ignored because the calculated collapse pressure for the wellbore drilled through the basement of Basin X is quite low (1450 psia) which will cause the right boundary moving far to the right side of LGRW. Therefore, even increasing gas flow rate and liquid flow rate to the maximum capacity of the compressor, these flow rates have not still reached the right boundary.

- Coupling the productivity and drilling parameters in UBD have been extended in this research. According to reservoirs in which UBD has been conducted, proper flow monitoring of the produced fluids at surface can provide a good indication of productive zones of the reservoir and using the

information of produced fluids, reservoir properties and productivity will be calculated. In some areas where UBD has not been applied such as Vietnam, this research suggested a method to predict the productivity capacity in UBD operations. Once this information is known, the advantage of UBD in comparison to overbalanced drilling (OBD) will be qualified. And this is the important factor for operators to decide if UBD should be applied or not.

- Calculating pressure drops in the annulus, drillpipes, and through drill bit will help to quantify the total pressure drop in the drilling system. Besides, the process of compressor unit selection requires that the borehole requirements be compared to the capabilities of the available compressor units. These comparisons are made between (a) the volumetric flow rate required by the borehole and the volumetric capability of the compressor unit and (b) the injection pressure required by the borehole (calculated based on the compressor volumetric flow rate) and the pressure capability of the compressor unit. At the end, the compressor should be sized based on gas injection rate and required injection pressure.

- UBD by foam is impossible for wells in Basin X due to the fact that the potential production capacity of Basin X is high. Therefore, there is a large amount of formation fluid flowing into the wellbore while UBD which makes the foam quality reduce when the fluid content develops quickly at the bottomhole. This disadvantage can be recovered by controlling the wellhead pressure or raising gas injection volume. Unfortunately, this possibility can not be carried out because of the limitation of compressor capacity.

- Low collapse pressure is an advantage of Basin X for applying foam drilling because the widening of LGRW to the right boundary. However, the potential capacity of the reservoir in Basin X is a disadvantage for foam drilling because the formation influx fluid breaks down foam structures. In this calculation, the disadvantage has dominated so applying foam in UBD for Basin X is not a good choice.

To sum up, these above studies help to determine the viability of applying UBD technology to the granite basement in the Basin X by investigating technical feasibilities of the project candidate selection of underbalanced drilling techniques. It is the opinion of the author that UBD is the best available technology that will allow all of operator objectives of the well to be met for the proposed well in the Basin X. Technically, all aspects of UBD using gasified sea water as the drilling fluid are feasible in this case. A BHP can be imposed to ensure the stability of the wellbore, and UBD condition while drilling and tripping. Hole cleaning is shown to be adequate. In summary, UBD is technically feasible, and should be considered further for the implementation in the Basin X. Some new ideas and works developed in this research include:

- Estimating the wellbore stability in the making general assumptions such as pore pressure, temperature, anisotropic stress condition, directional wells, time dependent.

- Modifying the formulas of Guo and Ghalambor by taking into account the compressibility factor and fluid formation volume factors in the calculation of fluid properties.
- Applying a new method (IFDM) to solve the differential equations.
- Two simulators have been established on MATLAB and EXCEL. The first one is WELLST which helps to model the wellbore stability condition in UBD. The second one is UBDRILL which helps to analyse the drilling hydraulics condition in UBD.
- It is possible to estimate the productivity in UBD which helps the operators have an initial decision whether UBD should be applied or not.
- Commercial software have been applied such as ABAQUS, PERFORM, HYDMOD to compare the accuracy of the results.
- Sensitivity analysis proved that liquid phase density of drilling fluid influences significantly the BHP while other drilling parameters such as rate of penetration, gas injection density, and wellhead pressure cause a slight impact on the BHP which has an important role in the success of UBD operations.

7.2. Recommedations

The recommendations which should be done to bring this research to possibility in practical condition of Vietnam include:

- Investigate economic feasibilities of this project.
- Evaluate the effect of chemical interaction between the drilling fluids and the in-situ formation fluids on the wellbore stability.
- Additional study for multilateral wells.
- Investigate impact of other flow regimes in the annulus of the UBD well.
- Extend the application of work to other rock types.
- Take account of thermal convection in thermal and hydraulics diffusivity calculations.
- Take account of the fracture system in the wellbore stability calculations.
- Modify implications of using other failure models on the results of WELLST.
- Develop the work for real time monitoring of drilling optimization as well elongates.

APPENDIX A

Table 1. *Data for estimating the transient pressure and temperature profiles*

Parameters	**Input Data**	**Units**	**Notes**
Young 's modulus (E)	42,811 – 96,323	MPa	
Poison ratio (ν)	0.28		
Granite density	2800	kg/m^3	
Fluid compressibility (C_f)	7.90E-04	1/MPa	
Void ratio	0.45		
Oil density	828.4	kg/m^3	API = 39.3
Fluid thermal expansion coefficient (α_f)	9.00E-04	$1/^oC$	
Drained thermal expansion coefficient (α_B)	8.50E-06		
Specific heat of granite (C_ε)	750	$J/kg.^oC$	
Permeability (k)	0.0001	Darcy	
Oil Viscosity (μ_o)	0.5	Cp	
Thermal conductivity (κ)	5	$W/m.^oC$	
Reservoir Temperature (T_R)	131	^oC	
Wellbore Temperature (T_{wf})	98	^oC	
Reservoir Pressure (P_R)	34.45	MPa	
Wellbore Pressure (P_{wf})	32.34	MPa	
Wellbore Radius (R_w)	0.1	M	
Boundary Radius (R_e)	1.5	M	
Biot elastic constraint	1		
Time dependent effect	0; 10; 600; 3,600; 18,000; 36,000	s	

Table 2. *Data for estimating the stress distribution*

Parameters	**Input Data**	**Units**	**Notes**
Young 's modulus (E)	68,670	MPa	
Poison ratio (ν)	0.28		
Granite density	2800	kg/m^3	
Maximum horizontal stress (σ_H)	**88**	MPa	Fig 2.6
Minimum horizontal stress (σ_h)	**54**	MPa	Fig 2.6
Vertical stress (σ_V)	**85**	MPa	Fig 2.6
Fluid compressibility (C_f)	7.90E-04	1/MPa	
Void ratio	0.45		
Oil density	828.4	kg/m^3	API = 39.3
Fluid thermal expansion coefficient (α_f)	9.00E-04	$1/^oC$	
Drained thermal expansion coefficient (α_B)	8.50E-06		
Specific heat of granite (C_ε)	750	$J/kg.^oC$	
Permeability (k)	0.0001	Darcy	
Oil Viscosity (μ_o)	0.5	Cp	
Thermal conductivity (κ)	5	$W/m.^oC$	
Reservoir Temperature (T_R)	131	^oC	
Wellbore Temperature (T_{wf})	98	^oC	
Reservoir Pressure (P_R)	34.45	MPa	
Wellbore Pressure (P_{wf})	32.34	MPa	
Wellbore Radius (R_w)	0.1	M	
Boundary Radius (R_e)	1.5	M	
Biot elastic constraint	1		
Wellbore azimuth	**0**	Degree	
Wellbore inclination	**0**	Degree	
The angle around the wellbore	**0**	Degree	
Time dependent effect	0; 10; 600; 3,600; 36,000	s	

Table 3 *Data for estimating the failure index*

Parameters	**Input Data**	**Units**	**Notes**
Young 's modulus (E)	68,670	MPa	
Poison ratio (ν)	0.28		
Granite density	2800	kg/m^3	
Cohesion of material (c)	**54.6**	MPa	
Frictional angle (ϕ)	**28**	Degree	
Maximum horizontal stress (σ_H)	88	MPa	Fig 2.6
Minimum horizontal stress (σ_h)	54	MPa	Fig 2.6
Vertical stress (σ_V)	85	MPa	Fig 2.6
Fluid compressibility (C_f)	7.90E-04	1/MPa	
Void ratio	0.45		
Oil density	828.4	kg/m^3	API = 39.3
Fluid thermal expansion coefficient (α_f)	9.00E-04	$1/^oC$	
Drained thermal expansion coefficient (α_B)	8.50E-06		
Specific heat of granite (C_ε)	750	$J/kg.^oC$	
Permeability (k)	0.0001	Darcy	
Oil Viscosity (μ_o)	0.5	Cp	
Thermal conductivity (κ)	5	$W/m.^oC$	
Reservoir Temperature (T_R)	131	^oC	
Wellbore Temperature (T_{wf})	98	^oC	
Reservoir Pressure (P_R)	34.45	MPa	
Wellbore Pressure (P_{wf})	32.34	MPa	
Wellbore Radius (R_w)	0.1	M	
Boundary Radius (R_e)	1.5	M	
Biot elastic constraint	1		
Wellbore azimuth	0	Degree	
Wellbore inclination	0	Degree	
The angle around the wellbore	0	Degree	
Time dependent effect	0; 10; 600; 3,600; 36,000	s	

APPENDIX B

Table 1. *Data for estimating the effect of permeability and viscosity*

Parameters	**Input Data**	**Units**	**Notes**
Young 's modulus (E)	68,670	MPa	
Poison ratio (ν)	0.28		
Granite density	2800	Kg/m^3	
Cohesion of material (c)	**20 – 54.6**	MPa	
Frictional angle (ϕ)	**28**	Degree	
Maximum horizontal stress (σ_H)	88	MPa	Fig 2.6
Minimum horizontal stress (σ_h)	54	MPa	Fig 2.6
Vertical stress (σ_V)	85	MPa	Fig 2.6
Fluid compressibility (C_f)	7.90E-04	1/MPa	
Void ratio	0.45		
Oil density	828.4	Kg/m^3	API = 39.3
Fluid thermal expansion coefficient (α_f)	9.00E-04	$1/^oC$	
Drained thermal expansion coefficient (α_B)	8.50E-06		
Specific heat of granite (C_ε)	750	$J/kg.^oC$	
Permeability (k)	**0.00005 – 0.001**	Darcy	
Oil Viscosity (μ_o)	**0.5 – 1**	Cp	
Thermal conductivity (κ)	5	$W/m.^oC$	
Reservoir Temperature (T_R)	131	^oC	
Wellbore Temperature (T_{wf})	98	^oC	
Reservoir Pressure (P_R)	34.45	MPa	
Wellbore Pressure (P_{wf})	32.34	MPa	
Wellbore Radius (R_w)	0.1-0.15	m	
Boundary Radius (R_e)	1.5	m	
Biot elastic constraint	1		
Time dependent effect	**600**	s	

APPENDIX C

Table 1. *Data for estimating the effect of wellbore pressure and the position around the wellbore in the basement formation*

Parameters	**Input Data**	**Units**	**Notes**
Young 's modulus (E)	68,670	MPa	
Poison ratio (ν)	0.28		
Granite density	2800	Kg/m^3	
Cohesion of material (c)	54.6	MPa	
Frictional angle (ϕ)	28	Degree	
Maximum horizontal stress (σ_H)	88	MPa	Fig 2.6
Minimum horizontal stress (σ_h)	54	MPa	Fig 2.6
Vertical stress (σ_V)	85	MPa	Fig 2.6
Fluid compressibility (C_f)	7.90E-04	1/MPa	
Void ratio	0.45		
Oil density	828.4	Kg/m^3	API = 39.3
Fluid thermal expansion coefficient (α_f)	9.00E-04	$1/^oC$	
Drained thermal expansion coefficient (α_B)	8.50E-06		
Specific heat of granite (C_ε)	750	$J/kg.^oC$	
Permeability (k)	0.001	Darcy	
Oil Viscosity (μ_o)	0.5	Cp	
Thermal conductivity (κ)	5	$W/m.^oC$	
Reservoir Temperature (T_R)	131	^oC	
Wellbore Temperature (T_{wf})	98	^oC	
Reservoir Pressure (P_R)	34.45	MPa	
Wellbore Pressure (P_{wf})	**0-34.45**	MPa	
Wellbore Radius (R_w)	0.1	m	
Boundary Radius (R_e)	1.5	m	
Biot elastic constraint	1		
Wellbore azimuth	0	Degree	
Wellbore inclination	0	Degree	
The angle around the wellbore	**0-90**	Degree	
Time dependent effect	10	s	

Table 2. *Data for estimating the effect of wellbore pressure and the position around the wellbore in the clastic formation*

Parameters	**Input Data**	**Units**	**Notes**
Young 's modulus (E)	20,000	MPa	
Poison ratio (ν)	0.28		
Granite density	2,600	Kg/m^3	
Cohesion of material (c)	12	MPa	
Frictional angle (ϕ)	28	Degree	
Maximum horizontal stress (σ_H)	43.91	MPa	
Minimum horizontal stress (σ_h)	38.23	MPa	
Vertical stress (σ_V)	56.54	MPa	
Fluid compressibility (C_f)	7.90E-04	1/MPa	
Void ratio	0.5		
Oil density	828.4	Kg/m^3	API = 39.3
Fluid thermal expansion coefficient (α_f)	9.00E-04	$1/^oC$	
Drained thermal expansion coefficient (α_B)	1.250E-05		
Specific heat of granite (C_ε)	750	$J/kg.^oC$	
Permeability (k)	0.0001	Darcy	
Oil Viscosity (μ_o)	1	Cp	
Thermal conductivity (κ)	5.2	$W/m.^oC$	
Reservoir Temperature (T_R)	110	^oC	
Wellbore Temperature (T_{wf})	85	^oC	
Reservoir Pressure (P_R)	25.02	MPa	
Wellbore Pressure (P_{wf})	**0-25.02**	MPa	
Wellbore Radius (R_w)	0.15	m	
Boundary Radius (R_e)	1.5	m	
Biot elastic constraint	1		
Wellbore azimuth	0	Degree	
Wellbore inclination	0	Degree	
The angle around the wellbore	**0-90**	Degree	
Time dependent effect	10	s	

APPENDIX D

Table 1. *Data for estimating the effect of wellbore inclination and azimuth variation in the basement formation*

Parameters	**Input Data**	**Units**	**Notes**
Young 's modulus (E)	68,670	MPa	
Poison ratio (ν)	0.28		
Granite density	2800	Kg/m^3	
Cohesion of material (c)	54.6	MPa	
Frictional angle (ϕ)	28	Degree	
Maximum horizontal stress (σ_H)	88	MPa	Fig 2.6
Minimum horizontal stress (σ_h)	54	MPa	Fig 2.6
Vertical stress (σ_V)	85	MPa	Fig 2.6
Fluid compressibility (C_f)	7.90E-04	1/MPa	
Void ratio	0.45		
Oil density	828.4	Kg/m^3	API = 39.3
Fluid thermal expansion coefficient (α_f)	9.00E-04	$1/^oC$	
Drained thermal expansion coefficient (α_B)	8.50E-06		
Specific heat of granite (C_ε)	750	$J/kg.^oC$	
Permeability (k)	0.001	Darcy	
Oil Viscosity (μ_o)	0.5	Cp	
Thermal conductivity (κ)	5	$W/m.^oC$	
Reservoir Temperature (T_R)	131	^oC	
Wellbore Temperature (T_{wf})	98	^oC	
Reservoir Pressure (P_R)	34.45	MPa	
Wellbore Pressure (P_{wf})	**0-32.34**	MPa	
Wellbore Radius (R_w)	0.1	m	
Boundary Radius (R_e)	1.5	m	
Biot elastic constraint	1		
Wellbore azimuth	**0-90**	Degree	
Wellbore inclination	**0-90**	Degree	
The angle around the wellbore	**0-90**	Degree	
Time dependent effect	10	s	

Table 2. *Data for estimating the effect of wellbore inclination and azimuth variation in the clastic formation*

Parameters	**Input Data**	**Units**	**Notes**
Young 's modulus (E)	20,000	MPa	
Poison ratio (ν)	0.28		
Granite density	2,600	Kg/m^3	
Cohesion of material (c)	12	MPa	
Frictional angle (ϕ)	28	Degree	
Maximum horizontal stress (σ_H)	43.91	MPa	
Minimum horizontal stress (σ_h)	38.23	MPa	
Vertical stress (σ_V)	56.54	MPa	
Fluid compressibility (C_f)	7.90E-04	1/MPa	
Void ratio	0.5		
Oil density	828.4	Kg/m^3	API = 39.3
Fluid thermal expansion coefficient (α_f)	9.00E-04	$1/^oC$	
Drained thermal expansion coefficient (α_B)	1.250E-05		
Specific heat of granite (C_ε)	750	$J/kg.^oC$	
Permeability (k)	0.0001	Darcy	
Oil Viscosity (μ_o)	1	Cp	
Thermal conductivity (κ)	5.2	$W/m.^oC$	
Reservoir Temperature (T_R)	110	^oC	
Wellbore Temperature (T_{wf})	85	^oC	
Reservoir Pressure (P_R)	25.02	MPa	
Wellbore Pressure (P_{wf})	**0-25.02**	MPa	
Wellbore Radius (R_w)	0.15	m	
Boundary Radius (R_e)	1.5	m	
Biot elastic constraint	1		
Wellbore azimuth	**0-90**	Degree	
Wellbore inclination	**0-90**	Degree	
The angle around the wellbore	**0-90**	Degree	
Time dependent effect	10	s	

APPENDIX E

Table 1. *Data for estimating the transient poroelastic and thermo-poroelastic effects*

Parameters	**Input Data**	**Units**	**Notes**
Young 's modulus (E)	68,670	MPa	
Poison ratio (ν)	0.28		
Granite density	2800	Kg/m^3	
Cohesion of material (c)	54.6	MPa	
Frictional angle (ϕ)	28	Degree	
Maximum horizontal stress (σ_H)	88	MPa	Fig 2.6
Minimum horizontal stress (σ_h)	54	MPa	Fig 2.6
Vertical stress (σ_V)	85	MPa	Fig 2.6
Fluid compressibility (C_f)	7.90E-04	1/MPa	
Void ratio	0.45		
Oil density	828.4	Kg/m^3	API = 39.3
Fluid thermal expansion coefficient (α_f)	9.00E-04	$1/^oC$	
Drained thermal expansion coefficient (α_B)	8.50E-06		
Specific heat of granite (C_ε)	750	$J/kg.^oC$	
Permeability (k)	0.001	Darcy	
Oil Viscosity (μ_o)	0.5	Cp	
Thermal conductivity (κ)	5	$W/m.^oC$	
Reservoir Temperature (T_R)	131	^oC	
Wellbore Temperature (T_{wf})	98	^oC	
Reservoir Pressure (P_R)	34.45	MPa	
Wellbore Pressure (P_{wf})	**31**	MPa	
Wellbore Radius (R_w)	0.1	m	
Boundary Radius (R_e)	1.5	m	
Biot elastic constraint	1		
Wellbore azimuth	**0-90**	Degree	
Wellbore inclination	**0-90**	Degree	
The angle around the wellbore	**0-90**	Degree	
Time dependent effect	10	s	

Table 2. *Data for estimating the effect of wellbore inclination and azimuth variation in the clastic formation*

Parameters	**Input Data**	**Units**	**Notes**
Young 's modulus (E)	20,000	MPa	
Poison ratio (ν)	0.28		
Granite density	2,600	Kg/m^3	
Cohesion of material (c)	12	MPa	
Frictional angle (ϕ)	28	Degree	
Maximum horizontal stress (σ_H)	43.91	MPa	
Minimum horizontal stress (σ_h)	38.23	MPa	
Vertical stress (σ_V)	56.54	MPa	
Fluid compressibility (C_f)	7.90E-04	1/MPa	
Void ratio	0.5		
Oil density	828.4	Kg/m^3	API = 39.3
Fluid thermal expansion coefficient (α_f)	9.00E-04	$1/^oC$	
Drained thermal expansion coefficient (α_B)	1.250E-05		
Specific heat of granite (C_ε)	750	$J/kg.^oC$	
Permeability (k)	0.0001	Darcy	
Oil Viscosity (μ_o)	1	Cp	
Thermal conductivity (κ)	5.2	$W/m.^oC$	
Reservoir Temperature (T_R)	110	^oC	
Wellbore Temperature (T_{wf})	85	^oC	
Reservoir Pressure (P_R)	25.02	MPa	
Wellbore Pressure (P_{wf})	**21.58**	MPa	
Wellbore Radius (R_w)	0.15	m	
Boundary Radius (R_e)	1.5	m	
Biot elastic constraint	1		
Wellbore azimuth	**0-90**	Degree	
Wellbore inclination	**0-90**	Degree	
The angle around the wellbore	**0-90**	Degree	
Time dependent effect	10	s	

Table 3. *Data for estimating the poroelastic and thermo-poroelastic effects*

Parameters	**Input Data**	**Units**	**Notes**
Young 's modulus (E)	68,670	MPa	
Poison ratio (ν)	0.28		
Granite density	2800	Kg/m^3	
Cohesion of material (c)	54.6	MPa	
Frictional angle (ϕ)	28	Degree	
Maximum horizontal stress (σ_H)	88	MPa	Fig 2.6
Minimum horizontal stress (σ_h)	54	MPa	Fig 2.6
Vertical stress (σ_V)	85	MPa	Fig 2.6
Fluid compressibility (C_f)	7.90E-04	1/MPa	
Void ratio	0.45		
Oil density	828.4	Kg/m^3	API = 39.3
Fluid thermal expansion coefficient (α_f)	9.00E-04	$1/^oC$	
Drained thermal expansion coefficient (α_B)	8.50E-06		
Specific heat of granite (C_ε)	750	$J/kg.^oC$	
Permeability (k)	0.001	Darcy	
Oil Viscosity (μ_o)	0.5	Cp	
Thermal conductivity (κ)	5	$W/m.^oC$	
Reservoir Temperature (T_R)	131	^oC	
Wellbore Temperature (T_{wf})	98	^oC	
Reservoir Pressure (P_R)	34.45	MPa	
Wellbore Pressure (P_{wf})	**10, 31**	MPa	
Wellbore Radius (R_w)	0.1	m	
Boundary Radius (R_e)	1.5	m	
Biot elastic constraint	1		
Wellbore azimuth	**0, 30**	Degree	
Wellbore inclination	30	Degree	
The angle around the wellbore	**0-90**	Degree	
Time dependent effect	10	s	

Table 4. *Data for estimating the transient poroelastic and thermo-poroelastic effects*

Parameters	**Input Data**	**Units**	**Notes**
Young 's modulus (E)	68,670	MPa	
Poison ratio (ν)	0.28		
Granite density	2800	Kg/m^3	
Cohesion of material (c)	54.6	MPa	
Frictional angle (ϕ)	28	Degree	
Maximum horizontal stress (σ_H)	88	MPa	Fig 2.6
Minimum horizontal stress (σ_h)	54	MPa	Fig 2.6
Vertical stress (σ_V)	85	MPa	Fig 2.6
Fluid compressibility (C_f)	7.90E-04	1/MPa	
Void ratio	0.45		
Oil density	828.4	Kg/m^3	API = 39.3
Fluid thermal expansion coefficient (α_f)	9.00E-04	$1/^oC$	
Drained thermal expansion coefficient (α_B)	8.50E-06		
Specific heat of granite (C_ε)	750	$J/kg.^oC$	
Permeability (k)	0.001	Darcy	
Oil Viscosity (μ_o)	0.5	Cp	
Thermal conductivity (κ)	5	$W/m.^oC$	
Reservoir Temperature (T_R)	131	^oC	
Wellbore Temperature (T_{wf})	98	^oC	
Reservoir Pressure (P_R)	34.45	MPa	
Wellbore Pressure (P_{wf})	**10**	MPa	
Wellbore Radius (R_w)	0.1	m	
Boundary Radius (R_e)	1.5	m	
Biot elastic constraint	1		
Wellbore azimuth	30	Degree	
Wellbore inclination	30	Degree	
The angle around the wellbore	0	Degree	
Time dependent effect	**10, 3600**	s	

APPENDIX F

Table 1. *Data for estimating the cooling and heating effects to the wellbore stability in the basement section*

Parameters	**Input Data**	**Units**	**Notes**
Young 's modulus (E)	68,670	MPa	
Poison ratio (ν)	0.28		
Granite density	2800	Kg/m^3	
Cohesion of material (c)	54.6	MPa	
Frictional angle (ϕ)	28	Degree	
Maximum horizontal stress (σ_H)	88	MPa	Fig 2.6
Minimum horizontal stress (σ_h)	54	MPa	Fig 2.6
Vertical stress (σ_V)	85	MPa	Fig 2.6
Fluid compressibility (C_f)	7.90E-04	1/MPa	
Void ratio	0.45		
Oil density	828.4	Kg/m^3	API = 39.3
Fluid thermal expansion coefficient (α_f)	9.00E-04	$1/^oC$	
Drained thermal expansion coefficient (α_B)	8.50E-06		
Specific heat of granite (C_ε)	750	$J/kg.^oC$	
Permeability (k)	0.001	Darcy	
Oil Viscosity (μ_o)	0.5	Cp	
Thermal conductivity (κ)	5	$W/m.^oC$	
Reservoir Temperature (T_R)	131	^oC	
Wellbore Temperature (T_{wf})	**98, 131, 150**	^oC	
Reservoir Pressure (P_R)	34.45	MPa	
Wellbore Pressure (P_{wf})	32.34	MPa	
Wellbore Radius (R_w)	0.1	m	
Boundary Radius (R_e)	1.5	m	
Biot elastic constraint	1		
Wellbore azimuth	0	Degree	
Wellbore inclination	0	Degree	
The angle around the wellbore	0	Degree	
Time dependent effect	**0, 600, 3600**	s	

Table 2. *Data for estimating the cooling and heating effects to the wellbore stability in the clastic section*

Parameters	**Input Data**	**Units**	**Notes**
Young 's modulus (E)	20,000	MPa	
Poison ratio (ν)	0.28		
Granite density	2,600	Kg/m^3	
Cohesion of material (c)	12	MPa	
Frictional angle (ϕ)	28	Degree	
Maximum horizontal stress (σ_H)	43.91	MPa	Fig 2.6
Minimum horizontal stress (σ_h)	38.23	MPa	Fig 2.6
Vertical stress (σ_V)	56.54	MPa	Fig 2.6
Fluid compressibility (C_f)	7.90E-04	1/MPa	
Void ratio	0.5		
Oil density	828.4	Kg/m^3	API = 39.3
Fluid thermal expansion coefficient (α_f)	9.00E-04	$1/^oC$	
Drained thermal expansion coefficient (α_B)	1.250E-05		
Specific heat of granite (C_ε)	750	$J/kg.^oC$	
Permeability (k)	0.0001	Darcy	
Oil Viscosity (μ_o)	1	Cp	
Thermal conductivity (κ)	5.2	$W/m.^oC$	
Reservoir Temperature (T_R)	110	^oC	
Wellbore Temperature (T_{wf})	**85, 110, 135**	^oC	
Reservoir Pressure (P_R)	25.02	MPa	
Wellbore Pressure (P_{wf})	21.58	MPa	
Wellbore Radius (R_w)	0.15	m	
Boundary Radius (R_e)	1.5	m	
Biot elastic constraint	1		
Wellbore azimuth	0	Degree	
Wellbore inclination	0	Degree	
The angle around the wellbore	0	Degree	
Time dependent effect	**0, 600, 3600**	s	

Table 3. *Data for estimating the cooling and heating effects to the wellbore stability in the basement section*

Parameters	**Input Data**	**Units**	**Notes**
Young 's modulus (E)	68,670	MPa	
Poison ratio (ν)	0.28		
Granite density	2800	Kg/m^3	
Cohesion of material (c)	54.6	MPa	
Frictional angle (ϕ)	28	Degree	
Maximum horizontal stress (σ_H)	88	MPa	Fig 2.6
Minimum horizontal stress (σ_h)	54	MPa	Fig 2.6
Vertical stress (σ_V)	85	MPa	Fig 2.6
Fluid compressibility (C_f)	7.90E-04	1/MPa	
Void ratio	0.45		
Oil density	828.4	Kg/m^3	API = 39.3
Fluid thermal expansion coefficient (α_f)	9.00E-04	$1/^oC$	
Drained thermal expansion coefficient (α_B)	8.50E-06		
Specific heat of granite (C_ε)	750	$J/kg.^oC$	
Permeability (k)	0.001	Darcy	
Oil Viscosity (μ_o)	0.5	Cp	
Thermal conductivity (κ)	5	$W/m.^oC$	
Reservoir Temperature (T_R)	131	^oC	
Wellbore Temperature (T_{wf})	**98, 131, 150**	^oC	
Reservoir Pressure (P_R)	34.45	MPa	
Wellbore Pressure (P_{wf})	32.34	MPa	
Wellbore Radius (R_w)	0.1	m	
Boundary Radius (R_e)	1.5	m	
Biot elastic constraint	1		
Wellbore azimuth	**0, 30, 60**	Degree	
Wellbore inclination	**0, 60, 90**	Degree	
The angle around the wellbore	**0-180**	Degree	
Time dependent effect	3600	s	

Table 4. *Data for estimating the cooling and heating effects to the wellbore stability in the clastic section*

Parameters	**Input Data**	**Units**	**Notes**
Young 's modulus (E)	20,000	MPa	
Poison ratio (ν)	0.28		
Granite density	2,600	Kg/m^3	
Cohesion of material (c)	12	MPa	
Frictional angle (ϕ)	28	Degree	
Maximum horizontal stress (σ_H)	43.91	MPa	Fig 2.6
Minimum horizontal stress (σ_h)	38.23	MPa	Fig 2.6
Vertical stress (σ_V)	56.54	MPa	Fig 2.6
Fluid compressibility (C_f)	7.90E-04	1/MPa	
Void ratio	0.5		
Oil density	828.4	Kg/m^3	API = 39.3
Fluid thermal expansion coefficient (α_f)	9.00E-04	$1/^oC$	
Drained thermal expansion coefficient (α_B)	1.250E-05		
Specific heat of granite (C_ε)	750	$J/kg.^oC$	
Permeability (k)	0.0001	Darcy	
Oil Viscosity (μ_o)	1	Cp	
Thermal conductivity (κ)	5.2	$W/m.^oC$	
Reservoir Temperature (T_R)	110	^oC	
Wellbore Temperature (T_{wf})	**85, 110, 135**	^oC	
Reservoir Pressure (P_R)	25.02	MPa	
Wellbore Pressure (P_{wf})	21.58	MPa	
Wellbore Radius (R_w)	0.15	m	
Boundary Radius (R_e)	1.5	m	
Biot elastic constraint	1		
Wellbore azimuth	**0, 30, 60**	Degree	
Wellbore inclination	**0, 60, 90**	Degree	
The angle around the wellbore	**0-180**	Degree	
Time dependent effect	3600	s	

APPENDIX G

Table 1. *Data for estimating thermal expansion coefficient effect*

Parameters	**Input Data**	**Units**	**Notes**
Young 's modulus (E)	68,670	MPa	
Poison ratio (ν)	0.28		
Granite density	2800	Kg/m^3	
Cohesion of material (c)	54.6	MPa	
Frictional angle (ϕ)	28	Degree	
Maximum horizontal stress (σ_H)	88	MPa	Fig 2.6
Minimum horizontal stress (σ_h)	54	MPa	Fig 2.6
Vertical stress (σ_V)	85	MPa	Fig 2.6
Fluid compressibility (C_f)	7.90E-04	1/MPa	
Void ratio	0.45		
Oil density	828.4	Kg/m^3	API = 39.3
Fluid thermal expansion coefficient (α_f)	9.00E-04	$1/^oC$	
Drained thermal expansion coefficient (α_B)	**5E-6, 10E-6**		
Specific heat of granite (C_ε)	750	$J/kg.^oC$	
Permeability (k)	0.001	Darcy	
Oil Viscosity (μ_o)	0.5	Cp	
Thermal conductivity (κ)	5	$W/m.^oC$	
Reservoir Temperature (T_R)	131	^oC	
Wellbore Temperature (T_{wf})	98	^oC	
Reservoir Pressure (P_R)	34.45	MPa	
Wellbore Pressure (P_{wf})	32.34	MPa	
Wellbore Radius (R_w)	0.1	m	
Boundary Radius (R_e)	1.5	m	
Biot elastic constraint	1		
Wellbore azimuth	0	Degree	
Wellbore inclination	0	Degree	
The angle around the wellbore	0	Degree	
Time dependent effect	3600	s	

APPENDIX H

Table 1. *Data for estimating the collapse pressure of the wellbore in basement formation*

Parameters	**Input Data**	**Units**	**Notes**
Young 's modulus (E)	68,670	MPa	
Poison ratio (ν)	0.28		
Granite density	2800	Kg/m^3	
Cohesion of material (c)	54.6	MPa	
Frictional angle (ϕ)	28	Degree	
Maximum horizontal stress (σ_H)	88	MPa	Fig 2.6
Minimum horizontal stress (σ_h)	54	MPa	Fig 2.6
Vertical stress (σ_V)	85	MPa	Fig 2.6
Fluid compressibility (C_f)	7.90E-04	1/MPa	
Void ratio	0.45		
Oil density	828.4	Kg/m^3	API = 39.3
Fluid thermal expansion coefficient (α_f)	9.00E-04	$1/^oC$	
Drained thermal expansion coefficient (α_B)	8.50E-06		
Specific heat of granite (C_ε)	750	$J/kg.^oC$	
Permeability (k)	0.001	Darcy	
Oil Viscosity (μ_o)	0.5	Cp	
Thermal conductivity (κ)	5	$W/m.^oC$	
Reservoir Temperature (T_R)	131	^oC	
Wellbore Temperature (T_{wf})	98	^oC	
Reservoir Pressure (P_R)	34.45	MPa	
Wellbore Pressure (P_{wf})	**0 - 34.45**	MPa	
Wellbore Radius (R_w)	0.1	m	
Boundary Radius (R_e)	1.5	m	
Biot elastic constraint	1		
Wellbore azimuth	**0 - 90**	Degree	
Wellbore inclination	**90**	Degree	
The angle around the wellbore	**0 - 90**	Degree	
Time dependent effect	10	s	

Table 2. *Data for estimating the collapse pressure of the wellbore in clastic formation*

Parameters	**Input Data**	**Units**	**Notes**
Young 's modulus (E)	20,000	MPa	
Poison ratio (ν)	0.28		
Granite density	2,600	Kg/m^3	
Cohesion of material (c)	**12-33**	MPa	
Frictional angle (ϕ)	28	Degree	
Maximum horizontal stress (σ_H)	43.91	MPa	Fig 2.6
Minimum horizontal stress (σ_h)	38.23	MPa	Fig 2.6
Vertical stress (σ_V)	56.54	MPa	Fig 2.6
Fluid compressibility (C_f)	7.90E-04	1/MPa	
Void ratio	0.5		
Oil density	828.4	Kg/m^3	API = 39.3
Fluid thermal expansion coefficient (α_f)	9.00E-04	$1/^oC$	
Drained thermal expansion coefficient (α_B)	1.250E-05		
Specific heat of granite (C_ε)	750	$J/kg.^oC$	
Permeability (k)	0.0001	Darcy	
Oil Viscosity (μ_o)	1	Cp	
Thermal conductivity (κ)	5.2	$W/m.^oC$	
Reservoir Temperature (T_R)	110	^oC	
Wellbore Temperature (T_{wf})	85	^oC	
Reservoir Pressure (P_R)	25.02	MPa	
Wellbore Pressure (P_{wf})	**0-25.02**	MPa	
Wellbore Radius (R_w)	0.15	m	
Boundary Radius (R_e)	1.5	m	
Biot elastic constraint	1		
Wellbore azimuth	**0 - 90**	Degree	
Wellbore inclination	**17.26**	Degree	
The angle around the wellbore	**0 - 90**	Degree	
Time dependent effect	10	s	

IADC/SPE SPE-122266-PP

PREDICTING THE PRODUCTION CAPACITY DURING UNDERBALANCED DRILLING OPERATIONS IN VIETNAM

C. Nguyen, J.M. Somerville, SPE, and B.G.D. Smart, SPE, Heriot-Watt University

This paper was prepared for presentation at the IADC/SPE Managed Pressure Drilling and Underbalanced Operations Conference and Exhibition held in San Antonio, Texas, 12–13 February 2009.

Abstract

During recent years, interest in underbalanced drilling (UBD) has grown rapidly. As a drilling technique it has gained acceptance because it provides a method of minimizing formation damage, preventing lost circulation risks and increasing penetration rates. One of the most important tasks in UBD design is to estimate how much oil can be produced during the drilling operation. This task is very difficult because of the complex nature of the multiphase flow in the UBD system, especially in the annulus between the drillpipe, collars and the wellbore where water, gas, cuttings and fluid influx from the penetrated formations are present. To accomplish this task, the bottomhole pressure must be calculated. However, the bottomhole pressure, fluid influx flow rates, and fluid properties along the wellbore are interdependent parameters and can only be derived through a combination of iterative and finite differential methods. It is therefore necessary to use a computer program to carry out the work.

This paper presents a method to predict production capacity by coupling drilling parameters and inflow performance parameters such as surface choke pressure, gas injection rates, liquid flow rates and fluid production rates for UBD. A software tool named UBDRILL has been developed which can be used to perform thorough investigations of UBD hydraulic calculations and the estimation of production capacity.

The proposed method and developed software are validated by application examples of UBD in granite basement reservoirs in Vietnam, SE Asia.

Introduction

UBD is defined as a technique in which the dynamic wellbore pressure is maintained less than the formation pore pressure. As a result, an influx of formation fluids is allowed into the wellbore during drilling, then circulated out and controlled at the surface. This condition can be achieved by using lightened drilling fluids such as air, gas, foam, mist, and gasified liquid. However, inflow gas or fluid sometimes appears while drilling through the basement reservoirs in Vietnam so the application of dry air or foam drilling technique is not a good choice because the foam structure can be changed by the invading gas or fluid, and the possibility of combustion can develop in dry air drilling when gas influxes to the wellbore. That is the reason only gasified sea water drilling technique is involved in this research.

The simple answer to the question “Why drill underbalanced?” is that it can improve the financial returns on drilling the well. This improvement can come from a variety of different advantages from reducing the cost of drilling the well to increasing its productivity once drilled. When a well is drilled underbalanced, hydrocarbon production can begin as soon as a productive zone is penetrated. With suitable surface equipment, it is possible to collect oil while drilling. Some underbalanced wells have paid for themselves entirely from production before drilling operations were completed (GRI, 1997). However, in some areas where UBD has not been applied such as Vietnam, evaluating how much oil can be obtained from the reservoir during UBD has always been a difficult question to drilling engineers because the relationship between drilling and productivity parameters is quite complex. The study of coupling the production flow rate and drilling parameters in UBD has not been investigated fully so far, so this

research will focus on the approach which is established to evaluate the relationship of the production capacity and drilling hydraulic parameters, and to predict the productivity under UBD. Once this information is known, the advantage of UBD in comparison to overbalanced drilling (OBD) will be qualified. And this is the important factor for operators to decide whether UBD should be applied or not.

In the literature, there are just a few papers dealing with multiphase flow modeling and predicting production capacity in UBD. Butler and Gregory (1995), and Smith et al (1998) presented the application of multiphase flow modeling to UBD which was considered a key tool for UBD engineer to identify the bottomhole pressure and access how to achieve this target.

Guo (2002) presented three analytical models that are coded in a spreadsheet program to simulate solid, water, oil and gas flow in underbalanced drilling. These three models account for the influence of formation influx fluid and cover commonly used drilling fluids from air through stable foam to aerated liquid. The author specified the production capacity as the given data and independent to bottomhole pressure in his research.

However, multiphase modeling alone without coupling the inflow performance relationship (IPR) of the reservoir is not enough to evaluate the production capacity in UBD. Mykytiw, Suryanarayana, and Brand (2004) described a methodology of multiphase modeling in UBD with the present of reservoir inflow. According to the authors, faced with such a situation, UBD engineers typically resort to either specifying a volume of influx (without explicit consideration of the dependence of the volume on local productivity or drawdown), or simply modeling additional fluid injection and evaluating impact on the operating window. Unfortunately, as even the most rudimentary production analysis will reveal, this approach does not adequately capture the coupling between the inflow and wellbore pressure. Moreover, the IPR is almost always nonlinear with drawdown, and the nonlinearity should be respected in the prediction of influx volumes.

This following discussion describes an approach to model multiphase flow and estimate production capacity during UBD in which the influence of reservoir inflow and the nonlinearity of IPR are accounted for. The main contents of this paper include:

- The prospect of UBD application in Vietnam
- Modeling gasified sea water flow in UBD
- Predicting the production capacity in UBD
- Example study
- Conclusions

The prospect of UBD application in Vietnam

There are some oil companies in Vietnam interested in applying UBD for basement reservoirs. However, they have not utilised this technique so far resulting from the lack of thorough research about the ability of UBD application to Vietnam reservoirs, especially in granite basement formations.

First of all, the geological view points need to be surveyed to consider whether basement reservoirs in Vietnam are really good candidates for UBD or not. One of the most important problems in drilling is lost circulation while drilling caused by faults or fractures with large apertures up to 10 mm. Sometimes, severe lost circulation in drilling reached 40,000 bbl/well (Nguyen, 2006) causing pipe sticking and blow out because of the difference between wellbore pressure and formation pressure. Drilling engineers often proceed in two ways to limit this severe lost circulation:

(1) Using Lost Circulation Material (LCM) to prevent the invasion of drilling fluid into the formation. This method is used in limiting lost circulation but often causes formation damage.

(2) Filling the annulus with sea water to maintain the hydrostatic pressure then using sea water to drill through low pore pressure zones to reduce the cost of drilling mud through lost circulation. This solution is really effective because drilling by sea water is inexpensive. In the case of a kick, engineers close the annular space at the surface then pump sea water under high pressure through the drillstrings to push all drilling fluid and cuttings into the formation. It has not been known so far where sea water and cuttings lost in drilling will go because there is no trace of drilling sea water and cuttings in produced oil after kicking off. It may be that the fractures in this case are very large and communicate together.

Applying UBD in basement reservoirs of Vietnam may overcome these above difficulties because the low wellbore pressure helps to eliminate lost circulation problems while drilling. Besides, granite formations in the basement are often very hard, consolidated, and stable with the unconfined compressive strength (UCS) from 20,000 to 30,000 psi, and modulus of elasticity (E) approximately 60 GPa. It is possible to apply UBD because a good candidate for UBD requires the stability of the wellbore during drilling operations. Moreover, if conventional drilling is used to drill through hard rock formations, it will take a lot of time and cost. So, replacing conventional drilling by UBD will not only increase considerably penetration rate but also reduce the cost of drilling and saving time, and the cost of personnel and equipment. Last but not least, the fact that there are a lot of wells with skin factors of 5 or higher in basement reservoirs promoting them as good candidates for UBD.

Secondly, economical studies should be considered as well. Oil production and exploration industries of Vietnam are developing quickly. In addition to producing oilfields such as White Tiger, Big Bear,

Ruby, Pearl, Black Lion, Nam Con Son, there are a lot of oilfields having been discovered. These are planned for development. Therefore, the prospect of drilling oil wells of new oilfields and extending the exploration around the existing oilfields is significant. Applying UBD in Vietnam now has a very good market, especially when JVPC, Petronas, CuuLong JOC, and Vietsovpetro are carrying out drilling over thousands meters everyday and the oil price has increased significantly in recent years.

In summary, the granite basement reservoirs in Vietnam are prospective candidates for applying UBD. However, to ensure that the UBD projects will be profitable, the investigation and preparation should be evaluated carefully.

Modeling gasified sea water flow in UBD

Guo and Ghalambor (2002a) set up multiphase flow equations in UBD with the major assumption that the influence of cutting volume (not weight) on the annulus pressure is negligible. This is usually valid because the volumetric flow rate of solid is normally less than 5% of the total volumetric flow rate in gasified liquid (Guo and Ghalambor, 2002a). These equations formulate the pressure drop in each section along the wellbore in the case that the drilling fluid properties are assumed to be constant in the section of interest. So the method of Guo and Ghalambor (2002a) should be valid whenever the section length is small enough to satisfy the fact that the drilling fluid properties are constant. However, in equations developed by Guo and Ghalambor (2002a), they consider formation influx fluid flow rate, and liquid injection flow rate as constant while these values, in reality, are decided by the bottomhole pressure and formation volume factors so they will change correspondingly to pressure and temperature. Unfortunately, the pressure is the unknown parameter so the best way to solve this problem is to use a combination of the iterative method and the finite differential method, named IFD. The following borehole pressure equation is formulated on the first law of thermodynamics and the modification of equations of Guo and Ghalambor (2002a).

$$\frac{\Delta p}{\Delta L} = \rho_m \cos\phi + \frac{6\rho_m f_m v_m^2}{g d_H}, \quad (1)$$

where

ρ_m: mixture density, lb/ft^3

ϕ: wellbore inclination, degree

f_m: friction factor

v_m: mixture velocity, ft/s

$d_H = d_{out}$-d_{in}: hydraulic diameter of flow path, in

dL: length increment, ft

Because the volumetric flow rate of a solid is usually negligible (less than 5% of the total volumetric flow rate) in gasified fluid, the mixture density can be expressed as:

$$\rho_m = \frac{\dot{W}_s + \dot{W}_g + \dot{W}_l}{Q_g + Q_l}, \quad (2)$$

in which the weight rate of a solid $\dot{W}_s$ (lb/sec) depends on bit diameter d_b (in), rate of penetration R_p (ft/hr), and specific gravity of solids S_s.

$$\dot{W}_s = 62.4\frac{\pi}{4}\left(\frac{d_b}{12}\right)^2 S_s\left(\frac{R_p}{3600}\right) = 9.45\times10^{-5} d_b^2 S_s R_p, \quad (3)$$

The weight rate of gas $\dot{W}_g$ (lb/sec) depends on volumetric gas flow rate Q_{gs} (scf/min) at the surface condition and the specific gravity of gas S_g:

$$\dot{W}_g = \gamma_{air} S_g \frac{Q_{gs}}{60} = 1.275\times10^{-3} S_g Q_{gs}, \quad (4)$$

where

γ_{air} = 0.0765: specific weight of standard air, lb/ft^3

The weight rate of liquid $\dot{W}_l$ (lb/sec) depends on the sea water flow rate Q_x (gal/min) delivered by pump, formation fluid influx rate Q_f (STB/D), sea water density W_{x0} (kg/m^3) (Unesco, 1981) at surface conditions, and specific gravity of formation fluid related to fresh water S_f:

$$\dot{W}_l = 8.344\times10^{-3} W_{x0}\left(\frac{Q_x}{60}\right) + 62.4 S_f\left(\frac{5.615 Q_f}{3600\times24}\right) = 1.391\times10^{-4} W_{x0} Q_x + 4.056\times10^{-3} S_f Q_f, \quad (5)$$

The in-situ volumetric flow rate of gas Q_g (ft^3/sec) can be expressed through the real gas law (Beggs, 1991):

$$Q_g = B_g \frac{Q_{gs}}{60} = \frac{p_{sc} Z(T+460)}{T_{sc} p} \frac{Q_{gs}}{60} = \frac{14.7 Z(T+460)}{520 p} \frac{Q_{gs}}{60} = 4.711 \times 10^{-4} \frac{(T+460)}{p} Q_{gs}, \quad (6)$$

where

B_g: gas formation volume factor, ft^3/scf

T: temperature, ^oF

p: pressure, psia

Z: compressibility factor

p_{sc}: standard pressure, 14.7 psia

T_{sc}: standard temperature, 520^oR

The volumetric flow rate of liquid Q_l (ft^3/sec) can be expressed in terms of sea water volume factor B_x (bbl/STB) which can be derived in Appendix A (Unesco, 1981), and fluid formation volume factor B_f (bbl/STB) (Beggs, 1991):

$$Q_l = \frac{0.1337 Q_x B_x}{60} + \frac{5.615 Q_f B_f}{3{,}600 \times 24} = 2.2283 \times 10^{-3} Q_x B_x + 6.499 \times 10^{-5} Q_f B_f, \quad (7)$$

Mixture velocity in the annulus v_m (ft/sec) is calculated by the formula:

$$v_m = \frac{Q_g + Q_l}{A} = \frac{Q_g + Q_l}{\frac{1}{144} \frac{\pi}{4} (d_{out}^2 - d_{in}^2)}, \quad (8)$$

where

A: cross sectional of flow path area, ft^2

d_{out}: outside diameter, in

d_{in}: inside diameter, in

Nikuradse's friction factor f_m (Nikuradse, 1933) in Eq. 1 can be calculated from the equation:

$$f_m = \left[\frac{1}{1.74 - 2\log\left(\frac{2\varepsilon}{d_H}\right)} \right]^2, \quad (9)$$

In the annulus, the outside roughness can be the borehole roughness if the well is open hole completed or casing roughness if completed with casing. In that case, the borehole roughness often falls into the range from 0.06 to 0.12 in, and the roughness of commercial steel casing is 0.0018 in. The inside roughness is the roughness of the outside drillpipe which approximates 0.0018 in.

$$\varepsilon = \left(\frac{\varepsilon_{out} d_{out} + \varepsilon_{in} d_{in}}{d_{out} + d_{in}} \right), \quad (10)$$

The IFD approach is suggested to solve the differential Eq. 1. The fundamentals of the IFD approach and the method of Guo and Ghalambor (2002a) are the same. However, the IFD method solves the borehole pressure equation by combining the iterative method and finite differential method in which variables of this equation such as mixture density and mixture velocity are modified by adding parameters such as formation volume factors to account for the alteration of fluid volume along the wellbore, compressibility factor to calculate the gas compressibility, and sea water properties to apply for gasified sea water drilling. The IFD method can be presented in the following steps:

1. With the given $\Delta L = L/n$, for example 50 ft, it was assumed the respective Δp_s = 5 psi. So the average pressure and temperature in this length increment are $p_{av} = p_s + \Delta p_s/2$, and $T_{av} = T_s + G\Delta L/2\cos\phi$ with G, T_s, and p_s are geothermal gradient, surface temperature, and surface choke pressure. Notice that the smaller ΔL, the better the result, however, the longer the run time.

2. At this average pressure and temperature, all parameters on the right hand of Eq. 1 are calculated to give Δp_c on the left hand.

3. The assumed and calculated values of pressure drop in steps 1 and 2 are compared. If they are not sufficiently close, use Δp_c as the new Δp_s and go to step 1. Repeat steps 1 through 2 until the assumed and calculated values are sufficiently close.

4. Continue to the next section until the total $\sum \Delta L = L$. L is measured depth (ft) which is based on trajectory shape.

All steps above are applied to solve the pressure gradient equation in the annulus. According to the pressure gradient equation in the drillpipe, the calculation will be carried out from the bottom hole to the surface. So, p_{av} and T_{av} in step 1 will be $p_{av} = p_{bot} + \Delta p_s/2$ and $T_{av} = T_{bot} - G\Delta L/2\cos\phi$.

These algorithms will help to model the pressure, temperature and drilling fluid properties both in the annulus and inside the drillpipe. As a result, modeling gasified sea water flow in UBD can be simulated by the IFD approach as suggested.

Predicting the production capacity in UBD

When a well is drilled underbalanced, formation fluids flow into the wellbore from any permeable formation in the openhole section. It should be possible to use the volumes of produced hydrocarbons, from a well drilled underbalanced, to give an indication of the productivity of any pay zones that have been penetrated (GRI, 1997). Therefore, estimating this produced hydrocarbon volume while UBD helps the operator to calculate the productivity capacity of the reservoir and to make a more accurate decision. The coupling of the production flow rate and drilling parameters in UBD work will be accomplished by the opposite approach in which well data and reservoir data are collected from historical conventional wells. Then, these input data can be used to estimate how much formation fluids can be produced in the case of UBD. This work is fulfilled by the following steps:

Step 1: establishing the inflow performance relationship

A plot of production rate versus bottomhole flowing pressure (p_{wf}) is produced. Although the form of the IPR equation can be quite different for various types of fluids, the basic equation on which all of various forms are based is Darcy's Law (Beggs, 1991). The IPR can be set up through correlations such as Vogel (1968), Standing (1970), Fetkovich (1973), and Jones, Blount and Glaze (1976) for a variety of well types from vertical to inclined, or even fractured horizontal wells (Appendix B). Most of these correlations require at least one stabilized test on a well, and some require several tests in which Q_f and p_{wf} were obtained. The result of IPR is the set of data of Q_f versus p_{wf} or the relationship in terms of $Q_f = f(p_{wf})$ when formulated through the above correlations. The IPR data are collected from well test data of historical conventional wells in the same reservoir and used as the input data in this work.

Step 2: coupling the production flow rate and drilling parameters in UBD

The bottomhole flowing pressure is expressed as:

$$p_{wf} = \sum_{i=1}^{n} \Delta p \,, \qquad (11)$$

The borehole pressure Eq. 1 can be written as:

$$\Delta p = \left(\rho_m \cos\phi + \frac{6\rho_m f_m v_m^2}{g d_H} \right) \Delta L = \left(\rho_m \cos\phi + \frac{6\rho_m f_m v_m^2}{g d_H} \right) \left(\frac{L}{n} \right), \qquad (12)$$

in which n is the number of divided sections along the well trajectory.

So the bottomhole pressure can be calculated by the equation:

$$p_{wf} = \sum_{i=1}^{n} \Delta p_i = \sum_{i=1}^{n} \left(\rho_m \cos\phi + \frac{6\rho_m f_m v_m^2}{g d_H} \right)_i \left(\frac{L}{n} \right), \qquad (13)$$

ρ_m, v_m, and f_m in Eq. 13 are average values in each section of interest and can be calculated by Eqs. 2, 8, and 9.

Substituting $Q_f = f(p_{wf})$ from step 1 (obtained from historical drilled wells in the same reservoir) into Eqs. 2 and 8 gives:

$$\rho_m = \frac{9.45\times10^{-5} d_b^2 S_s R_p + 1.275\times10^{-3} S_g Q_{gs} + 1.391\times10^{-4} W_{x0} Q_x + 4.056\times10^{-3} S_f f(p_{wf})}{4.711\times10^{-4} \dfrac{(T+460)}{p} Q_{gs} + 2.2283\times10^{-3} Q_x B_x + 6.499\times10^{-5} f(p_{wf}) B_f}, \qquad (14)$$

$$v_m = \frac{4.711\times10^{-4} \dfrac{(T+460)}{p} Q_{gs} + 2.2283\times10^{-3} Q_x B_x + 6.499\times10^{-3} f(p_{wf}) B_f}{\dfrac{1}{144}\dfrac{\pi}{4}(d_{out}^2 - d_{in}^2)}, \qquad (15)$$

Step 3: solving the coupling equations

Eqs. 12 to 15 can be solved by numerical methods (**Fig 1**) and the results obtained from this solution are the bottomhole flowing pressure (p_{wf}), the gradient pressure along the wellbore, and the estimated hydrocarbon rate in UBD.

a. Assuming that the bottomhole pressure is p_{wfe}.

b. With the given $\Delta L = L/n$, for example 50 ft, it was assumed the respective Δp_s = 5 psi. The average pressure and temperature therefore in this length increment are $p_{av} = p_s + \Delta p_s/2$, and $T_{av} = T_s + G\Delta L/2\cos\phi$.

c. At this average pressure and temperature, all parameters on the right hand of Eq. 12 are calculated to give Δp_c on the left hand. Note that the value of p_{wf} substituted into Eq. 14, and Eq. 15 to solve Eq. 12 is the assumed value p_{wfe} of the step a.

d. The assumed and calculated values of pressure drop in steps b and c are compared. If they are not sufficiently close, use Δp_c as the new Δp_s and go to step b. Repeat steps b through c until the assumed and calculated values are sufficiently close.

e. Continue to the next section until the total $\sum \Delta L = L$, so the bottomhole pressure p_{wfc} will be calculated.

f. The calculated bottomhole pressure, p_{wfc} will be compared with the estimated bottomhole pressure in step a, p_{wfe}. If p_{wfc} and p_{wfe} are sufficiently close, it means the bottomhole pressure is accurate; otherwise a new estimated value of bottomhole pressure will be used.

Example study

This research applies UBDRILL, a simulation tool codified from the IFD method and the equations presented to perform thorough investigations of the multiphase flow in a directional well, and to estimate production flow rate in UBD. Assume an 14,340 ft MD deep well (**Figs. 2 and 3**) is to be drilled underbalanced in Basin X of South Vietnam using gasified sea water as a circulating fluid at an ROP of 30 ft/hr. The input parameters used in this example (Nguyen, 2006) are summarized from **Tables 1** to **3** including IPR data (**Table 1**), well structure data (**Table 2**), drilling and PVT data (**Table 3**). The results of this calculation are shown in **Tables 4** to **5**.

The graphical results include fluid property gradient profiles, pressure gradient profiles (**Figs. 4** to **7**), bottomhole pressure and predicted production flow rate corresponding to gas-liquid injection rates (**Figs. 8** to **9**). The first group (Figs. 4 to 7) is simulated to verify the accuracy of the IFD method and UBDRILL program, and to serve for the calculation of the second group (Figs. 8 to 9) which is the main result of this paper. In order words, these final results (bottomhole pressure, and production capacity) can only be accepted whenever the intermediate results (fluid property gradients) used to calculate them are accepted. Therefore, the purpose of modeling fluid property gradient is to ensure the accuracy of the main results as no research else has been published to compare.

Fig. 4 presents the distribution of drilling fluid density in the annulus. The general trend of this parameter is that the mixture density increases correspondingly to the development of pressure from the surface to the bottomhole. Its alteration is inversely proportional to that of gas injection rates. So the mixture density of drilling fluid in the annulus while UBD can be reduced by increasing the gas injected volume. According to the calculated results, the values of gasified sea water density under in-situ borehole conditions is between 50 to 58 lbm/ft^3 (6.7-7.7 lbm/gal) while values stated in Underbalanced drilling manual (GRI, 1997) is from 4 to 7 lbm/gal. This difference is definitely accepted because the alteration of in-situ conditions, gas density, and liquid-gas injection rates will also lead to the difference of mixture density. Therefore, the verification of calculated mixture density proved that this result is possible at least in comparison to results stated in the previous research (GRI, 1997). Fig. 5 displays the mixture velocity gradient of drilling fluid in the annulus while UBD. Notice that the mixture here includes liquid phase from penetrated formations and from the injection, gas phase from the injection, and solid phase of cuttings in drilling mud. There are two remarkable changes of mixture velocities in the annulus. The first one is from the surface to 4,500 ft. In this section, the mixture velocity reduces considerably because the reducing gas formation volume factor makes the gas volume in the mixture decrease. In the second section (7,439-14,340 ft), mixture velocities change because the well diameter reduces from 12.615 through 8.681 to 8.5 inch, and drillpipes (4 ½ inch OD) were replaced by drill collars (4 ¾ and 5 inch OD). Fig. 6 shows the friction factor in the annulus and this value changes significantly in the last sections once the openhole interval is drilled in horizontal direction with the narrowed annulus diameter and the increased borehole roughness.

Pressure gradient profiles are set up as observed in Fig. 7. This parameter has been contributed to significantly by surface choke pressure, liquid-gas injection flow rates, and drilling fluid density. Any change of these will cause the alteration of wellbore pressure which affects the production capacity in UBD operations. The graphical results plotted from Figs. 3 to 6 show clearly the properties of drilling fluid in the annulus and this is an intermediate step used to estimate the bottomhole pressure (**Table 4** and **Fig. 8**), and production flow rates in UBD (**Table 5** and **Fig. 9**).

The answer for the question how much oil can be produced while UBD is shown in Table 5 when liquid injection rates are set up from 500 to 700 gal/min, and gas injection rates from zero to 1200 scf/min. Combinations of sea water flow rates and gas injection rates will give different values of formation fluid influx flow rates. For example, if the sea water flow rate is 600 gal/min and gas injection rate is 120 scf/min, the formation influx fluid flow rate will equal zero because this combination is in range of overbalanced drilling (OBD) when it gives a bottomhole pressure of approximately 5,045 psia (see Table 4) which is higher than the formation pressure. It means that the UBD condition does not remain. In another combination of sea water and air flow rate, 600 gal/min and 480 scf/min, the production capacity can be estimated approximately 1,196 STB/D corresponding to the bottomhole

pressure of 4,698 psia. This pair of values (1,196 STB/D, and 4,698 psia) must be located on the IPR in the coupled solution so it can be verified by interpolating the IPR. According to Table 5, it is also observed that the lowering sea water rate will increase the production rate and the increasing gas injection rate will increase the production capacity.

Briefly, coupling productivity in UBD can help to qualify the produced oil capacity from the formation into wellbore in UBD operations. However, these production rates corresponding to the given sea water rates and gas injection rates then must be checked to ensure that they satisfy the Liquid Gas Rate Window conditions (UBD condition, cuttings carrying capacity criterion, collapse pressure limit criterion) (Guo and Ghalambor, 2002b). At the end, values will be compared to select the maximum values of formation influx fluid (oil). And the combination of gas injection rate and sea water flow rate which gives the maximum of production oil is the optimum combination.

Conclusions

All calculation steps presented will help not only to formulate the distribution of pressure, temperature, drilling fluid properties along the wellbore, and bottomhole pressure but also to predict the formation influx flow rate while UBD. Therefore, the success of coupling the productivity and UBD parameters will supply two important results. First of all, the estimation of production rate made while UBD will support enough information that drillstem testing is not required. From that, it will reduce the cost of evaluating the well because rig time is reduced by not having to make a round trip, rig up and rig down the test tool. Secondly, it will introduce an approximate figure of the financial return prospect to the investment once the operator is able to predict the production rate in UBD operations.

Nomenclature

A = *cross sectional of flow path area, ft^2*
B_f = *fluid formation volume factor, bbl/STB*
B_g = *gas formation volume factor, ft^3/scf*
B_x = *sea water formation volume factor, bbl/STB*
d_b = *bit diameter, in*
d_H = *hydraulic diameter of flow path, in*
dL = *length increment, ft*
d_{in} = *inside diameter, in*
d_{out} = *outside diameter, in*
E = *Young's module, MPa*
FE = *Flow Efficiency*
f_m = *Nikuradse's friction factor*
g = *acceleration of gravity, ft/s^2*
G = *geothermal gradient, $^oF/ft$*
IFD = *combination of **I**terative method and **F**inite **D**ifferential method*
IPR = *inflow performance relationship*
J = *productivity index, STB/D-psi*
K = *secant bulk modulus*
L = *measured depth, ft*
p = *pressure of interest, psia*
p_{av} = *the average pressure, psia*
p_b = *bubblepoint pressure, psia*
p_R = *reservoir pressure, psia*
p_s = *surface pressure, psia*
p_{wf} = *wellbore flowing pressure, psia*
p_{wfe} = *estimated bottomhole pressure, psia*
p_{wfc} = *calculated bottomhole pressure, psia*
Q_f = *formation fluid influx flow rate under the surface condition, STB/D*
$Q_{f(max)}$ = *inflow rate corresponding to zero wellbore flowing pressure, STB/D*
Q_g = *volumetric flow rate of gas, ft^3/sec*
Q_{gs} = *volumetric of injected gas flow rate under the surface conditions, scf/min*
Q_l = *volumetric flow rate of liquid, ft^3/sec*
Q_{pump} = *maximum compressor rate, scf/min*
Q_s = *volumetric flow rate of solid, ft^3/sec*
Q_x = *sea water flow rate under the surface condition, gal/min*
R_p = *rate of penetration, ft/hr*
S_g = *specific gravity of gas related to air*
S_f = *specific gravity of formation fluid related to fresh water*
S_s = *specific gravity of solid (cutting)*
T = *temperature of interest, ^oF*
T_{av} = *the average temperature, ^oF*

T_s = *surface temperature,* ^oF
UBD = *underbalanced drilling*
UCS = *unconfined compressive strength, MPa*
v_m = *mixture velocity, ft/sec*
$\dot{W}_g$ = *weight flow rate of gas, lb/sec*
$\dot{W}_l$ = *weight flow rate of liquid, lb/sec*
$\dot{W}_s$ = *weight flow rate of solid, lb/sec*
W_{x0} = *sea water density under the surface condition, kg/m*^{3}
W_x = *sea water density under the in-situ condition, lbm/gal*
W_{xmow} = *the standard mean ocean water density, kg/m*^{3}
Z = *compressibility factor*
ε = *equivalent roughness, in*
ϕ = *wellbore inclination, degree*
ρ_m = *mixture density, lb/ft*^{3}
Δp_c = *calculated pressure drop, psi*
Δp_s = *assumed pressure drop, psi*
$\Delta p/\Delta L$ = *pressure gradient in the direction of flow*
γ_{air} = *specific weight of standard air, lb/ft*^{3}

References

Beggs, H.D. 1991. *Production Optimization Using Nodal Analysis*, 72-81. OGCI Publications, Tulsa.

Butler, S.D., and Gregory, G.A. 1995. Multiphase Flow Considerations in Underbalanced Drilling of Horizontal Wells. Presented at the BHR Group 7th International Conference-Multiphase 95, Cannes, France, June.

Fetkovich, M.J. 1973. The Isochronal Testing of Oil Wells. Paper SPE 4529 presented at SPE 48th Annual Fall Meeting, LA.

Gas Research Institute. 1997. *Underbalanced Drilling Manual*, GRI-97/0236, Gas Research Institute, Chicago, Illinois, USA.

Guo, B., and Galambor, A. 2002a. *Gas Volume Requirements for UBD Deviated Holes*. PennWell Corporation, Tulsa, Oklahoma.

Guo, B., Ghalambor, A. 2002b. An Innovation In Designing Underbalanced Drilling Flow Rates: A Gas-Liquid Rate Window (GLRW) Approach. Paper SPE 77237 presented at the IADC/SPE Asia Pacific Drilling Technology, Jakarta, Indonesia, 9-11 September.

Jones, L.G., Blount, E.M., and Glaze, O.H. 1976. Use of Short Term Multiple Rate Flow tests to Predict Performance of Wells Having Turbulence. Paper SPE 6133 presented at SPE 51st Annual Fall Meeting, New Orleans, LA.

Mykytiw, C., Suryanarayana, P.V., and Brand, P.R. 2004. Practical Use of a Multiphase Flow Simulator for Underbalanced Drilling Applications Design-The Tricks of the Trade. Paper SPE 91598 presented at the SPE/IADC Underbalanced Technology Conference and Exhibition, Houston, Texas, USA, 11-12 October.

Nguyen, V.K. 2006. Feasibility Study for the Implementation of Underbalanced Drilling in the Basin A, Offshore Vietnam. MSc dissertation, Heriot Watt University., Edinburgh.

Nikuradse, J. 1933. *A New Corellation for Friction Factor,* 301-307. Forschungshelf.

Smith, S.P., Gregory, G.A., Munro, N., and Muqeen, M. 1998. Application of Multiphase Flow Methods to Horizontal Underbalanced Drilling. Presented at the BHR Group 1th North American Conference on Multiphase Technology, Banff, Canada, June.

Standing, M.B. 1970. Inflow Performance Relationships for Solution Gas Drive Wells. *JPT* (November 1970).

Unesco 1981. *Background papers and supporting data on the international equation of state of seawater 1980*. Unesco tech, Pap. In Sci., **39**: 7-9

Vogel, J.V. 1968. Inflow Performance Relationships for Solution Gas Drive Wells. *JPT* (January 1968).

Appendix A

The density of the Standard Mean Ocean Water (SMOW) (kg/m^3) taken as pure water reference is:

$$W_{xmow} = a_0 + a_1\frac{T-32}{1.8} + a_2\left(\frac{T-32}{1.8}\right)^2 + a_3\left(\frac{T-32}{1.8}\right)^3 + a_4\left(\frac{T-32}{1.8}\right)^4 + a_5\left(\frac{T-32}{1.8}\right)^5, \qquad \text{(A-1)}$$

where

$a_0 = 999.842594$
$a_1 = 6.793952 \times 10^{-2}$
$a_2 = -9.095290 \times 10^{-3}$
$a_3 = 1.001685 \times 10^{-4}$
$a_4 = -1.120083 \times 10^{-6}$
$a_5 = 6.536332 \times 10^{-9}$
T: temperature, ^{o}F

The density of sea water W_{x0} (kg/m^3) at standard condition is computed from the water salinity $S(^o/_{oo})$ and the temperature (^{o}F) by the following equation:

$$W_{x0} = W_{xmow} + b_0 + b_1\frac{T-32}{1.8} + b_2\left(\frac{T-32}{1.8}\right)^2 + b_3\left(\frac{T-32}{1.8}\right)^3 + b_4\left(\frac{T-32}{1.8}\right)^4 + \left[c_0 + c_1\frac{T-32}{1.8} + c_2\left(\frac{T-32}{1.8}\right)^2\right]S\sqrt{S} + d_0S^2$$

, (A-2)

where

$b_0 = 8.24493 \times 10^{-1}$
$b_1 = -4.0899 \times 10^{-3}$
$b_2 = 7.6438 \times 10^{-5}$
$b_3 = -8.2467 \times 10^{-7}$
$b_4 = 5.3875 \times 10^{-9}$
$c_0 = -5.72466e \times 10^{-3}$
$c_1 = 1.0227 \times 10^{-4}$
$c_2 = -1.6546 \times 10^{-6}$
$d_0 = 4.8314 \times 10^{-4}$

The density of seawater W_x (kg/m^3) at in-situ condition is computed from the practical salinity (S), the temperature (^{o}F), and the applied pressure (psia):

$$W_x = \frac{W_{xo}}{1-\left(\frac{p}{14.7}\right)\left(\frac{1}{K}\right)}, \quad \text{(A-3)}$$

If the unit of density is pound per gallon (lbm/gal)

$$W_x = 8.344\times10^{-3}\frac{W_{xo}}{1-\left(\frac{p}{14.7}\right)\left(\frac{1}{K}\right)}, \quad \text{(A-4)}$$

K is secant bulk modulus given by:

$$K = K_0 + A_s\left(\frac{p}{14.7}\right) + B_s\left(\frac{p}{14.7}\right)^2, \quad \text{(A-5)}$$

$$A_s = A_{sw} + \left[i_0 + i_1\frac{T-32}{1.8} + i_2\left(\frac{T-32}{1.8}\right)^2\right]S + j_0S\sqrt{S}, \quad \text{(A-6)}$$

$$B_s = B_{sw} + \left[m_0 + m_1\frac{T-32}{1.8} + m_2\left(\frac{T-32}{1.8}\right)^2\right]S, \quad \text{(A-7)}$$

$$K_0 = K_{sw} + \left[g_0 + g_1\left(\frac{T-32}{1.8}\right) + g_2\left(\frac{T-32}{1.8}\right)^2\right]S\sqrt{S} + \left[f_0 + f_1\left(\frac{T-32}{1.8}\right) + f_2\left(\frac{T-32}{1.8}\right)^2 + f_3\left(\frac{T-32}{1.8}\right)^3\right]S,$$

(A-8)

where

$f_0 = 54.6746$
$f_1 = -0.603459$
$f_2 = 1.09987 \times 10^{-2}$
$f_3 = -6.1670 \times 10^{-5}$
$g_0 = 7.944 \times 10^{-2}$
$g_1 = 1.6483 \times 10^{-2}$
$g_2 = -5.3009 \times 10^{-4}$
$i_0 = 2.2838 \times 10^{-3}$
$i_1 = -1.0981 \times 10^{-5}$
$i_2 = -1.6078 \times 10^{-6}$
$j_0 = 1.91075 \times 10^{-4}$
$m_0 = -9.9348 \times 10^{-7}$
$m_1 = 2.0816 \times 10^{-8}$
$m_2 = 9.1697 \times 10^{-10}$

The pure water terms K_{sw}, A_{sw}, and B_{sw} of the secant bulk modulus are given by:

$$K_{sw} = e_0 + e_1\frac{T-32}{1.8} + e_2\left(\frac{T-32}{1.8}\right)^2 + e_3\left(\frac{T-32}{1.8}\right)^3 + e_4\left(\frac{T-32}{1.8}\right)^4, \quad \text{(A-9)}$$

$$A_{sw} = h_0 + h_1 \frac{T-32}{1.8} + h_2 \left(\frac{T-32}{1.8} \right)^2 + h_3 \left(\frac{T-32}{1.8} \right)^3, \qquad \text{(A-10)}$$

$$B_{sw} = k_0 + k_1 \frac{T-32}{1.8} + k_2 \left(\frac{T-32}{1.8} \right)^2, \qquad \text{(A-11)}$$

where

$e_0 = 19652.21$
$e_1 = 148.4206$
$e_2 = -2.327105$
$e_3 = 1.360477 \times 10^{-2}$
$e_4 = -5.155288 \times 10^{-5}$
$h_0 = 3.239908$
$h_1 = 1.43713 \times 10^{-3}$
$h_2 = 1.16092 \times 10^{-4}$
$h_3 = -5.77905 \times 10^{-7}$
$k_0 = 8.50935 \times 10^{-5}$
$k_1 = -6.12293 \times 10^{-6}$
$k_2 = 5.2787 \times 10^{-8}$

Seawater formation volume factor B_x (bbl/STB) is given by:

$$B_x = \frac{W_{x0}}{W_x} = \frac{1 - \left(\frac{p}{14.7} \right) \left(\frac{1}{K} \right)}{8.344 \times 10^{-3}}, \qquad \text{(A-12)}$$

Appendix B

The Vogel's equation for generating an IPR is:

$$Q_f = Q_{f(\max)} \left[1 - 0.2 \frac{p_{wf}}{p_R} - 0.8 \left(\frac{p_{wf}}{p_R} \right)^2 \right], \qquad \text{(B-1)}$$

where

p_R: reservoir pressure, psia
$Q_{f(max)}$: inflow rate corresponding to zero wellbore flowing pressure, STB/D

Standing proposed an equation to modify Vogel's method to account for either damage or stimulation around the wellbore:

$$Q_f = J(p_R - p_b) + \frac{J p_b}{1.8} \left[1.8 \left(1 - \frac{p_{wf}}{p_b} \right) - 0.8 (FE) \left(1 - \frac{p_{wf}}{p_R} \right)^2 \right], \qquad \text{(B-2)}$$

where

FE: flow efficiency
p_b: bubblepoint pressure, psia
J: productivity index, STB/D-psi

Table 1-Inflow Performance Relationship

Flow Rate (STB/D)	Pressure (psia)
0	5,000
988	4,750
1,963	4,500
2,894	4,250
3,777	4,000
4,613	3,750
5,403	3,500
6,145	3,250
6,840	3,000
7,488	2,750
8,089	2,500
8,643	2,250
9,150	2,000

9,610	1,750
10,023	1,500
10,388	1,250
10,707	1,000
10,979	750
11,203	500
11,381	250
11,505	15

Table 2-Well structure

MD (ft)	Angle (degrees)	Azimuth (Degrees)	Well Diameter (inch)	OD (inch)	ID (inch)	Annulus's Roughness (inch)	Drillpipe's Roughness (inch)
592	0	0	12.615	4.5	3.826	0.0018	0.0018
1,148	2.4	225	12.615	4.5	3.826	0.0018	0.0018
1,329	2.4	225	12.615	4.5	3.826	0.0018	0.0018
1,629	10.61	180	12.615	4.5	3.826	0.0018	0.0018
1,729	13.6	177	12.615	4.5	3.826	0.0018	0.0018
1,945	17.09	175.32	12.615	4.5	3.826	0.0018	0.0018
7,439	17.26	175.4	12.615	4.5	3.826	0.0018	0.0018
11,080	17.26	175.4	8.681	4.5	3.826	0.0018	0.0018
11,142	21.81	175.42	8.5	4.5	3.826	0.197	0.0018
11,342	26.36	175.42	8.5	4.5	3.826	0.197	0.0018
11,442	30.91	175.43	8.5	4.5	3.826	0.197	0.0018
11,542	35.46	175.43	8.5	4.5	3.826	0.197	0.0018
11,642	40.02	175.44	8.5	4.5	3.826	0.197	0.0018
11,742	44.57	175.44	8.5	4.5	3.826	0.197	0.0018
11,842	49.12	175.44	8.5	4.5	3.826	0.197	0.0018
11,942	53.67	175.44	8.5	4.5	3.826	0.197	0.0018
12,042	58.22	175.45	8.5	4.5	3.826	0.197	0.0018
12,142	62.78	175.45	8.5	4.5	3.826	0.197	0.0018
12,242	67.33	175.45	8.5	4.5	3.826	0.197	0.0018
12,342	71.88	175.45	8.5	4.5	3.826	0.197	0.0018
12,442	76.43	175.45	8.5	4.5	3.826	0.197	0.0018
12,542	80.98	175.45	8.5	4.5	3.826	0.197	0.0018
12,642	85.54	175.45	8.5	4.5	3.826	0.197	0.0018
13,377	90	175.46	8.5	4.5	3.826	0.197	0.0018
14,144	90	175.46	8.5	4.75	2.25	0.193	0.0018
14,340	90	175.46	8.5	5	2.25	0.190	0.0018

Table 3-Drilling & PVT data

Parameters	Input Data	Units	Notes
Bit Diameter (d_b)	8.5	in	
Specific Gravity of Solid Phase (S_s)	2.8		
Rate of Penetration (R_p)	30	ft/hr	
Rotary Speed	120	rpm	
Bit Nozzle Diameter (d_b)	0.625	in	$3 \times 20\ ^{1}/_{32}$
Formation Pressure (p_R)	5,000	psia	
Maximum compressor rate (p_{pump})	2,400	scf/min	
Bubble Point Pressure (p_b)	4,678	psia	
Surface Pressure (p_{sur})	80	psia	
Surface Temperature (T_{sur})	139	^{o}F	
Thermal gradient	0.01	^{o}F/ft	
Gas Gravity (S_g)	0.65		
API Gravity (API)	39.3		
Sea Water Salinity	35	$^{o}/_{oo}$	

Table 4-Bottomhole pressure					
Q_x (gal/min)	500	550	600	650	700
Q_{gs} (scf/min)	**Bottomhole pressure (psia)**				
0	5,132.33	5,152.96	5,173.06	5,194.53	5,215.22
120	4,967.87	5,007.91	5,045.57	5,081.99	5,115.90
240	4,814.04	4,871.01	4,924.02	4,973.65	5,019.35
360	4,670.84	4,742.25	4,808.43	4,869.50	4,925.54
480	4,538.28	4,621.65	4,698.77	4,769.54	4,834.50
600	4,416.34	4,509.19	4,595.07	4,673.77	4,746.21
720	4,305.04	4,404.87	4,497.31	4,582.20	4,660.68
840	4,204.36	4,308.71	4,405.50	4,494.82	4,577.90
960	4,114.32	4,220.69	4,319.63	4,411.63	4,497.88
1,080	4,034.91	4,140.83	4,239.72	4,332.63	4,420.62
1,200	3,966.13	4,069.11	4,165.74	4,257.83	4,346.11

Table 5-Formation fluid influx flow rate					
Q_x (gal/min)	500	550	600	650	700
Q_{gs} (scf/min)	**Formation fluid influx rate (STB/D)**				
0					
120	11.54	Overbalanced drilling region			
240	818.08	506.39	254.14	18.72	
360	1,318.50	1,092.45	793.73	539.55	251.99
480	1,834.54	1,517.50	1,196.06	945.64	681.80
600	2,267.24	1,930.91	1,617.22	1,301.94	1,063.77
720	2,659.55	2,309.31	1,981.07	1,670.79	1,351.77
840	3,017.43	2,657.12	2,317.93	1,996.25	1,689.19
960	3,345.49	2,978.36	2,630.90	2,300.26	1,983.88
1,080	3,647.76	3,276.06	2,922.59	2,585.09	2,261.22
1,200	3,927.31	3,553.10	3,195.43	2,852.59	2,522.75

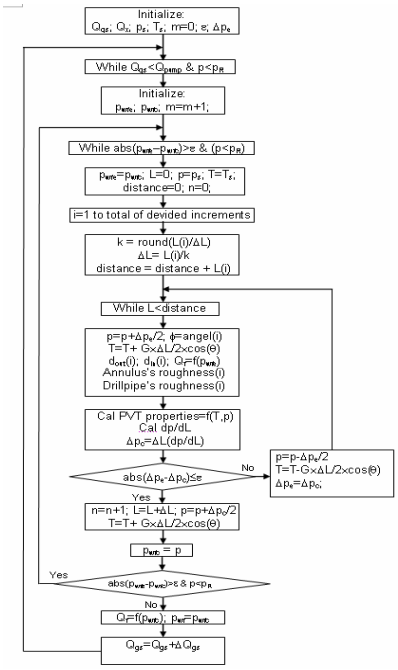

Fig. 1-Flow chart for calculating gradient pressure profiles

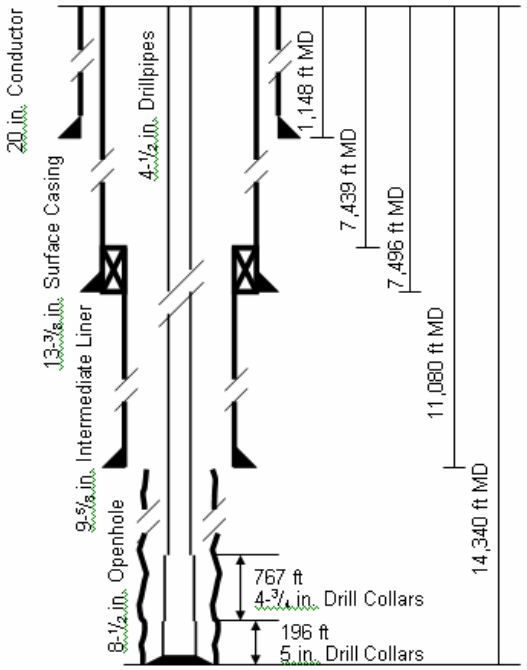

Fig. 2-Diagram of the well

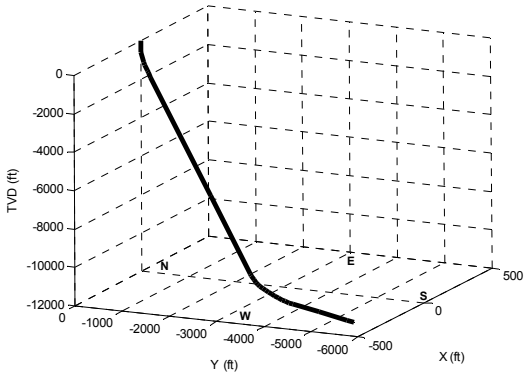

Fig. 3-Wellbore trajectory

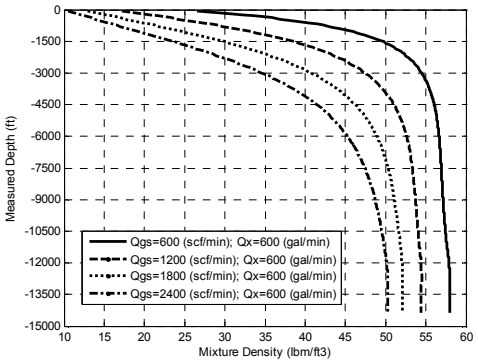

Fig. 4-Mixture density gradient in the annulus

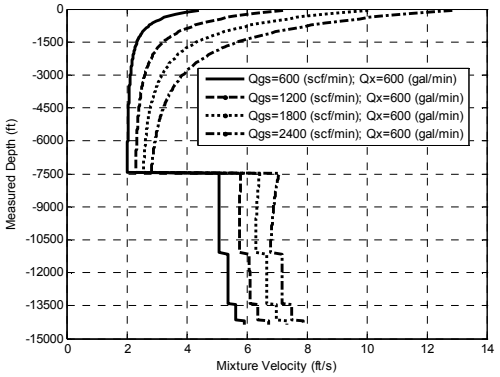

Fig. 5-Mixture velocity gradient in the annulus

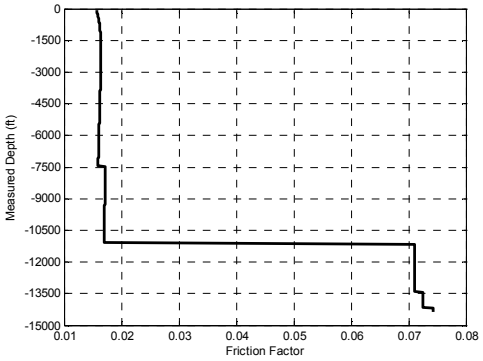

Fig. 6-Friction factor gradient in the annulus

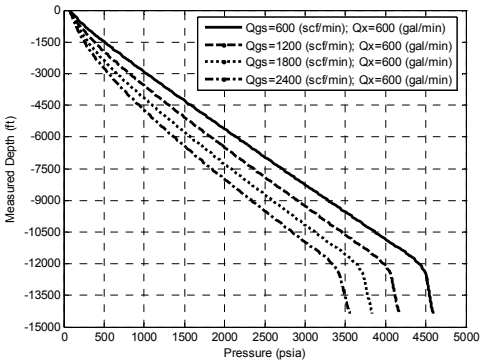

Fig. 7-Pressure gradient in the annulus

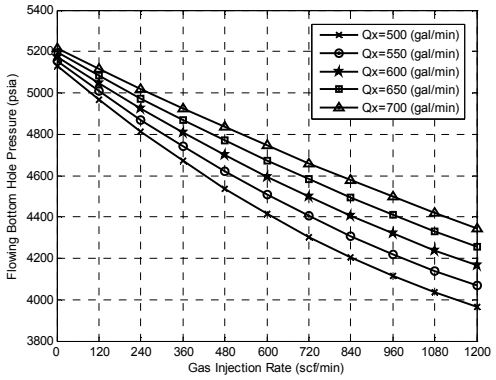

Fig. 8-Flowing bottomhole pressure

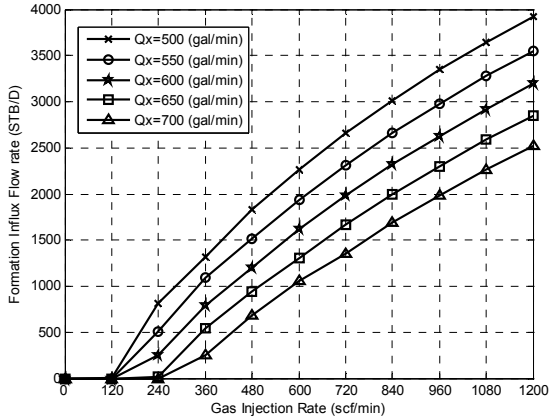

Fig. 9-Predicted formation influx flow rate

REFERENCES

[1] Bennion, D.B. et al.: "Underbalanced Drilling: Praises and Perils," SPE 35242 presented at the 1996 SPE Permian Basin Oil&Gas Recovery Conference, Midland, 27-29 March, 2006.

[2] McLennan, J. et al., *Underbalanced Drilling Manual*, GRI-97/0236, Gas Research Institute, Chicago, Illinois, U.S.A, 1997.

[3] Wong, A., and Arco, M.J.: "Use of Hollow Glass Bubbles as a Density Reducing Agent for Drilling," Paper No. 2001-31 presented at CADE/CAODC Drilling Conference held in Calgary, Alberta, Canada, 23-24 October, 2001.

[4] Arco, M.J. et.: "Field Application of Glass Bubbles as a Density-Reducing Agent," SPE 62899 was prepared for presentation at the 2000 Annual Technical Conference and Exhibition held in Dallas, Texas, 1-4 October, 2000.

[5] Weatherford Underbalanced Services.: "General Underbalanced Presentation to the DTI,", 2002.

[6] Saad E. Alajmi., Jerome J. Schubert.: "Optimum Selection of Underbalanced Techniques," SPE 85322 presented at Middle East Drilling Technology Conference & Exhibition held in Abu Dhabi, UAE, 20-22 October, 2003.

[7] Guo, B., and Rajtar, J. "Volume requirements for Aerated Mud Drilling. " *SPE Drilling & Completion Journal* (June 1995), pp. 23-30.

[8] Guo, B., Hareland, G., and Rajtar, J. "Computer Simulation Predicts Unfavorable Mud Rate and Optimum Air Injection Rate for Aerated Mud Drilling." *SPE Drilling and Completion Journal* (March 1996), pp. 25-34.

[9] Nguyen, V, K.: "*Feasibility Study for the Implementation of Underbalanced Drilling in the Basin A, Offshore Vietnam,"* MSc Thesis, Heriot Watt University, 2006.

[10] Hydmod, Maurer Engineering Ltd, Australia

[11] Charlez, P.A.: "*Rock Mechanics Theoretical Fundementals*," Vol 1, Editions Technip, Paris, 1991, pp. 136-181.

[12] Charlez, P.A.: "*Rock Mechanics Petroleum Application*," Vol 2, Editions Technip, Paris, 1997a, pp. 39-59.

[13] Farahani, H. S., Yu, M., Miska, S., Takach, N., Chen, G., "Modelling Transient Thermo-Poroelastic Effects on 3D Wellbore Stability," SPE 103159 presented at the 2006 SPE Annual Technical Conference and Exhibition held in San Antonio, Texas, U.S.A., 24-27 September, 2006.

[14] Alberto, L.M.: "Finite element modelling of the stability of single wellbores and multilateral junctions," PhD Dissertation, The University of Texas at Austin, Austin, Texas, U.S.A., 2003.

[15] Bradley, W.B.: "Failure of Inclined Boreholes," *J. Energy Res. Tech*. (Dec. 1979), 232 – 39. Trans. AIME, 101.

[16] Bradley, W.B.: "Mathematical concept – Stress Cloud can Predict Borehole Failure," The Oil and Gas Journal, (Feb. 1979).

[17] Biot, MA.: *"General Theory of Three-Dimensional Consolidation,"* Journal of Applied physics, 12 (Feb. 1941), 155-164.

[18] Skempton, A.W.: *"The Pore Pressure Coefficients A and B,"* Pore Pressure and Suction in Soils, Butterworths, (1954), 4-16.

[19] Rice, J.R, and Cleary, M.P.: *"Some Basic Stress Diffusion Solutions for Fluid-Saturated Elastic Porous Media with Compressible Constituents,"* Reviews of Geophysics and Space Physics, 14(2) (1976), 227-241.

[20] Bratli, R.K., Horsrud, P, and Risnes R.: *"Rock Mechanics Applied to the Region near wellbore,"* Proc. 5th International Congress on Rock Mechanics, (1983), F1-F17.

[21] Aadnoy, BS., and Chenevert, M.E.: "Stability of Highly Inclined Boreholes," *SPE Drilling Engineering* (Dec. 1987), p 364-374.

[22] Aadnoy, B.S.: *"Modelling of the Stability of Highly Inclined Boreholes in Anisotropic Rock Formations,"* SPE Drilling Engineering, (September 1988), 259-68.

[23] Jaeger, J.C., and Cook, N.G.W.: "*Fundamentals of Rock Mechanics,*" Third Edition. Chapman and Hall, London, (1979).

[24] McLean, M.R. and Addis, M.A.: *"Wellbore Stability: The Effect of Strength Criteria on Mud Weight Recommendations,"* paper SPE 20405 presented at the 65th Annual technique Conference and Exhibition of the SPE held in New Orleans, LA, (September 1990b), 9-17.

[25] Ong, S. H., and Roegiers, J. C.: *"Influence of Anisotropies in Borehole Stability,"* International Journal of Rock Mechanics and Mining Sciences and Geomechanics, (1993), Vol.30, No.7, 1069-1075.

[26] Detournay, E. and Cheng, A.: *"Poroelastic Response of a Borehole in a Nonhydrostatic Stress Field*," International Journal of Rock Mechanics and Mining Sciences and Geomechanics, (1988), Vol.25, No.3, 171-182.

[27] Cui, L., Cheng, A., and Abousleiman, Y.: *"Poroelastic Solution for an Inclined Borehole,"* Journal of Applied Mathematics, Transactions of the ASME, (March 1997), Vol.64.

[28] Yew, C.H. and Liu, G.: "Pore Fluid and Wellbore Stability," SPE 22381 presented at 1992 International Meeting on Petroleum Engineering, Beijing, China, Mar. 24-27.

[29] Fonseca, C.: "*Chemical-Mechanical Modelling of Wellbore Instability in shales,*" Ph.D. Dissertation, The University of Texas at Austin, Austin, Texas, (1998).

[30] Pan, X.D. and Hudson, J.A.: *"Plane Strain Analysis in Modelling Threedimensional Tunnel Excavations,"* International Journal of Rock Mechanics and Mining Sciences and Geomechanics. (1988), Vol.25, No.5, 331-337.

[31] Zienckiewicz, O.C. and Cormeau, I.C.: "*Visco-plasticity-plasticity and creep in elastic solids-a unified numerical approach,*" Int. J. Numer. Engr., (1974), Vol.8, 821-845.

[32] Ewy, R.T.: *"Yield and Closure of Directional and Horizontal Wells,"* International Journal of Rock Mechanics and Mining Sciences and Geomechanics, (1993), Vol.30, No.7, 1061-1067.

[33] Zervos, A., Papanastasiou, P., and Cook, J.: *"Elastoplastic Finite Element Analysis of Inclined Wellbores,"* paper SPE/ISRM 47322 presented at the Eurock '98 held in Trondheim, Norway, (July, 1998).

[34] Wang, Y.L., and Papamichos, E.: *"Conductive Heat Flow and Thermally Induced Fluid Flow Around a Wellbore in a Poroelastic Medium,"* Water Resources Research, 30(12), (Dec. 1994), 3375-3384.

[35] Yu, M., Chen, G., Chenevert, M.E. and Sharma, M.M.: *"Chemical and Thermal Effects on Wellbore Stability of Shale Formations,"* paper SPE 71366 presented at the SPE Annual Technical Conference and Exhibition held in New Orleans, Louisiana, (September 30 – October 3, 2001).

[36] Basement Drilling Workshop Seminar Document presented at Halong City, Vietnam, 9 August, 2003.

[37] Fjaer, E, R.M. Holt, P. Horsrud, A. M. Raaen and R. Risnes: *Petroleum related rock mechanics*, Elsevier Amsterdam, 1992.

[38] Coussy, O.: *Mécanique des Milieux Poreux*, Éditions technip, Paris, 1991.

[39] Watson, G.N.: *A Treatise on the Theory of Bessel Functions, 2nd ed*, Cambridge, England, Cambridge University Press, 1966.

[40] McLean, M.R. and Addis, M.A.: *"Wellbore Stability: A Review of Current Methods of Analysis and their Field Application,"* paper SPE 19941 presented at the 1990 SPE/IADC Drilling Conference, Houston, Texas, February 27-March 2, pp. 261-274.

[41] Bobo, R.A., and Barrett, H.M.: "Aeration of Drilling Fluid," *World Oil*, Vol 145, No 4, 1953, pp. 17-24.

[42] Murray, A.S., and Cunningham, R.A.: "Effect of Mud Column Pressure on Drilling Rates," *Trans. AIME*, Vol 204, 1955, pp. 196-204.

[43] Eckel, J.R.: "Effect of Pressure on Rock Drillability," *Trans. AIME*, Vol 213, 1957, pp. 1-6.

[44] Guo, B., Galambor, A.: *Gas Volume Requirements for UBD Deviated Holes*, Petroleum Extension Services, Austin, (2002).

[45] Guo, B., Ghalambor, A.: "An Innovation in Designing Underbalanced Drilling Flow Rates: A Gas-Liquid Rate Window (GLRW) Approach," SPE 77237, (2002), p 1.

[46] UNESCO 1981. "*Background papers and supporting data on the international equation of state of seawater 1980*." UNESCO tech, Pap. In Sci., No. 38, pp. 7-9

[47] Beggs, H. D.: "*Production Optimization Using Nodal Analysis*," OGCI Publications, Tulsa, 1991

[48] Standing, M. B. and Katz, D. L.: "*Density of natural gases*," Trans. AIME, 1942.

[49] Brill, J. P. and Beggs, H. D.: "*Two-Phase Flow in Pipes,*" Univ of Tulsa, Tulsa, OK, 1978.

[50] Standing, M. B.: "Inflow Performance Relationships for Solution Gas Drive Wells," JPT, Nov. 1970.

[51] Vogel, J. V.: "*Inflow Performance Relationships for Solution Gas Drive Wells*," JPT, Jan., 1968.

[52] Craft, B. C. and Hawkins, M. F.: "*Applied Petroleum Reservoir Engineering,*" Prentice-Hall, NJ 1959.

[53] Nikuradse, J. 1933. *A New Corellation for Friction Factor,* 301-307. Forschungshelf.

[54] Colebrook, C.F.: "*J. Inst. Civil Engrs*,", London, 1938.

[55] ITTC QS Group.: "Testing and Extrapolation Methods, General Density and Viscosity of Water," ITTC 22nd, 1999.

[56] Hutchison, S.O.: "Foam Workovers Cut Cost 50%," *World Oil*, Jan. 27, 1969, pp. 33-34.

[57] Hutchinson, S.O., and Anderson, G.W.: "Preformed Stable Foam Aids Workover, Drilling," *Oil & Gas Journal*, March 14, 1972, pp. 13-18.

[58] Bleakley, W.B.: "West Texas Workovers with Foam Gain Favor," *Oil & Gas Journal*, May 28, 1973, pp. 15-17.

[59] Essary, R.L., and Rogers, E.E., "Techniques and Results of Foam Redrilling Operations – San Joaquin Valley, California," Proceeding, 1976 Symposium on Formation Damage Control, SPE of AIME, pp. 237-244.

[60] Bentsen, N.W., and Veny, J.N.: "Preformed Stable Foam Performance in Drilling and Evaluating Shallow Gas Wells in Alberta," Journal of Petroleum Technology, July 1976, pp. 1237-1240.

[61] Lincicome, J.D.: "Using Foam to Drill Deep, Underpressured Zones," *World Oil*, Sep. 24, 1984, pp. 11-14.

[62] Anderson, G.W.: "Use of Preformed Foam in Low Pressure Reservoir Wells," Proceedings, SPE Offshore South East Asia Conference, 1984, pp. 17-26.

[63] Russell, B.A.: "How Surface Hole Drilling Performance Was Improved 65%," Proceedings, Drilling Conference, SPE/IADC, 1993, pp. 853-860.

[64] Guo, B.: "Use of Spreadsheet and Analytical Models to Simulate Solid, Water, Oil and Gas Flow in Underbalanced Drilling," SPE 72328, (2001).

[65] Moody, L.F.: "Friction Factor for Pipe Flow," *Trans. ASME*, Vol 66, 1944, pp. 671-685.

[66] Gray, K.E.: "The Cutting Carrying Capacity of Air at Pressures above Atmospheric," *Trans. AIME*, Vol 213, 1958, pp.180-185.

[67] Gilbert, W. E.: "Flowing and Gas-Lift Well Performance," API Drill. Prod. Practice, 1954.

[68] Collins, R. E.: "*Flow of Fluids through Porous Materials*," Reinhold Publishing Corporation NewYork, 1987.

[69] Haider, M.L.: "The Productivity Index," SPE 937112-G, Fort Worth Meeting, Oct. 1936.

[70] Golan, M., and Curtis, H.W.: "Well Performance," NUNU, Norway, Tapir Edition, 1996.

[71] Wattenbarger, R.A.: "Well Performance Equations," *Petroleum Engineering Handbook*, edited by H.B. Bradley et. al., 2nd cd., Society of Petroleum Engineers, Richardson, Texas (1987), 35-1-35-21.

[72] Standing, M. B.: "*Concerning the Calculation of Inflow Performance of Wells Producing from Solution Gas Drive Reservoirs*," JPT, Sept., 1971.

[73] Curtis, H. W.: "*Well Performance*," Prentice Hall, New Jersey, 1991.

[74] Fetkovich, M. J.: "The Isochronal testing of Oil Wells,": Paper 4529, 48th Annual Fall Meeting of SPE, Las Vegas, Nov., 1973.

[75] Jones, L. G., Blount, E. M., and Glaze, O. H.: "Use of Short Term Multiple Rate Flow tests to Predict Performance of Wells Having Turbulence," SPE 6133, presented at SPE 51st Annual Fall Meeting, New Orleans, LA, 1976.

[76] Thomas, L.K., Todd, B.J., Evans, C.E., and Pierson, R.G.: "Horizontal Well IPR Calculations," SPE 51396 presented at the 1996 SPE Annual Technical Conference and Exhibition, Denver, Colorado, 6-9 Oct 1996.

[77] Akhimiona, N., and Wiggins, M.L.: "An Inflow Performance Relationship for Horizontal Gas Wells," SPE 97627 presented at the 2005 SPE Eastern Regional Conference held in Morgantown, West Virginia, 12-16 September, 2005.

[78] Sherrard, D. W., Brice, W. B., and MacDonald, D. G.: "Application of Horizontal Wells at Prudhoe Bay," JPT, Nov., 1987.

[79] Bendakhlia, H., and Aziz, K.: "Inflow Performance Relationship for Solution-Gas Drive Horizontal Wells," SPE 19823, 64th Annual Fall Meeting of SPE, San Antonio, TX, Oct. 1989.

[80] PERFORM 3.0, Petroleum Information/Dwights LLC d/b/a IHS Energy Group, 1999.

[81] http://www.efunda.com/math/leastsquares/lstsqr2dcurve.cfm

[82] Matlab 7.0, MathWorks, 2003.

[83] Nguyen, K.C.: "*Applying Nodal Analysis to select the optimum tubing diameter,"* MSc Thesis, HoChiMinh City University of Technology, 2003.

[84] Becker, E.B., Carey, G.F., and Oden, J.T.: "Finite Elements an Introduction," Vol 1, Texas Institute for Computational Mechnics, The University of Texas Austin, Prentice-Hall, Inc, Enlewood Cliffs, New Jersey, 1981.

[85] Hibbitt, Karlsson, and Sorensen, Inc.: Abaqus/Standard User's Manual, Vol. 3, version 6.6, U.S.A, (2006).

[86] Starfield, A.M. and Cundall, P.A.: *"Towards a Methodology for Rock Mechanics Modelling,"* International Journal of Rock Mechanics, Mining, Sciences and Geomechanics, (1988), Vol.25, No.3, 99-106.

[87] Yu, M.: "*Chemical and Thermal Effects on Wellbore Stability of Shale Formations,"* PhD Dissertation, The University of Texas at Austin, Austin, Texas, U.S.A., 2002.

[88] Pacific Energy Corporation Seminar Document., "*Underbalanced Drilling Technology: Introduction & Its Application to Vietnam Fractured Basement,*", 2000.

[89] http://www.supercivillcd.com/THERMAL.htm